Characterization of Industrial Powder Metallurgy Produced 410L ODS Steel

Thesis

UNRESTRICTED

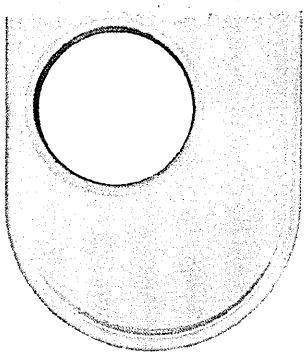

The Open University

Faculty of Mathematics, Computing & Technology

Department of Design, Development, Environment and Materials

Materials Engineering Group

CHARACTERIZATION OF INDUSTRIAL POWDER METALLURGY PRODUCED 410L ODS STEEL

by

ASIM ZEYBEK

June 2012

A THESIS SUMMITTED TO THE DEPARTMENT OF DESIGN, DEVELOPMENT, ENVIRONMENT AND MATERIALS OF THE OPEN UNIVERSITY FOR THE DEGREE OF DOCTOR OF PHILOSOPHY

Date of Submission: 15 June 2012

Date of Award: 14 November 2012

ProQuest LLC.
789 East Eisenhower Parkway
P.O. Box 1346
Ann Arbor, MI 48106 – 1346

PREFACE

This thesis is submitted for the degree of Doctor of Philosophy of The Open University. The work described in this dissertation was carried out in the Department of Materials Engineering of the Faculty of Technology, between October 2008 and June 2012, under the supervision of Prof. M. E. Fitzpatrick, Prof. P. John Bouchard and Dr. Jim Moffatt. It is an original work of the author except where reference is made to the work of others. None of this work is submitted or is in the process of submission in whole or part for a degree at any other university.

ASIM ZEYBEK

June 2012

CHARACTERIZATION OF INDUSTRIAL POWDER METALLURGY PRODUCED 410L ODS STEEL

ABSTRACT

The overall aim of this project is to characterize a powder metallurgy produced Oxide Dispersion Strengthened (ODS) 410L steel in terms of mechanical and microstructural analysis. An industrial/commercial existing production route was followed instead of a laboratory production. A professional powder metallurgy company did the production of the materials with high-tech manufacturing facility.

Materials were based on 12 Cr 410L steel. Four kinds of materials were manufactured based on 410L: "410L HIPed", which is 410L powder compacted via hot isostatic pressing (HIP) without mechanical alloying process; "410L MA", mechanically alloyed and then HIPed; "ODS 0.9 μm", mechanically alloyed 410L + 0.25 wt. % Y_2O_3 powder of 0.9 μm size and HIPed; and "ODS 50 nm", mechanically alloyed 410L + 0.25 wt. % Y_2O_3 powder of 50 nm size and HIPed.

Tensile tests and creep tests were performed for mechanical characterization. Yield strength and ultimate tensile strength of the samples at room temperature are comparable and around 680 MPa and 830 MPa respectively.

The best creep life belongs to non-ODS HIPed sample with a creep life of 679 hours at 625 °C under 75 MPa stress. Mechanical performance of the materials are found not promising when compared to other ODS alternatives from the literature, owing to compositional variations and non-metallic inclusions (up to 2 μm) in the materials. It was expected to have significant increase in the strength in ODS samples as it is seen in other ODS alternatives. However mechanical strengths of all the samples were comparable to each other.

The 410L powder was not clean with contaminations and many inclusions in it. Those inclusions are found as SiO_2 and MnS with scanning electron microscope (SEM) and energy dispersive X-Ray (EDX) analysis. These inclusions have a negative effect on mechanical behaviour of the materials as they ease void nucleation and propagation because of very weak interface bonds to the matrix. Another effect of SiO_2 particles are found as those particles play a role in formation of oxide clusters during mechanical alloying and high temperature compaction. It is concluded that either SiO_2 particles hinder Y_2O_3 dissolutions via reacting in ball milling and/or serving as nucleation sites to Y_2O_3 during precipitation. In both cases $Y_2Si_2O_7$ particles are observed due to the interaction between SiO_2 and Y_2O_3.

Small Angle Neutron Scattering (SANS) revealed pure Y_2O_3 particles in the system as well and clarified the effect of heat treatment on the size of oxide clusters. It is found that yttria particles had not been dissolving during ball milling. It is discovered that the size of the initial yttria powder is as important as the amount. Heat treatment increases the size of the Y_2O_3 particles but decreases

the size of complex $Y_2Si_2O_7$ particles. This can be considered as there is a Y and/or Y_2O_3 move from complex particles to pure Y_2O_3 particles at high temperatures.

The main outcome of this project is: understanding possible manufacturing problems and contaminations due to industrial production route and causes on material performance; mechanical and material characterization of a novel ODS alloy from 410L matrix; effects of steel inclusions on ODS manufacturing like hindering yttria dissolution and/or chemical interaction with yttria and forming complex oxides; importance of size of initial yttria powders on ODS manufacturing.

ACKNOWLEDGEMENTS

First of all, I would like to acknowledge The Open University for this great opportunity and financial support for my PhD studies. Funding from EPSRC is greatly acknowledged.

I would like to thank to all my supervisors especially Prof. Mike Fitzpatrick for assistance and guidance during my studies and also support and encouragement for my motivation.

Thanks to Mike Drew, Elizabeth Budzakoska-Testone and Bob Harrisson from ANSTO for great support and help during my studies at ANSTO.

I am also grateful to high skilled technicians in our group: Peter Ledgard for his high-skilled workshop assistance, Stan Hiller for his instruction and help on metallography and mechanical testing, and Gordon Imlach for his support and advice on electron microscopy, Colin Gagg for creep tests. Thanks also to other staff; Ian, Courtney and Angie.

I am grateful to my housemates, sincere fiends for more than 7 years, colleagues, and countrymen: Dr. Murat ACAR and Burak TOPARLI. Years we had in UK are unforgettable. Special thanks to Sanjoo PADDEA and Yeli TRAORE for their great support and help and most important one great friendship. Thanks to

all of my sincere friends in Turkey, UK and USA for their emotional support and help, especially Emre GULTURK for cheerful and encouraging conversations.

I have had the pleasure of working with a number of students within the group. Their assistance during these years has been invaluable. Thanks to Dr. Kashif KHAN, David GITHINJI, Jino MATTHEW, Bilal AHMAD, Yuki PHILIPS, Dr. Sue STORER, Genoveva BURCA and especially Dr. Soraia BARROSO for helps inmy studies and Dr. Boon CHONG for great help and effort for SANS experiment and all others.

Finally, my deepest and sincere regards to my family for all their encouragement, good wishes and support.

ASIM ZEYBEK

June 2012

TABLE OF CONTENTS

LIST OF FIGURES

Chapter 2:

Chapter 3:

LIST OF TABLES

Chapter 3:

Chapter 4:

CHAPTER 1: INTRODUCTION

1.1 Background and Aim

Energy is fundamental to the quality of our lives. Nowadays, we are totally dependent on an abundant and uninterrupted supply of energy for living and working. It is a key ingredient in all sectors of modern economies [1]. Some major techniques to produce this energy are, wind energy, solar energy, hydro energy, geothermal energy, fossil fuel energy and nuclear energy. Nuclear energy's role in the total energy production is rapidly increasing and probably it will be the leading energy production technique in the future.

Fundamental mechanism in Nuclear energy is the conversion of atomic energy to heat energy via nuclear fission and then to mechanical energy by using steam turbines. Turbine rotation is directly transferred to generators to produce electricity. About 14 % of the world's electricity is coming from nuclear power plants [2]. Building new nuclear power plants in all over the world shows the demand and importance of nuclear energy for countries.

For more reliable and safe nuclear energy, structural components of these power plants shall be selected and produced very carefully. Otherwise maintenance of those components will cause huge loss in terms of cost and electricity production. For example life and stability of the structural components are major concerns for maintenance as poor performance of the materials causes frequent maintenances so start up and shut downs which make a huge loss.

Operating conditions are the main elements for material selection as components operate at high temperatures and under radioactive environment.

The current most common commercialised fission reactors, also known as generation III, work at approximately temperature range of 250-300 °C, pressure range of 7-15 MPa and displacement per atom (dpa) range of 10-25. Future innovative nuclear systems and technologies, Generation III, and 4th Generation nuclear power plants, defined by acronym GEN IV, have designs much more demanding on material performance. GEN IV designs operate at the range 300-1100 °C, 0.1-24 MPa and displacement per atom at the order of 10-150.

New generation nuclear power plants need to operate at higher temperatures and pressures to increase their efficiency. These harsh conditions call for materials with better mechanical properties. Ferritic-martensitic steels have been identified as possible structural and/or cladding materials. At the upper temperature, creep, corrosion, and/or fuel cladding chemical interactions (FCCI) will be the lifetime-limiting mechanisms for the steels [3]. Proposed materials shall not weaken too much by temperature and shall not get affected by point defects nucleated in the system due to radiation displacement. This has resulted in focussing structural material research on ferritic-martensitic (F/M) steels. Presently, F/M steels are the primary candidate for the components, like pressure headers and main stem pipes, on the advanced reactor systems [4]. Dispersion strengthening appears to be one of the most promising approaches to widening the operating temperature window of structural materials [5]. By dispersion strengthening it is aimed that dispersions will hinder dislocation motion and help

to maintain mechanical strength at high temperatures [6]. Dispersions are also important for acting as trapping sites for nucleated radiation defects in the system [7]. So modifying F/M steels with dispersion particles is developed for both fossil fired and nuclear structural materials.

Using oxides like yttria and/or titania as dispersions is the only way of producing dispersion strengthened nuclear structural materials because of high temperature stability of yttrium and titanium oxides. Those materials are called oxide dispersion strengthened (ODS) materials. These materials are being developed and investigated for nuclear fission and nuclear fusion applications in India, Japan, Europe and the United States [8]. Recent study shows that; oxide dispersion strengthened tempered martensitic steels appear to be promising candidates for the future fusion reactors [9-11]. Powder metallurgy is the method of producing these ODS steels [5, 12, 13]. Powder metallurgy provides a feasible way of manufacturing components with complex shapes and advantages good dimensional precision and good isotropic mechanical properties. Consolidation of a mechanically alloyed powder by hot isostatic pressing (HIP) is one of the most common ways of compaction. Dissolution of the oxide powders during mechanical milling and precipitation of oxide particles during compaction are the main steps of producing ODS steels. More details about ODS steels are mentioned in later chapters.

The overall aim of this project is to characterize a powder metallurgy produced Oxide Dispersion Strengthened (ODS) 410L steel in terms of mechanical and microstructural analysis. An industrial/commercial existing production route

is followed instead of a laboratory production. Production of the materials was done by a professional powder metallurgy company, Aerospace Metal Composites (AMC), with high tech manufacturing facility. 410L is an off the shelf extensively tested basic 12% Cr martensitic steel, dispersed with yttria to make it an ODS steel. Four different materials are produced based on 410L steel. One non-ODS materials is just compacted via HIP without mechanical alloying (MA) and considered as just HIPed; an other material was first mechanically alloyed then compacted so is identified as MA. The ODS materials were first mechanically alloyed with yttria and then compacted. Two sizes of yttria particles were used, 0.9 μm and 50 nm. One other important point of this project is also to determine the effect of powder metallurgy and mechanical alloying on mechanical properties. Tensile and creep tests are used to determine mechanical properties at room and high temperatures. For microstructural characterization before and after tests, optical and electron microscopy are utilized. Energy dispersive X-Ray Spectroscopy (EDX) is used for particle analysis and composition determination.

1.2 Structure of Thesis

This thesis is formed of seven chapters. Figures, tables and references are at the end of each chapter. The structure of the thesis is as follows:

In chapter 2, after some basic information, types and properties of stainless steels and 410L martensitic steel, material strengthening mechanisms are explained for better understanding of ODS materials as they are dispersion strengthened materials. There is a separate ODS steel section explaining these

steels in detail and importance for nuclear industry. The production route of powder metallurgy is explained in details. Basic requirements of nuclear structural materials and how ODS steels cover those requirements are mentioned. Finally basic principals about creep are explained.

The experimental methods and test specimens used in this project are described in chapter 3. Microscopic techniques as well as mechanical tests are explained in detail of how they are applied and what results can be achieved after that analysis.

Mechanical property determinations are presented in chapter 4. Results of mechanical tests are explained in this section. Comparisons of tests with each other are carried out via graphs and mechanical parameters like strain rate and Larsson Miller Parameter (LMP) and some conclusions related to the mechanical tests are mentioned.

Chapter 5 presents images from optical and electron microscopes for microstructural characterization and information about material properties. This chapter also includes effects of production technique on materials and reveals some inclusion formations and production faults like porosity in the materials before and after tests.

Chapter 6 is about discussion of the obtained results. Results of mechanical properties and material characterization are discussed in detail and their correlations are explained. Comparisons with other ODS alternatives are

mentioned and possible reasons and solutions to differences are covered. Effect of some manufacturing related problems on mechanical properties and their mechanisms during tests are investigated. Potential roots of manufacturing problems are mentioned and suggestions to overcome those problems are stated. Small angle neutron scattering (SANS) results are discussed to clarify the case of yttria during mechanical alloying. Some cluster formations like $Y_2Si_2O_7$ in the material are characterized and their effect and relation with other formations are discussed.

Finally chapter 7 presents a conclusion to sum up what is covered in this project and what is the main outcome of the work and what else can be done to take forward this project and broaden this research and area of interest.

References

1. *European Commission.* Available from: http://ec.europa.eu/research/energy/gp/gp_imp/article_1081_en.htm [Accessed May 2011]
2. *World Nuclear Association.* Available from: http://www.world-nuclear.org/info/inf16.html [Accessed May 2011]
3. Klueh, R.L., *Elevated temperature ferritic and martensitic steels and their application to future nuclear reactors.* International Materials Reviews, 2005. **50**(5): p. 287-310.
4. Sakasegawa, H., S. Ohtsuka, S. Ukai, H. Tanigawa, M. Fujiwara, H. Ogiwara, and A. Kohyama, *Particle size effects in mechanically alloyed 9Cr ODS steel powder.* Journal of Nuclear Materials, 2007. **367-370**(Part 1): p. 185-190.
5. de Castro, V., T. Leguey, A. Muñoz, M.A. Monge, P. Fernández, A.M. Lancha, and R. Pareja, *Mechanical and microstructural behaviour of Y2O3 ODS EUROFER 97.* Journal of Nuclear Materials, 2007. **367-370**(Part 1): p. 196-201.
6. Furrer, D.U. and S.L. Semiatin, *ASM Handbook, Volume 22A - Fundamentals of Modeling for Metals Processing*, ASM International. p. 383.
7. Aleev, A.A., N.A. Iskandarov, M. Klimenkov, R. Lindau, A. Möslang, A.A. Nikitin, S.V. Rogozhkin, P. Vladimirov, and A.G. Zaluzhnyi, *Investigation of oxide particles in unirradiated ODS Eurofer by tomographic atom probe.* Journal of Nuclear Materials. **409**(2): p. 65-71.
8. Klueh, R.L., J.P. Shingledecker, R.W. Swindeman, and D.T. Hoelzer, *Oxide dispersion-strengthened steels: A comparison of some commercial and experimental alloys.* Journal of Nuclear Materials, 2005. **341**(2-3): p. 103-114.
9. Ramar, A., P. Spätig, and R. Schäublin, *Analysis of high temperature deformation mechanism in ODS EUROFER97 alloy.* Journal of Nuclear Materials, 2008. **382**(2-3): p. 210-216.
10. Ukai, S., T. Narita, A. Alamo, and P. Parmentier, *Tube manufacturing trials by different routes in 9CrW-ODS martensitic steels.* Journal of Nuclear Materials, 2004. **329-333**(Part 1): p. 356-361.
11. UKAI, S., T. KAITO, S. OHTSUKA, T. NARITA, M. FUJIWARA, and T. KOBAYASHI, *Production and Properties of Nano-scale Oxide Dispersion Strengthened (ODS) 9Cr Martensitic Steel Claddings.* ISIJ International, 2003. **43**(12): p. 2038-2045.
12. Chen, Y. and A. Jones, *Reduction of porosity in oxide dispersion-strengthened alloys produced by powder metallurgy.* Metallurgical and Materials Transactions A, 2001. **32**(8): p. 2077-2085.
13. de Castro, V., T. Leguey, M.A. Monge, A. Muñoz, R. Pareja, D.R. Amador, J.M. Torralba, and M. Victoria, *Mechanical dispersion of Y2O3 nanoparticles in steel EUROFER 97: process and optimisation.* Journal of Nuclear Materials, 2003. **322**(2-3): p. 228-234.

CHAPTER 2: LITERATURE REVIEW

2.1 Stainless Steels

2.1.1 Introduction to Stainless Steels

Most of the innovations in stainless steel were found while trying to solve problems such as stains on rifle barrels. In 1913, English metallurgist Harry Brearly was working on the stain problem on rifle barrels and he accidently discovered that adding chromium to low carbon steel gives it stain resistance [1]. Initially the word "stainless" was a term coined early in development of these steels for cutlery purposes only, but now it is used for a wide range of steels which exhibit good oxidation and corrosion resistance [2]. The stainless property is achieved by "dissolving sufficient chromium in the iron to produce a coherent, adherent, insulating and regenerating chromium oxide protective film on the surface" [3].

Stainless Steels are Fe-Iron alloys with no less than 10.5-11 % Chromium in the composition. More other elements can be used for specific applications and to achieve specific properties, some of most frequently used elements are nickel, molybdenum, titanium, carbon and nitrogen.

2.1.2 Types of Stainless Steels

There are three main types of stainless steel classified by their microstructure. These are martensitic (4XX), ferritic (4XX) and austenitic (2XX and 3XX) stainless steels [4].

Austenitic stainless steels have high ductility. They have relatively high ultimate tensile strength when compared to typical carbon steel, although they have low yield stress. They also occupy the major part of stainless steel production.

Austenitic stainless steels are formed as a result of reducing the transformation of austenite into a mixture of ferrite and cementite. They are not magnetic. Most common austenitic stainless steels are iron-nickel-chromium steels, known as 300 series [5]. Due to high chromium and nickel they provide the highest corrosion resistance among all stainless steels. The basic composition (304) is 18 wt. % chromium with 8 wt. % nickel. The family tree of austenitic steels is shown in Fig. 2.1. They can be used up to temperatures around 500 °C. These steels are used in the beverage industry and for heat exchangers. Specified austenitic grades are shown in Fig. 2.2.

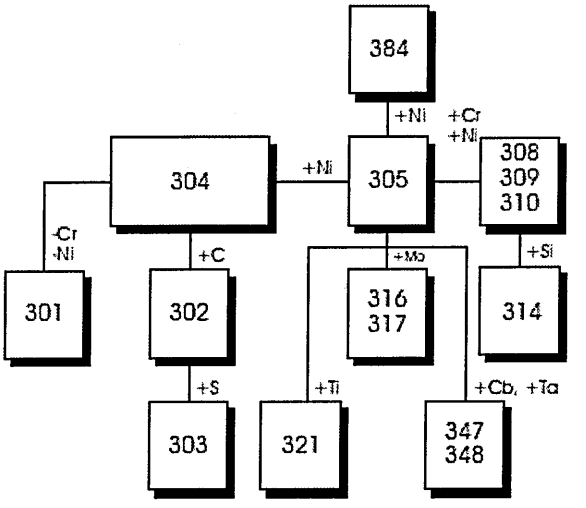

Fig.2.1 Austenitic Grades [5]

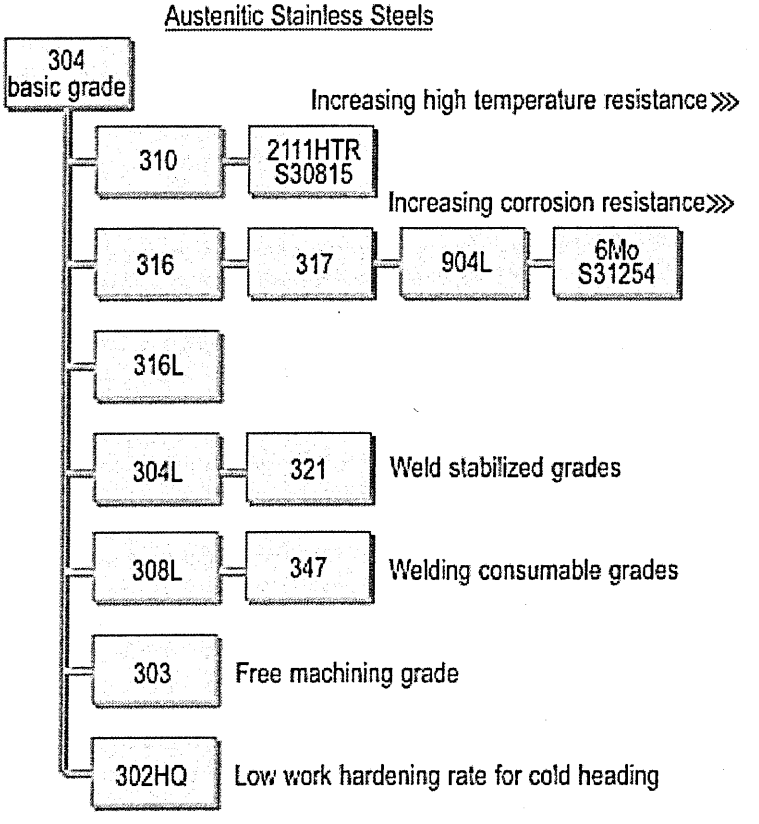

Fig.2.2 Austenitic Stainless Steels [6]

Ferritic grades are highly magnetic. These steels are iron-chromium alloys with chromium composition exceeding 12 wt. % [7]. 430 is the most popular grade of ferritic stainless steels [7]. The family tree of ferritic steels is shown in Fig. 2.3. Ferritic steels are used in exhaust systems and sinks. They are more decorative than austenitic steels [8]. Ferritic steels are easily drawn and pressed and they have very good machinability [9]. The corrosion resistance of ordinary ferritic steels is not as good as austenitic stainless steels [10]. They have higher proof stress than austenitic stainless steels with lower rate of work hardening, moderate ultimate tensile stress and reasonable ductility [10]. Specific ferritic grades are shown in Fig. 2.4.

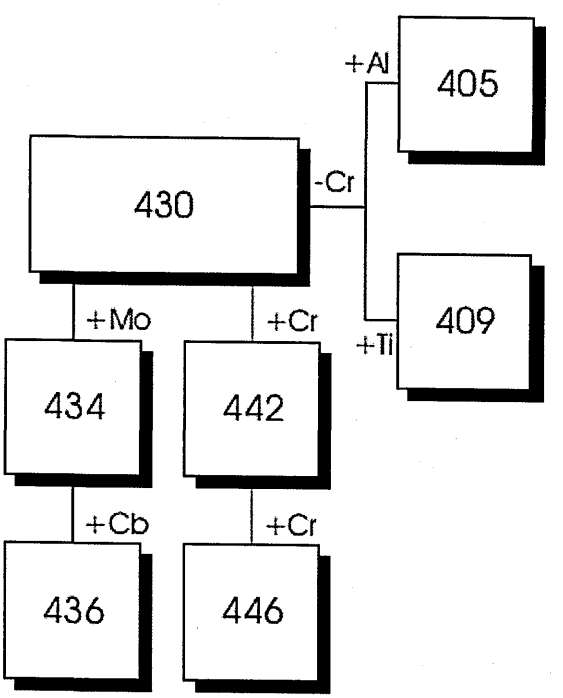

Fig.2.3 Ferritic Grades [5]

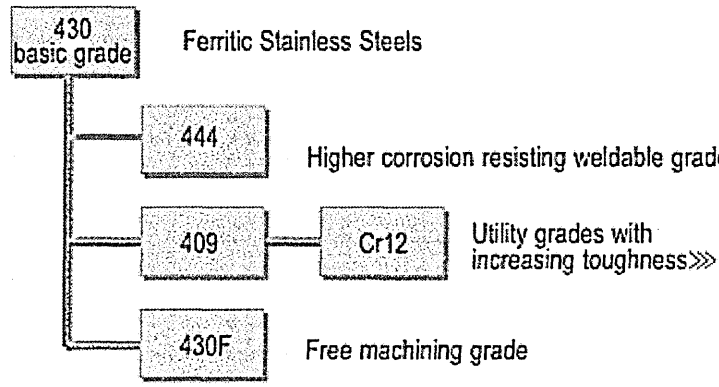

Fig.2.4 Ferritic Stainless Steels [6]

Martensitic steels will be discussed further in detail in later sections.

2.1.3 Effect of Alloying Elements

Various elements have different effects on properties of stainless steel. Here there are most commonly used elements and their specific properties.

Carbon

Carbon is the most common alloying element in steels [11]. Carbon is the principal hardening element in all steel [12]. It is also important in classification of iron alloys, for example if an iron based alloy contains more than 2 wt. % C it is classified as cast iron [13]. Carbon amount is also important for determination of hypo-eutectoid and hypereutectoid steels. Carbon can precipitate as carbides at high temperatures when they combine with other elements. Those carbides may improve mechanical properties by hindering dislocation motions, but they may

have detrimental effect by reducing corrosion resistance due to formation of high chromium carbides.

Chromium

Chromium improves hardenability, wear resistance and corrosion resistance [13]. It is also used to have high temperature strength and good oxidation resistance [14]. Chromium is also a very good ferrite stabilizer and carbide former [15]. Chromium carbides prevent softening at high temperatures in steels due to their stability up to high temperatures. The most common chromium carbide is $M_{23}C_6$. Chromium can also provide superior mechanical properties when used with nickel which is a good toughening element [14].

Nickel

As mentioned earlier Nickel is a good toughness provider [12]. Nickel does not form carbides, it remains in the solid solution [11]. Nickel toughens and strengthens the ferrite as it is a ferrite strengthener although it is an austenite stabilizer [14]. Nickel also has been associated with a reduction in stress-corrosion cracking resistance [16].

Phosphorus

Phosphorus is generally considered as a residual element in steels so that amount is limited up to 0.02wt% [11]. The main purpose of using phosphorus in steels is improving machinability.

Silicon

Silicon is the most common de-oxidizing agent. Oxygen is an undesirable element due to reducing mechanical properties by oxides and inclusions [11]. It also has a well known effect of promoting ferrite.

Sulphur

Like phosphorus, sulphur is considered as another residual element which helps machinability of steels. Sulphur has a small atomic diameter but it is not considered as interstitial alloying element, because it is not soluble in iron [11].

Manganese

Manganese is a good de-sulphurizer. It forms the stable MnS phase so that it eliminates the incidence of solidification cracking or sulphur embrittlement. It has a significant effect on hardenability of steels and is a good austenite stabilizer.

2.1.4 Martensitic Stainless Steels

Martensitic grades are the hardest form of stainless steels. They are magnetic and their mechanical properties can be modified by heat treatment. Their corrosion resistance is not as good as other grades due to a relatively low chromium content around 12-14 wt. % [17]. These kinds of steels are quite brittle so are usually used after tempering. The family tree of martensitic steels is shown in Fig. 2.5.

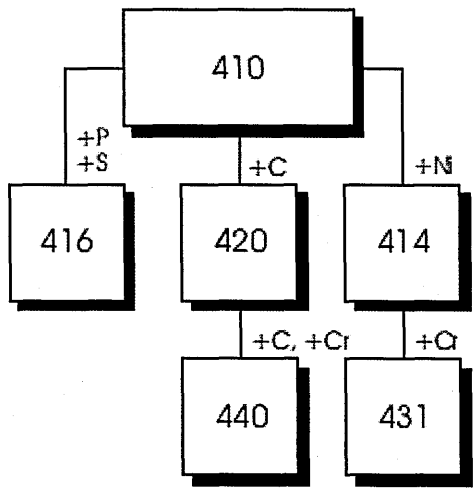

Fig.2.5 Martensitic Grades [5]

Martensite is actually a metastable form of austenite. It is formed by rapidly cooling or quenching austenite [18]. Carbon atoms are entrapped in the martensitic structure due to very fast cooling rates and a distorted lattice structure occurrs, body centred tetragonal (BCT). With the addition of alloying elements the martensitic structure can also be achieved by slower cooling rates. Some of those

elements can shift the continuous cooling transformation (CCT) diagram, so that even slower cooling rates will be enough to complete martensitic transformation.

Tempering is very important for martensitic stainless steel. Because of low ductility and toughness, these kinds of steel are generally preferred to be used after heat treatments. The aim of a basic heat treatment is to hold the material at a specific high temperature to allow entrapped carbon atoms to diffuse out from the crystal structure and to form another structure like pearlite.

The main application areas of martensitic steels are engine turbine blades, steam piping and cutlery applications where hardness, strength and wear resistance are required. Specific martensitic grades are shown in Fig. 2.6.

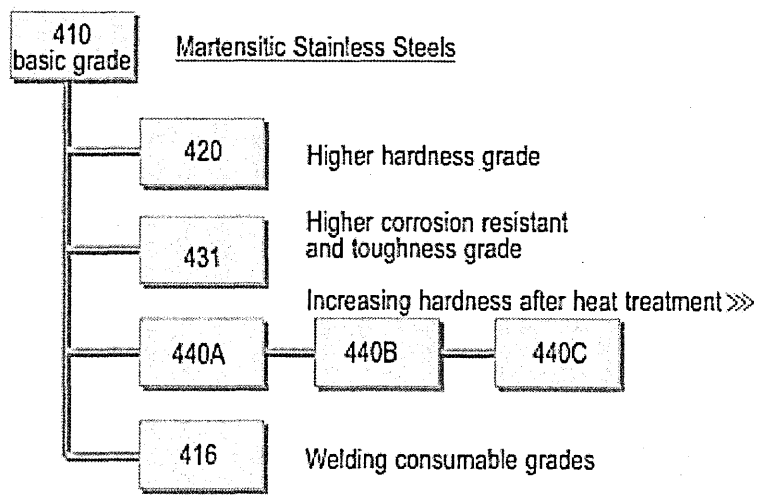

Fig.2.6 Martensitic Stainless Steels [6]

2.1.5 410 Type Stainless Steel

410 is the basic 12 Cr martensitic stainless steel with 11.5-13.5 wt. % chromium content with max 0.15 wt. % carbon. It does not provide as good corrosion resistance as austenitic stainless steels with this chromium content. Type 410 is a general-purpose martensitic steel mainly used for steam valves, pump shafts, bolts and various parts requiring corrosion resistance and moderate strength: they are the lowest strength group of all martensitic steels [14].

2.2 Strengthening Mechanisms

2.2.1 Solid-Solution Strengthening

The simplest way of increasing the strength of a metal is solid-solution strengthening [19]. The main mechanism of this type of strengthening is distortions due to solute atoms which impede dislocation movements, so that there is an increase in yield strength. There are two types of solid solutions: substitutional and interstitial solid solutions. When the atoms of the added element are very small compared to the parent material, they can fit into the interstices or spaces in the crystal lattice of the parent material. This type of solid solution is called an interstitial solid solution [20]. When the atoms of solute and solvent are roughly same in size, this will allow solute atoms to occupy the lattice points of solvent atoms. This type of solid solution is called a substitutional solid solution. Types of solid solutions are shown in Fig. 2.7.

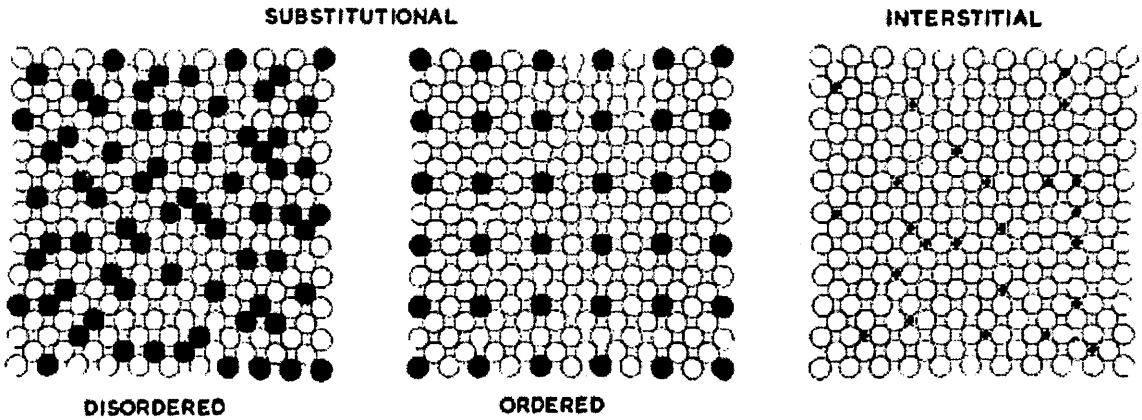

Fig.2.7 Types of Solid Solutions [20]

The most common example of this type of strengthening is steels. They are formed by carbon and iron, which are solute and solvent respectively.

2.2.2 Precipitation Strengthening

Precipitates are secondary phase particles and strengthen materials by impeding motion of dislocations. Precipitation hardening or age hardening requires second phase particles which are soluble at high temperatures but have a lower solubility at lower temperatures. There are three steps in precipitation hardening. The first step is holding the sample at high temperatures to dissolve the second phase. Then quenching takes place to have a supersaturated condition at room temperature. After quenching material is heated up to temperatures below the solvus temperature and held for some time for second phase particles to precipitate. The time and temperature of aging depends on the desired combination of strength and ductility.

2.2.3 Dispersion Strengthening

Dispersion strengthening is an active mechanism in alloys to be used at elevated temperatures [21]. As for precipitation hardening, dispersion strengthening also involves a second phase. When the solubility of a material is exceeded by adding too much of an alloying element, a second phase forms and a two-phase alloy is produced. These second phase particles hinder dislocation motion and lead to strengthening. This type of strengthening mechanism is called dispersion strengthening.

Usually round shaped particles are preferred, rather than needle like or sharp edged particles, because cracks can be initiated from local stress concentrations if particles are pointed. Particles are also preferred to be small and numerous associated with the interactions with dislocations.

2.2.4 Dislocation Interactions

Basically in all strengthening mechanisms discussed above, the principle is to hinder dislocation motions to achieve strength. Strengthening produced by interaction of dislocations with a dispersion of particles or precipitations within a matrix phase was first described by Orowan in 1948 [18, 22].

When a dislocation line meets particles it will exert force on the particles because the dislocation line is in tension and dislocation line has to bow round the particles. This can be seen in Fig.2.8.

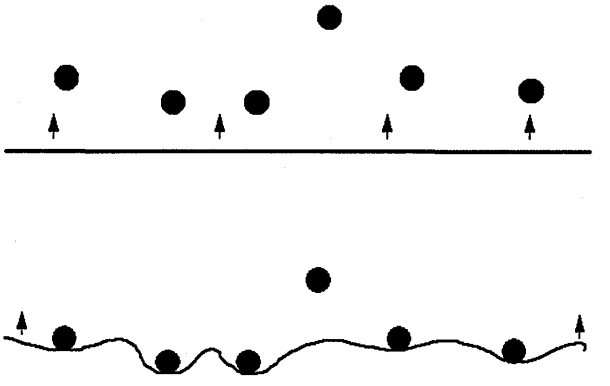

Fig.2.8 Dislocation movement when it meets particles [23]

Due to the applied stress the dislocation wants to progress further. And to do so dislocations either need to cut through or form Orowan Loops as shown in Fig.2.9.

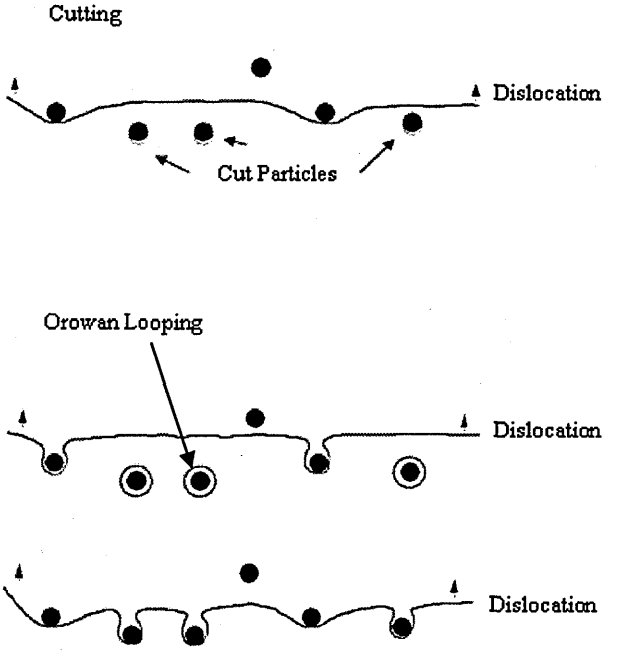

Fig.2.9 Cutting and Orowan Looping [86]

In order to optimise the toughening benefit of precipitates, their size and spacing must be controlled. Material strength equations are developed for better understanding.

For Orowan Looping; $$\tau = (const)\frac{Gbf^{1/2}}{r}\ln\left(\frac{2r}{r_0}\right) \quad (2.1)\ [24]$$

Where the constant is 0.093 for edge dislocations and 0.14 for screw dislocations, G is shear modulus, b is Burgers vectors, f is volume fraction of particles and r_0 is the radius of the bowed dislocation between particles and r is the particle radius.

For Dislocation Cutting; $$\tau = \frac{1.1}{\sqrt{a}}\frac{\gamma^{3/2}f^{1/2}}{Gb^2}r^{1/2} \quad (2.2)\ [24]$$

(Short-range Interactions)

$$\tau = \left[\frac{27.4E^3\varepsilon^3 b}{\pi T(1+\nu)^3}\right]^{1/2} f^{5/6}r^{1/2} \quad (2.3)\ [24]$$

(Long-range Interactions)

Where a is 0.16 for edge and 0.24 for screw dislocations, γ is surface energy, E is Young's modulus, T is line tension, ν is Poisson's ratio and ε is a function of spacing between dislocations.

It can be seen from the equations that for Orowan looping material strength is increasing as particle radius r becomes small and particle fraction f increases as $$\tau = \alpha \frac{f^{1/2}}{r} \qquad (2.4)\ [25]$$

For dislocation looping material strength is increasing as particle radius, r becomes bigger and particle fraction f increases as $\tau = \beta f^{1/2} r^{1/2}$ (2.5) and β and the exponent of f will depend on the controlling dislocation-particle interaction mechanisms for any individual system [25].

So to define critical radius for best material strength, the strength vs radius graph is plotted in Fig. 2.10. As seen from the graph when small particles are present in the material the dislocation cutting mechanism is dominating, and determining the material strength, while for material with large particles Orowan looping is the main mechanism for dislocation-particle interactions and strengthening.

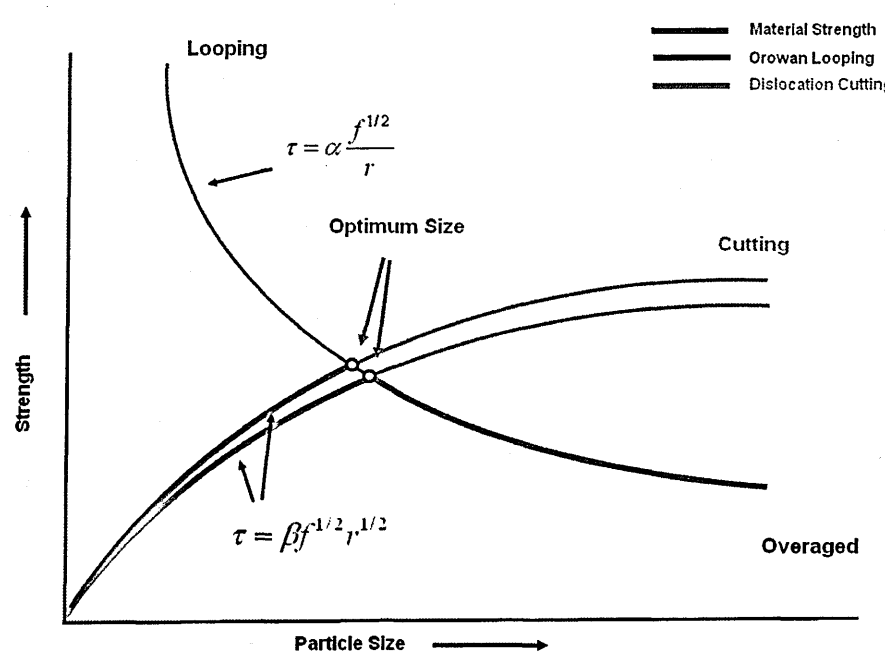

Fig.2.10 Material strength and particle size relationship [22, 23, 86]

Optimum particle size is determined at the point where Orowan looping and dislocation cutting lines intersect.

2.3 Powder Metallurgy

2.3.1 Production Route

Powder metallurgy is defined as the art and science of producing metal powders and making objects from individual, mixed or alloyed powders [26]. Powder metallurgy offers an effective way of manufacturing small and precise metal solid components from powders [27]. The production route of those metal components consists of three stages: firstly primary metal is physically powdered; secondly fine metal powders are pressed into a desired shape, usually in a metal die and under high pressure; and after that compacted powder is then heated (sintered), with an inert atmosphere [28].

To produce powders there are various ways like reduction methods, electrolytic decomposition, carbonyl methods, grinding [26]. But the most common way of producing powders is atomisation. There are two main types of atomisation: gas atomisation (Fig. 2.11) and water atomisation (Fig. 2.12).

The basic mechanism is the same in both atomisation methods; introducing a high pressure of either water or gas to the molten metal just before it leaves the nozzle to comminute it to smaller sized particles and cooling them before they reach a solid surface. The shape of the small powders depends on cooling speed;

they will have spherical shapes if they are cooled via low cooling capacity gas or they will have complex shapes if they are cooled via high cooling capacity water [29].

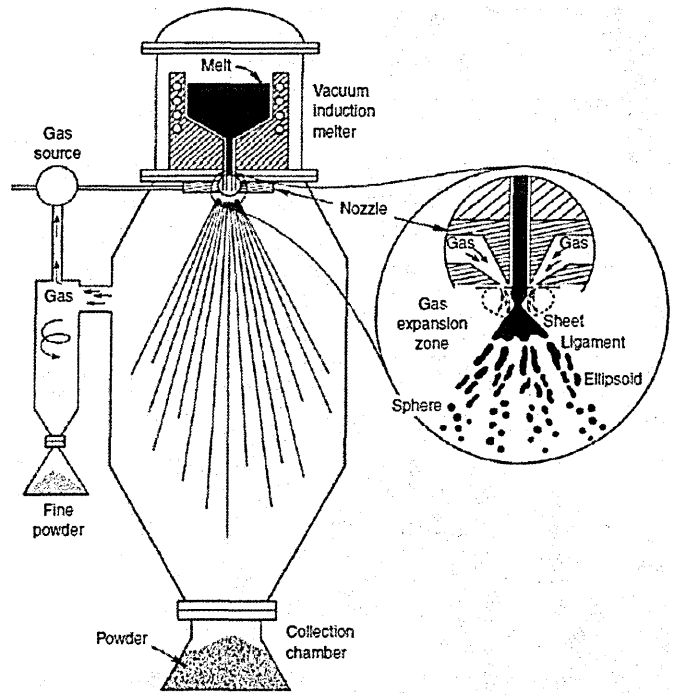

Fig.2.11 Schematic Representation of Gas Atomisation [24]

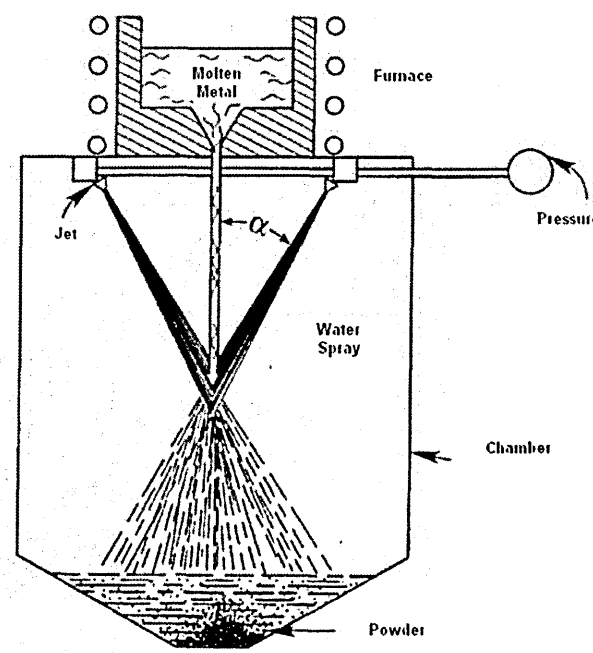

Fig.2.12 Schematic Representation of Water Atomisation [87]

For gas atomisation usually air, argon or nitrogen is used. Generally spherical shaped powders are obtained after gas atomisation. The main consideration is the expansion of gas just after it leaves the nozzle and loses energy as its lost kinetic energy comminutes the molten metal into small pieces. Usually tall chambers are used for gas atomisation to allow molten metal to cool down before it reaches the surface.

For water atomisation water jets are utilized. Due to very fast cooling complex shapes are obtained after water atomisation. By increasing the speed of the water smaller sized particles can be obtained. Cratering, splashing, stripping and bursting are the main mechanisms in water atomisation after the water particle hits the molten metal. These mechanisms are clearly shown in Fig. 2.13.

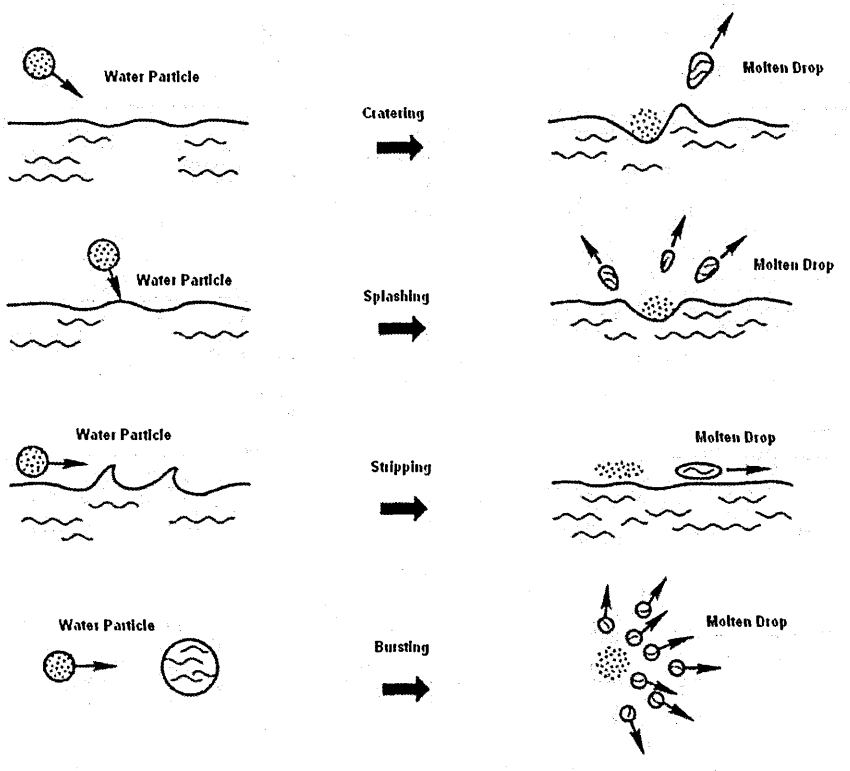

Fig.2.13 Mechanisms in Water Atomisation [87]

2.3.2 Mechanical Alloying

Mechanical alloying is a key technology in powder metallurgy production. It is a means for producing alloy metal powders with controlled, extremely fine microstructures and it can be used to produce alloys that are difficult or impossible to produce by conventional melting and casting techniques [30]. For example if there are two metals with a huge difference in melting points then conventional casting may not be a feasible way to produce that alloy [31].

Mechanical alloying is a ball milling process where a powder mixture is placed in the ball mill and subjected to high energy collision from the balls in an inert atmosphere [32]. Basically the ball milling is the combination and repetition of welding and fracturing mechanisms of small powder particles via the milling balls. There are many factors that can affect the properties of the material in the mechanical alloying process. The two most important factors are the type of milling and the time of milling. There are various types of milling but the most frequently used ones are planetary and attritor type of milling. Each of these milling types introduces different characteristics to the material. There should be optimum time for milling to optimize the powder particles' structure. Short milling time or long milling time may cause problems like agglomeration and poor mechanical properties. With milling time the grain size decreases up to a certain time, and beyond that agglomeration take place due to significant welding at that stage [33]. There is an optimum time for milling up to which properties are increased. At that time welding and fracturing mechanisms are in balance. It is found that after 24 hr milling there is no apparent change of morphology and size

of particles in Eurofer 97 ODS alloy [34]. Milling time can also affect density; more milling can cause a reduction in density. The main reason is the refinement of particles leads to a more monomodal size distribution that does not provide as good densification as bi-modal size distribution due to compaction phenomena [35]. Small particles can fit between big particles and eliminate porosity, so that at the end better densification will be achieved if bimodal size distribution is achieved. Another reason might be contamination during the process such as entrapment of milling atmosphere gases and/or oxygen etc [33, 34]. An optimized milling parameter for Eurofer 97 is mentioned as 24 hr milling in a 800 rpm attritor type of mill with 13:1 ball to powder ratio [34]. Canning and degassing process can take around 10 hrs[36]. HIP process can take between 2 hours to more than 7 hours depending on the sample.

Main Types of Milling

Planetary milling is a very commonly used type of milling which operates on the basic of centrifugal force. The direction of movement of the grinding bowl and the milling balls are opposite. Centrifugal forces cause milling balls to roll on the inner wall of the grinding bowl and lift up, and they are then thrown off across the bowl at high speed [31]. A Schematic illustration of planetary type of milling is shown in Fig. 2.14.

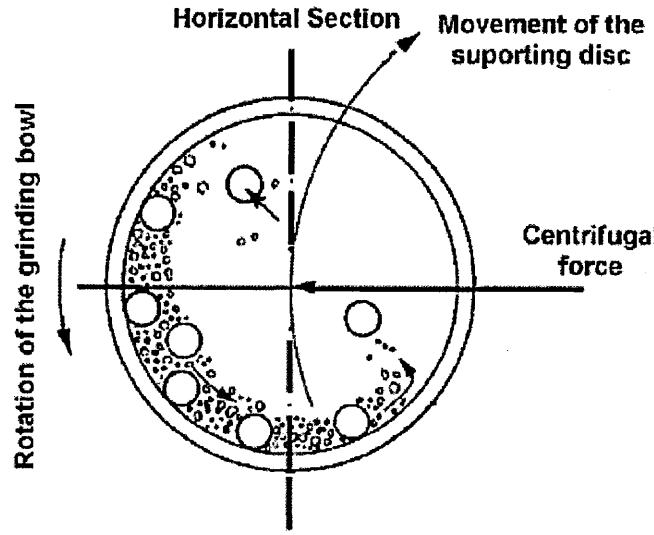

Fig.2.14 Planetary Ball Milling [29]

Attritor milling is a high energy milling type. The mechanism of attritor milling is the stirring action of a rotating shaft with impellers. A typical rotation speed of the central shaft is 250 rpm. A schematic illustration of attritor milling is shown in Fig. 2.15.

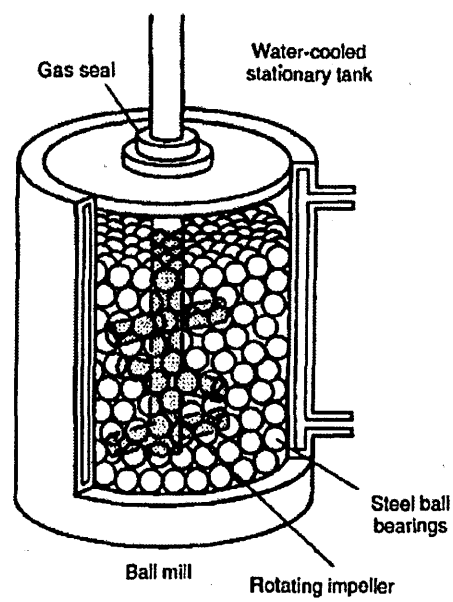

Fig.2.15 Attritor milling [88]

2.3.3 Hot Isostatic Pressing

Hot isostatic pressing (HIP) is a manufacturing method to reduce porosity and compact and densify powder materials. The method is based on powder metallurgy and combines some of the advantages of casting technology with those of forging technology. It is done at high temperatures and under gas pressure. Inert gas must be used to prevent reaction of gas and material. Mostly argon is used for isostatic pressing. To achieve a fully dense structure, material to be subjected to HIP must be degassed before the process so that gaseous pores will be eliminated. Sometimes even during manufacturing inert gas entrapment can cause some problems after manufacturing like density problems so that there is a reduction in mechanical properties. After degassing the can is sealed and subjected to high pressure and HIPing starts. The application of high inert gas pressures and elevated temperatures results in the removal of internal voids and creates a strong metallurgical bond throughout the material, and the result is a clean homogeneous material with a uniformly fine grain size and a near 100% density [37]. A simple HIP environment is shown in Fig. 2.16.

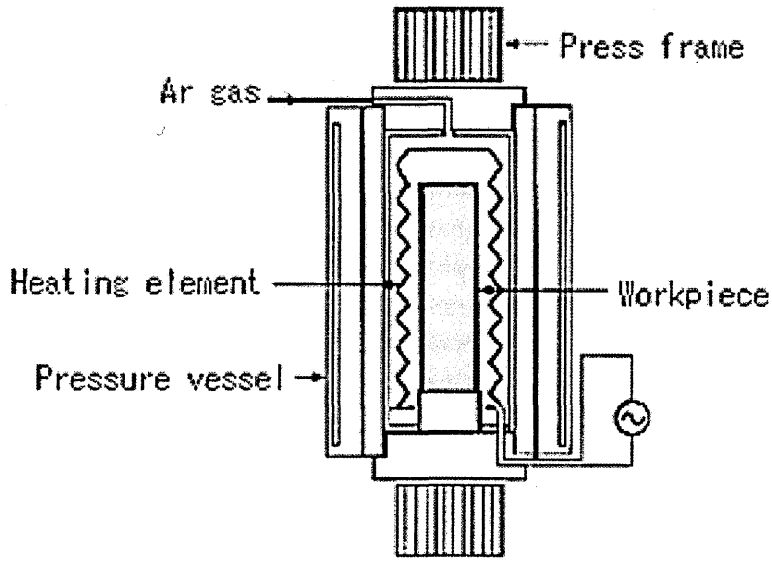

Fig.2.16 Hot Isostatic Pressing [89]

Improved mechanical properties, workability and clean and uniform microstructure are the main advantages of HIP. It is also a very cost-effective way of producing components because of near-net-shape production. Only a small amount of machining is necessary after HIPing compared to conventional methods. Huge amount of machining is necessary after conventional methods like casting to achieve desired product.

2.3.4 Advantages and Disadvantages

Powder metallurgy parts can be mass produced to net or near-net shape, eliminating or reducing the need for subsequent machining. It is a very good method to produce complex shaped parts. Sometimes complex shaped components may not be produced by conventional methods. For example, in

casting, flow of melt and solidification rate may not be good enough to produce homogenous parts. Certain metals that are very difficult to fabricate by other methods can be shaped by powder metallurgy like tungsten filaments for incandescent lamp bulbs.

Another very important fact of powder metallurgy is efficiency in production. In conventional methods only a limited amount of the starting material is used in the final product. Each subsequent operation removes some material, mostly by machining. However in powder metallurgy net or near-net shape parts can be produced with a clean surface finish. This is also important for environmental and energy efficiency.

To achieve all the advantages of powder metallurgy, production steps must be very well organized and optimized. Powder metallurgy is a very good production method. There are many factors that can affect the final product as well as the mechanical properties. The most important step is the mechanical alloying step: there are various factors that can change alloying properties like type of mills, milling tools, milling media, milling atmosphere, milling environment, milling temperature, milling time etc. By playing with these parameters various types of the same material can be produced. It is even possible to control porosity in powder metallurgy to produce porous metals like metal filters, oil-impregnated bearings etc [38].

However there are also some disadvantages and limitations for powder metallurgy. Equipment and tools used for powder metallurgy production are not

cheap. In addition to equipment and tooling costs metal powders are expensive as well.

In dealing with very small particles, storing and handling is another problem for powder metallurgy. Some powders are dangerous for human health and many of them are flammable. They can also degrade if the storing conditions are not good enough.

Finally, powder metallurgy is a very sensitive production method. All parameters need to be examined very carefully to achieve a very good product. Even small changes can cause big differences in the product.

2.4 Nuclear Structural Materials

2.4.1 Introduction to Nuclear Structural Materials

Widely used pressurized-water nuclear fission reactors have an operating temperature range of 250-300°C, pressure range of 7-15 MPa and displacement per atom (dpa) range of 10-25. Next generation nuclear power plants are planned to operate at tougher conditions with temperature range between 300-1100°C, pressure between 0.1-24 MPa and displacement per atom of the order of 10-150. This improvement brings new challenges like material selection.

Materials play a crucial role for safe, reliable and economic operation of nuclear power plants where they encounter hostile environment and aggressive

media during service, and are expected to retain their structural and metallurgical integrity over a long period of use [39]. So to achieve better performance, new types of materials are intended by modifying conventional steels.

Efforts to develop new Fe-Cr-Mo type heat resistant steels were initiated for steam generators in the early 1970s. During the development of high chromium (9 to 12%) steels for high temperature application the use of stainless steel for nuclear applications was demonstrated. This included attempts to replace Mo with W due to lower activation characteristic [40]. Since then long-term experience has been achieved with components fabricated with high Cr martensitic steel [41]. However austenitic stainless steels are not considered for advanced power plant reactor applications because of high swelling rates and high thermal stresses caused by low thermal conductivity and high thermal expansion coefficient [41-43]. Limitations from swelling and inferior thermal properties forced investigators to explore other paths [42]. Reduced activation ferritic/martensitic (RAFM) steels with Cr contents ranging from 9 to 12 wt% have proven to be a good alternative to austenitic steels as structural materials in fission applications for their higher swelling resistance, lower damage accumulation and improved thermal properties, although their creep resistance is also limited to a moderate temperature level (<850 K) [43, 44].

2.4.2 Reduced Activation Ferritic/Martensitic (RAFM) Steels

There are three important factors that the safety of a fission power plant depends on: firstly, the structural integrity of the plant and the probability of its

failure; secondly, the radioactive decay heat generated in the absence of coolant; and finally, the paths for dispersion of radioactivity to the plant surroundings during an accident [45]. So it is essential that the structural materials to be used in these power plants would not activate or in other words shall not become radioactive or if activated should decay very quickly within minutes or hours [45]. The requirements for safe, routine operation and decommissioning of a fission power plant and disposal or radioactive wastes have required researchers to develop new kind of steels with enhanced radioactive decay characteristics and as a consequence of these researches new steels called "reduced activation steels" have been developed [46].

Reduced activation ferritic/martensitic steels are reference structural materials for fission nuclear power plants, because a huge amount of work done on these steels to characterise and analyse like qualifying fabrication routes, welding technology and mechanical behaviour as well as general industrial experience is available [47]. This high-level of technological maturity puts reduced activation ferritic/martensitic steels one step forward ahead of other alternative low activation materials such as vanadium alloys and SiC composites [45, 48].

Basically the technology of reduced activation ferritic/martensitic steels is replacing the radioactive tramp elements with non-radioactive alternatives in Fe-Cr-Mo steels. Radioactive tramp elements are commonly Mo, Nb, B, Cu, Ni, Al, Co and Ti [49]. Basic modifications in RAFM steels are replacing Mo, Ni and Nb with W, V and Ta for the purpose of obtaining low activation characteristics [50]. The investigations performed in RAFM alloys have also shown that the final

radioactivity levels for a RAFM steel could be over two orders of magnitude lower than for conventional Cr-Mo steels after a cooling-off period [45]. But while achieving this low activation status mechanical and physical properties shall be kept or improved when compared to conventional Cr-Mo compositions [46].

2.4.3 Oxide Dispersion Strengthened (ODS) Materials

RAFM steels will have limited upper operating temperatures if they are considered to be used in power generation utilities and nuclear structural materials. Maximum operating temperature for RAFM steels are around 550 – 600 °C as steels' mechanical properties are lowered at high temperatures [51]. Reason for poor mechanical properties at high temperatures is related to dislocation movements. Dislocation climb is a vacancy diffusion dependent process and as all diffusion processes, it is highly dependent on temperature and is favoured at high temperatures. At higher temperatures dislocations will more easily be able to move around obstacles. For this reason, many hardened materials become exponentially weaker at higher temperatures. However, if a dislocation meets an obstacle at room temperature, obviously where the diffusion process is very limited, dislocations pile up in front of the obstacle. So there are two options to go further in the materials either Orowan looping or dislocation cutting because diffusion is limited so dislocation climb is not possible and this makes the material harder. Operating temperature of the nuclear power plants is very important for efficiency. Higher the temperature means higher the efficiency. Having operating temperatures more than 700°C in future fusion may result in an improved efficiency of more than 40 % [52]. To achieve higher plant operating temperature

for improved thermal efficiency investigators have tried to improve the upper operating temperature limit without making concessions from mechanical properties and maintaining the advantages of reduced activation ferritic/martensitic steels like high thermal conductivity and low swelling [53]. To achieve this a new kind of steel is developed with a microstructure that consists of a metal matrix of RAFM steel with uniformly distributed oxide particles, called oxide dispersion strengthened steels (ODS) [54].

Oxide Dispersion-Strengthened steels are being developed and investigated for nuclear fission and nuclear fusion applications in Japan, Europe and the United States [51]. Recent studies show that oxide dispersion strengthened tempered martensitic steels appear to be promising candidates for the future fission reactor [55]. The use of ODS alloys for increasing the working temperatures of materials started in the 1950s and was widely developed in 1960s [56].

Oxide Dispersion Strengthened alloys have excellent potential for use in next-generation high-temperature applications where superior creep strength and oxidation resistance is required compared to precipitation strengthened alloys. They have higher operating temperatures than High-Cr steels, good thermal conductivity, high swelling resistance and low radiation damage [51]. Their creep strength is also very good compared to other alternative structural materials. And these steels are considered as the most effective way to improve creep properties [57].

Elevated temperature strength in these steels is obtained through microstructures that contain a high density of small Y_2O_3 and/or TiO_2 particles dispersed in a ferrite matrix [51]. In this project Y_2O_3 strengthened materials will be examined. Matrix material 410L is a martensitic stainless steel material so TiO_2 strengthening will not be beneficial due to titanium's limiting effect on the martensitic transformation. An increase in the matrix titanium content leads to a limited martensitic transformation in a specimen consolidated using large mechanically alloyed powder, because titanium is a ferrite promoter element [58].

ODS steels are promising materials with the potential to be used in next generation power plants at elevated temperatures due to the addition of small thermally stable oxide particles [59]. The oxide particles used in ODS steels act as obstacles in front of dislocations and harden the material. A basic explanation of this hardening is the effect of oxide particles as hindering dislocation motion. The amount, size and distribution of these oxide particles are very important for mechanical and microstructural properties of oxide dispersion strengthened steels. For optimum dispersion strengthening in these steels, distributing a given volume fraction of dispersoids more finely is more effective than increasing the volume fraction [60]. So in other words homogeneity is more important than quantity in this strengthening mechanism. Particle size of the dispersoids is also very important for determining the mechanical properties. The smaller the particle sizes the better are the mechanical properties. A research on two simple materials found much larger Y_2O_3 particles in the weaker one, explaining why that steel had inferior tensile and creep properties [51]. The amount of dispersion in these ODS steels affects the mechanical properties as stated above. For the same processing

conditions, an increase of the Y_2O_3 content from 0.3% at 0.5% leads to a slight improvement of the tensile properties [61]. In order to produce ODS steels with improved mechanical properties, oxygen and carbon contents have to be reduced to very low values. This shows the critical issue of oxides and carbides in the microstructure [62].

Another effect of these oxide particles is they are serving as trapping sites for point defects induced by radiation displacement and thus reduces remarkably irradiation swelling [63]. Oxide nanoclusters are very efficient in trapping high quantitites of gas atoms, in particular helium, produced by transmutation reactions in fusion and spallation environements, so that they could help in mitigating helium embrittlement [64].

A promising way of fabricating oxide dispersion strengthened (ODS) steels is consolidation of a mechanically alloyed powder by hot isostatic pressing (HIP) as shown in Fig. 2.17. This production route is recommended as an alternative to hot extrusion as it avoids strong anisotropy of the materials [65]. In extrusion process mechanical properties in the longitudinal direction will be very good but in transverse direction inferior properties will be observed. After hot isostatic pressing a dense material with very complex geometry can be obtained [66]. Mechanical alloying and powder metallurgy processes are applied to finely disperse these small oxide particles in the matrix, because oxide particles aggregate together and coarsen during conventional casting processes [58]. This aggregation and coarsening causes some reductions in mechanical properties. Fine distribution and small particle size is beneficial.

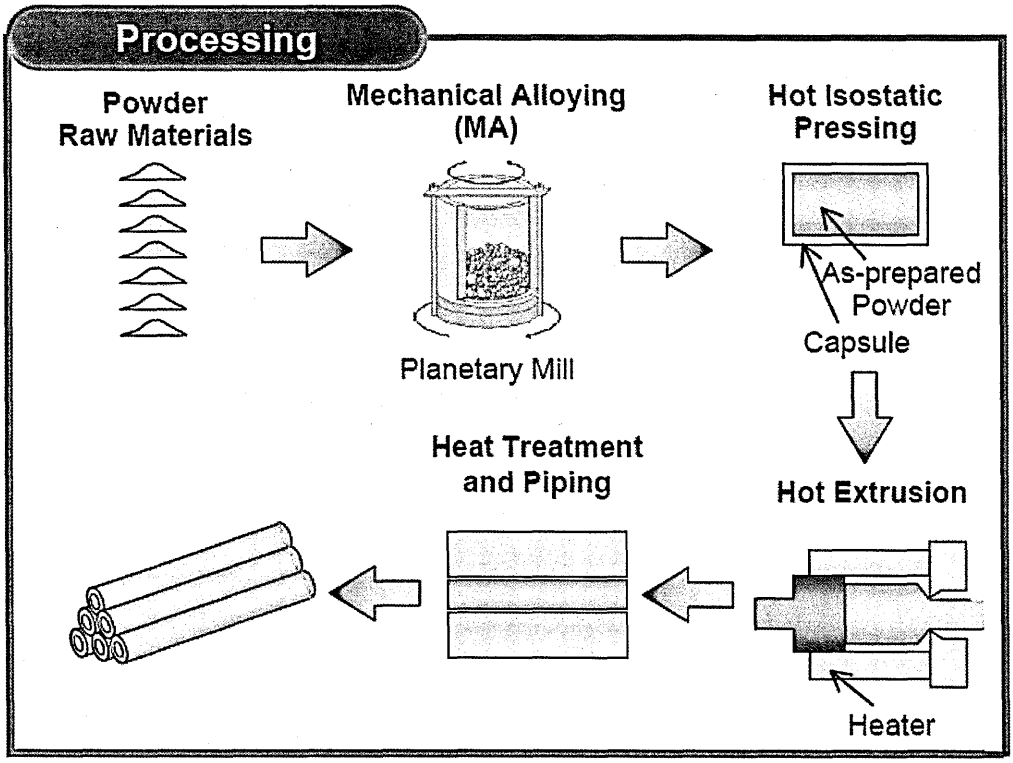

Fig.2.17 Processing route for ODS Steels [90]

Lots of research has been done on the effect of mechanical alloying on mechanical properties of ODS steels and some crucial understandings achieved. One of the most important points is the dissolving of Y_2O_3 particles during milling. This affects hardness and mechanical properties. The Y_2O_3 oxides have a direct effect on the hardness of the steel powders in which they incorporate, which can be explained by their size reduction and dissolution during milling [67]. Amount of lattice defects and strains generated during mechanical alloying has the major role in oxide particle dissolution [68]. The dissolution/precipitation mechanisms of the Y_2O_3 oxides during the ODS steel production was claimed to be effective for improving the mechanical properties of the ODS steels at high temperatures [54, 69]. The main reason of this improvement in the mechanical

properties is because of finer precipitation of the oxide particles after dissolution in the mechanical alloying process. As mentioned earlier smaller particle sizes of oxide particles are favoured in oxide dispersion strengthened steels.

2.5 Mechanical Testing and Fracture

2.5.1 Tensile Testing

Tensile testing reveals the elastic and inelastic behaviour of a material and measures the strength of the material when a load is applied. Strength refers to the ability of a structure to resist loads without failure. The strength of a material under tension has long been regarded as one of the most important characteristics required for design, production quality control and life prediction of industrial plant [70].

A tensile test, also known as tension test, is probably the most fundamental type of mechanical test that can be performed on a material. Tensile tests are simple, inexpensive, and fully standardized. By pulling on something, you will very quickly determine how the material will react to forces being applied in tension. As the material is being pulled, you will find its strength along with how much it will elongate [71].

In an extension controlled tensile test, a sample is extended at constant rate, and the load needed to maintain this extension is measured. The stress, σ, calculated from the load, and strain, ε, calculated from the extension can either be

plotted as nominal stress against nominal strain (also known as engineering stress and strain), or as true stress against true strain (also known as logarithmic stress and strain). In nominal stress and strain the original dimensions of the sample are used for calculations but in true stress and strain the actual dimensions are considered. In other words for nominal values, initial dimensions are considered but for true values, dimensions of the sample, at the moment of calculation, is considered as sample gets thinner during plastic deformation so dimensions are not stable. When sample's dimensions changes stress values also changes because cross-section area of the sample under the load is changing. For example after necking starts the actual cross-sectional area is always changing as the test continues due to non-uniform plastic deformation in the material. A typical stress vs strain graph after an ordinary tensile test is shown in Fig.2.18.

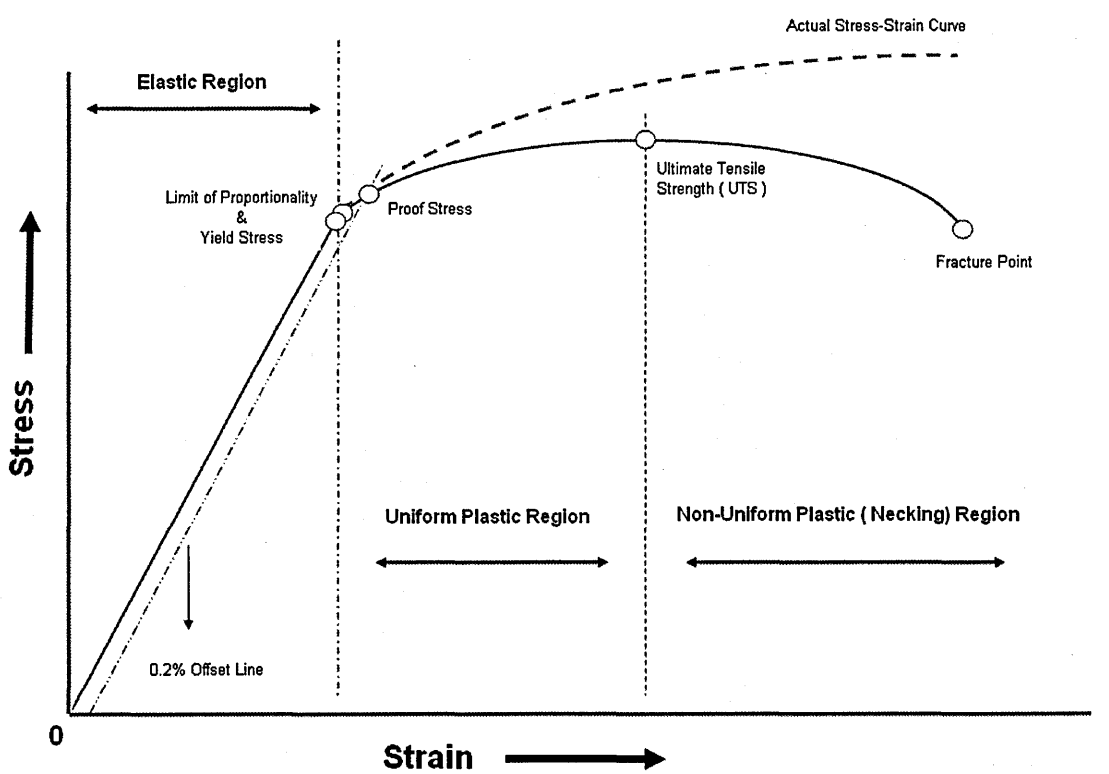

Fig.2.18 Typical Stress vs Strain Curve

Stress is defined as load per unit area with units of Pascal, and strain is deformation due to applied load. Strain in a tensile test can be expressed as the ratio of change in length to original length for nominal values ($\Delta l/l_0$). For true strain, basic theory is same but values are instantaneous values as strain is the ratio of the extension at the moment to the previous length before last extension ($\ln (l_f/l_0)$).

The first straight red line characterises the proportional relationship between stress and strain up to the limit of proportionality. The slope of the curve is constant up to that point and deformation is elastic. The relationship between stress and the strain is defined as E, called Young's modulus or elastic modulus of the material where E is the slope of the curve, σ/ε, and this relationship is known as Hooke's Law.

$$\sigma = E * \varepsilon \qquad (2.6)$$

Hooke's law is obeyed up to the proportionality limit. The modulus of elasticity determines the stiffness of the material, which is defined as the resistance of a body to elastic deformation caused by an applied force. Up to this point material reacts elastically to the applied load and will return to its original condition after load removal.

The point where yielding just starts across the whole specimen is called the yield stress or yield strength. After this point in a tensile test, some permanent deformation occurs in the specimen and the material is said to react plastically to

any further increase in load or stress. The material will not return to its original, unstressed condition when the load is removed.

With most materials there is a gradual transition from elastic to plastic behaviour, and the exact point at which plastic deformation begins to occur is hard to determine. Therefore, an offset method to determine the yield strength of the material tested is often applied. The offset yield strength or proof stress is the stress corresponding to the intersection of the stress-strain curve and a line parallel to the elastic part of the curve offset by a specified strain, usually 0.2 % for metals.

For ductile materials the point where uniform plastic deformation ends and the material starts to form a neck is called the ultimate tensile strength (UTS). UTS is the peak value in nominal tensile tests for both ductile and brittle materials. For brittle specimens the UTS value may equal the strength at the yield point as brittle materials do not show significant plasticity. Brittle and ductile stress-strain curves are shown in Fig. 2.19.

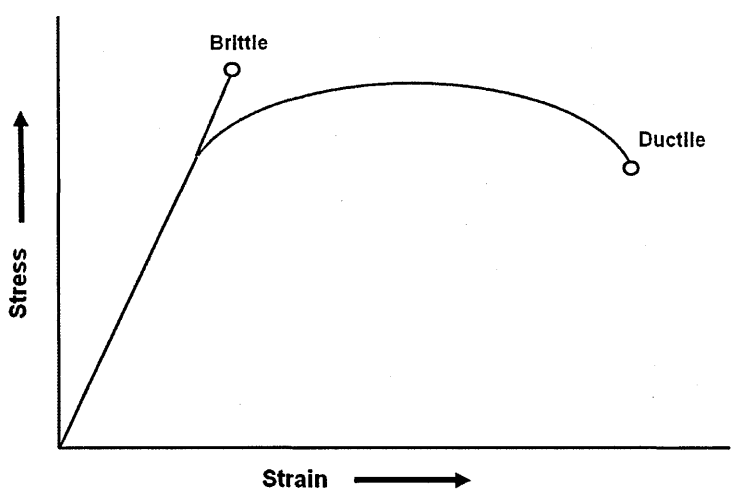

Fig.2.19 Brittle and Ductile Stress-Strain Curve

Continuation of the deformation will result in fracture and the stress where fracture takes place is called the fracture point.

Another important characteristic of metals is ductility which is defined as the ability of a material to deform under tension without rupture. The conventional measures of ductility are the engineering strain at fracture, usually called the elongation, and the reduction of area at fracture. Elongation is expressed as a percentage. Reduction of area is the change in cross-sectional area divided by the original cross-sectional area. This change is measured in the necked region of the specimen. Like elongation, it is usually expressed as a percentage.

2.5.2 Fracture

Fracture is a process of breaking a solid into pieces as a result of applied stress. There are two types of fracture: ductile and brittle fracture. The main difference between ductile and brittle fractures is in ductile fracture materials experience observable plastic deformation prior to fracture; however in brittle fracture materials experience little or no plastic deformation prior to fracture as shown in Fig.2.20. Brittle failures are usually catastrophic failures without any warning.

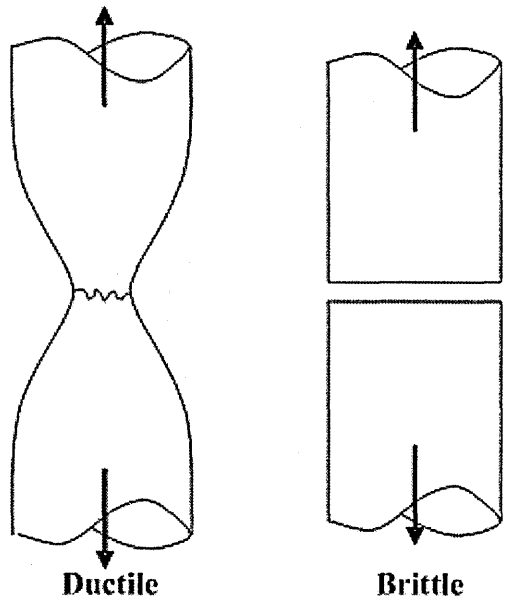

Fig.2.20 Ductile and Brittle fracture [91]

Brittle fracture is characterized by rapid crack propagation with low energy release and without significant plastic deformation. Brittle fracture displays either cleavage (transgranular) or intergranular fracture. This depends upon whether the grain boundaries are stronger or weaker than the grains. After fracture the solid may be separated into several pieces. The fracture surface of a brittle material will appear bright and granular.

Ductile materials undergo observable plastic deformation and absorb significant energy before fracture. Contrary to brittle fracture, a crack, formed as a result of ductile fracture, propagates slowly. Ductile fractures are desirable because of plastic deformation. They do not lead to unexpected failures in service. Fracture surfaces of ductile materials are in cup and cone structure with dimples. After fracture a large residual deformation will be observed.

The basic mechanism of ductile fracture is micro-void nucleation and coalescence [72]. Plastic deformation of a multi-phase material causes the formation and coalescence of voids on the phase boundaries and inclusions. One of the most important factors in the nucleation of voids is the interface bonds. As inclusions in a materials tend to have very low strength interface bonds, they are potential void nucleation points [73]. These voids are responsible for the specific appearance of the ductile fracture surface, consisting of numerous spherical micro-cavities (dimples), and initiating formation of the crack. Progress of a ductile fracture is shown in Fig.2.21.

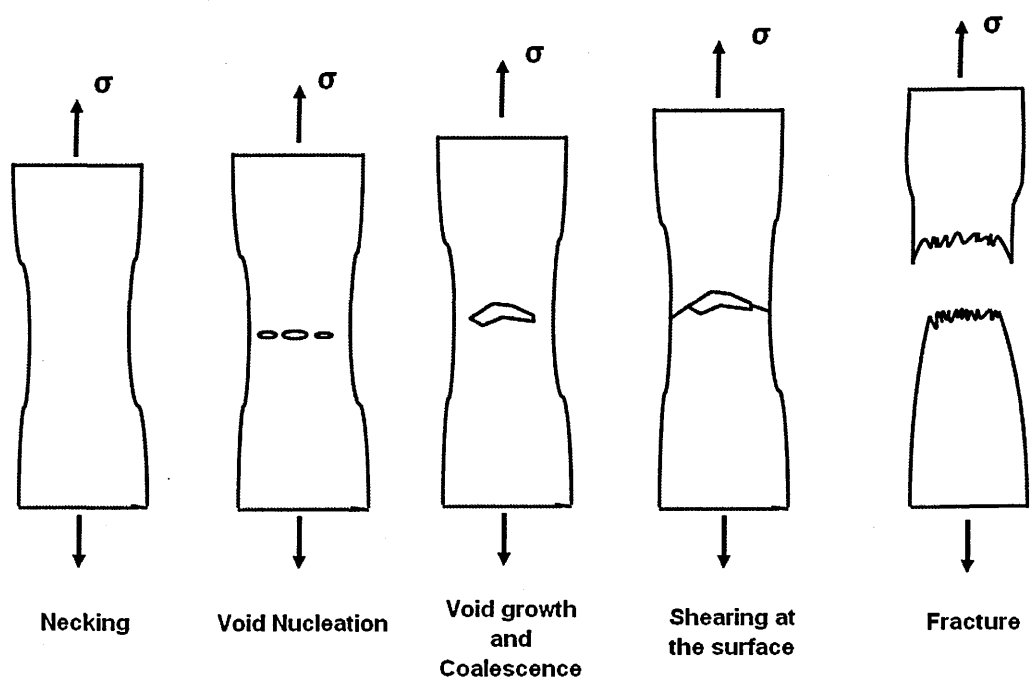

Fig.2.21 Progress of a ductile fracture

2.6 Creep

At room temperature, and at loads lower than the yield stress, materials can only deform elastically. When the applied stress is higher than the yield stress, materials deform plastically. So properly designed member will support its static design load forever if there is no corrosive environment [74]. However at elevated temperatures, the situation is different. Loads lower than the design loads can cause inelastic strains in the material which may result in plastic deformation and fracture. This time-dependent deformation is called creep. Creep can occur at all temperatures above absolute zero but the dimensional changes in the material due to creep deformation at low temperatures are extremely small and negligible [75].

By increasing the temperature, the mobility of the atoms in the material increases. These dynamic atoms play a great role in diffusion-controlled mechanisms and affect the material characteristics. At elevated temperatures different slip systems in the materials are activated so deformation mechanisms may change. The motion of dislocations will increase and more energetic dislocations will climb more easily, and material properties will be affected [75].

As mentioned earlier creep can take place at any temperature above absolute zero but usually it is prominent at temperatures above 0.3 T_m, where T_m is the melting temperature of the material in K [76]. As creep is a temperature related mechanism where the stresses below yield stresses are applied, the controlling parameters of creep are temperature and stress [77].

Ordinary creep tests are load controlled mechanical tests at a certain temperature where the load and temperature are fixed during the tests. The basic outcome of a creep test is to measure strain in the material at fixed time intervals. A typical creep curve as in Fig.2.22 can be divided into three stages, called primary, secondary and tertiary creep, and these regions are distinguished via the behaviour of the strain rate during the test. The strain rate is decreasing in the primary creep region and in the secondary creep region strain rate is constant so that this region is also called steady-state creep; and finally tertiary creep is the region where the strain rate is increasing towards final failure.

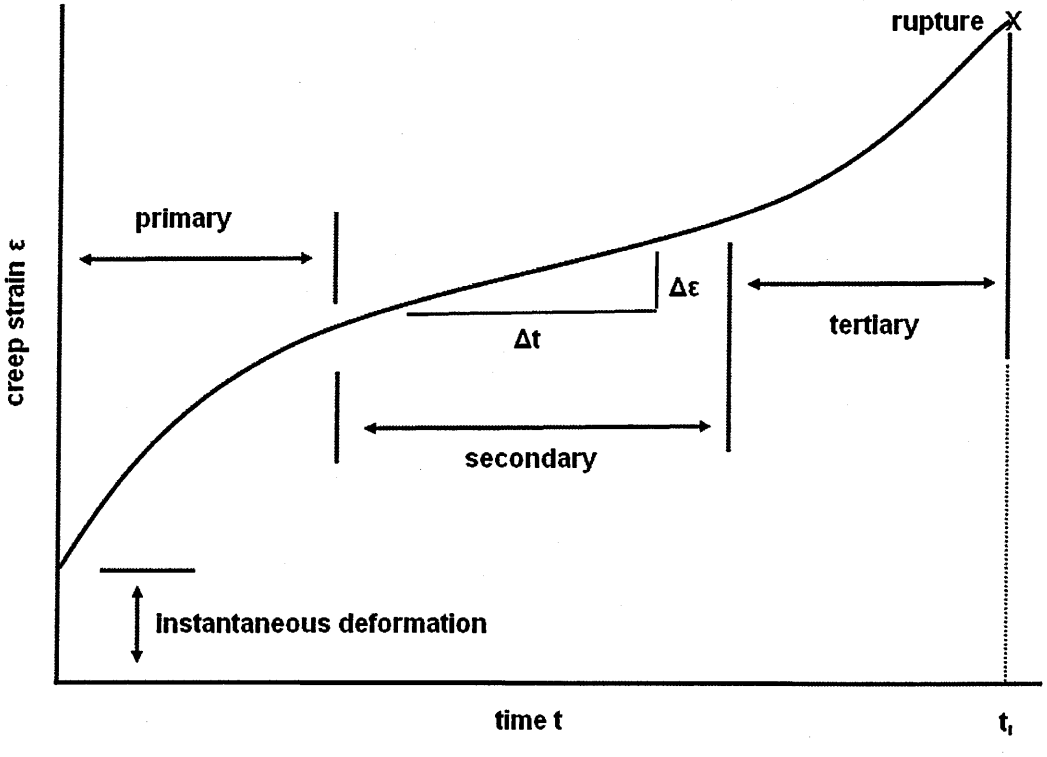

Fig.2.22 Typical Creep Curve [92]

2.6.1 Primary Creep

Primary creep is the first stage in a creep test. The creep strain rate is quite high but decreases with increasing strain. Material is being deformed and strain hardening occurs during this section due to dislocation movements. Stress induced dislocations accumulate, pile up and cause hardening in primary creep.

2.6.2 Secondary Creep

After primary creep the strain rate eventually reaches a minimum and becomes near constant. At that point the secondary creep work hardening of the materials and thermal softening due to the high temperature are in balance. Diffusional, Nabarro-Herring and Coble Creep and dislocation creep mechanisms take place in secondary creep. Typically, secondary creep rate can be described by an Arrhenius type equation:

$$\dot{\varepsilon} = A\sigma^n \exp\left(\frac{-Q}{RT}\right) \qquad (2.7)$$

Where σ is the stress, n is the stress exponent, Q is the activation energy, T is the absolute temperature, R is the universal gas constant and A is a material constant.

2.6.2.1 Diffusion Creep

Diffusion creep occurs by transport of material via diffusion of atoms within a grain. Like all diffusional processes, it is driven by a gradient of free energy (chemical potential), created in creep by the applied stress [78]. Diffusion creep is actually deformation of the grains when the transport of atomic vacancies (opposite to the direction of atom transport) is biased by an applied stress [79]. When a stress is applied to a material and when the mechanism is considered at a grain level, atoms within the grains will move along the applied stress direction to achieve a low energy state. Because of the load applied to the material the edges of the grains will be under stress and atoms in those high stress regions will tend to move into a low stress regions along the applied stress direction to reduce their energy. Vacancy transport will be in the opposite direction so that grains will elongate on the applied load direction. A typical illustration of atomic flow in a body is shown in Fig. 2.23.

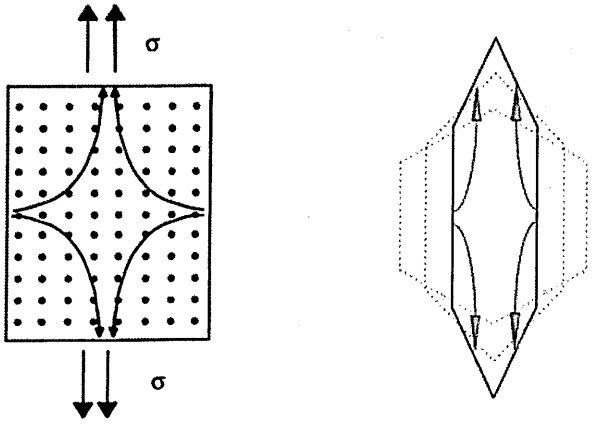

Fig.2.23 Schematic representation atomic flow and Nabarro-Herring Creep [79, 93]

There are two types of diffusion creep, depending on whether the diffusion paths are predominantly through the grain boundaries, termed Coble creep shown in Fig.2.24, or through the grains themselves, termed Nabarro-Herring creep which is shown in Fig.2.23. Diffusion through grain boundaries requires less activation energy because those regions are already high energy regions. Coble creep dominates at lower stress and temperatures. In contrast more mobility and activation energy is necessary for atoms to diffuse in the main body of the grains and this mobility is supplied by temperature. Hence the Nabarro-Herring creep mechanism is more dominant at high temperatures. Coble creep is still temperature dependent, as the temperature increases so does the grain boundary diffusion. However, since the number of nearest neighbours is effectively limited along the interface of the grains, and thermal generation of vacancies along the boundaries is less prevalent, the temperature dependence is not as strong as in Nabarro-Herring creep. The major difference between Coble creep and Nabarro Herring creep is that creep rate is dependent on the grain size and also the activation energies for bulk diffusion and grain boundary diffusion [80].

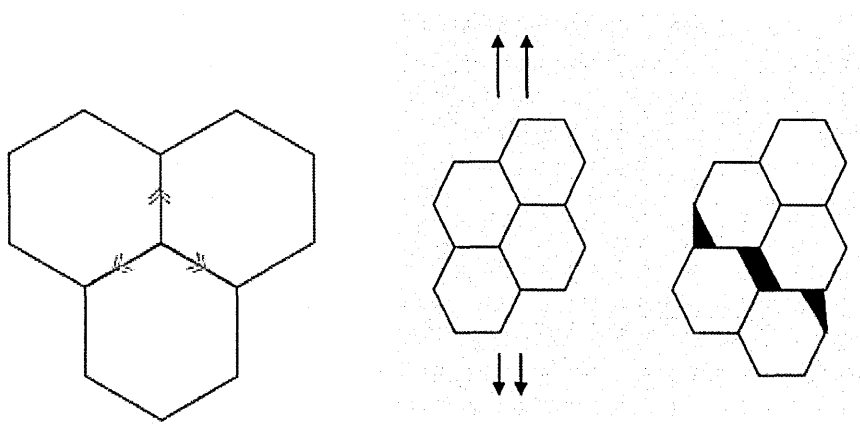

Fig.2.24 Grain boundary diffusion and formation of vacancies due to grain boundary sliding [79, 94]

Since the diffusion creep mechanism occurs on the scale of individual grains, the effect of grain size is a very important parameter in determining creep properties. If the grain size is big then atoms will need to migrate through long distances, so that creep rate will be decreased for Nabarro Herring creep. For Coble creep, if the grain size is big this means fewer grain boundaries, which is favoured for better creep resistance as the mechanism of Coble creep is grain boundary diffusion.

2.6.2.2 Dislocation Creep

This mechanism is based on movement of dislocations and generally dominates at high stresses. Dislocations can move by gliding in a slip plane. Dislocation gliding process requires little thermal activation. However, the rate-determining step for their motion is often a climb process, which requires diffusion of vacancies and/or interstitials and is thus time-dependent and favoured by higher temperatures. Dislocation gliding and climbing is shown in Fig. 2.25. Atomic diffusion is therefore important in dislocation climb process as in dislocation creep. Obstacles in the slip plane, such as other dislocations, precipitates or grain boundaries, can lead to dislocation climb [78].

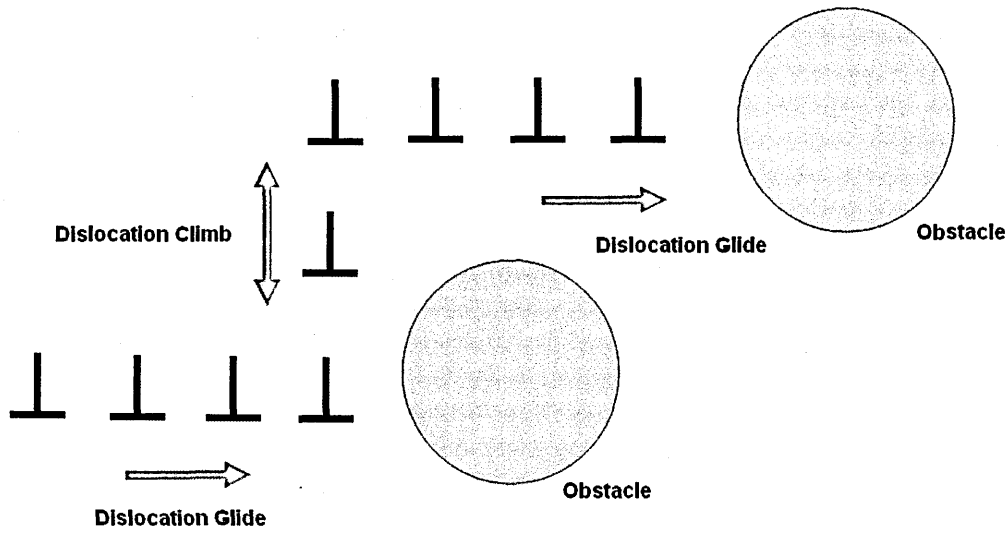

Fig.2.25 Dislocation Glide and Climb

If the applied stress is increased, the ability of the vacancies to transport will be higher and dislocation climb will be easier. After dislocation climb, the speed of the process up to the next obstacle for dislocation glide depends on the applied stress minus the internal stress in the material which is in the opposite direction of the applied stress [75].

2.6.3 Tertiary Creep

Tertiary creep is the final stage in creep leading to rupture. It is a period of increasing strain rate as the cavities which are formed in the material will coalesce and form creep cracks leading to failure, and because of necking phenomena [75]. At the end of tertiary creep, rupture takes place and rupture life and ductility values are obtained.

2.6.4 Effect of Stress and Temperature on Creep Behaviour

The applied stress provides a driving force for dislocation movement and diffusion of atoms [78]. As the stress is increased, the rate of deformation also increases. In general, it is found that:

$$\dot{\varepsilon} \sim \sigma^n \quad (2.8)$$

Where n is termed the stress exponent and its value depends on which mechanism of creep is operating. For example, for diffusion creep its value is approximately 1, while for dislocation creep it is usually in the range 3-8.

Both of the mechanisms in secondary creep, diffusion creep and dislocation creep are dependent on diffusion which is favoured by temperature. Temperature dependence of creep can be explained in an exponential way:

$$\dot{\varepsilon} \sim \exp\left(-\frac{Q}{RT}\right) \quad (2.9)$$

At high temperatures creep mechanisms proceed faster due to improved self diffusion of atoms and vacancies. However, what constitutes a high temperature is different for different metals. When considering creep, the concept of a homologous temperature is useful. The homologous temperature is the actual temperature divided by the melting point of the metal, with both being expressed in K. In general, creep tends to occur at a significant rate when the homologous temperature is 0.3 or higher [76, 78].

2.6.5 Extrapolation of Creep Results

In many applications, such as power plants and aircraft engines, components must be designed for long service at high temperatures (usually 20,000 – 100,000 hours). Accelerated creep tests are usually performed and by using a suitable extrapolation method,the performance of materials in the long term can be predicted from short term tests. The most commonly used parametric method is the Larson-Miller Parameter (LMP) and The Larson-Miller equation is in the form:

$$LMP = T(\log t_r + C) \qquad (2.10) \qquad [81]$$

Where C is an alloy-dependent constant, t_r is time to rupture in hours, T is temperature in Kelvin. If C is known for a particular alloy, one can find the rupture times at any temperature [82].

2.7 Summary

Martensitic steels are the hardest form of stainless steels and they can be modified by heat treatments according to desired properties.

The basic mechanism of the strengthening mechanisms by secondary particles is hindering dislocation motion.

A simple explanation of powder metallurgy production is to mechanically alloy the powders first and then consolidate. It is important for ODS material because mechanical alloying has the potential to achieve a fine and uniform particle dispersion which is one of the most important criteria to get good mechanical properties for ODS steels [83].

Oxide Dispersion Strengthened alloys have excellent potential for use in next-generation high-temperature applications where superior creep strength and oxidation resistance is required compared to precipitation strengthened alloys. In addition to that they have higher operating temperatures than high-Cr steels, good thermal conductivity, high swelling resistance and low radiation damage.

The strength of a material under tension has long been regarded as one of the most important characteristics required for design, production quality control and life prediction of industrial plant.

Creep is a temperature and stress dependant mechanism that usually becomes important at elevated temperature. Both diffusion and dislocation controlled mechanisms can occur and effect material properties significantly.

Rerefences

1. Helmenstine, A.M. *Why is Stainless Steel Stainless.* [Online] Available from: http://chemistry.about.com/cs/metalsandalloys/a/aa071201a.htm [Accessed November 2011]
2. Association, B.S.S. *The basics about stainless steel.* [Online] Available from: http://www.bssa.org.uk/about_stainless_steel.php [Accessed November 2011]
3. Sourmail, T. and H.K.D.H. Bhadeshia. *Stainless Steel.* Available from: http://www.msm.cam.ac.uk/phase-trans/2005/Stainless_steels/stainless.html [Accessed Date 2011
4. Prepared by the Working Party on Corrosion of Reinforcement in Concrete - Edited by Nurnberger, U., *Stainless Steel in Concrete - A State of the Art Report: (EFC 18)*, Maney Publishing. p. 4.
5. Products, S.P. *A Brief Overview of Stainless Steel.* [Online] Available from: http://www.sppusa.com/reference/white_paper/wp_ss.pdf [Accessed November 2011]
6. Azom. *Stainless Steels - Introduction To The Grades And Families.* [Online] Available from: http://www.azom.com/Details.asp?ArticleID=470 [Accessed December 2011]
7. John D. Verhoeven, *Steel Metallurgy for the Non-Metallurgist.* 2007: ASM International. 203.
8. Efunda. *Stainless Steels.* [Online] Available from: http://www.efunda.com/materials/alloys/stainless_steels/stainless.cfm [Accessed November 2011]
9. Kreysa, G. and M. SchÃ¼tze, *DECHEMA Corrosion Handbook - Revised and Extended 2nd Edition*, DECHEMA. p. 36.
10. Buschow, K.H.J., R.W. Cahn, M.C. Flemings, B. Ilschner, E.J. Kramer, and S. Mahajan, *Encyclopedia of Materials - Science and Technology, Volumes 1-11*, Elsevier. p. 3038.
11. Kutz, M., *Handbook of Materials Selection*, John Wiley & Sons. p. 44-46.
12. Oberg, E., F.D. Jones, H.L. Horton, and H.H. Ryffel, *Machinery's Handbook (27th Edition) & Guide to Machinery's Handbook*, Industrial Press. p. 480.
13. Deeley, P., K.J.A. Kundig, and J. Howard R. Spendelow, *Ferroalloys & Alloying Additives Online Handbook.* 2000.
14. Committee, A.S.M.I.H., *ASM Handbook, Volume 01 - Properties and Selection: Irons, Steels, and High-Performance Alloys*, ASM International. p. 144-146, 940.
15. Kopeliovich, D.D. *Effect of alloying elements on steel properties.* [Online] Available from: http://www.substech.com/dokuwiki/doku.php?id=effect_of_alloying_elements_on_steel_properties [Accessed November 2011]
16. H.R.Copson, *Physical Metallurgy of Stress Corrosion Fracture.* 1959 Interscience.
17. Lippold, J.C. and D.J. Kotecki, *Welding Metallurgy and Weldability of Stainless Steels*, John Wiley & Sons. p. 56.
18. Buschow, K.H.J., R.W. Cahn, M.C. Flemings, B. Ilschner, E.J. Kramer, and S. Mahajan, *Encyclopedia of Materials - Science and Technology, Volumes 1-11*, Elsevier. p. 8880.
19. Palmer, A.C. and R.A. King, *Subsea Pipeline Engineering (2nd Edition)*, PennWell. p. 36.

20. Higgins, R.A., *Engineering Metallurgy - Applied Physical Metallurgy (6th Edition)*, Elsevier. p. 162.
21. Furrer, D.U. and S.L. Semiatin, *ASM Handbook, Volume 22A - Fundamentals of Modeling for Metals Processing*, ASM International. p. 383.
22. Meyers, M.A. and K.K. Chawla, *Mechanical Behavior of Materials (2nd Edition)*, Cambridge University Press. p. 580.
23. A.M.Donald, *Obstacles to Dislocation Motion*, in *Crystalline Solids*, Cambridge University.
24. Verhoeven, J.D., *Fundamentals of Physical Metallurgy*. 1975: John Wiley & Sons.
25. Soboyejo, W., *Mechanical Properties of Engineered Materials*. 2002: CRC Press.
26. Angelo, P.C. and R. Subramanian, *Powder Metallurgy Science: Technology and Applications*. 2008: PHI Learning Private Limited.
27. Vadiraja, S., *Failure Analysis Approach to Fracture Studies in Powder Metallurgy Parts.* Powder Metallurgy and Metal Ceramics, 2004. **43**(1): p. 105-109.
28. Kutz, M., *Handbook of Materials Selection*, John Wiley & Sons. p. 959.
29. Evcin, A., *Toz Uretim Teknikleri*. 2007, Afyonkarahisar Kocatepe University.
30. Gilman, P.S. and J.S. Benjamin, *Mechanical Alloying.* Annual Review Materials Science, 1983. **13**: p. 279-300.
31. El-Eskandarany, M.S., *Mechanical Alloying for Fabrication of Advanced Engineering Materials*. 2001, William Andrew Publishing/Noyes. p. 17.
32. Li Lü and M.O. Lai, *Mechanical alloying*. 1998: Kluwer Academic Publishers.
33. Liu, D.-h., Y. Liu, D.-p. Zhao, Y. Wang, J.-h. Fang, Y.-r. Wen, and Z.-m. Liu, *Effect of ball milling time on microstructures and mechanical properties of mechanically-alloyed iron-based materials.* Transactions of Nonferrous Metals Society of China. **20**(5): p. 831-838.
34. de Castro, V., T. Leguey, M.A. Monge, A. Muñoz, R. Pareja, D.R. Amador, J.M. Torralba, and M. Victoria, *Mechanical dispersion of Y2O3 nanoparticles in steel EUROFER 97: process and optimisation.* Journal of Nuclear Materials, 2003. **322**(2-3): p. 228-234.
35. Avettand-Fènoël, M.N., R. Taillard, J. Dhers, and J. Foct, *Effect of ball milling parameters on the microstructure of W-Y powders and sintered samples.* International Journal of Refractory Metals and Hard Materials. **21**(3-4): p. 205-213.
36. de Castro, V., T. Leguey, A. Muñoz, M.A. Monge, R. Pareja, E.A. Marquis, S. Lozano-Perez, and M.L. Jenkins, *Microstructural characterization of Y2O3 ODS-Fe-Cr model alloys.* Journal of Nuclear Materials, 2009. **386-388**: p. 449-452.
37. Azom. *Hot Isostatic Pressing.* Available from: http://www.azom.com/article.aspx?ArticleID=924 [Accessed Date 2011
38. Malicky, D., *Powder Metallurgy (P/M)*, University of San Diego: San Diego.
39. Rao, M.N., *Materials Development for Indian Nuclear Power Programme: an Industry Perspective* Energy Procedia, 2010. **7**: p. 199-204.
40. Kohyama, A., A. Hishinuma, D.S. Gelles, R.L. Klueh, W. Dietz, and K. Ehrlich, *Low-activation ferritic and martensitic steels for fusion application.* Journal of Nuclear Materials, 1996. **233-237**(Part 1): p. 138-147.
41. Shibli, I.A. and D.G. Robertson, *Review of the use of new high strength steels in conventional and HRSG boilers: R&D and plant experience*, in *ETD Report N.* 2006, European Technology Development LTD.
42. van der Schaaf, B., D.S. Gelles, S. Jitsukawa, A. Kimura, R.L. Klueh, A. Möslang, and G.R. Odette, *Progress and critical issues of reduced activation ferritic/martensitic steel development.* Journal of Nuclear Materials, 2000. **283-287**(Part 1): p. 52-59.
43. Verhiest, K., A. Almazouzi, N.D. Wispelaere, R. Petrov, and S. Claessens, *Development of oxides dispersion strengthened steels for high temperature nuclear reactor applications.* Journal of Nuclear Materials, 2009. **385**(2): p. 308-311.

44. Yu, G., N. Nita, and N. Baluc, *Thermal creep behaviour of the EUROFER 97 RAFM steel and two European ODS EUROFER 97 steels.* Fusion Engineering and Design, 2005. **75-79**: p. 1037-1041.
45. Klueh, R. and D.R. Harries, *High Chromium ferritic and martensitic steels for nuclear application.* 2001: ASTM.
46. Fernández, P., A.M. Lancha, J. Lapeña, M. Serrano, and M. Hernández-Mayoral, *Reduced Activation Ferritic/Martensitic Steel Eurofer'97 as Possible Structural Material for Fusion Devices, Metallurgical Characterization on As-Received Condition and after Simulated Service Conditions.* 2004, Departamento de Fusión Nuclear.
47. Baluc, N., D.S. Gelles, S. Jitsukawa, A. Kimura, R.L. Klueh, G.R. Odette, B. van der Schaaf, and J. Yu, *Status of reduced activation ferritic/martensitic steel development.* Journal of Nuclear Materials, 2007. **367-370**(Part 1): p. 33-41.
48. Kurtz, R.J., A. Alamo, E. Lucon, Q. Huang, S. Jitsukawa, A. Kimura, R.L. Klueh, G.R. Odette, C. Petersen, M.A. Sokolov, P. Spätig, and J.W. Rensman, *Recent progress toward development of reduced activation ferritic/martensitic steels for fusion structural applications.* Journal of Nuclear Materials, 2009. **386-388**: p. 411-417.
49. Raj, B. and T. Jayakumar, *Development of Reduced Activation Ferritic-Martensitic Steels and fabrication technologies for Indian test blanket module.* Journal of Nuclear Materials, 2011. **417**(1-3): p. 72-76.
50. Muroga, T., M. Gasparotto, and S.J. Zinkle, *Overview of materials research for fusion reactors.* Fusion Engineering and Design, 2002. **61-62**: p. 13-25.
51. Klueh, R.L., J.P. Shingledecker, R.W. Swindeman, and D.T. Hoelzer, *Oxide dispersion-strengthened steels: A comparison of some commercial and experimental alloys.* Journal of Nuclear Materials, 2005. **341**(2-3): p. 103-114.
52. Hsiung, L.L., M.J. Fluss, S.J. Tumey, B.W. Choi, Y. Serruys, F. Willaime, and A. Kimura, *Formation mechanism and the role of nanoparticles in Fe-Cr ODS steels developed for radiation tolerance.* Physical Review B. **82**(18): p. 184103.
53. Klueh, R.L., P.J. Maziasz, I.S. Kim, L. Heatherly, D.T. Hoelzer, N. Hashimoto, E.A. Kenik, and K. Miyahara, *Tensile and creep properties of an oxide dispersion-strengthened ferritic steel.* Journal of Nuclear Materials, 2002. **307-311**(Part 1): p. 773-777.
54. Mukhopadhyay, D.K., F.H. Froes, and D.S. Gelles, *Development of oxide dispersion strengthened ferritic steels for fusion.* Journal of Nuclear Materials, 1998. **258-263**(Part 2): p. 1209-1215.
55. Ramar, A., P. Spätig, and R. Schäublin, *Analysis of high temperature deformation mechanism in ODS EUROFER97 alloy.* Journal of Nuclear Materials, 2008. **382**(2-3): p. 210-216.
56. Ault, G.M., H.M. Burte, G.S. Ansell, T.D. Cooper, and F.V. Lenel. *Oxide Dispersion Strengthening.* in *Second Bolton Landing Conference.* 1966. New York: Metallurgical Society Conferences.
57. Sakasegawa, H., S. Ohtsuka, S. Ukai, H. Tanigawa, M. Fujiwara, H. Ogiwara, and A. Kohyama, *Microstructural evolution during creep of 9Cr-ODS steels.* Fusion Engineering and Design, 2006. **81**(8-14): p. 1013-1018.
58. Sakasegawa, H., S. Ohtsuka, S. Ukai, H. Tanigawa, M. Fujiwara, H. Ogiwara, and A. Kohyama, *Particle size effects in mechanically alloyed 9Cr ODS steel powder.* Journal of Nuclear Materials, 2007. **367-370**(Part 1): p. 185-190.
59. Ukai, S. and M. Fujiwara, *Perspective of ODS alloys application in nuclear environments.* Journal of Nuclear Materials, 2002. **307-311**(Part 1): p. 749-757.
60. Badmos, A.Y., *Some Properties of Mechanically Alloyed Oxide Dispersion Strengthened Metals,PhD Thesis*, in *Department of Materials Science and Metallurgy*. 1997, University of Cambridge: Cambidge.

61. Olier, P., A. Bougault, A. Alamo, and Y. de Carlan, *Effects of the forming processes and Y2O3 content on ODS-Eurofer mechanical properties.* Journal of Nuclear Materials, 2009. **386-388**: p. 561-563.
62. Oksiuta, Z. and N. Baluc, *Effect of mechanical alloying atmosphere on the microstructure and Charpy impact properties of an ODS ferritic steel.* Journal of Nuclear Materials, 2009. **386-388**: p. 426-429.
63. Hadraba, H., B. Kazimierzak, L. Stratil, and I. Dlouhy, *Microstructure and impact properties of ferritic ODS ODM401 (14%Cr-ODS of MA957 type).* Journal of Nuclear Materials, 2011. **417**(1-3): p. 241-244.
64. Henry, J., X. Averty, Y. Dai, J.P. Pizzanelli, and J.J. Espinas, *Tensile properties of ODS-14%Cr ferritic alloy irradiated in a spallation environment.* Journal of Nuclear Materials, 2009. **386-388**: p. 345-348.
65. Oksiuta, Z. and N. Baluc, *Microstructure and Charpy impact properties of 12-14Cr oxide dispersion-strengthened ferritic steels.* Journal of Nuclear Materials, 2008. **374**(1-2): p. 178-184.
66. Suryanarayana, C., E. Ivanov, and V.V. Boldyrev, *The science and technology of mechanical alloying.* Materials Science and Engineering, 2001. **A304-306**: p. 151-158.
67. Cayron, C., E. Rath, I. Chu, and S. Launois, *Microstructural evolution of Y2O3 and MgAl2O4 ODS EUROFER steels during their elaboration by mechanical milling and hot isostatic pressing.* Journal of Nuclear Materials, 2004. **335**(1): p. 83-102.
68. Rahmanifard, R., H. Farhangi, and A.J. Novinrooz, *Optimization of mechanical alloying parameters in 12YWT ferritic steel nanocomposite.* Materials Science and Engineering: A. **527**(26): p. 6853-6857.
69. Romanski, G.R., L.L. Snead, R.L. Klueh, and D.T. Hoezler, Journal of Nuclear Materials, 2000. **283-287**: p. 642.
70. Loveday, M.S., T. Gray, and J. Aegerter, *Tensile Testing of Metallic Materials: A Review*. 2004, NPL Management Ltd.
71. Instron. *Tensile Testing*. Test Types [Online] Available from: http://www.instron.us/wa/applications/test_types/tension/default.aspx [Accessed January 2012]
72. Sabirov, I. and O. Kolednik, *The effect of inclusion size on the local conditions for void nucleation near a crack tip in a mild steel.* Scripta Materialia, 2005. **53**(12): p. 1373-1378.
73. Becker, W.T. and R.J. Shipley, *ASM Handbook, Volume 11 - Failure Analysis and Prevention*, ASM International. p. 591-593.
74. Boresi, A.P. and R.J. Schmidt, *Advanced Mechanics of Materials (6th Edition)*, John Wiley & Sons. p. 624.
75. Rao, A., *Creep and Anelastic Deformation in Austenitic Steels,PhD Thesis*. 2010, The Open University: Milton Keynes.
76. Evans, R.W. and B. Wilshire, *Creep of Metals and Alloys*. 1985, London: The Institue of Metals.
77. Evans, R.W. and B. Wilshire, *Introduction to Creep*. 1993: The Institute of Materials.
78. Cambridge, U., *Creep deformation of Metals*, in *Dissemination of IT for the Promotion of Materials Science (DOITPOMS)*. 2010.
79. Kuhn, H. and D. Medlin, *ASM Handbook, Volume 08 - Mechanical Testing and Evaluation*, ASM International. p. 363-368.
80. J.P.Poirier, *Creep of crystals: High-temperature deformation processes in metals*. Cambridge Earth Science Series. 1985.
81. William D. Callister, J., *Materials Science and Engineering: An Introduction*. 2007: John Wiley & Sons.

82. Meyers, M.A. and K.K. Chawla, *Mechanical Behavior of Materials (2nd Edition)*, Cambridge University Press.
83. Zakine, C., C. Prioul, and D. François, *Creep behaviour of ODS steels.* Materials Science and Engineering A, 1996. **219**(1-2): p. 102-108.
84. Zeren, M., *Toz Metalurjisi.* 2007, Kocaeli University.
85. Eisen, W.B., B.L. Ferguson, G. R.M., R. Iacocca, P.W. Lee, D. Madan, K. Moyer, H. Sanderow, and Y. Trudel, *ASM Handbook, Volume 07 - Powder Metal Technologies and Applications*, ASM International. p. 64.
86. Steel, D. *Target Technology.* [Online] Available from: http://dsuxgwns.daido.co.jp/english/products/raremetal/target_technology.html [Accessed December 2011]
87. Kimura, A., H.S. Cho, N. Toda, R. Kasada, H. Kishimoto, N. Iwata, S. Ukai, S. Ohnuki, and M. Fujiwara, *Super ODS Steels R&D.* Workshop on Structural Materials for Innovative Nuclear Systems, 2007.
88. Kopeliovich, D. *Fracture Toughness.* [Online] Available from: http://www.substech.com/dokuwiki/doku.php?id=fracture_toughness [Accessed December 2011]
89. Tarr, M., *Stress and its effect on materials.* 2007, University of Bolton.
90. T.G.Nieh, J.Wadsworth, and O.D.Sherby, *Superplasticity in metals and ceramics.* Cambridge Solid State Science Series. 1997.
91. Yuran, A.F., *Creep Deformation*, in *Lecture Notes*, Afyon Kocatepe University.

CHAPTER 3: EXPERIEMENTAL METHODS AND TEST SAMPLES

During this study various experimental techniques are utilized to characterize and examine microstructure and mechanical properties. These techniques are explained here in order to clarify how tests were conducted.

3.1 Materials and Compositions

Four different materials are used in this project for better understanding the effect of compositional and manufacturing differences. The base metal for all materials is 410L steel. 410L is a basic martensitic 12% Cr steel with maximum 1% alloying elements with nominal composition as shown in Table 3.1.

Material	Cr	Si	Mn	S	P
410	11.5 - 13	≤ 1	≤ 1	≤ 0.5	≤ 0.5

All values are in wt. %.

Table 3.1 Nominal Composition of 410L martensitic steel

Two of the materials are oxide-dispersion strengthened and the remaining two are non-ODS materials. Yttria, Y_2O_3, is used for dispersion strengthening. A different size of yttria was used in each ODS material for better understanding of the effect of the size of dispersion on the mechanical behaviour of the materials. The size of the yttria particles introduced in the ODS materials are 0.9 μm and 50 nm to understand the effect of size of oxide particles on the performance of ODS alloys. Usually oxide particles with sizes less than 100 nm especially less than 50

nm are used in other ODS alloys from the literature [1-4]. Smaller particle size means easier dissolution due to increased number of oxide particles (in a system having same weight percent of oxide content) and increased surface area of oxides to ease interactions. The non-ODS materials are different in their manufacturing steps. One is just hot-isostatic pressed (HIP) from the powder and will be referred to as un-milled, whereas the other is first mechanically alloyed and then HIPed, referred to as mechanically alloyed (MA). Both ODS materials are mechanically alloyed and then HIPed.

All materials were received as billets. To make machining and other processes easier big billets were machined into small cylinders. Each cylinder's diameter is 12 mm and length is between 90 mm to 100 mm depending on the height of the billets. One of the machined billets and an extruded cylinder can be seen in Fig. 3.1.

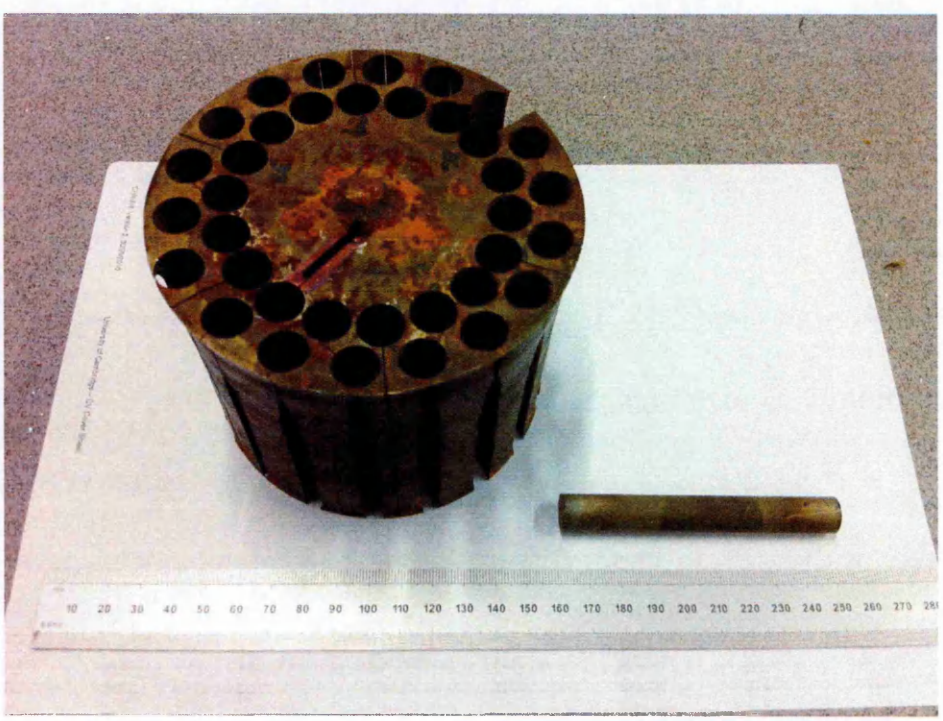

Fig. 3.1 Extruded billet with 12 mm cylinders extracted

3.2 Heat Treatments

Heat Treatment is the controlled heating and cooling of metals to alter their physical and mechanical properties without changing the product shape. As the matrix material 410L is a martensitic stainless steel with proper heat treatments where martensite is the hardest phase of steels with excess carbon saturation in BCT (body centred tetragonal) structure and this configuration makes the material very brittle with limited elongation, heat treatment is necessary to improve properties. Entrapping of carbon atoms occur due to rapid cooling referred to quenching from austenite. During quenching carbon atoms do not have enough time to diffuse out of the lattice structure so those carbon atoms stay in the lattice and strain the crystal structure.

To provide some toughness and ductility these kinds of steels usually undergo tempering a process. Recovery and recrystallization takes place at high temperatures during tempering and relaxation occurs and mobility of atoms increases. By heating, diffusion is made easier and this allows the trapped excess carbon atoms in the matrix to diffuse out and form carbides. After tempering the martensite structure is distorted and it partly decomposes into cementites and ferrites and is called tempered martensite. This decomposition depends on the tempering temperature. If tempering takes place above martensite start temperature in the range of ferrite and cementite, then, decomposition occurs otherwise there will be just some internal stress relaxation in the system.

Tempering results in a desired combination of hardness, ductility, toughness, strength, and structural stability.

There is another reason for heat treatment, in that the materials may not have the same initial microstructure after production. For this reason heat treatment was performed on the final billets to achieve a tempered martensitic stainless steel in all materials and remove production effects like residual ferrites at grain boundaries due to slow cooling after HIP.

The heat treatment was austenitizing at 1000 °C for 30 mins followed by oil quenching to achieve a fully martensitic microstructure, and tempering at 650 °C for 2 hrs and furnace cooling to have a tempered martensite structure. The heat treatment process was performed on 12 mm diameter cylindrical samples so the austenitizing time was set to 30 mins where one hour per inch of thickness is suitable for austenitizing 410 steel [5]. The same heat treatment procedure was followed for all samples for all tests.

3.3 Optical Microscopy

Images of microstructural features are obtained from microscopes that magnify the images obtained by the transmission or reflection of either light or electrons [6]. Optical microscopes are using the reflection of light so that they are also called light microscopes. The resolution of a typical light microscope is around 0.5 μm. The basic principle of the imaging in a light microscope is the contrast difference on the structure. Usually specimens are etched before imaging.

The etchant attacks specific constituents in the structure and causes roughness so that reflection of the light will be effected which causes contrast differences. Before this step samples must be prepared carefully for a clear image. These sample preparation steps are explained below.

3.3.1 Sample Preparation

Sectioning is the first step of metallographic sample preparation and must be performed very carefully in order not to destroy the structure of interest. Sectioning is necessary for easier handling [7]. For example instead of a huge heavy bulk specimen a small sized sample can be enough to make analysis where that small sample is representative for the whole bulk. Proper sectioning is required to minimize damage, which may alter the microstructure and produce false metallographic characterization.

The second step is mounting. Small samples can be difficult to hold safely during grinding and polishing operations, and their shape may not be suitable for observation on a flat surface [7]. So, small samples are generally mounted in plastic for convenience in handling and to protect the edges of the specimen being prepared. One of the most common mounting materials is a thermosetting phenolic, called Bakelite [8].

Grinding is generally considered the most important step in specimen preparation. Care must be taken to minimize mechanical surface damage. Grinding is generally performed by the abrasion of the specimen surface against a

water-lubricated abrasive. Grinding develops a flat surface with a minimum depth of deformed metal and usually is accomplished by using progressively finer abrasive grits on the grinding wheels [8]. There are a number of grades of grinding paper, with 220, 400, 500, 800, 1200 grains of silicon carbide per square inch. It is essential to start with the coarsest grinding paper and continue step by step. The same order was used in grinding of all the samples for this project. Scratches and damage to the specimen surface from each grit must be removed by the next finer grinding step.

The surface damage remaining on the specimen after grinding must be removed by polishing. Polishing usually consists of two steps: rough polishing and fine polishing. The polishers consist of rotating discs covered with soft cloth impregnated with diamond particles and an oily lubricant. Diamond particles used in the project are in 6 and 1 micron in size for rough and fine polishing respectively, starting with the 6 micron grade and continuing polishing until the grinding scratches had been removed.

3.3.2 Etching

Microstructures usually are not observable in the as-polished condition. However some constituents like voids and some inclusion particles can be seen under the microscope after polishing. Some analyses are done in un-etched conditions and will be discussed in following chapters.

Etching is one of the key steps in metallographic examinations and it is used for revealing microstructure and constituents. The etchant attacks high energy regions in the material and reveals various constituents like grain boundaries, precipitates and phases etc. So, etched regions can be easily distinguished via light microscope because light from the rough etched surface will be scattered and so the etched region will appear dark. Sometimes colouring is possible due to etching as well. Generally etchants are specific for different constituents. For example the etchant for revealing carbides may not be same with etchant for ferrite, so careful etchant selection is necessary. In addition the etchant application procedure is very important. Too much etching will cause burns (over-etching) on the surface and may need a new start from grinding a fresh surface.

Various etching techniques are available, including chemical attack, electrochemical attack, thermal treatments, vacuum cathodic etching, and mechanical treatments. In this project to conduct metallographic analysis chemical and electrochemical etchants are used to reveal microstructural features. Villela's reagent with composition; 1 g picric acid, 5 ml HCl and 100 ml ethanol [9], is the main etchant for all microstructures in this project. It is a commonly used etchant for revealing constituents and etching martensite. It is applied for between 10-20 seconds depending on the contrast of the microstructure. NaOH–water electrolytic etchant is used for revealing residual ferrites in the structure in the as-received condition of the materials. The composition of the electrolytic etchant is 20 g NaOH and 100 ml water [9]. It is a kind of controlling mechanism to check the microstructure before and after heat treatment to have all the materials are tempered martensite without any ferrite as desired.

3.4 Electron Microscope

The operating mechanism of electron microscopes is different than optical microscopes. They use electrons instead of light for imaging and they can achieve higher resolution when compared to light microscopes. Electron microscopes are able to reveal details smaller than 1nm.

Resolution is the finest detail that can be distinguished in an image. The resolving power of a microscope is not same as magnification. You can magnify an image indefinitely using more powerful lenses, but the image will blur. Therefore, increasing the magnification will not improve resolution. The minimum separation (d) that can be resolved by any kind of a microscope is given by the following formula:

$$d = \frac{n\lambda}{2\sin\theta} \qquad (3.1)$$

Where n is the refractive index (which is 1 in the vacuum of an electron microscope) and λ is the wavelength. Since resolution and d (spacing between atoms) are inversely proportional a smaller separation requires a higher resolution, this formula suggests that the way to improve resolution is to use shorter wavelengths and media with larger indices of refraction. The electron microscope is using extremely short wavelengths of accelerated electrons to form high-resolution images [10].

Examination of a specimen with electron microscopes can yield information about topography, morphology, composition and crystallographic information of the specimen [11].

3.4.1 Scanning Electron Microscope (SEM)

A scanning electron microscope is a type of electron microscope that images a sample by scanning it with a high-energy beam of electrons.

Electrons in the SEM are generated by an electron gun. When a positive electrical potential is applied to the filament (cathode) in the gun, the filament heats up and electrons are produced. The electrons are accelerated and repelled by the anode, called Wehnelt Cap, toward the optical axis. Then those electrons leave the gun through a small hole in the Wehnelt Cap to the lenses [11]. A schematic illustration of the electron gun is shown in Fig. 3.2. There are three main types of electron guns used in SEM. These are heated tungsten, lanthanum hexaboride (LaB_6) and tungsten field emission gun (FEG). The working principle of heated tungsten and lanthanum hexaboride is similar generating electrons by high thermal energy but FEG operates differently. In FEG, electrons are expelled by applying a very powerful electric field very close to the filament tip. A field emission gun scanning electron microscope Zeiss Supra 55VP FEG SEM is available at the OU and electron microscopy experiments were carried out in that.

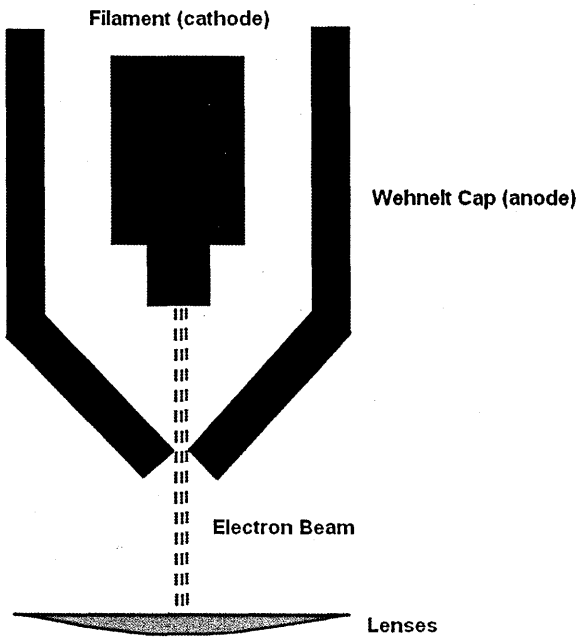

Fig. 3.2 Electron Gun

Next stop for the electrons in the chamber is the condenser lenses. These lenses are magnetic coils that have been tuned to focus and direct a passing electron beam. The function of these condenser lenses is to focus the electrons into a tight beam and control the size of the beam as well as the quantity of electrons travelling down to the column.

After the condenser lenses the electron beam comes to the scanning coils which is responsible for the movement of the beam on the specimen surface [12]. These coils make the beam play over the target. This movement is controlled by placing sets of plates around the beam and varying the potential between them, so that the electron beam can be deflected [13].

The last step before electrons reach the specimen is the objective lens. The objective lens is responsible for focussing the beam on the desired part of the specimen. This is necessary to have an image in proper focus.

After the electrons leave the objective lens they reach and hit the target specimen and interactions occur. A schematic illustration of a scanning electron microscope is shown in Fig. 3.3

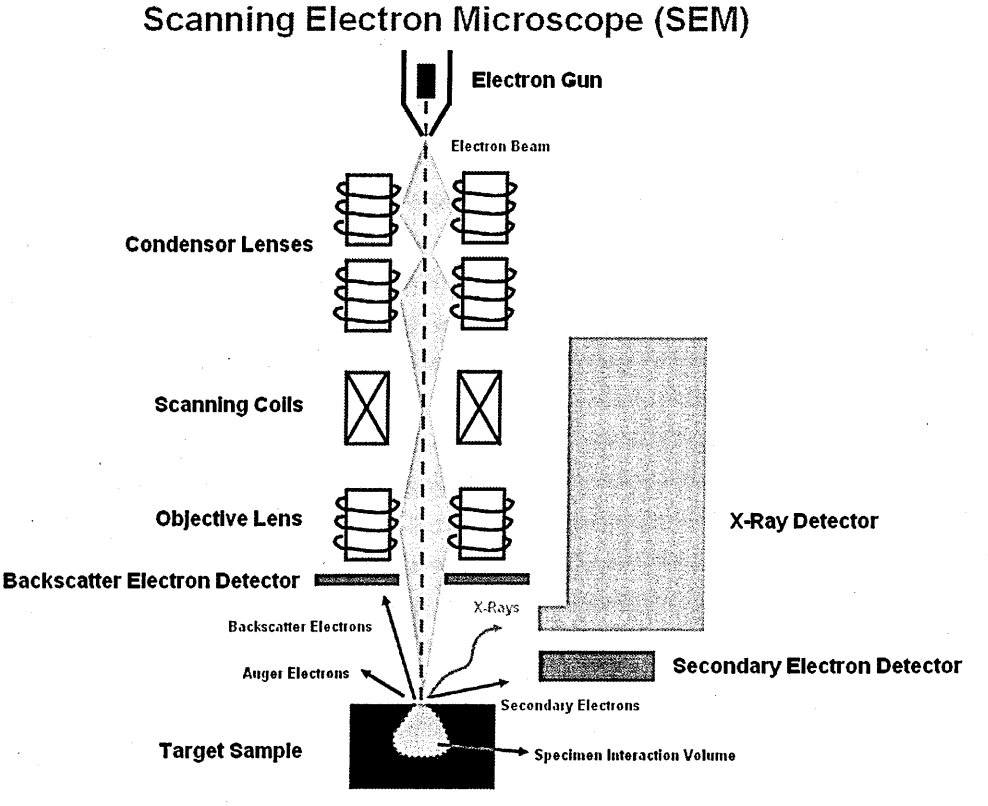

Fig. 3.3 Schematic illustration of Scanning Electron Microscope

There are also apertures in the system. Apertures are holes along the microscope column that can limit the size of the electron beam that passes through them. Depending on its location in the column an aperture can have different uses.

The first aperture, the condenser aperture, for example, is located near the top of the column and as the name implies, is used to condense and maintain the coherence of the electron beam. The second aperture, the objective aperture, is located below the sample just after the objective lens. The objective aperture is used primarily to control contrast in the image. For example if a small objective aperture is used, electrons that are deflected at a greater angle are blocked, and the contrast of the image is enhanced. However, electrons with a high deflection contain high resolution information but are lost. A balance needs to be achieved between having good contrast and having a high resolution.

Images are obtained after interaction of the electrons with the atoms of the specimen. These interactions are what make the electron microscopy possible. The energetic electrons in the microscope strike the sample and various reactions occur in the specimen interaction volume which is the volume inside the specimen in which interactions occur while being struck with an electron beam. This volume depends on three factors. First is the atomic number of the sample where higher atomic number materials absorb or stop more electrons and so have a smaller interaction volume. Secondly, it depends on accelerating voltage being used because higher voltages penetrate farther into the sample and generate larger interaction volumes. And finally it is related to angle of incidence for the electron beam where the greater the angle from the normal causes a smaller volume of interacton [11].

When an electron hits the specimen there are three possibilities. First, it can pass through the sample without colliding with any of the sample atoms. Second,

it can collide with electrons from the sample atoms, and create secondary electrons. Or third, it can collide with the nucleus of the sample atom, and create a backscattered electron [13]. Secondary electrons and backscattered electrons are shown in Fig. 3.4.

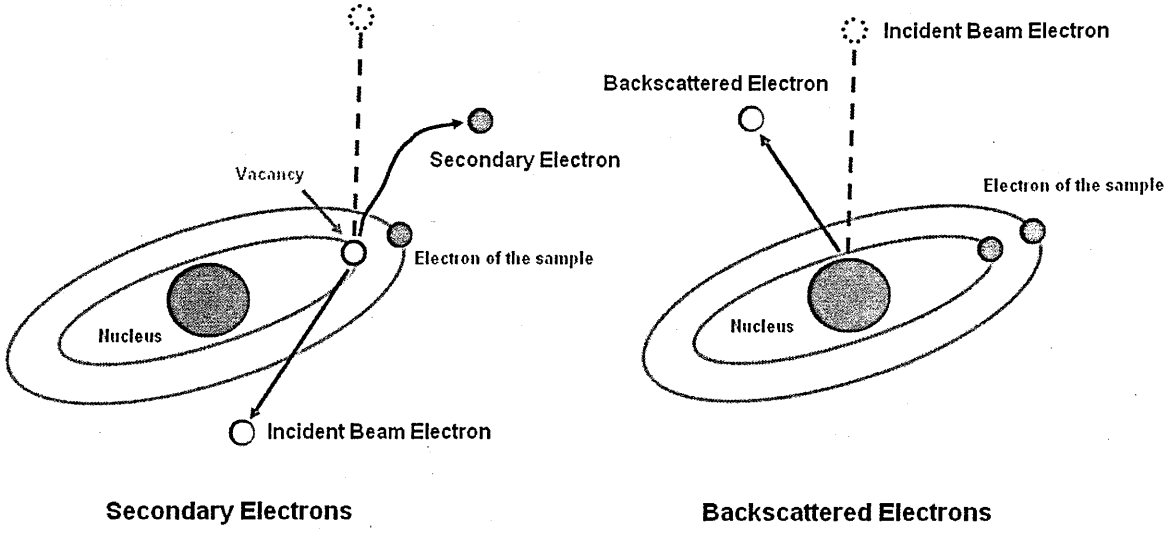

Fig. 3.4 Secondary electrons and backscattered electrons

The incident beam is composed of highly energized electrons. If one of these electrons collides with a sample atom electron, it will knock it out of its shell. This electron is called a secondary electron and the energy of that electron is low. Each incident electron can produce several secondary electrons. If these secondary electrons are close enough to the sample surface because they have very low energy (5eV), they can be collected in conjunction with the secondary electron detector to form an SEM image. The operating principle of the collector is simple

interactions. A positive potential applied to the collector attracts negatively charged secondary electrons. Those electrons then reaches the detector [11].

De-energization of the specimen atom after a secondary electron production causes two more events. Since a lower (usually K-shell) electron was emitted from the atom during the secondary electron process, that shell now has a vacancy. A higher energy electron from outer shell from the same atom can "fall" to a lower energy by filling the vacancy. After all these movements there will be energy surplus in the system. To compensate this, a lower energy (outer) electron is emitted from the specimen which is called an auger electron. Auger electrons have a characteristic energy and that energy is unique to each element. These electrons are collected and sorted according to energy to obtain compositional information about the specimen. In addition to that as the outer electron falls it emits energy as well and X-rays are produced to balance. X-rays are unique to each element as well and they can be utilized for compositional analysis [11].

The production of backscattered electrons varies directly with the specimen's atomic number. This causes higher atomic number elements to appear brighter than lower atomic number elements. This interaction is utilized to differentiate parts of the specimen that have different average atomic numbers.

For SEM, usually there is no need for sample preparation for conductive specimens like metals but however if there is a conductivity problem gold coating and/or silver painting may be utilized to improve conductivity. Both techniques were used for this project.

In this project SEM was mainly used for fracture surface analysis and characterization of metallographic specimens mostly for inclusions and oxide particles and some porosity issues.

3.4.2 Energy Dispersive X-Ray Spectroscopy (EDX)

Energy dispersive X-ray spectroscopy analysis, also known as EDS or EDX, is a technique used to identify the elemental composition of a sample or small area of interest on the sample imaged in the electron microscope. EDX can be used in conjunction with both scanning electron microscopy and transmission electron microscopy. When the electron beam in the microscope hits the sample, X-rays are emitted to balance the energy difference between the knocked out elecron and high energy electron from outer orbit. The X-ray energy is characteristic of the element from which it was emitted [14].

There are three shells around the nucleus called K, L and M shells. K is the inner one so is the closest one to the nucleus. When there is a vacancy in the K shell and that shell is filled by an electron from the L shell, the X-ray energy emitted from that process is called K_α but if the filling electron is from the M shell then it is called K_β. If the vacancy is in an L shell and filled by an electron from an M shell then energy is called L_α.

The EDX X-ray detector measures the relative abundance of emitted X-rays from the interactions versus their energy. The X-Ray detector is a solid-state device. When an X-ray strikes the detector, it creates a charge pulse that is proportional to the energy of the emitted X-ray. The charge pulse is converted to a voltage pulse by a charge-sensitive preamplifier. The voltage pulse is still proportional to the X-ray energy. The signal is then sent to a multichannel analyzer to sort the pulses by voltage. Energy is determined from these voltage measurements. The energy for each incident X-ray is sent to a computer for display and further data evaluation. The spectrum of X-ray energy versus counts is evaluated to determine the elemental composition of the target area of the sample [15]. A spectrum from EDX analysis of one of the powder particles in the matrix material, 410L, is shown below in Fig. 3.5. Quantitative analyses of the sample are determined from the X-ray counts.

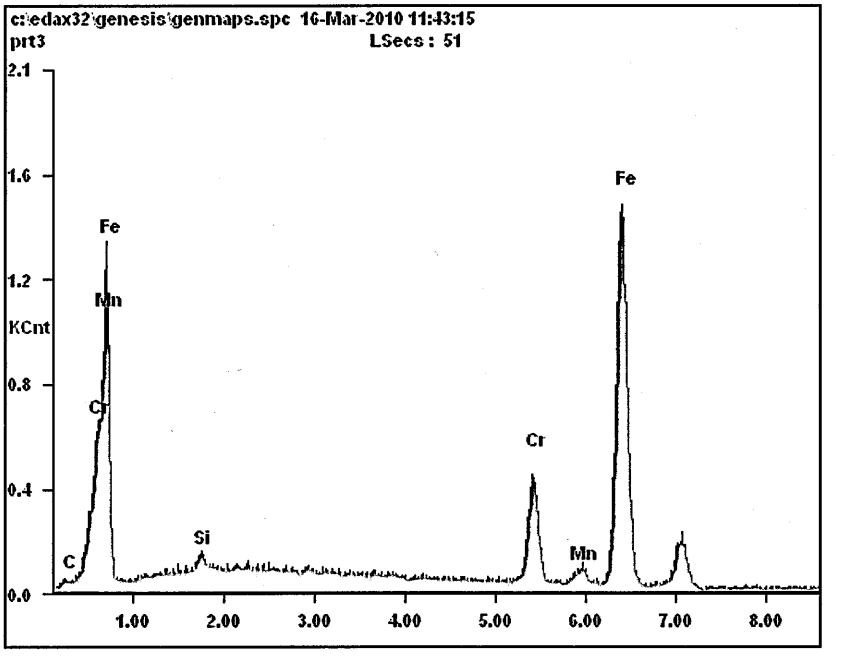

Fig. 3.5 EDX spectrum of a powder particle in 410L sample

Since X-ray energy is characteristic for different elements EDX is a reliable method for characterization. However there are some issues that may affect the accuracy of the analysis. Since the windows in front of the detectors can absorb low energy X-rays, they cannot detect elements with atomic number less than 4, that is H, He, and Li [16]. Some elements may have overlapping peaks in the spectrum which may lead to errors like Mn K_β and Fe K_α. Some X-rays may not be detected because X-rays can escape in any direction and they may not be detected so accuracy gets better with increasing detection time because more X-rays can be detected.

EDX analysis was extensively used in this project for identifying the particles in the material.

3.5 Tensile Testing

Room temperature and high temperature tensile tests are utilized for characterizing the materials for mechanical properties. Tensile testing in both conditions is carried out by an Instron 8862 servo-electric test machine with 100 kN load capacity. Fig. 3.6 shows the test equipment.

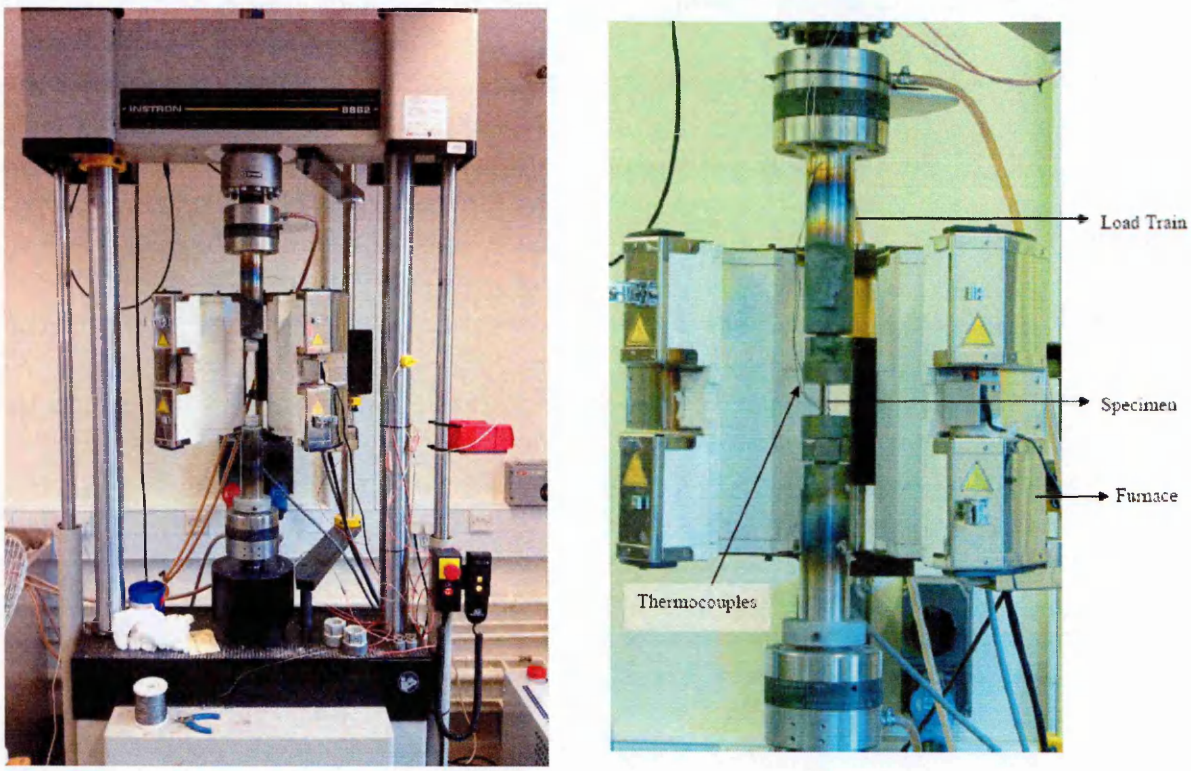

Fig. 3.6 Instron 8862 servo-electric test machine and specimen setup [17]

The specimens used for all tensile tests were manufactured from 12 mm diameter cylinders from the billets. The specimen size is 25 mm in the gauge length and 6.25 mm in diameter. The specimen design confirms to standards prescribed by ASTM A370-07b.

All tensile tests were performed under extension controlled 0.01 mm/sec extension rate. Bluehill software was used for test setup and control and data collection after tests. Extension (mm), load (N), tensile stress (MPa), tensile strain (mm/mm), displacement (mm) and time (sec) are recorded for raw data and later calculations. Major points in the stress-strain curve like yield stress and ultimate tensile stress values are calculated or determined manually from the graph.

An Instron extensometer was used to measure the elongation on the specimen for room temperature tensile tests. As shown in Fig. 3.7, the gauge length of the extensometer was set to 25 mm. Special high temperature strain gauges had to be used for the elevated temperature tests. The strain gauge consisted of two quartz legs placed in a housing. The knife edges at the end of the quartz pieces were placed on the specimen and tightened by special fibers. The length between the knife edges was 25 mm. Fig. 3.8 shows the placement of the strain gauge relative to the specimen.

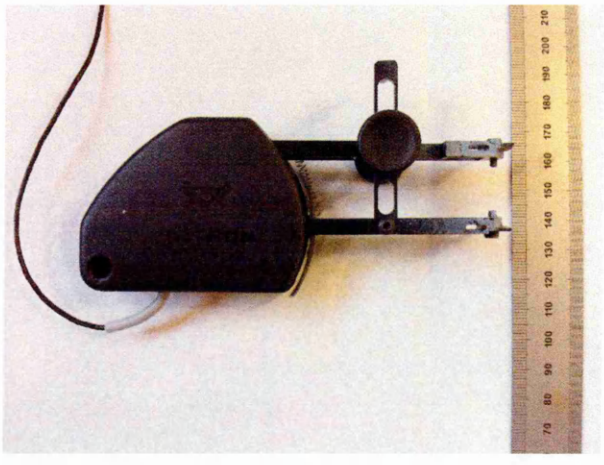

Fig.3.7 Extensometer used for room temperature tensile tests

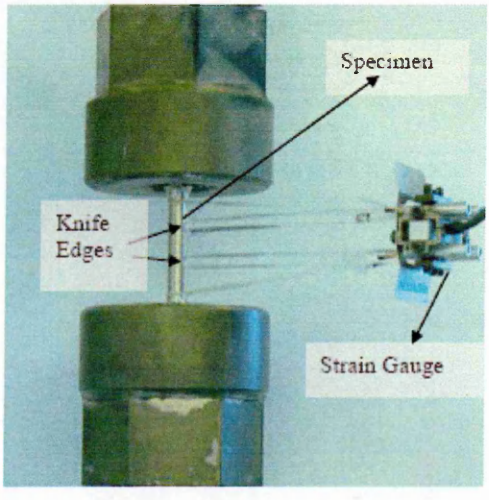

Fig.3.8 High temperature Strain Gauge and placement on to the sample [17]

The machine has a Eurotherm 3216 furnace with three separately controlled zones for more accurate temperature control. The thermocouples attached to the specimen were plugged directly to the controller unit so that instead of furnace temperature, the temperature of the specimen can be controlled directly. Three n-type thermocouples were used to monitor the specimen temperature. All three thermocouples are attached to top, middle and bottom parts of the specimen to check the temperature distribution on the sample. The furnace control unit can be seen in Fig. 3.9

Fig.3.9 Furnace control unit for high temperature tensile tests

3.6 Creep Testing

Creep tests are carried out by applying a known tensile load at various temperatures. The test samples used were smaller than conventional creep test samples so the test is called mini-creep testing. Dimensions of the test samples are 10 mm in gauge length and 2 mm in diameter. The specimen design confirms to standards prescribed by ANSTO's IME work instruction MI 1058 which is "Creep Rupture Testing of Miniature Tensile Specimens Using ANSTO Vacuum Creep Rigs".

Mini-creep tests were conducted at the Australian Nuclear Science and Technology Organisation (ANSTO) facilities in vacuum controlled creep frames in temperature controlled rooms. Fig. 3.10 is a schematic of the machines used to conduct the creep experiments.

As creep is a temperature dependent phenomenon, control of specimen temperature is quite important. Temperature stability is achieved and measured by two thermocouples placed in the small indents on the shoulder of the creep samples which are showed and numbered as 6 and 7 in Fig. 3.10.

Test rigs are based on a dead-weight design. That is, the load pan hangs off the creep test assembly and applies the load on to the sample under gravity. The pan is attached to the load coupling, numbered as 15 in Fig. 3.10. The load pan is loaded with small steel balls to produce a stress on the cross-sectional area of the

creep sample equivalent to that of the test stress which was 75, 100 and 150 MPa in our tests.

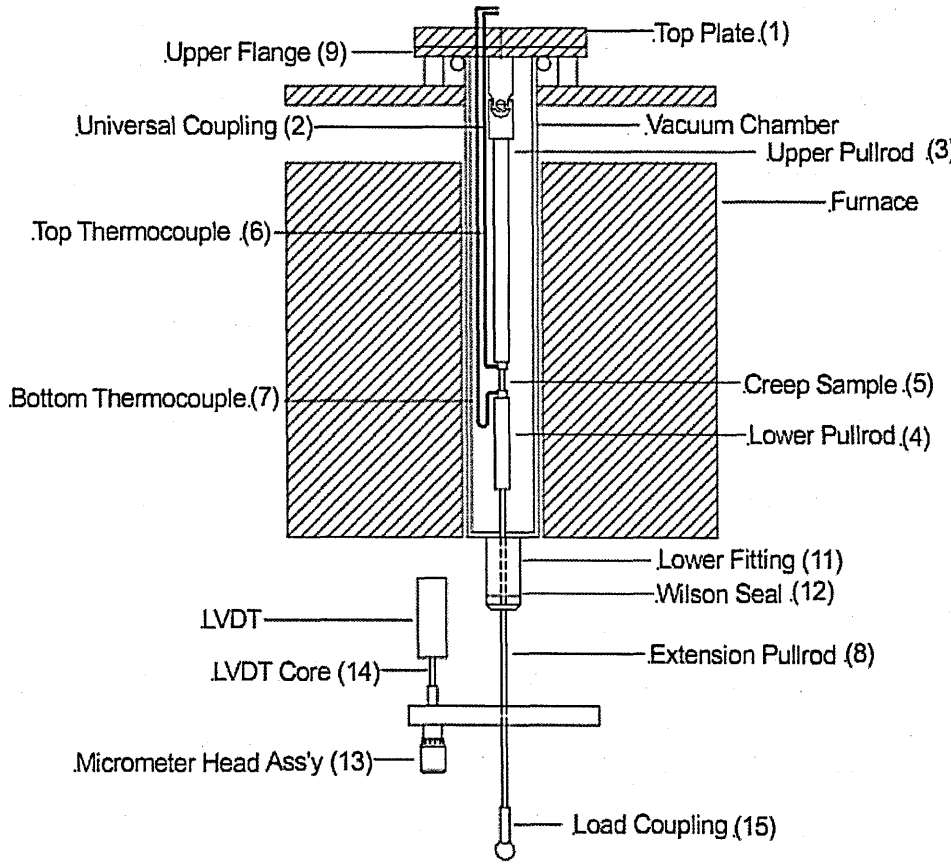

Fig. 3.10 Schematic of mini-creep test assembly [18]

Due to the small gauge diameter of the mini-creep samples, the test rigs are fitted with a vacuum system to avoid any effects of oxidation that can occur at elevated temperatures.

For a continuous creep test, strain has to be monitored constantly and recorded at regular time intervals. In most cases, displacement of the specimen under applied load is measured and then it is converted to strain. This measurement is done by a linear variable displacement transformer (LVDT) as

shown in the schematic as number 14. During the test, time and temperature values are also monitored and recorded at 5 or 30 minutes intervals depending on the duration of the each test. Test temperature for all three stress conditions was 625 °C.

3.7 Small Angle Neutron Scattering (SANS)

Small angle neutron scattering (SANS) is a powerful structural characterisation technique ranging from nanometers to micrometers depending on the instrument [19-22]. The nano-features of the ODS steels play a significant role in determine the macroscopic properties of the materials, thus this make SANS a promising tools for studing the nano-structures in the ODS steel [23, 24].

In SANS, the scattering of the object of interest must have different average scattering properties compared to the scattering of the matrix material which the object of interest is embedded in. The difference of the average scattering property is known as contrast. The object of interest can be precipitates, defects, or porosity etc. Small angle scattering is elastic, that is, with no energy change, and diffuse, that is non-Bragg, coherent neutron scattering. It is observed at low angles, or rather low scattering vector, **Q** (momentum transfer), about the incident neutron beam direction. Thus the small angle scattering measured magnitude of such a small angle scattering experiment is the intensity as a function of Q,

$$Q = \frac{4\pi}{\lambda} \sin \frac{\phi}{2} \qquad (3.2)$$

with the scattering angle ϕ and the wavelength λ of the neutrons. The momentum transfer $Q = |k_i - k_f| \sim \frac{2\pi}{\lambda}\phi$ due to the small angle approximation, and is the difference of the momenta of the incoming and scattered neutrons with wave vector $k = \frac{2\pi}{\lambda}$ as shown in Fig. 3.11. The length scale of the observed objects is given by the momentum transfer Q, which is in the range of 0.3 to 10^{-4}Å^{-1} due to $\lambda \sim 5-20$ Å and the small angles. The scattering process is defined in terms of a cross section, dσ, which is the rate of neutrons, C_0, scattered by an atom into a solid angle, ΔΩ, divided by the incident neutron flux, Φ_0. A differential cross section per atom, denoted by dσ/dΩ, will then be given by dσ/dΩ = C_0/ (Φ_0 ΔΩ). Therewith, SANS has the ability to characterise the object of interest with few atomic spacing to 10μm, depending on the capability of the instrument. Different instruments are optimized for different length scales.

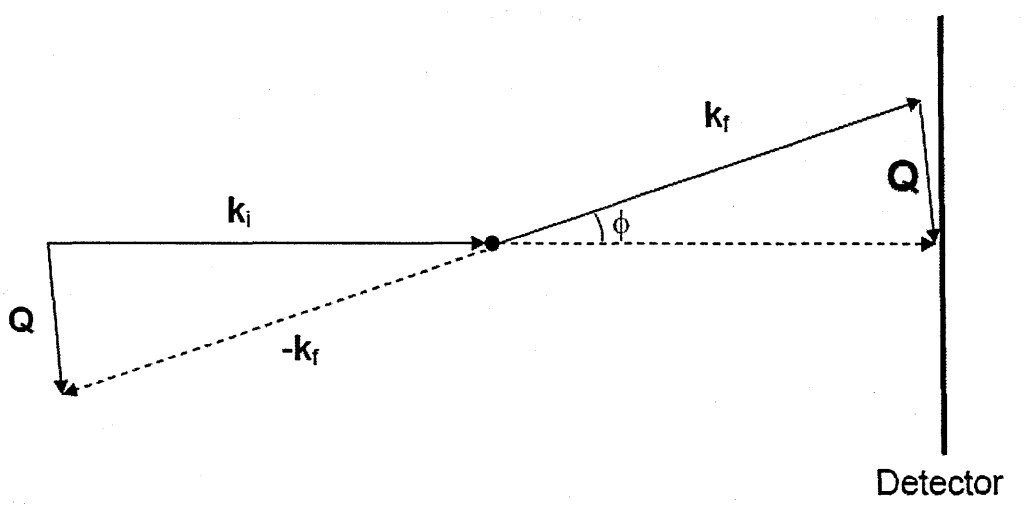

Fig. 3.11 Scattering for a neutron beam with incident wave vector by a sample with scattering angle ϕ.

3.7.1 Basic Principle in SANS

The nano-scale Y_2O_3 and Y-Si-O complex oxides as a result of interaction between SiO_2 and Y_2O_3 particles, were treated as precipitates in the steel matrix, and hence experiment can be performed by using the two phase (matrix and precipitates) distribution in the materials. As the precipitates and defects/cavities will give rise to contrast compared to the small angle scattering from matrix materials, thus SANS may need information like composition and shape of clusters from other aided technique (i.e. microscopy etc) in term of the full interpretation.

The measured intensity depends on the instrument, and it can be related to the macroscopic scattering cross section which should be independent of the instrument's details. The relationship between the measured intensity and macroscopic cross section is given by

$$\frac{\Delta I}{\Delta \Omega}(Q) = I_0 A T_r t \frac{d\Sigma}{d\Omega}(Q) \qquad (3.3)$$

With the intensity ΔI for one detector channel measured as a function of the scattering angle, and each detector channel has cover the full range of solid angle (Ω). From Eq. (3.3), it is easily found that the measured intensity is proportional to intensity at the sample I_0 , irradiated area A and thickness t of the sample, as well as the transmission of the sample T_r. Thus a calibration, conventionally using either water or plexiglass, is carried out. This calibration

allows us to obtain the instrument's details independent of macroscopic scattering cross section, which can be used to compare with results obtain from other small angle scattering instruments. For KWS-1, high flux, high resolution SANS instrument, it often uses plexiglass which scatters only incoherently for calibration.

The macroscopic scattering cross section is the rate of scattering events per incident neutron flux per unit volume of the sample, and has unit of cm^{-1}. In general, for the case of a dilute concentration of spherical precipitates with a range of diameters, the macroscopic scattering cross section can be written as:

$$\frac{d\Sigma}{d\Omega}(Q) = \left\{\int N(R)V(R)^2.(\Delta\rho)^2.P(Q,R)dR\right\}S(Q) + Background \quad (3.4)$$

Where the diameter $D = 2R$ and R is the radius of the spherical precipitate, $N(R)$ is the number of the precipitates with radius R and $V(R)$ is the volume of the precipitate, $\Delta\rho$ is the difference in scattering length. The structural form factor for the sphere is given by the relation:

$$P(Q,R) = \left\{\frac{3(\sin QR - QR\cos(QR))}{(QR)^3}\right\}^2 \quad (3.5)$$

$S(Q)$ is the inter-particle structure factor which is important for higher concentration at low-Q but tends to unity at high-Q. Its effect can be neglected as the measured precipitates we are interested in are small.

3.7.2 Experimental Details of SANS

The KWS-1 instrument at the Julich Centre for Neutron Science (JCNS, Germany) is a high flux high resolution instrument. The magnetic field system enables it to study a broad range of materials. It is useful for the study of ODS steel as if the ODS precipitate occurs it should increase the magnetic scattering because each phase (matrix and precipitates) in the material has different magnetic property. So, they behave different under magnetic field and causes anisotrophy in the material. This anisotrophy distinguished the phases. This is the first experimental information to prove the appearance of the ODS in the steel. The schematic diagram of the KWS1 instrument is shown in Fig. 3.12.

The most intense beams are from a 'cold' moderated source at liquid hydrogen temperatures which bias the neutron flux towards the long wavelengths needed for SANS. On this type of source the neutron beam is usually monochromated through velocity selectors before guided through an 18 m neutron guide. The set-up provides a high neutron flux with low background noise levels. A neutron wavelength of 7 Å was employed in the experiment. Rectangular samples were manufactured with dimension of (20×20) mm^2 with thickness of 2 mm for the experiment. This thickness was chosen as it has been reported that an increase in thickness can cause multiple scattering [25]. A magnetic system was use to applied external magnetic field up to 1.2T. This magnitude is sufficient to saturate the magnetic dipoles in specimens in other words it is sufficient to orient the dipoles of the matrix and precipitates in the material to cause anisotrophy. The detectors were chosen for four distances of 2, 4,

8 and 20 m in order to provide the maximum Q range. The instrument has an upper length scale limitation of 400 nm.

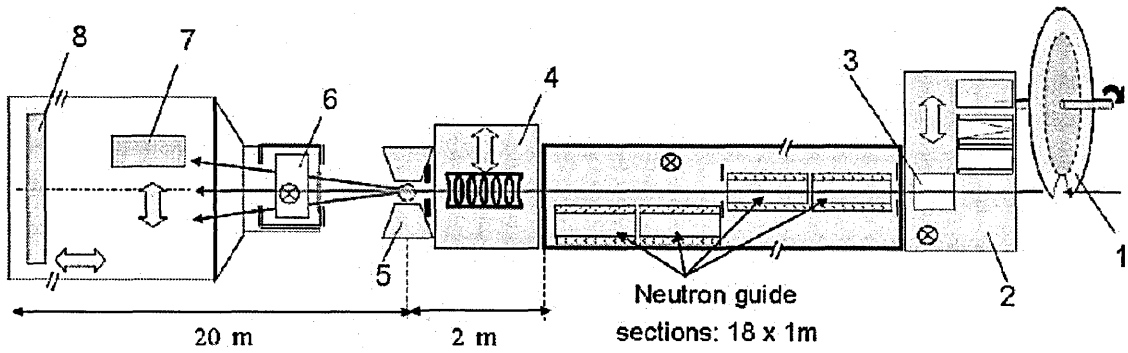

Fig. 3.12 Schematic presentation of the different components of KWS-1: 1- chopper, 2- polarizer changer, 3- flipper, 4- aspherical focusing lenses, 5- magnetic sample environment, 6- ^{3}He analyzer with reversible polarization, 7- high-resolution detector, 8- large area detector [26]

The specimens characterised in this study were 410L HIP (15991), 410 MA (15993), ODS 0.9 μm (15996) and ODS 50 nm (15997) in both as-received and heat treated condition. The heat treatment was two hours at 650 °C. A plexiglass and empty beam were used for the calibration. The experiments started with a particular detector distance and carried out for all detector distances without applied external magnetic field, and follow by two steps in the applying of the external magnetic field at 0.4 and 1.2T. It is assumed that all the samples are in the same condition in terms of porosity and/or other defects which can contribute to the macroscopic scattering cross section.

The data analyses begin with the data reduction using the JCNS in-house programme, QtiKWS for obtaining the absolute macroscopic scattering cross section as a function of scattering vector Q. This routine takes account of all the

necessary parameters mentioned in the calibration procedures. The data analysis has been performed only considering scattering from the elements for the object of interest: Y and O are the elements considered in the analysis for Y_2O_3 particle distribution, and Y, Si and O for the case of the Y-Si-O complex oxide. The complex chemistry interactions which could cause formation of other complex oxides and/or inclusion clusters which will contribute to the macroscopic scattering cross section have not been considered. The data were then fitted using theoretical models, and it has found that the best fitted model was a combination of two polydispersed spherical Schultz distributions /models. The Schultz distribution is a derivative of the log-normal distribution, and has been used extensively in the molecular weight distribution in polymer and also precipitates and/ cavities modelling in SANS. It is a two parameter distribution, and the number of spherical shape precipitate with diameter, $D = 2R$ is modelled as [27]:

$$N(R) = \left(\frac{z+1}{\overline{R}}\right)^{z+1} .R^{z}.\exp\left\{-\frac{z+1}{\overline{R}}R\right\}/\Gamma(z+1) \qquad (3.6)$$

Where $\overline{R}$ is the mean radii of the spherical precipitates, $z > -1$ is the width parameter characterising the degree of dispersion of the particles size and it is related to the polydispersity index σ, and Γ is the gamma function. For large z value, Schultz distribution is skewed to larger sizes and approximately Gaussian distributions. The volume of the sphere can easily calculated using a simple relation:

$$V(D) = \frac{\pi D^3}{6} \qquad (3.7)$$

Thus the particle size distribution of a sphere with diameter between D and $D+\delta D$ can be formulated as:

$$C_D = V(D).N(D) \tag{3.8}$$

Combination of Eq. (3.6) and (3.8) enables plotting of the particles size distribution as a function of diameter.

3.7.3 Outcome of SANS

Typical log-log plots for the macroscopic scattering against Q were found and reported in Fig. 3.13(a) which depicts the macroscopic scattering cross section for the ODS free and ODS steel. It indicates an increase in scattering in the ODS steel compared to the ODS free steel. Fig. 3.13(b) shows the increment in the magnetic macroscopic scattering cross section for the ODS steel compared to ODS free steel, due to Y_2O_3 and Y-Si-O particles because of magnetic anisotrophy. The relatively high macroscopic scattering cross section in the ODS free steel in the entire Q range may be due to porosity or Cr-rich regions surrounded by Cr-depleted regions.

The macroscopic scattering cross section for both as-received and heat-treated ODS 50 nm alloys has been fitted with using a combined polydisperse d Schultz model for Y_2O_3 and Y-Si-O oxides, and as shown in Fig. 3.14. Good fittings are achieved with χ^2 of 0.998 and 0.997 for as-received and heat-treated data respectively.

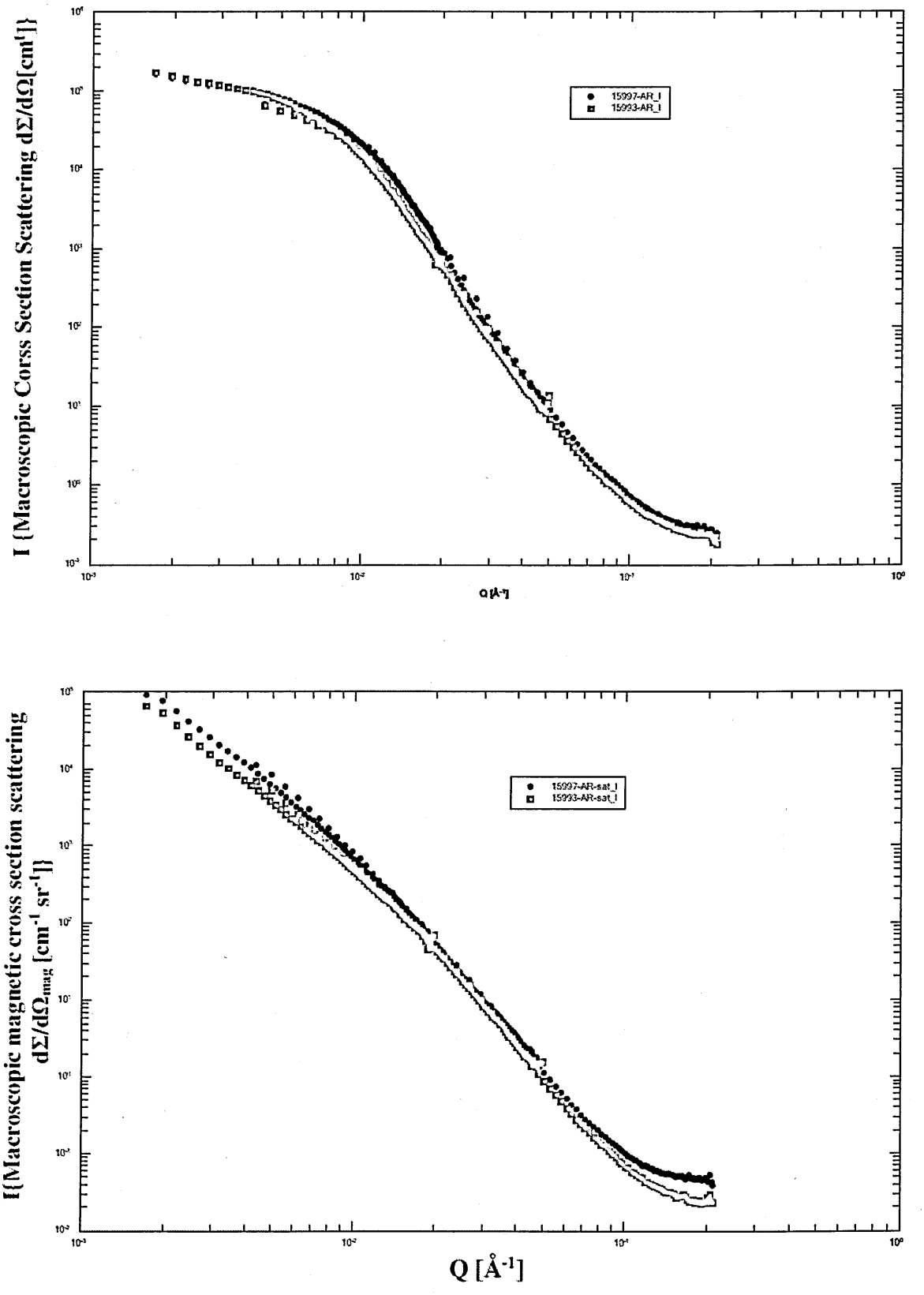

Fig. 3.13 (a)Macroscopic scattering cross section, (b)Magnetic macroscopic scattering cross section for both as-received ODS 50 nm and 410L MA

(a)

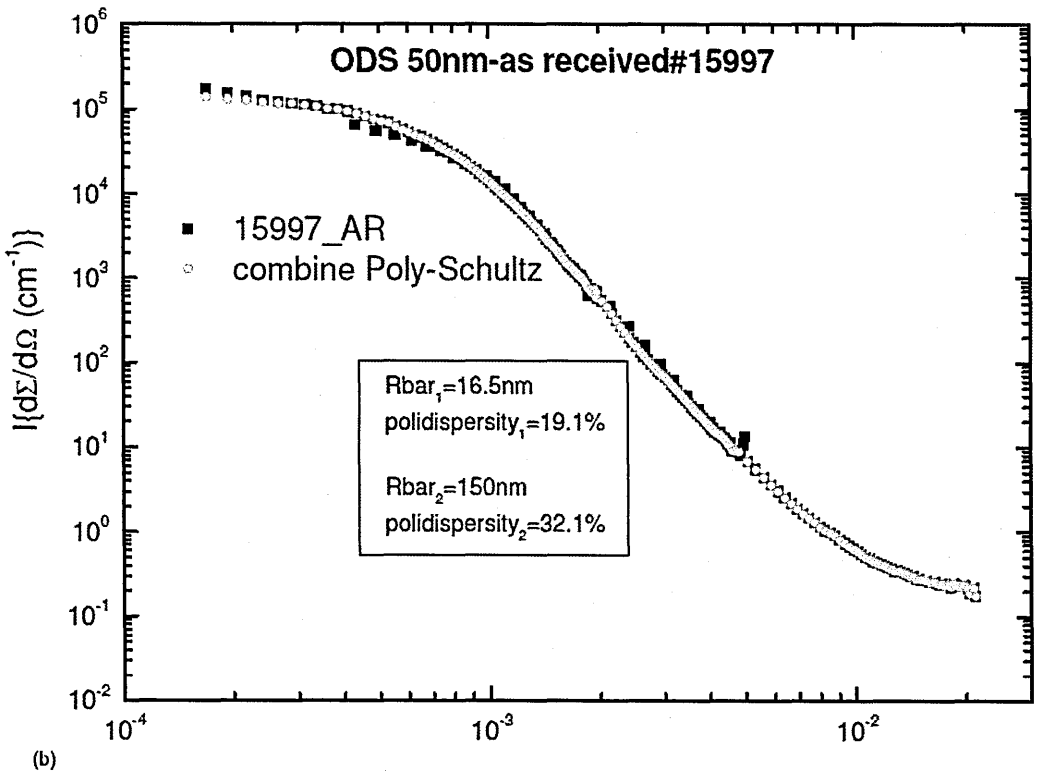

(b)

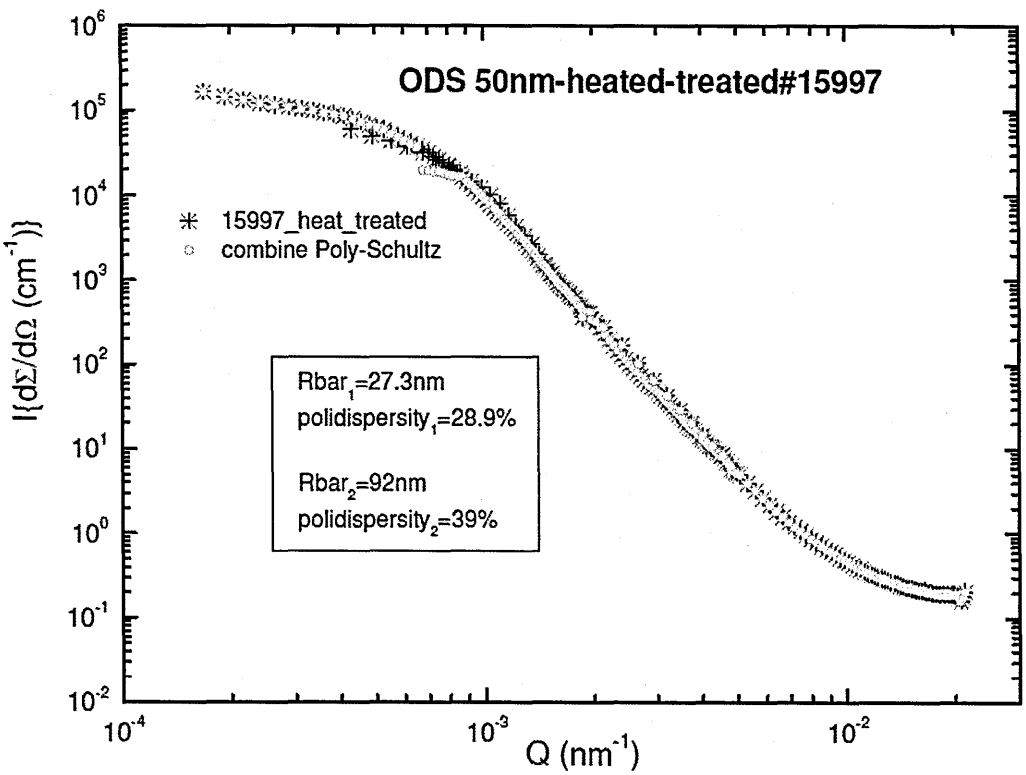

Fig. 3.14 Fitted macroscopic scattering cross section as a function of Q for (a) as-received, and (b) heat-treated

As the limitation of the instrument is an upper length scale of 400 nm, the large Y_2O_3 oxide and Y-Si-O complex oxide formed in the ODS 0.9 μm for both as-received and heat-treated alloys could not be identified for a concrete conclusion.

The particle size distribution for the materials tested and discussions about the results are included in the discussion chapter in conjunction with other results from other experiments.

3.8 Summary

Matrix materials of 410L steel with max 1 wt. % alloying elements and ODS materials were produced based on 410L steel with 0.9 μm and 50 nm yttria.

Heat treatment was austenitizing at 1000 °C for 30 mins followed by oil quenching and tempering at 650 °C for 2 hours and leaving for furnace cooling for a tempered martensite phase for initial microstructure to remove production effects like residual ferrites along grain boundaries.

Vilella's reagent and NaOH-water electrolytic etchants are used for detailed microscopy to reveal constituents.

Operating mechanisms of SEM and EDX and electron-sample interactions are explained for better understanding of the experiments.

Tests specimens and test equipments are described for tensile tests and creep tests.

SANS experiment and samples are explained.

References

1. de Castro, V., T. Leguey, A. Muñoz, M.A. Monge, R. Pareja, E.A. Marquis, S. Lozano-Perez, and M.L. Jenkins, *Microstructural characterization of Y2O3 ODS-Fe-Cr model alloys.* Journal of Nuclear Materials, 2009. **386-388**: p. 449-452.
2. Cayron, C., E. Rath, I. Chu, and S. Launois, *Microstructural evolution of Y2O3 and MgAl2O4 ODS EUROFER steels during their elaboration by mechanical milling and hot isostatic pressing.* Journal of Nuclear Materials, 2004. **335**(1): p. 83-102.
3. Ramar, A., Z. Oksiuta, N. Baluc, and R. Schäublin, *Effect of mechanical alloying on the mechanical and microstructural properties of ODS EUROFER 97.* Fusion Engineering and Design, 2007. **82**(15-24): p. 2543-2549.
4. Ahn, J.-H., H.-J. Kim, I.-H. Oh, and Y.-J. Kim, *Preparation of nano-sized ODS alloys by ball-milling using metallic salts.* Journal of Alloys and Compounds, 2009. **483**(1-2): p. 247-251.
5. *410 Specification Sheet,* Sandmeyer Steel Company.
6. Vander Voort, G.F., *ASM Handbook, Volume 09 - Metallography and Microstructures*, ASM International. p. 325.
7. Zipperian, D.C., *Metallographic Specimen Preparation Basics*, Pace Technologies.
8. Committee, *ASM Handbook, Volume 10 - Materials Characterization*, ASM International. p. 300,301.
9. Voort, G.F.V., *Metallography, Principles and Practice.* 1999: ASM International.
10. Elert, G. *Resolution of an Electron Microscope.* [Online] 2000 Available from: http://hypertextbook.com/facts/2000/IlyaSherman.shtml [Accessed December 2011]
11. *Electron Microscopy.* Available from: http://www.unl.edu/CMRAcfem/ [Accessed Date 2011
12. *Scanning Electron Microscope.* Available from: http://www.mos.org/sln/sem/ [Accessed Date 2011
13. *How SEM Works.* Instrumentation Available from: http://www.seallabs.com/hiw.htm [Accessed Date 2011
14. Martinez, M.V. *A Basic Understanding of Scanning Electron Microscopy (SEM) and Energy Dispersive X-ray Detection (EDX).* [Online] Available from: http://www.forensicevidence.net/iama/sem-edxtheory.html [Accessed December 2011]
15. Hanke, L.D., *Handbook of Analytical Methods for Materials.* 2001, Plymouth: Materials Evaluation and Engineering Inc.
16. Goldstein, J., D.E. Newbury, D.C. Joy, C.E. Lyman, P. Echlin, E. Lifshin, L. Sawyer, and J.R. Michael, *Scanning electron microscopy and x-ray microanalysis.* 2003, New York: Springer Science.
17. Rao, A., *Creep and Anelastic Deformation in Austenitic Steels,PhD Thesis.* 2010, The Open University: Milton Keynes.
18. Budzakoska-Testone, E., *Miniature Creep Testing of HIP, MA and ODS Alloy Steels.* 2011, ANSTO: Sydney.
19. Windsor, C.G., *Experimental techniques*, in *Neutron Scattering*, K. Skold and D.L. Price, Editors. 1986, London: Academic Press p. 97.
20. Windsor, C., *An introduction to small-angle neutron scattering.* Journal of Applied Crystallography, 1998. **21**(6): p. 582.
21. Hutchungs, M.T. and C.T. Windsor, *Industrial Applications*, in *Neutron Scattering*, K. Skold and D.L. Price, Editors. 1987, London: Academic Press. p. 405.

22. Vonk, C.G., *On two methods of determination of particle size distribution functions by means of small-angle X-ray scattering.* Journal of Applied Crystallography, 1976. **9**(6): p. 433.
23. Ohnuma, M., J. Suzuki, S. Ohtsuka, S.W. Kim, T. Kaito, M. Inoue, and H. Kitazawa, *A new method for the quantitative analysis of the scale and composition of nanosized oxide in 9Cr-ODS steel.* Acta Materialia, 2009. **57**(18): p. 5571-5581.
24. Coppola, R., M. Klimiankou, R. Lindau, R.P. May, and M. Valli, *SANS and TEM study of Y2O3 particle distributions in oxide-dispersion strengthened EUROFER martensitic steel for fusion reactors.* Physica B: Condensed Matter, 2004. **350**(1-3, Supplement 1): p. E545-E548.
25. Silas, J.A. and E.W. Kaler, *Effect of multiple scattering on SANS spectra from bicontinuous microemulsions.* Journal of Colloid and Interface Science, 2003. **257**: p. 291-298.
26. *Small Angle Neutron Scattering diffractometer.* KWS1 [Online] Available from: http://www.fz-juelich.de/jcns/EN/Leistungen/Instruments2/Structures/KWS1/_node.html [Accessed March 2012]
27. Kotlarchyk, M., R.B. Stephens, and J.S. Huang, *Study of Schultz distribution to model polydispersity of microemulsion droplets.* The Journal of Physical Chemistry, 1988. **92**(6): p. 1533-1538.

CHAPTER 4: MECHANICAL PROPERTIES AND TESTING

In this chapter results of the mechanical tests carried out on the materials are presented and some calculations for better understanding and comparing the results are shown. Discussions about the results are explained later in the discussion chapter (chapter 6) in an integrated way with material characterization.

4.1 Tensile Tests

The first step in mechanical characterizing of our materials is tensile testing. Initially tensile tests are carried out at room temperature to obtain values of yield strength, ultimate tensile strength and elongation to failure.

All of the samples were tested at room temperature. Samples from the first batch were tested in the as received condition also to determine the effect of heat treatment on mechanical behaviour of the samples. Results of the room temperature tensile tests are given in Table 4.1.

The tensile tests in the as-received condition of the first batch revealed some material related issues in the ODS 0.9 μm material. Yield strength and ultimate tensile strength (UTS) values of the samples are surprisingly low, around 360 MPa and 530 MPa respectively; whereas the ODS 50 nm showed 750 MPa and 1100 MPa respectively under the same conditions at room temperature. The yield

strength and UTS of the ODS 0.9 μm are less than half of the values of the ODS 50 nm sample.

Batch	Material	Condition	Yield Strength / MPa	Ultimate Tensile Strength / MPa	Fracture Strain
FIRST BATCH	410L HIP	As-Received	925	1330	4.7 %
		Heat Treated	670	825	18 %
	410 MA	As-Received	912	1280	3.9 %
		Heat Treated	677	813	7.6 %
	ODS 0.9 μm	As-Received	360	530	3.3 %
		Heat Treated	N/A	N/A	N/A
	ODS 50 nm	As-Received	750	1100	2.3 %
		Heat Treated	690	845	10.5 %
SECOND BATCH	410L HIP	Heat Treated	675	814	18 %
	410 MA	Heat Treated	677	842	15 %
	ODS 0.9 μm	Heat Treated	695	860	12 %
	ODS 50 nm	Heat Treated	673	812	6 %

Table 4.1 Room temperature tensile test results

The 410L HIP sample has 925 MPa for yield strength and 1330 MPa UTS. Fracture elongations of all the samples are quite low: the 410L HIP sample has the highest fracture elongation value at 4.7 %. The 410L MA sample is better than ODS samples in yield strength and UTS but worse than the basic 410L HIP sample. As-received tensile tests were only carried out for the first batch samples because it was realized that using the samples in the as-received condition was not appropriate due to their limited mechanical properties. So second batch samples only are tested only in the heat treated condition.

As be seen from Table 4.1 for both batches the basic 410L HIPed sample showed the highest fracture elongation, around 18 % in the heat treated condition. The effect of heat treatment is obvious in the 410L HIP sample from the first batch due to the improvement in the fracture elongation which was 4.7 % in the as-received condition. It appears that mechanical alloying effected ductility in a negative manner so that 410L MA samples showed lower fracture elongation than just HIPed ones because the mechanically alloying is the only difference between 410L HIP and 410L MA samples. For the ODS samples the situation is a little bit different because some of the ODS samples showed a surprisingly small amount of fracture elongation which can not be because of mechanical alloying. ODS 50 nm from the second batch showed around 6% fracture elongation whereas the same values for the same sample from first batch is around 10.5 %. ODS 0.9 μm from the second batch has fracture elongation as 12 % which is close to the value of ODS 50 nm. So it looks like there is a problem like porosity etc in ODS 50 nm sample from the second batch. Extensive investigation for the problem was carried out and is discussed in the material characterization chapter (chapter 5).

When the mechanical values of the samples are compared, values are quite consistent for the 410L HIP sample for both batches. The 410L HIP samples from the first and second batch have very close values as 670 MPa and 675 MPa yield strength and 825 MPa and 814 MPa UTS respectively. 410L MA values are similar as well with 677 MPa for yield strength for both batches and 813 MPa and 842 MPa for tensile strengths respectively for the first and second batches. Ductility of the 410L MA sample from the first batch is significantly less than second batch values which is 7.6 % for the first batch and 15 % for the second batch. Although there seems to be some porosity related problem in the ODS 50 nm sample from the second batch yield strength and UTS values are still comparable with the same sample from the first batch. Values for the first batch and second batch are 690 MPa and 673 MPa for yield strength and 845 MPa and 812 MPa for UTS.

It appears that the ODS 0.9 μm from the first batch and ODS 50 nm from the second batch have some ductility related problems. These problems are discussed in detail in the material characterization chapter (chapter 5). Due to these problems it is not possible to compare the two ODS samples from the same batch to understand the effect of size of yttria particles on mechanical properties. But when the ODS samples from the different batches are compared, it can be seen that the ODS 0.9 μm from the second batch has slightly better mechanical properties than the ODS 50 nm sample from the first batch. However we cannot trust this comparison because maybe those materials are produced under different conditions. Manufacturing variables have a great effect on mechanical properties

as they can effect densification, porosity and some temperature related phenomena like microstructural constituents.

When ODS and non-ODS samples are compared for investigating the effect of yttria particles on the mechanical properties, it is clear that ODS samples have better mechanical properties. However the improvement is very small. When we look at 410 MA and ODS 0.9 μm sample from the second batch, yield strengths are 677 and 695 MPa and UTS are 842 and 860 MPa as result average of 3 tests per material. This improvement can be observable from the first batch samples 410 MA and ODS 50 nm. Again a slight improvement is observable as yield strength of ODS 50 nm is slightly higher: 690 MPa whilts 410 MA has 677 MPa yield strength. A similar improvement is also seen on tensile strength of the samples as 845 MPa and 813 MPa for ODS 50 nm and 410L MA. Room temperature tensile tests results of second batch samples can be seen also in Fig. 4.1 as a graph for comparison.

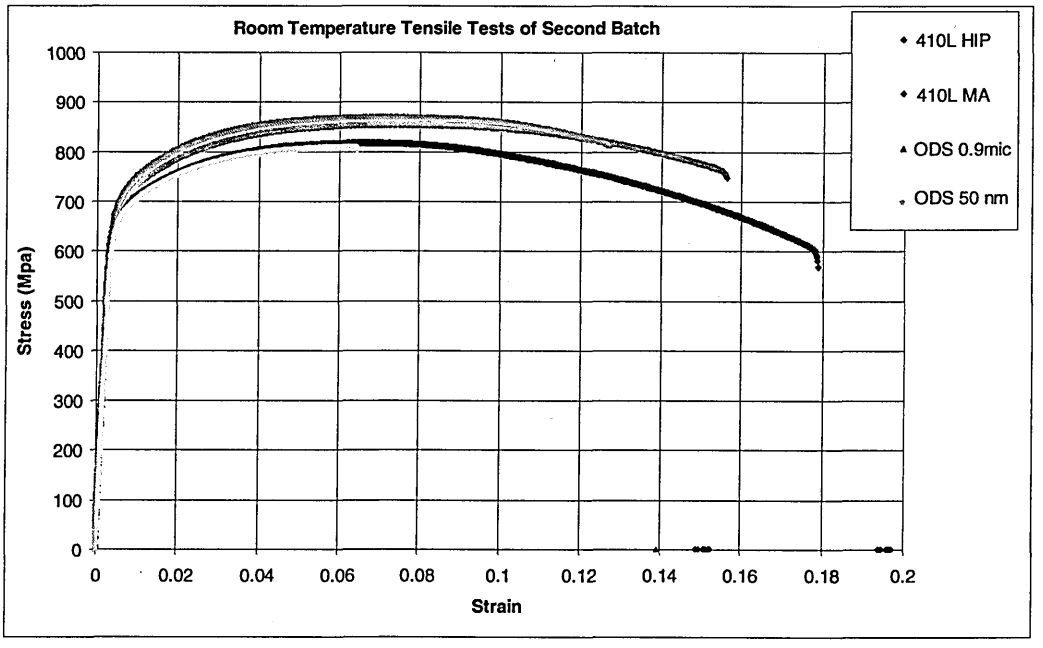

Fig. 4.1 Room temperature tensile tests of second batch sample

4.2 High Temperature Tensile Tests

High temperature tensile tests on the samples were conducted at 625 °C. Only second batch samples were tested at high temperatures and results of the tests are shown in Table 4.2. The Instron slow strain tensile test machine is used for high temperature tensile tests as well as room temperature tensile tests.

Material 410L Base	Yield Strength (σ_y) [MPa]	Ultimate Tensile Strength (UTS) (σ_{UTS}) [MPa]	Fracture Strain (ε_f)
Un-milled HIP	270	283	16 %
As-milled – MA & HIP	266	289	9 %
ODS – 0.9 µm Y_2O_3	275	292	10 %
ODS – 50 nm Y_2O_3	273	293	5 %

Table 4.2 High temperature tensile test results of samples from second batch

Both yield strength and tensile strength of all the samples are relatively close to each other which is the case for room temperature tensile tests as well. Yield strength values are around 270 MPa and ultimate tensile strength is around 285 MPa. As expected yield strength and UTS values are lower than room temperature values which were around 680 MPa and 840 MPa for yield and tensile strengths respectively. As in room temperature tensile tests the 410 HIP material

has the highest elongation with 16 % compared to 18 % at room temperature. Lowest elongation belongs to ODS 50 nm sample at 5 %. High temperature elongation values are comparable with the room temperature elongation values. The only noticeable change is in 410L MA sample where the elongation values dropped to 9 % at high temperature from 15 % at room temperature. High temperature tensile test graphs of samples from the second batch material can be seen in Fig. 4.2.

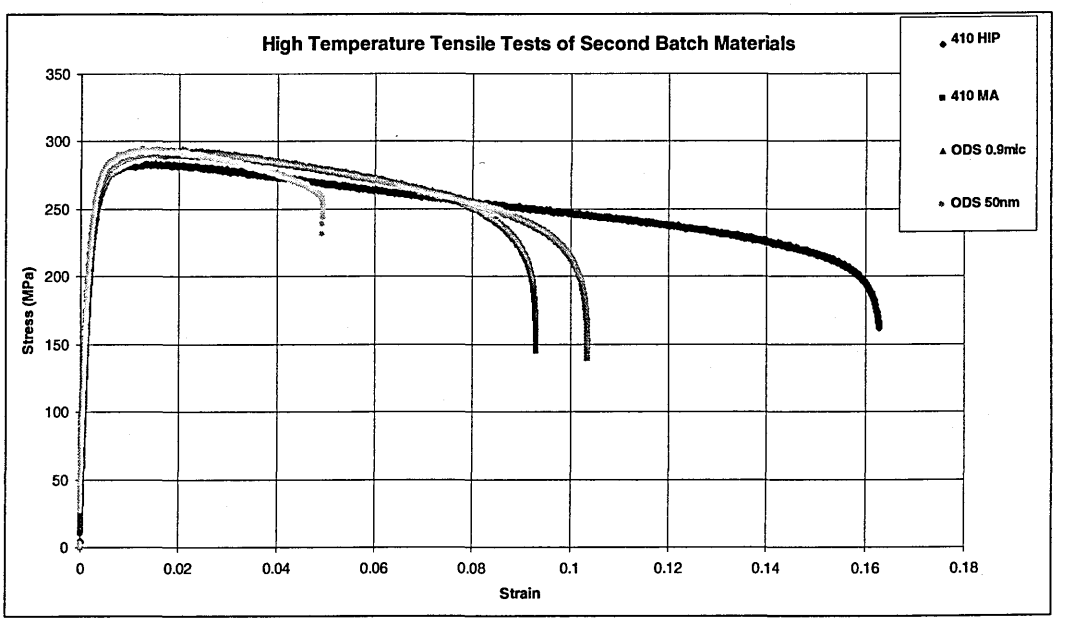

Fig. 4.2 High temperature tensile tests of second batch

4.3 Creep Tests

Creep tests were conducted in mini-creep rigs with small tests specimens. ANSTO's mini-creep facility was used for creep experiments.

Creep test results are shown in Table 4.3. All tests are conducted at 625 °C under three different loads which are 75, 100, 150 MPa. Creep tests were done only on second batch materials.

Material	Temp. (°C)	Stress (MPa)	Rupture Time (hrs)	Elongation	Strain Rate (10^{-4} hr^{-1})
410 HIP	625	150	20	26.0 %	44.44
	625	100	205	21.5 %	5.00
	625	75	679	16.4 %	1.36
410 MA	625	150	11	30.2 %	118.42
	625	100	117	23.7 %	9.37
	625	75	242	22.8 %	4.44
ODS 0.9 μm	625	150	7.3	24.2 %	142.85
	625	100	61	17.3 %	14.28
	625	75	216	9.5 %	3.00
ODS 50 nm	625	150	2.7	8.0 %	230.76
	625	100	27	7.4 %	17.14
	625	75	108	6.9 %	4.44

Table 4.3 Mini-Creep test results of samples from second batch

As seen from the Table 4.3 it is quite clear that the creep lives of the materials are very low but components are expected to go up till hundred thousands hours in power plants. Reasons of poor creep life are explained in discussion chapter (chapter 6). The best creep life belongs to 410 HIP with 679 hours under 75 MPa load at 625 °C. Worst creep life is experienced with ODS 50 nm sample. ODS 50 nm sample has 108 hours creep life under 75 MPa at 625 °C. As mentioned earlier this ODS sample's high temperature properties are poor with only 5 % fracture elongation. The same sample has just 2.7 hours creep life under 150 MPa load. Other samples 410 MA and ODS 0.9 μm have reasonable properties when compared to 410 HIP and tensile properties discussed earlier.

When elongation values are compared it can be seen that the highest elongation is in the 410 MA sample under 150 MPa load, compared to room temperature tensile tests where 410 HIP was the one with highest elongation value in both as-received and heat treated conditions. In high temperature tensile tests the elongation values of 410 HIP and 410 MA are 16 % and 9 % respectively. As expected ODS 50 nm has the smallest elongation with 7.5 % under 75 MPa load which was the same for room temperature tensile tests and high temperature tensile tests. Elongation values decreases by decreasing load. For example when 410 HIP is considered, it has 26 % elongation under 150 MPa load and 21.5 % under 100 MPa and 16.4 % under 75 MPa. This is true for all the samples tested; as the load decreases elongation decreases as well which can be seen from Table 4.3 clearly.

For better comparison of the samples' creep performance creep strain vs time graphs are shown below in Fig. 4.3 for all conditions. It is quite clear how creep performance is changing with changing stress at the same test temperature. Both creep strain rate and total elongation are increasing with increasing creep stress. The highest creep rate belongs to ODS 50 nm material with 230.76 x 10^{-4} hr^{-1} from Table 4.3.

a)

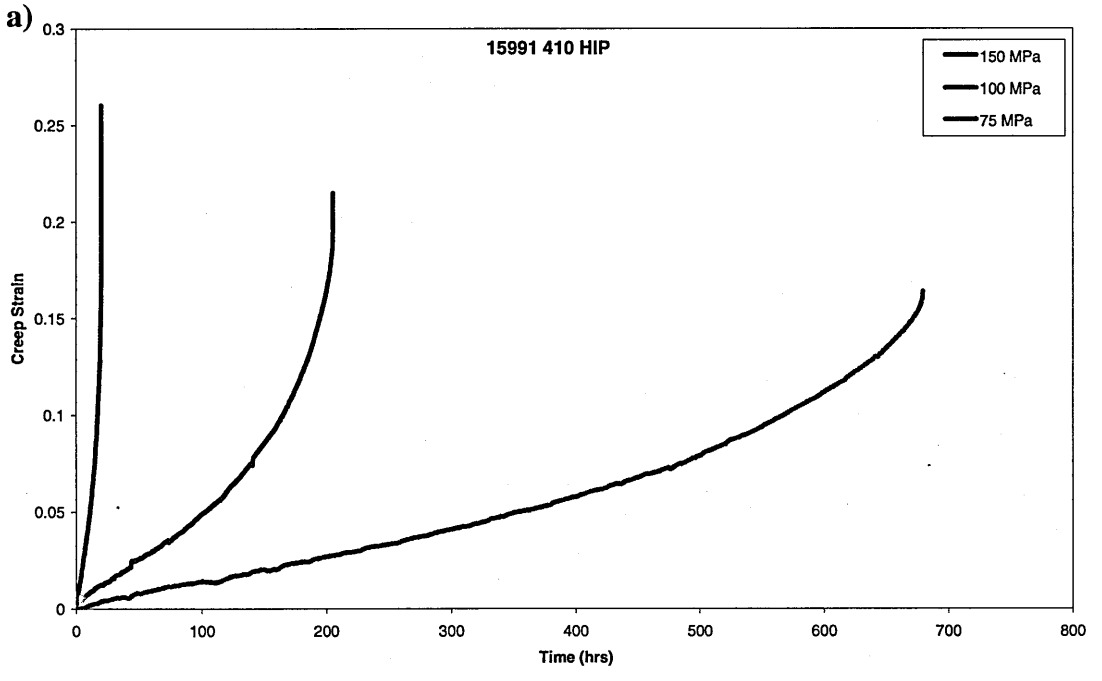

b)

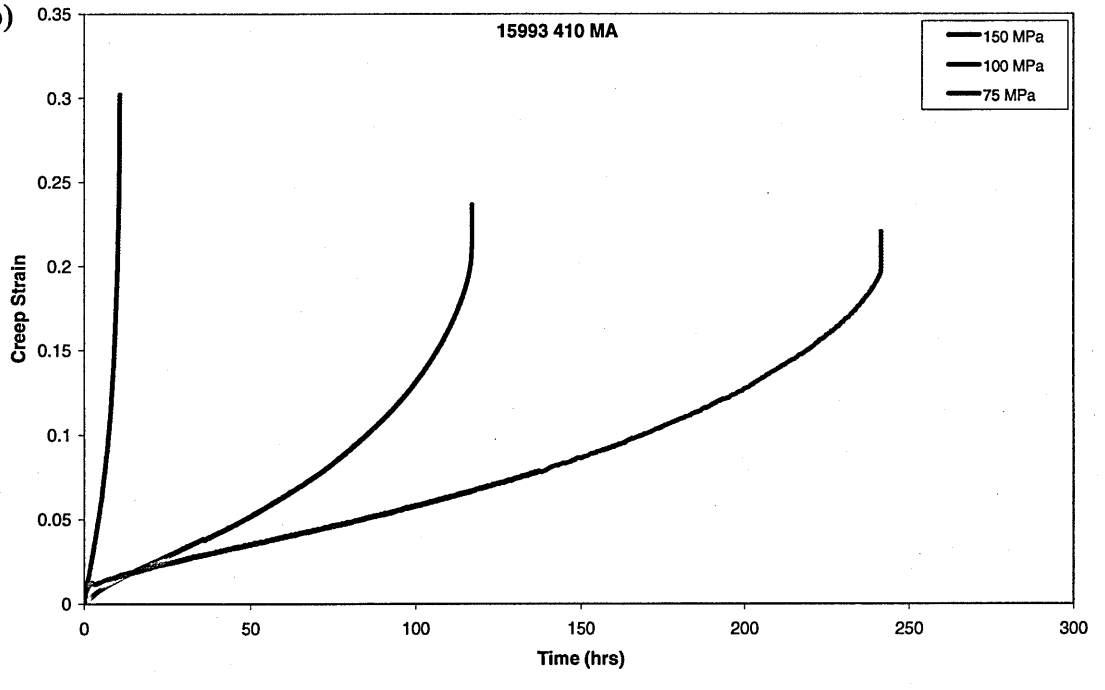

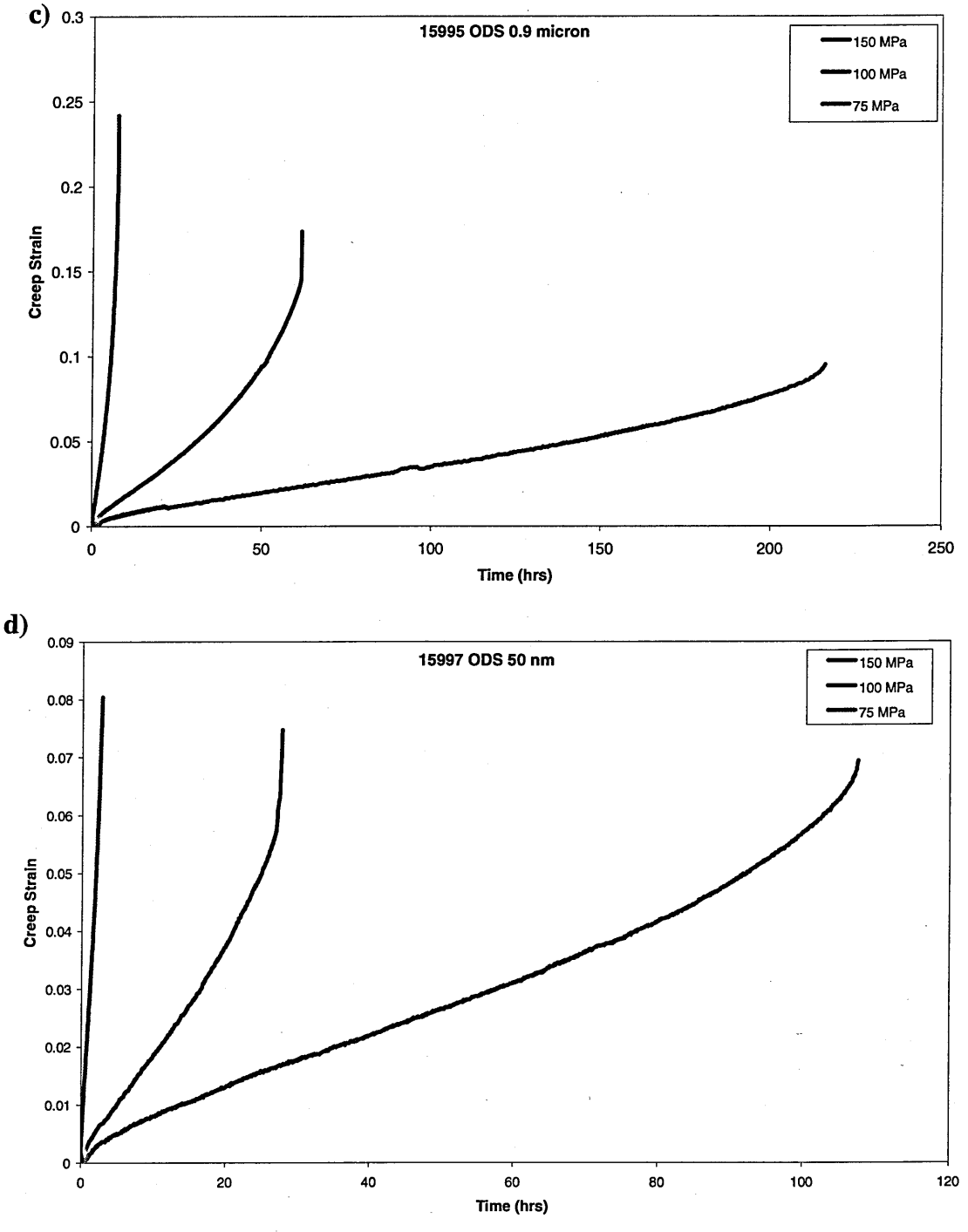

Fig. 4.3 Creep strain vs time graphs of (a) 410L HIP (b) 410L MA (c) ODS 0.9 mic (d) ODS 50 nm

Stress exponent n is also calculated according to the Arrhenius creep equation from the slope of log ($\dot{\varepsilon}$) (creep rate) and log (σ) (creep stress) graph. The stress exponents for all of the materials are similar which are 5.05, 4.83, 5.58 and

5.74 for 410L HIP, 410L MA, ODS 0.9 μm and ODS 50 nm respectively. It is mentioned in previous chapters that the type of creep can be determined from the stress exponent where the mechanism of creep is stated diffusion creep when n value is approximately 1 and is dislocation creep when n is in the range 3-8. So for this case it can be said that dislocation creep is dominant for this project's creep tests.

Creep results were extrapolated for better understanding of creep behaviour at various stresses and shown in creep stress and time graph shown in Fig. 4.4. All of the samples have similar curves.

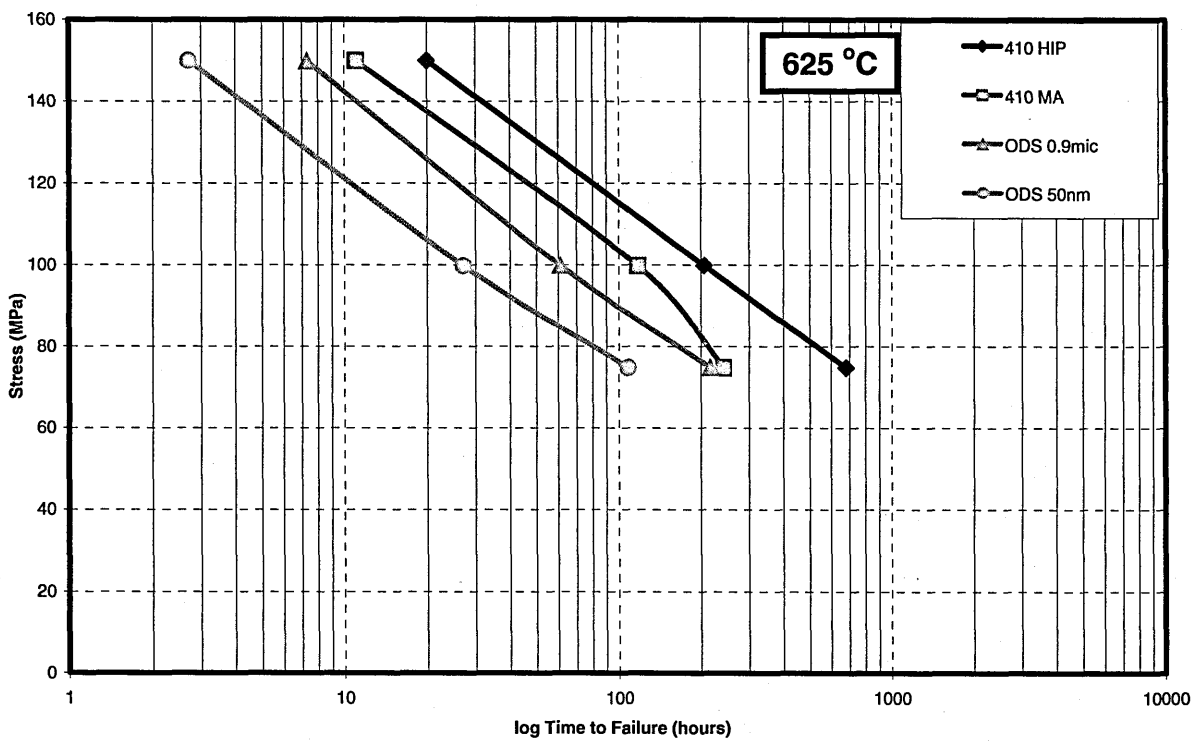

Fig. 4.4 Creep results in stress vs time graph for extrapolation

Larsson-Miller parameters are calculated as well according to the formula:

$$LMP = T(\log t_r + C)$$

Where C is an alloy-dependent constant, t_r is time to rupture in hours, T is temperature in Kelvin. C is taken as 20 for the calculations because it is usually accepted as ~20 for various steels and stainless steels and 410L is a kind of martensitic stainless steel.

LMP values are quite useful when comparing the results of the samples with other alloys and composition. LMP values are shown in the stress vs LMP graph in Fig. 4.5.

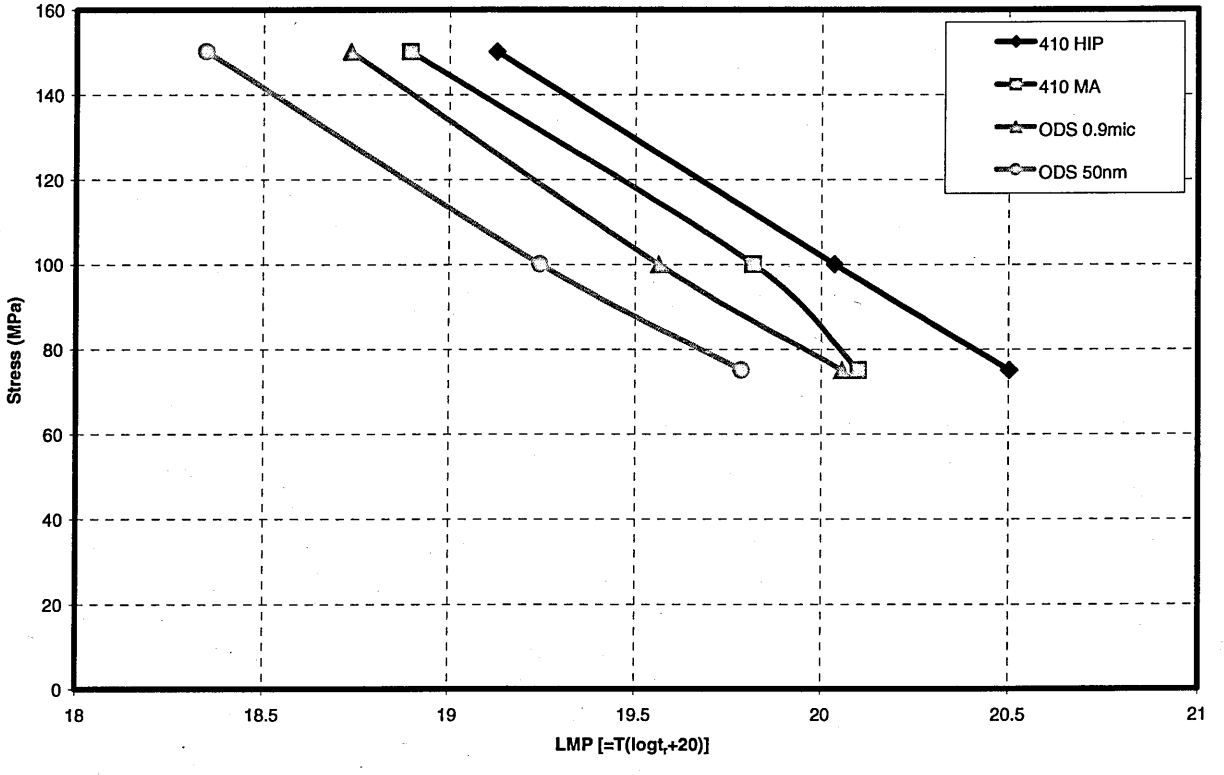

Fig. 4.5 Larsson miller parameter values for creep results

Stress – fracture elongation relation is shown in Fig. 4.6. As the creep stress increases elongation at fracture increases as expected. However unlike the room temperature tensile tests elongation of 410 MA sample is higher than 410 HIP in creep tests where all other samples' elongation values are consistent with the room temperature tensile test fracture elongation values. ODS samples' elongation values are less than non-ODS samples. ODS with 50 nm yttria particles has the lowest elongation and it is evident in Fig. 4.6. In high temperature tensile tests elongation values are 16 %, 9 %, 10 % and 5 % respectively for 410L HIP, 410 MA, ODS 0.9 μm and ODS 50 nm.

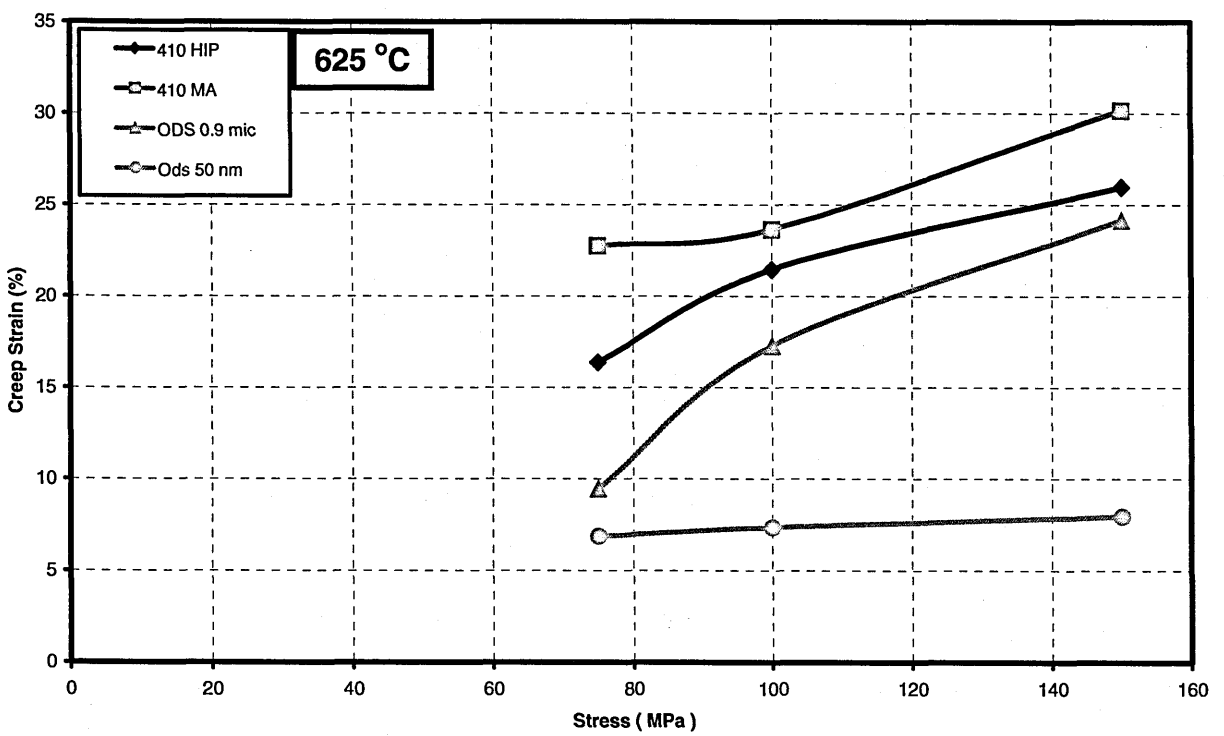

Fig. 4.6 Creep stress vs fracture elongation

4.4 Summary

Results from room temperature tensile tests results are presented and explained. All samples have comparable mechanical strengths. ODS materials have slight improvements. Highest fracture elongation belongs to 410L HIP.

ODS 0.9 μm from the first batch has very low YS (360 MPa) and UTS (530 MPa). This may be related to some material problems, most likely porosity.

High temperature tensile tests were performed at 625 °C. All samples have mechanical strengths around 270 MPa and 285 MPa for YS and UTS respectively.

Creep tests were performed at 625 °C under 3 different load conditions, 75, 100, 150 MPa. Creep lives of the materials are very low. Shortest creep life belongs to ODS 50 nm material with 2.7 hours under 150 MPa load. Best creep life is 679 hours for 410L HIP under 75 MPa load.

Extrapolation and strain rate calculations have been performed. LMP, stress-fracture time and creep strain-stress graphs are presented. It is observed that fracture elongation values are consistent with room temperature fracture elongation values.

CHAPTER 5: MICROSTRUCTURAL EXAMINATION AND MATERIAL CHARACTERIZATION

In this chapter microstructural characterization of the materials is presented and problems in the materials are revealed. Before and after test examinations are shown to aid understanding of the mechanical properties presented in the previous chapter but discussions are provided later in the discussion chapter (chapter 6).

5.1 Powder Samples

As this project is mainly about characterization of martensitic stainless 410L oxide-dispersion strengthened (ODS) steel, microstructural examination is one of the most important steps to achieve full characterisation of the material. The materials for this project are manufactured through a powder metallurgy route so initially the materials were in powder form. To run a full characterisation it is necessary to analyse the powder materials before examining the bulk forms.

Three powder samples were examined: 410L powder (provided by Sandvik) (matrix material) and yttria powders in different sizes as 50 nm (from Sigma Aldrich) and 0.9 μm (from HC Stark). These powders were examined under SEM for imaging and analysed by EDX for composition. To analyse these powders under SEM, a small amount of the powders were poured onto a sticky carbon pad, to prevent scattering of the powder particles in the vacuum chamber, and then placed into the SEM.

Examination of the powders showed spherical particles up to 120-130 µm size in the 410L sample. Higher magnification images show that those particles look like they are formed due to an agglomeration of small particles (Fig. 5.1). Some small particles can be seen as satellites to big powder particles. These powders are before the mechanical alloying step as mechanical alloying introduces deformation and the morphology of the particles changes. Yttria examinations showed the interesting result that the yttria particles are much bigger than they were supposed to be. Some yttria particles are observed in size around 30 µm. Both yttria powders, 0.9 µm and 50 nm, have these large particles in their structure. These particles are shown in Fig. 5.2 and Fig. 5.3 for both the yttria powders.

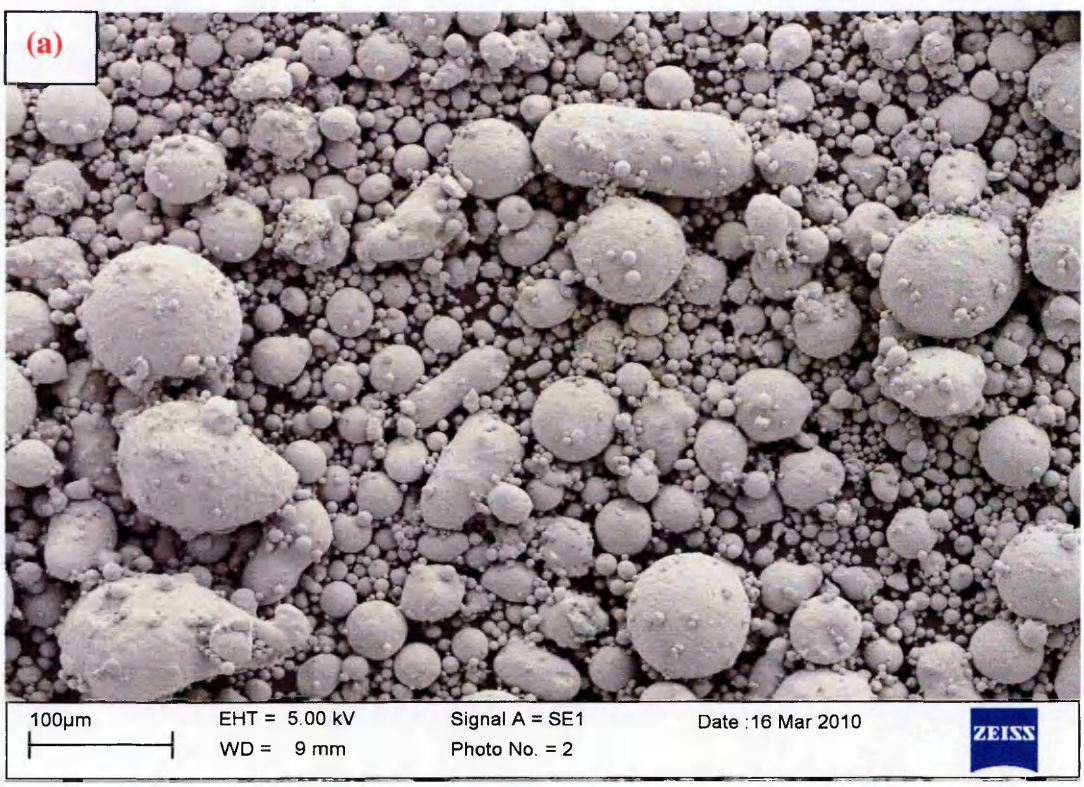

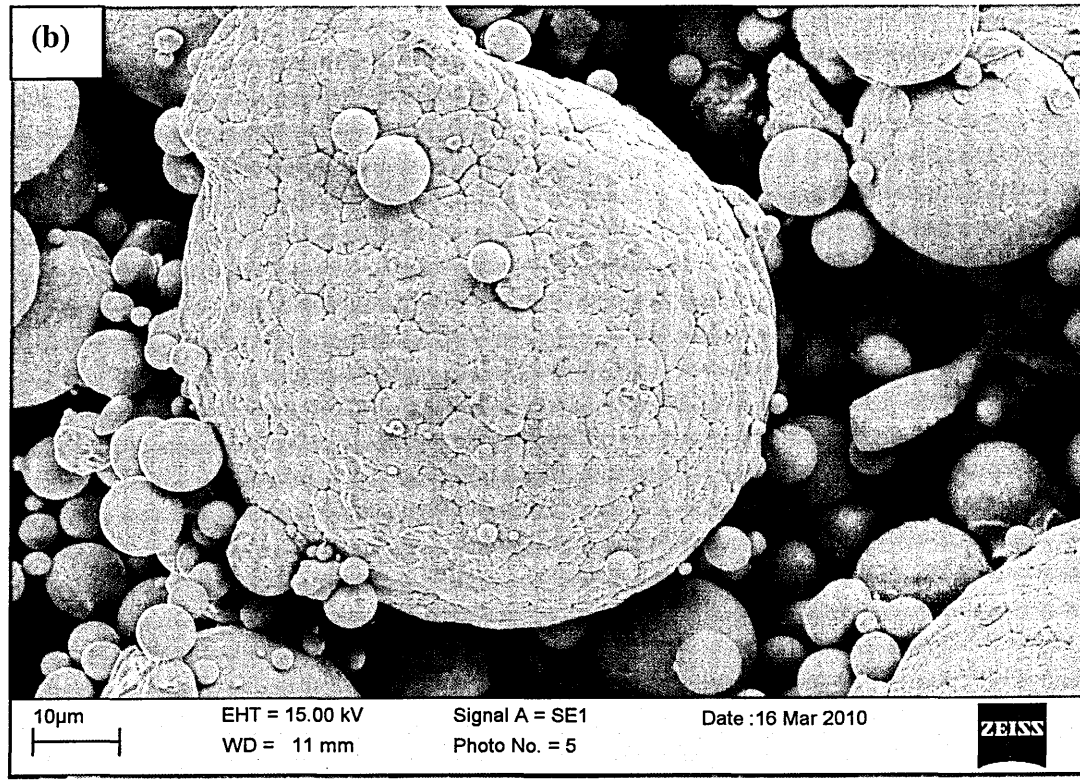

Fig. 5.1 410L powder SEM images

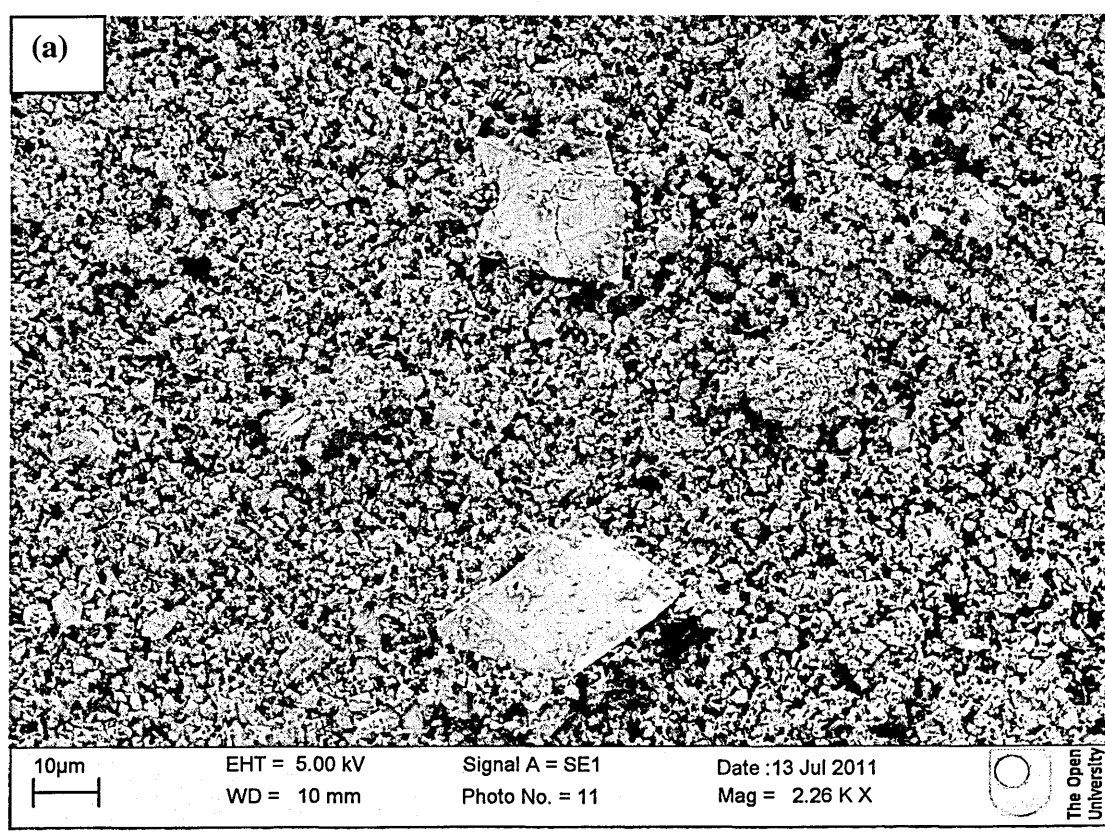

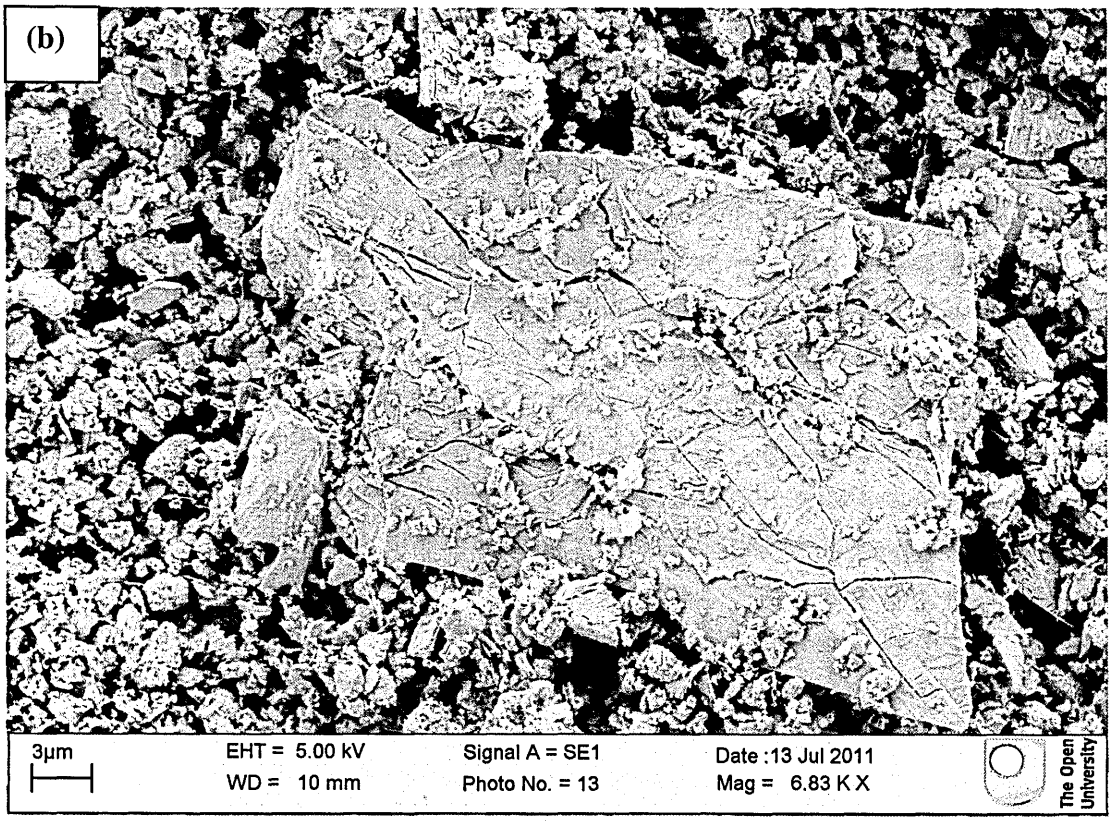

Fig. 5.2 SEM images of Yttria 0.9 µm powder

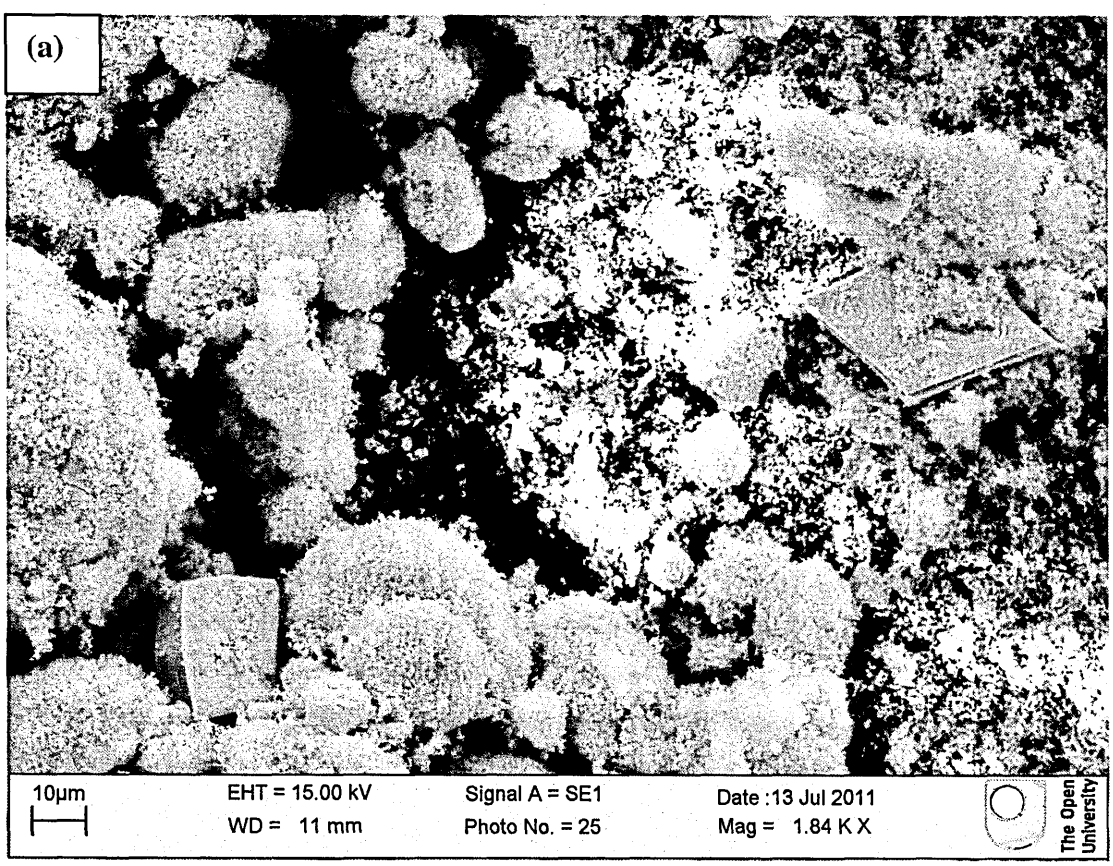

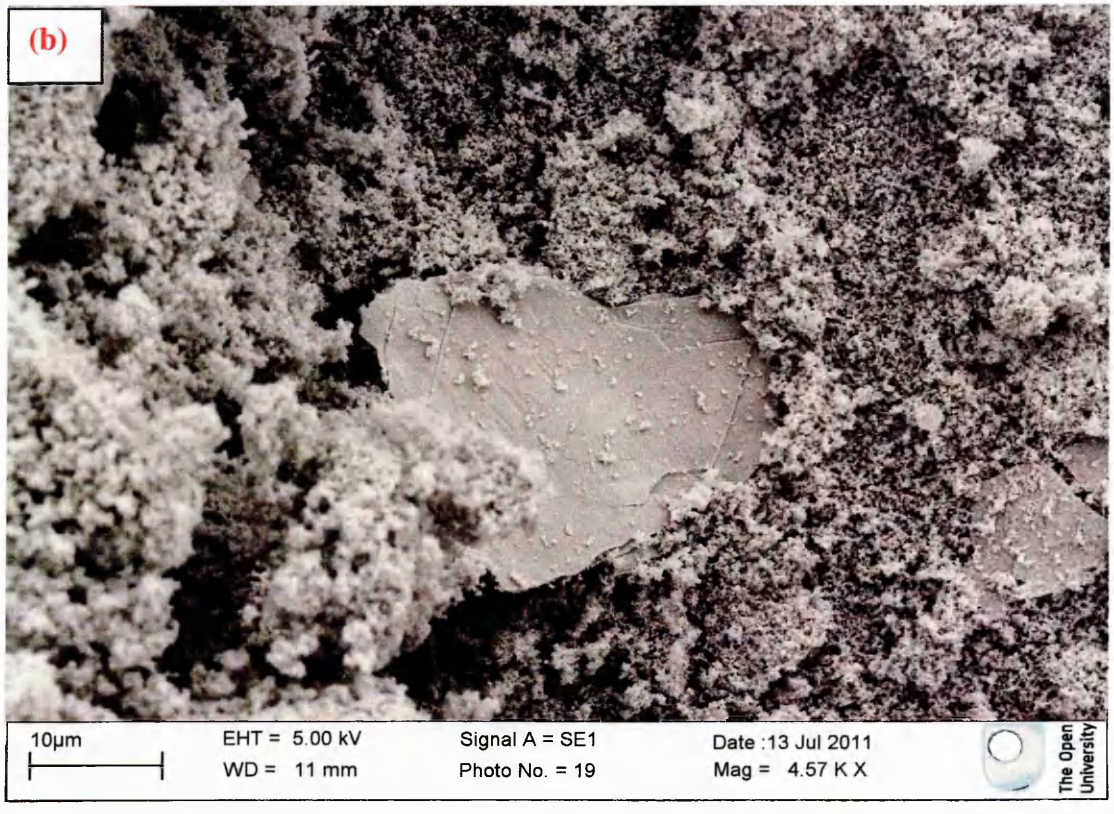

Fig. 5.3 SEM images of Yttria 50 nm powder

Compositions of these powder particles were verified via EDX. The compositions are as expected. Analysis on the 410L powder sample showed 12-13 wt. % Cr and max 1 wt. % Si and Mn which is fairly close to the compositon of standard 410L martensitic stainless steel. EDX results of 410L powder can be seen in Fig. 5.4.

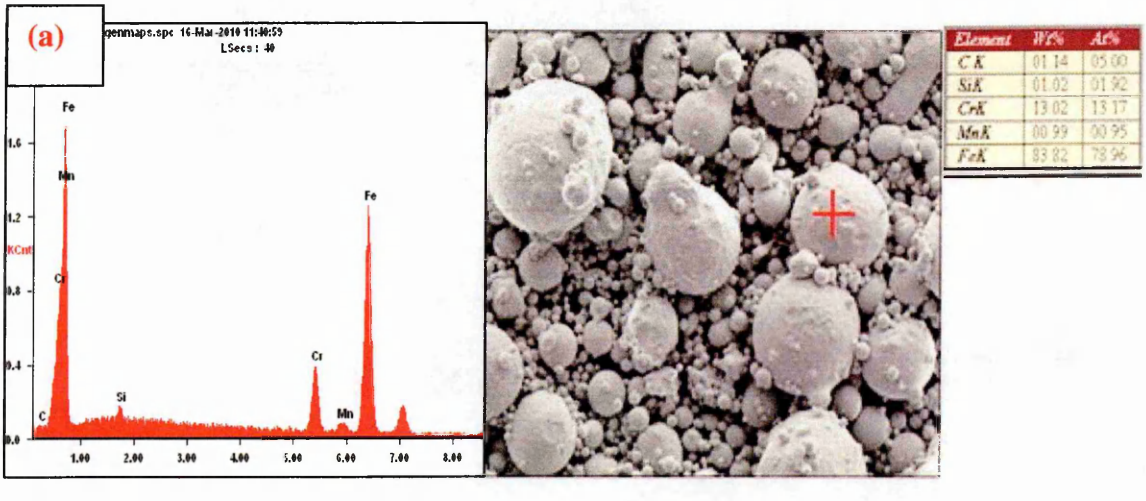

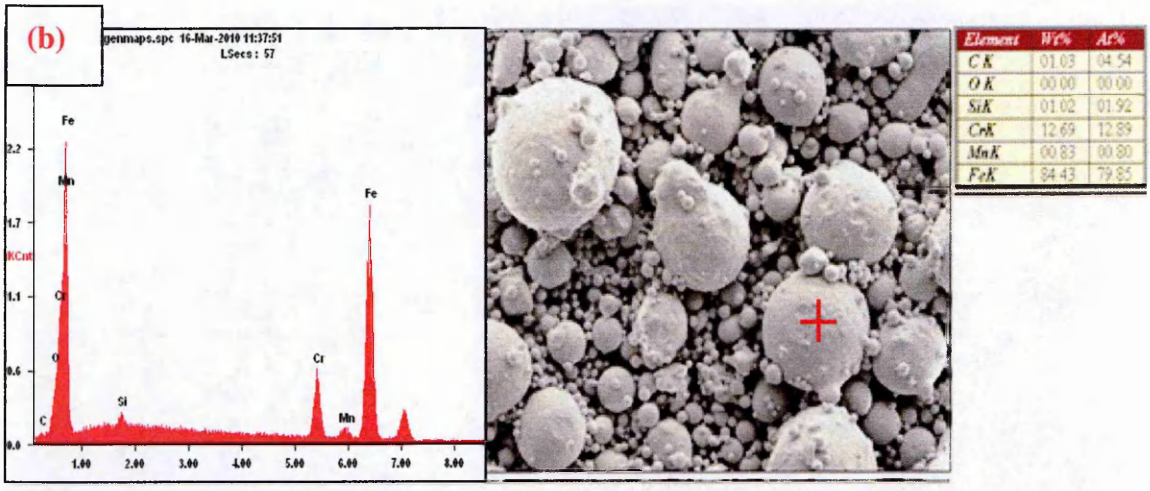

Fig. 5.4 EDX results of 410L Powder sample

EDX analysis on the yttria powders showed that the 50 nm yttria powder has some impurity in the composition. Yttrium and oxygen are detected as they should be but in addition to that some chlorine is detected as shown in Fig. 5.5. However for the 0.9 µm yttrium powder, it is verified that the powder is pure yttria without any impurity as can be seen in Fig. 5.6. Another issue with these powders is EDX analysis showed that the big particles mentioned earlier in both of the powders have a composition different than the yttria and they are more likely to be pure yttrium as shown in Fig. 5.5 and 5.6 due to 91-93 % yttrium content.

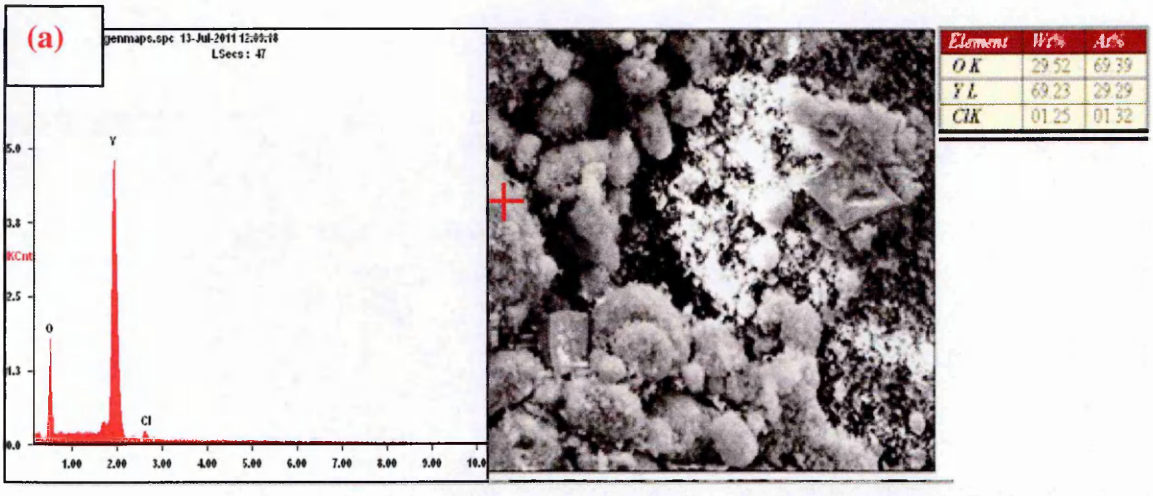

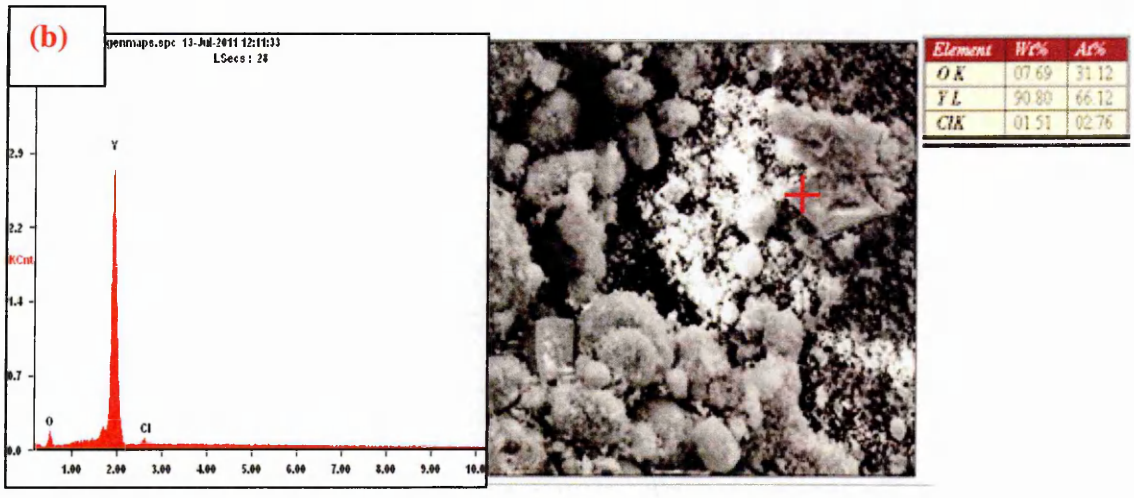

Fig. 5.5 EDX results of 50 nm Yttria powder

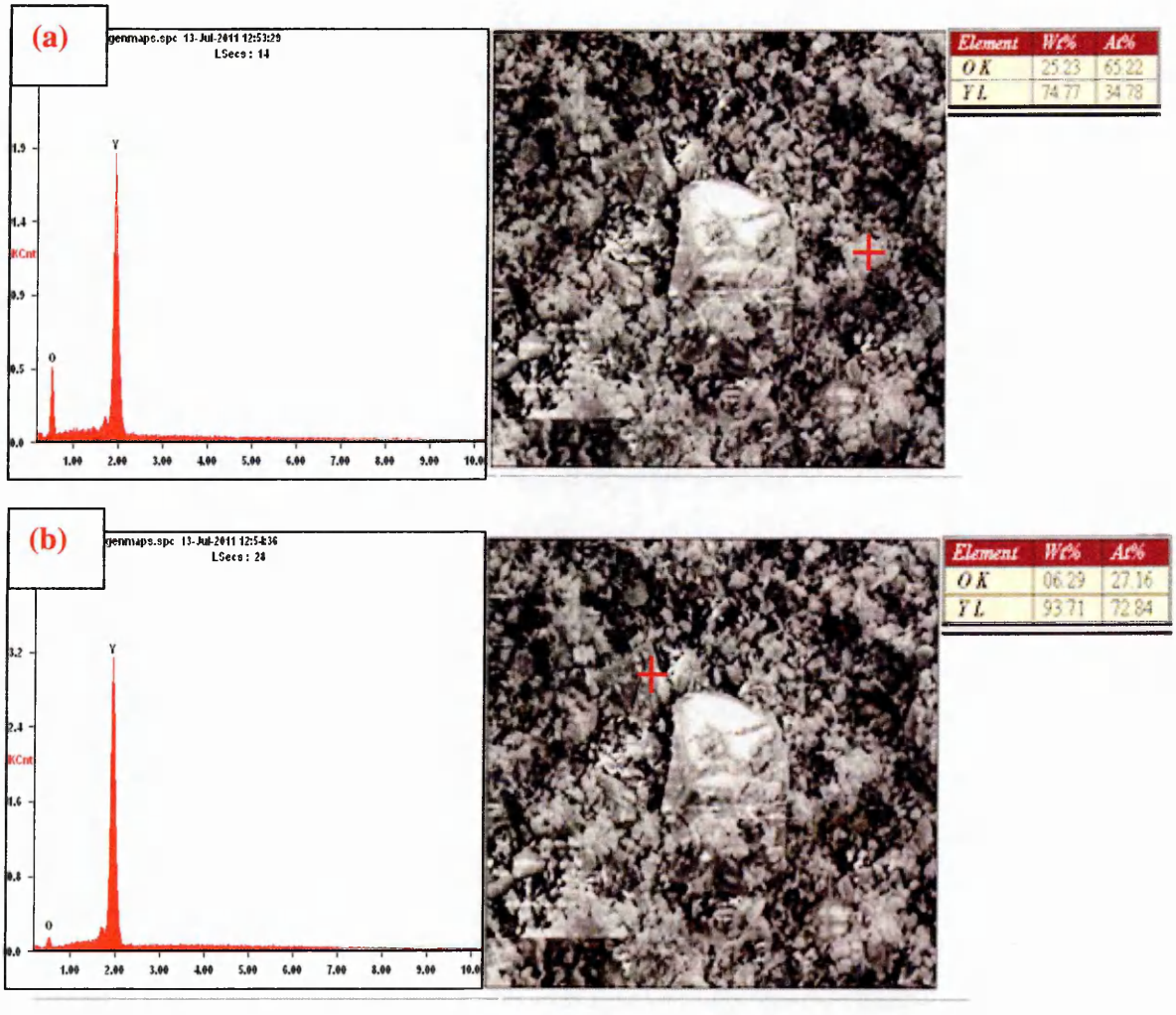

Fig. 5.6 EDX results of 0.9 µm Yttria powder

5.2 Metallography

After characterizing the powders basic metallographic analysis of the samples was done to examine the initial state of the samples and identify the constituents and the phases. For this examination, samples were prepared according to standard metallography sample preparation methods and examined under optical microscope.

Samples were initially examined in the as-received condition to determine the effect of heat treatment more clearly. Vilella's reagent was used to etch the sample to reveal the microstructure. In the as-received condition all of the samples showed similar microstructures with martensite inside the grains and some dark phases along grain boundaries which are thought to be residual ferrites. Some dark dots are observed as inclusions in the samples. Etched microstructures of the materials from the second batch are shown in Fig. 5.7.

Electrolytic etching was done on the samples to clarify the black regions along the grain boundaries to determine if they are really residual ferrites. For this purpose a specific ferrite etchant was used which is NaOH + water. This etchant etches only ferrites so just ferritic regions will be darkened during the etching process. The result of the etching is as expected. These black regions are residual ferrites due to the slow cooling after the HIP process, which is furnace cooling. Microstructures after electrolytic etching are shown in Fig. 5.8.

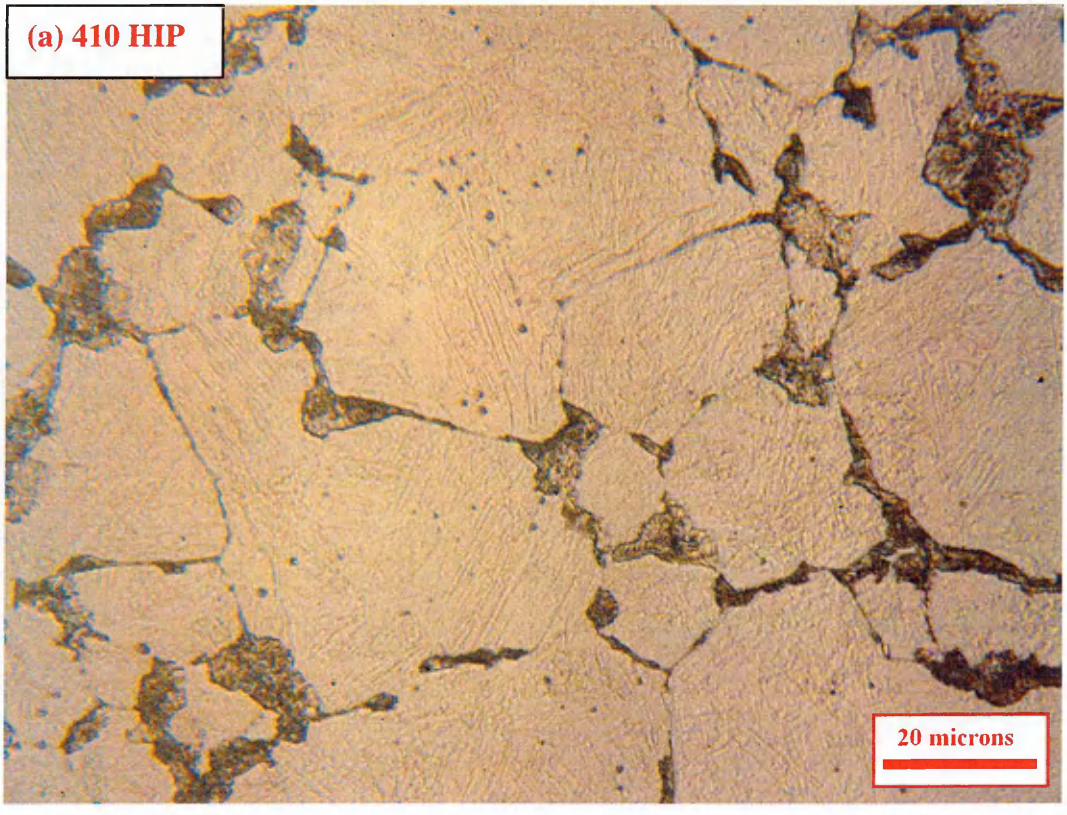
(a) 410 HIP
20 microns

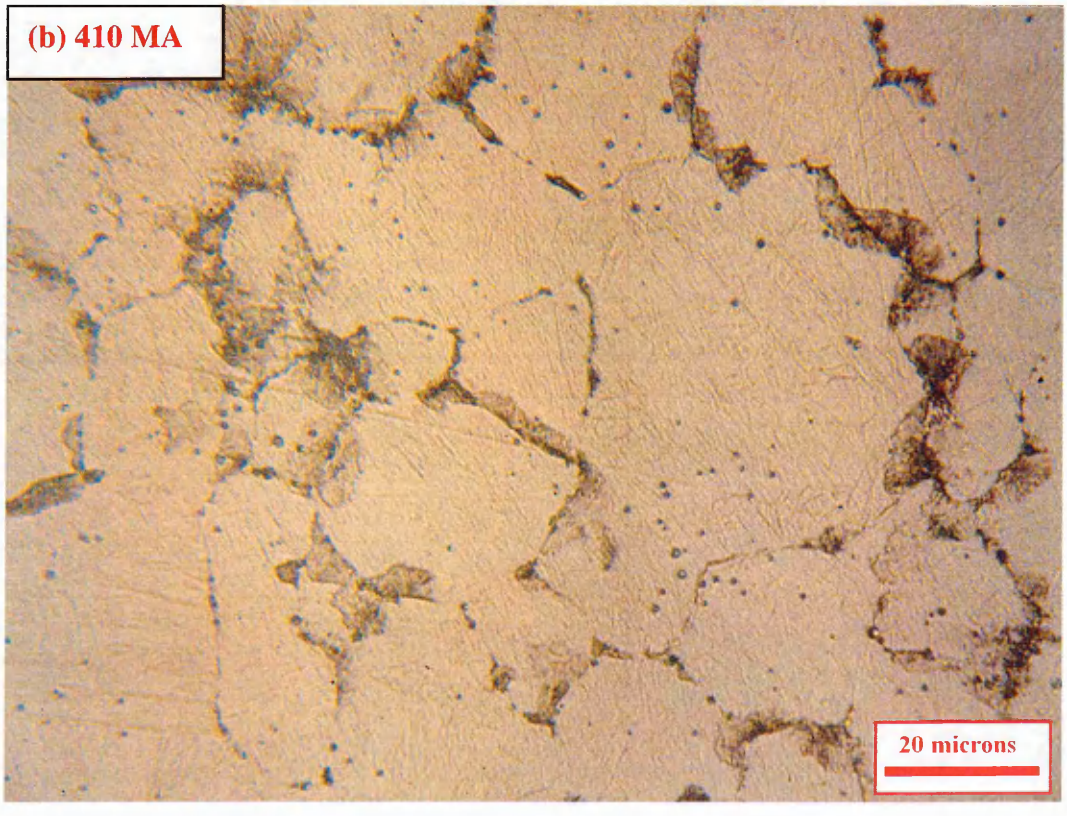
(b) 410 MA
20 microns

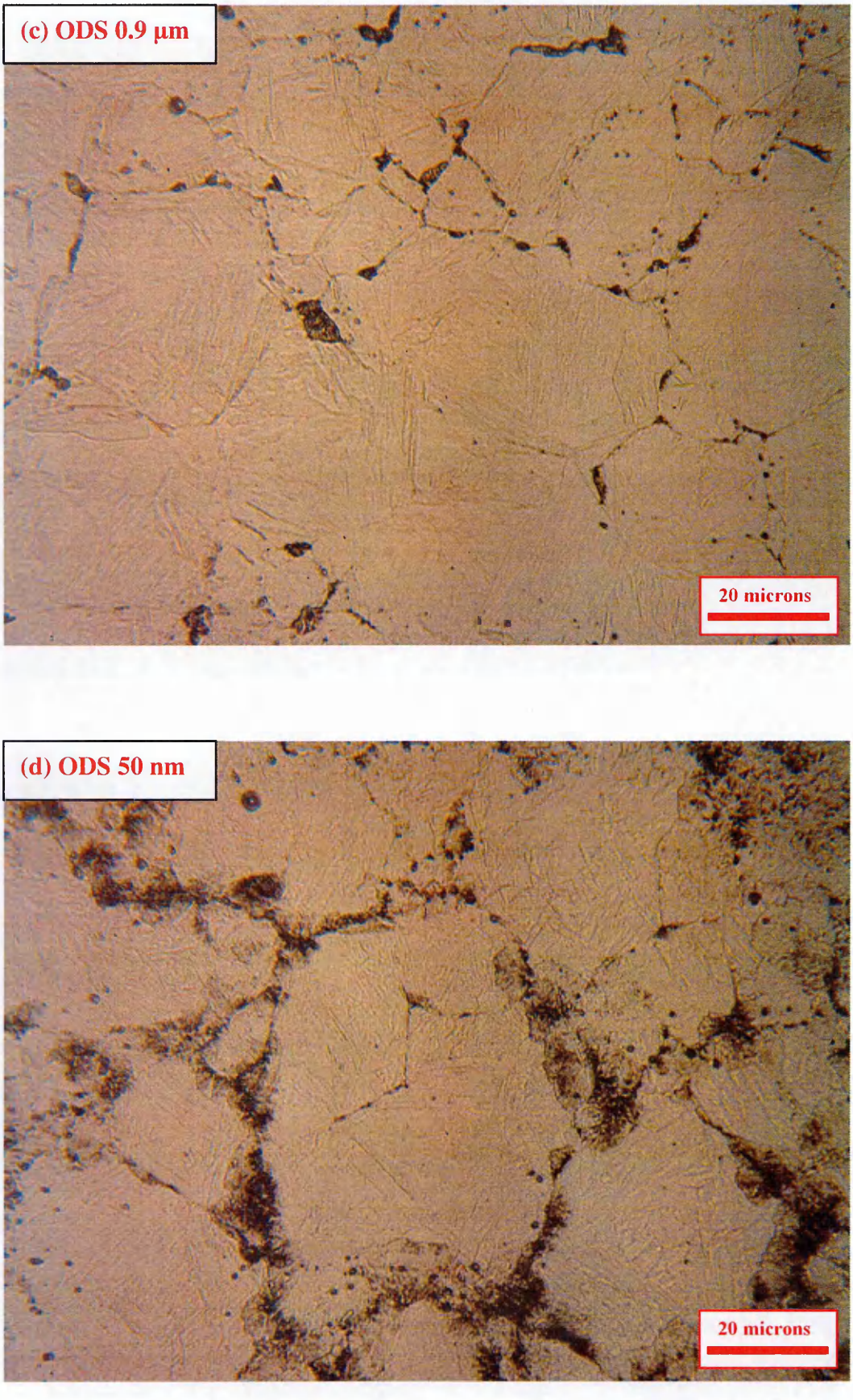

Fig. 5.7 As-received microsturcture images of the materials from the second batch etched with Vilella's reagent

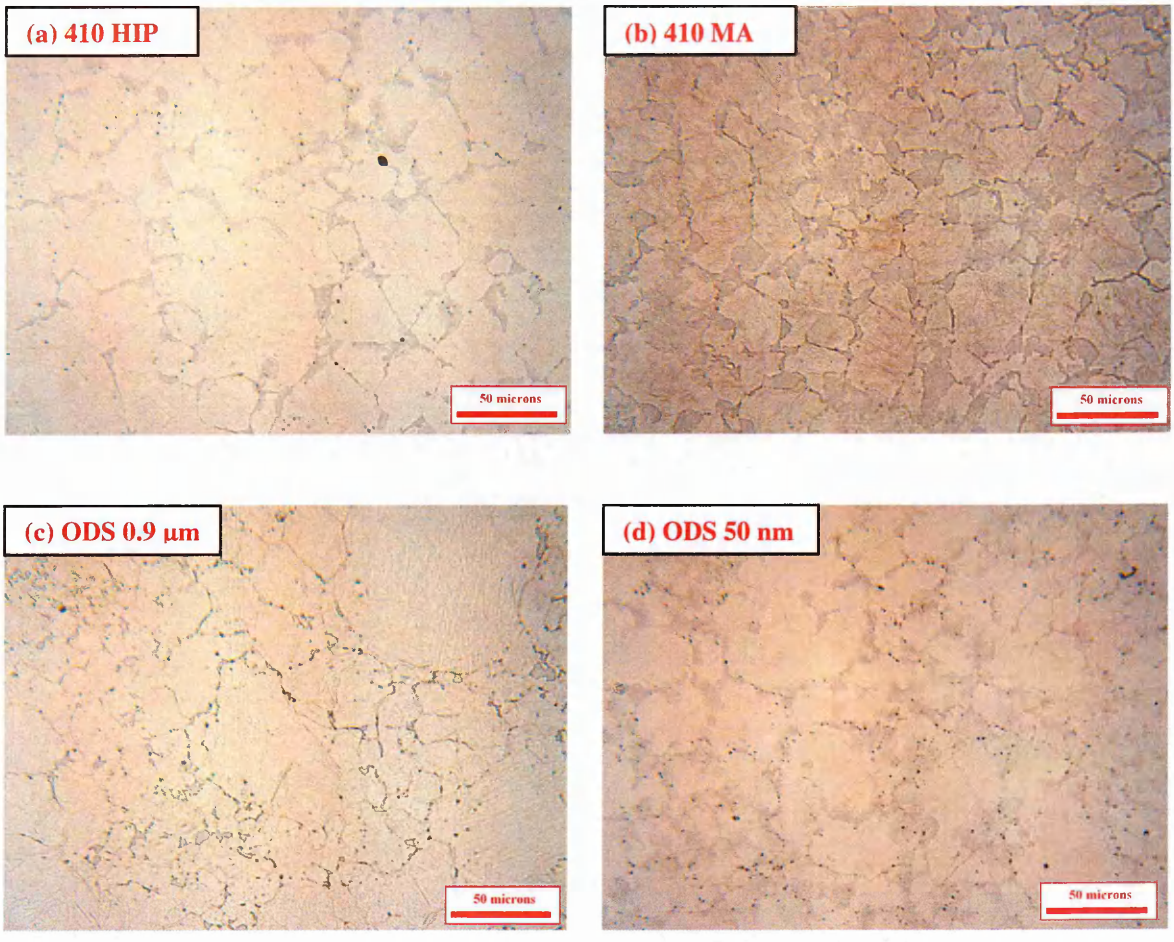

Fig. 5.8 Microsturctures of the samples after NaOH+ Water electrolytic etch showing residual ferrite regions

After heat treatment and quenching from 1000 °C all the austenite is transformed into martensite without residual ferrite. After heat treatment all the microstructures were etched with electrolytic etchant to confirm that all the microstructures are martensite and then transformed into tempered martensite after 650 °C tempering for 2 hours. These microstructures are shown in Fig. 5.9. As it can be seen this time no dark regions are observed at grain boundaries meaning that there is no longer any residual ferrite, as desired.

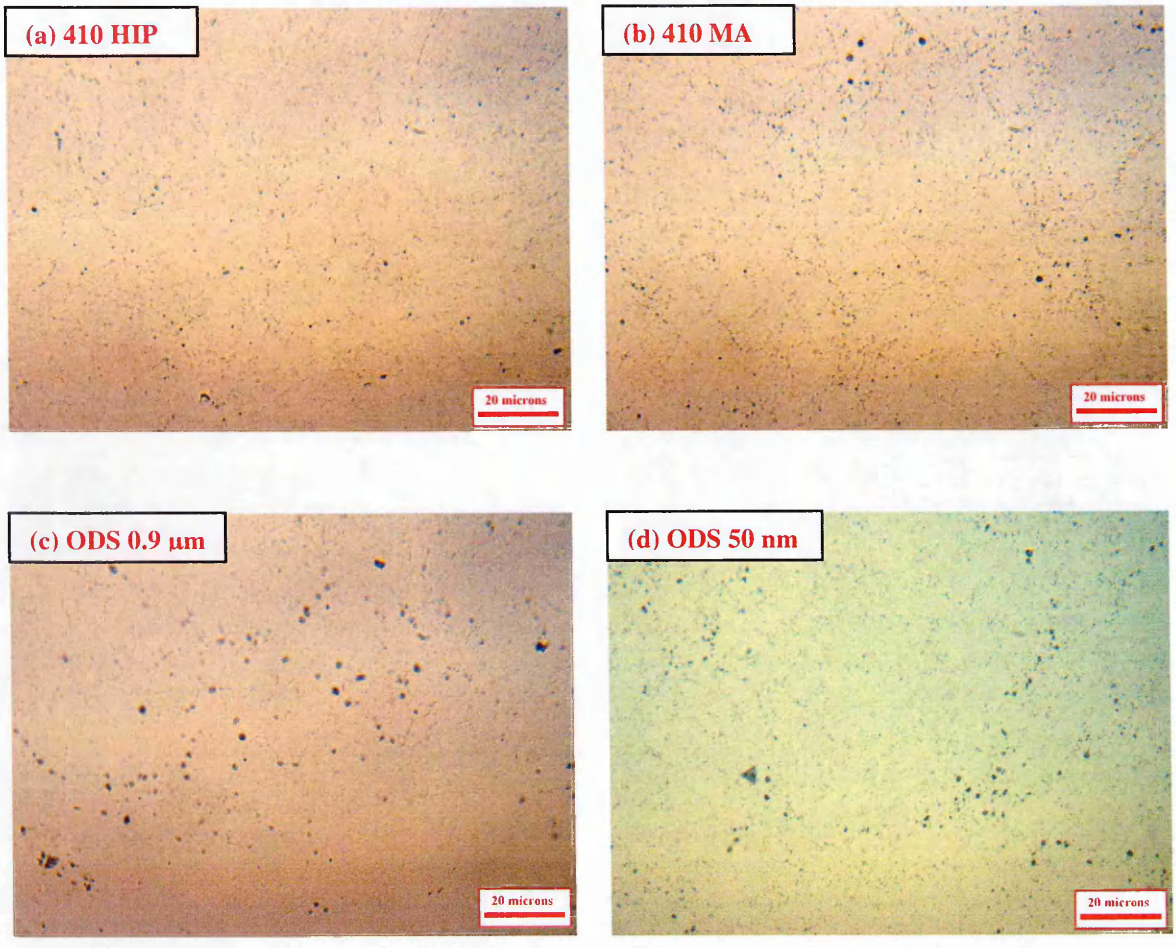

Fig. 5.9 Microstructures of the samples from the second batch after NaOH+ Water electrolytic etch showing all residual ferrite regions are disappeared after heat treatment processes

After examining the samples with electrolytic etchant, Vilella's reagent was used for revealing the final microstructure before starting mechanical testing. As can be seen from Fig. 5.10 all the microstructures are tempered martensite without any residual ferrites.

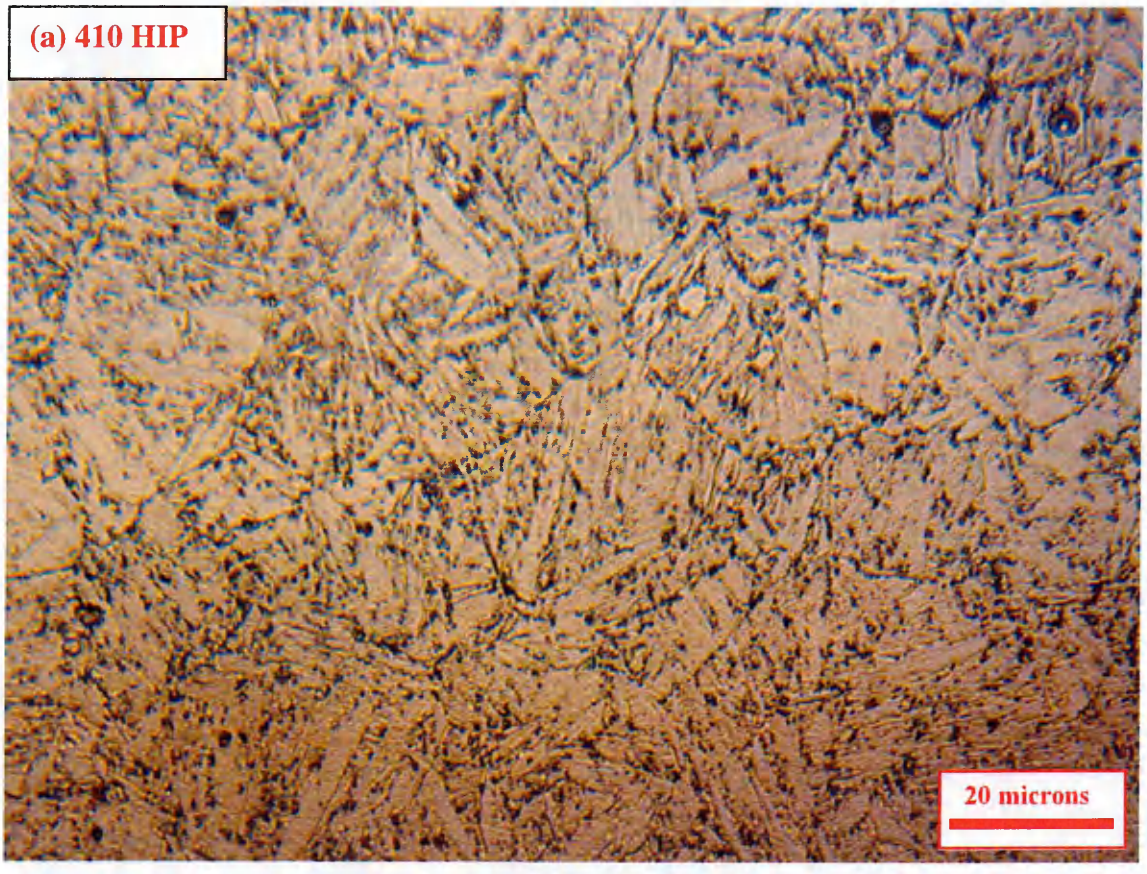
(a) 410 HIP
20 microns

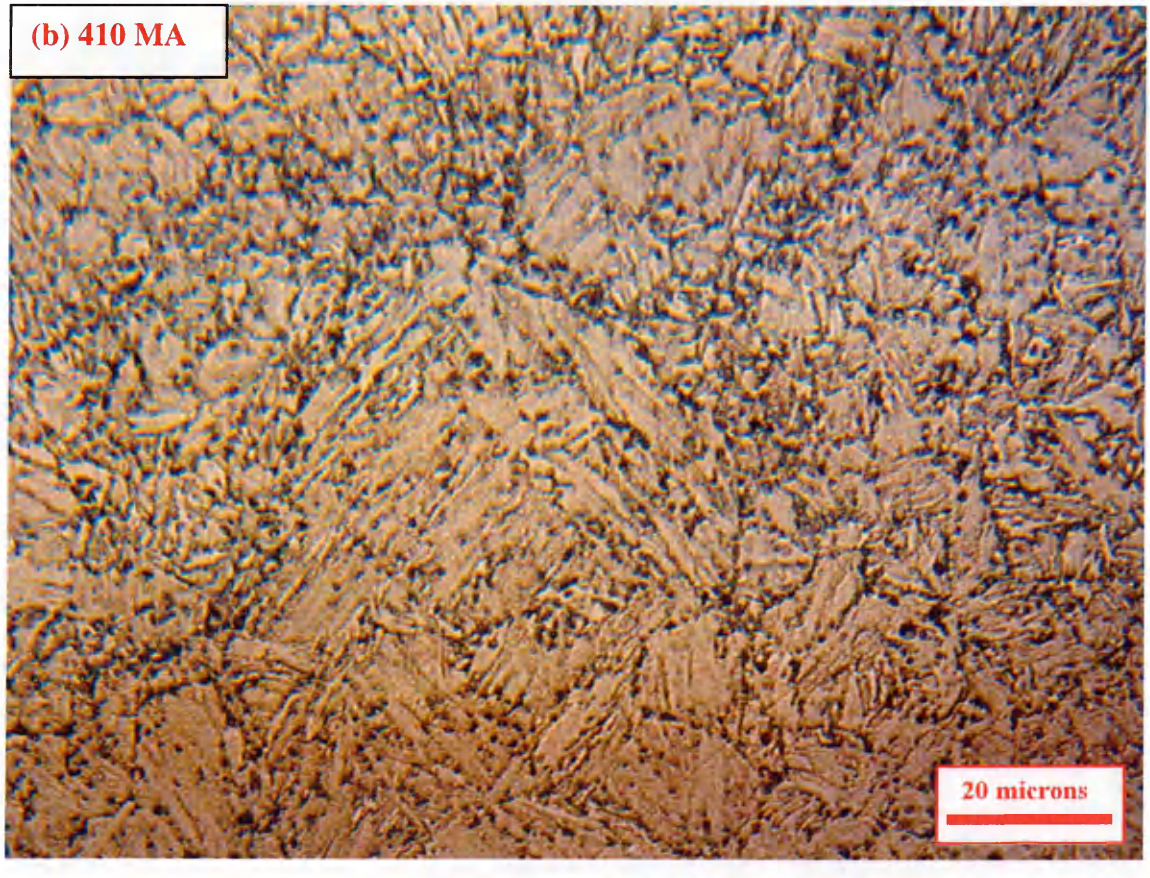
(b) 410 MA
20 microns

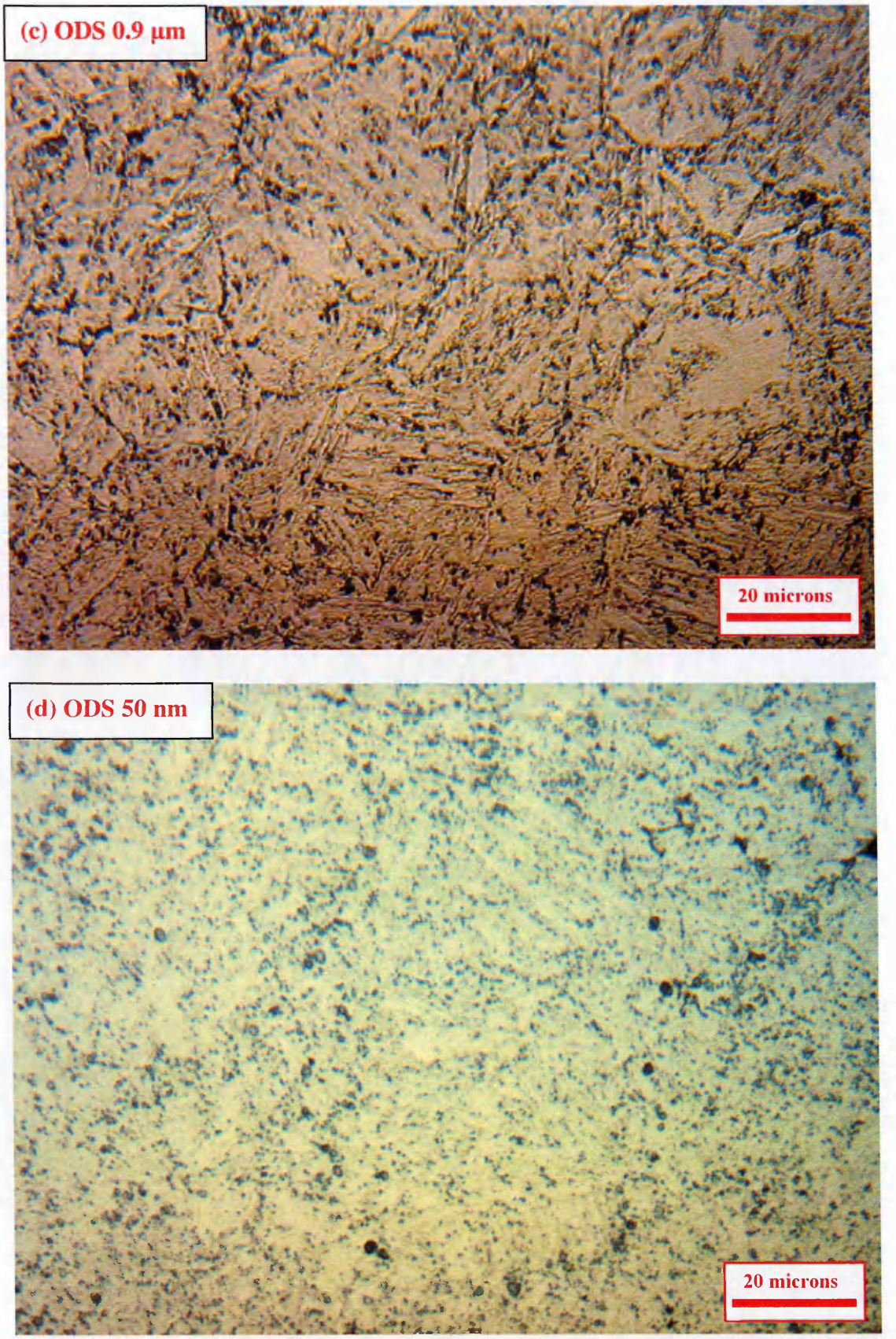

Fig. 5.10 Microstructures of the samples from the second batch after heat treatment process etched with Vilella's reagent showing tempered martensite

5.3 Macro Analysis of Room Temperature Tensile Tests

After room temperature tensile tests were conducted, the fracture surfaces of each sample were observed. As mentioned earlier brittle fracture surfaces are usually bright and shiny whereas ductile fracture surfaces are usually darker with a microscopic cup and cone morphology. Observations generally coincided with the ductile fracture mechanism.

However these observations revealed some inclusions on the fracture surfaces of some of the samples. These inclusions have a gold colour and are easily detectable by eye. Only two of the samples have these inclusions on their fracture surfaces: are ODS 50 nm sample from the first batch and 410L MA sample from the second batch. Macro images of these inclusions are shown in Fig. 5.11 for ODS 50 nm sample and Fig. 5.12 for 410L MA sample.

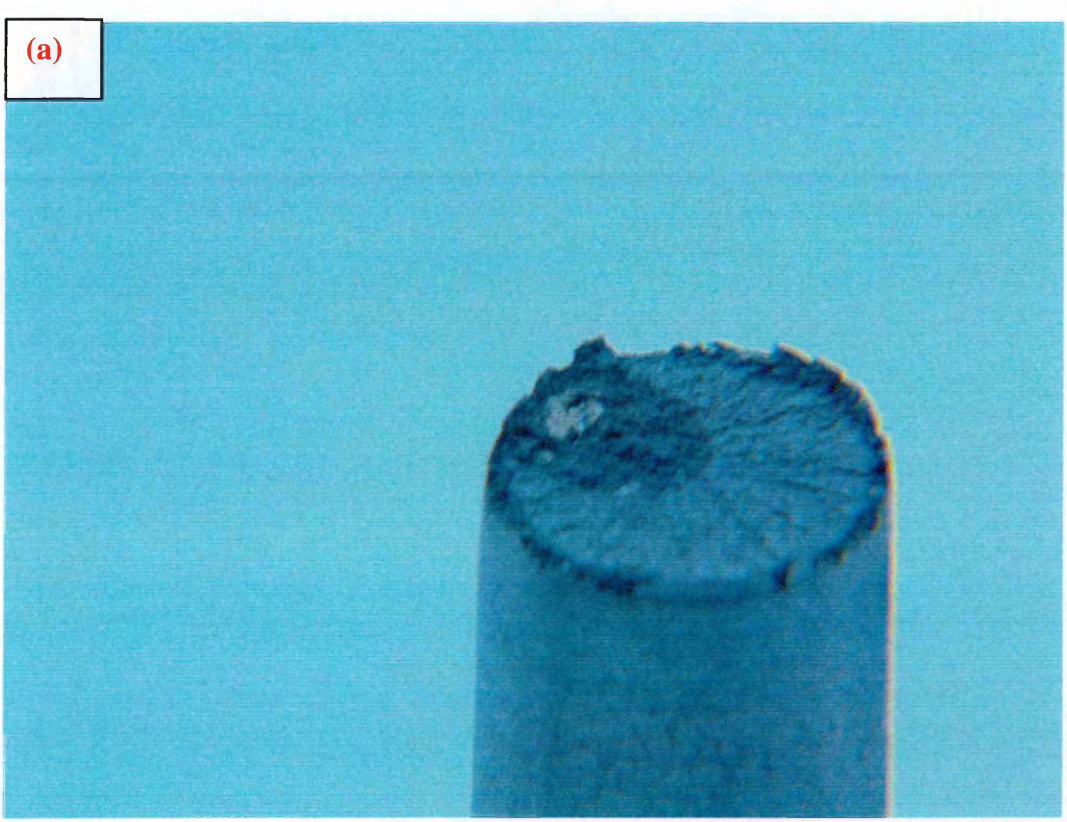

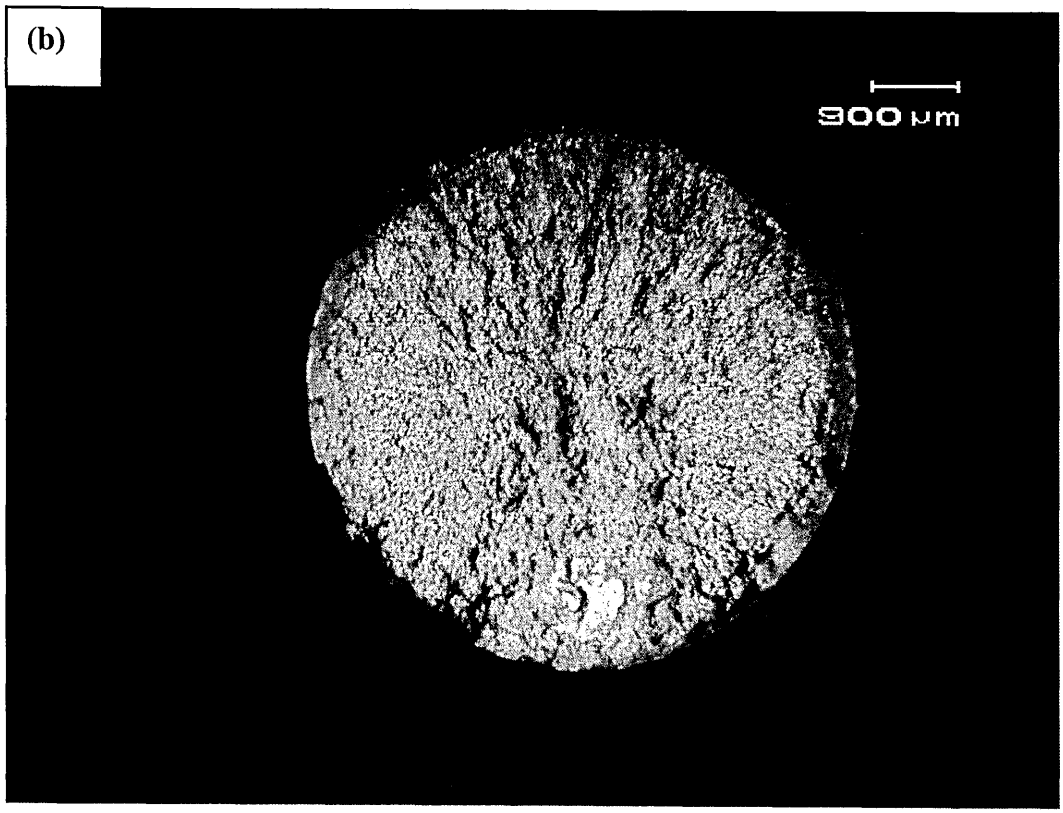

Fig. 5.11 Images showing gold coloured inclusions on fracture surface of ODS 50nm sample from the first batch (a) eye view (b) macro view

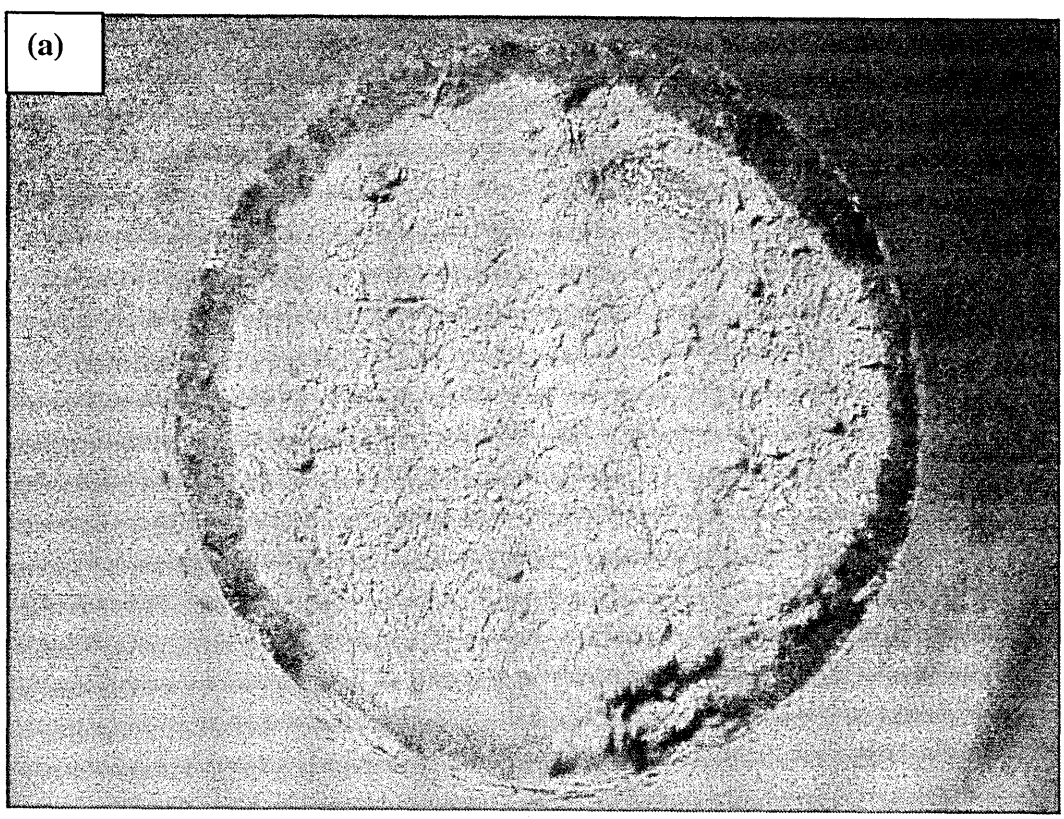

Fig. 5.12 Macro images showing gold coloured inclusions on fracture surface of different 410L MA samples from the second batch

EDX analysis was conducted to analyse what is the composition of the inclusion and titanium and nitrogen are detected as shown in Fig. 5.13. So it is thought that the inclusion is TiN which has a gold colour. This TiN inclusion will be discussed further in the discussion chapter (chapter 6).

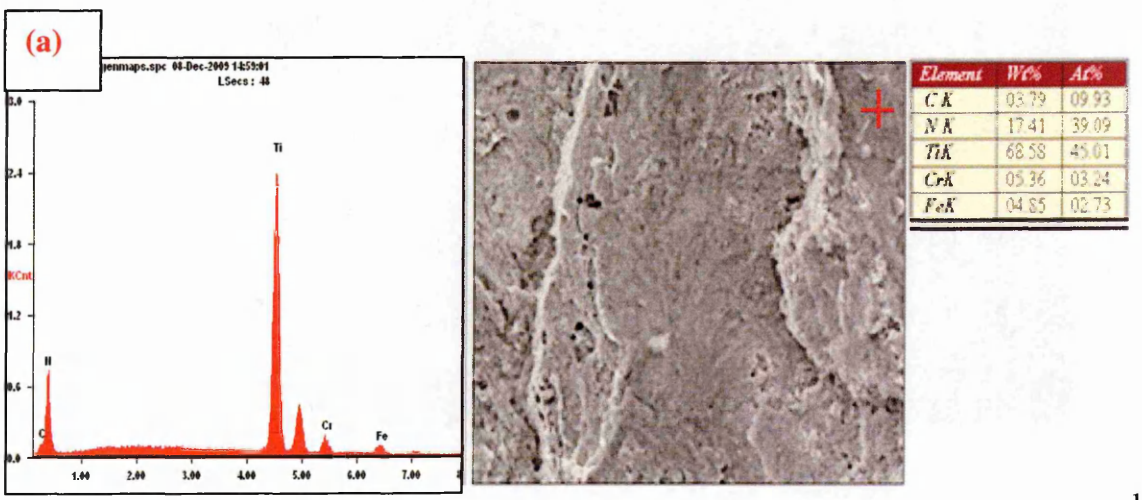

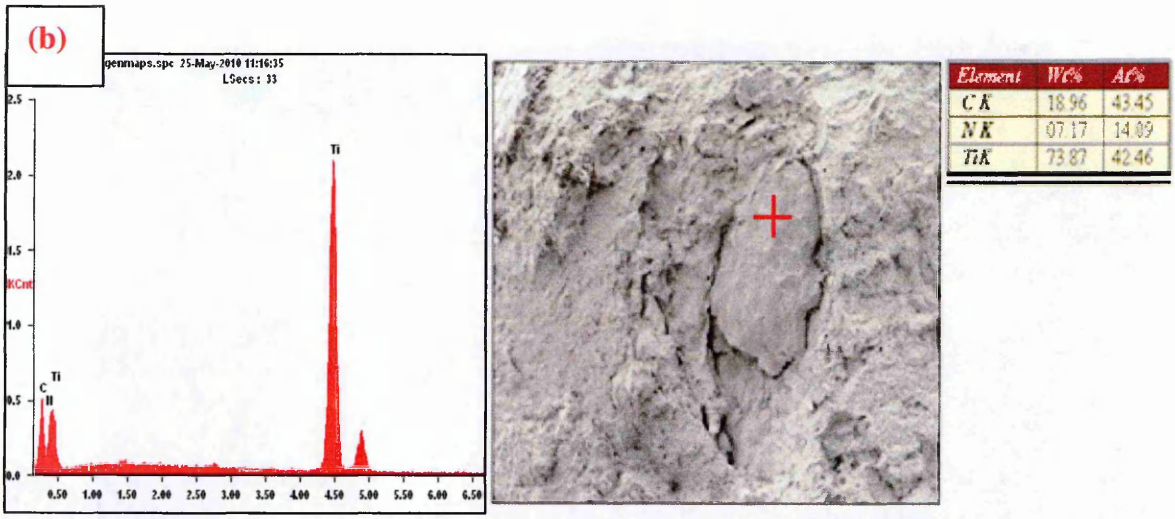

Fig. 13 EDX analysis on inclusion particles on fracture surfaces of ODS 50 nm and 410L MA

Another important point was revealed by macro analysis after room temperature tensile tests. ODS 0.9 µm from the first batch has some densification issues which was clearly observable by eye. When two ODS fracture surfaces are compared the ODS 50 nm shows a flat and shiny pattern whereas the ODS 0.9 µm shows a rough, dull surface like it is still in powder form as shown in Fig. 5.14.

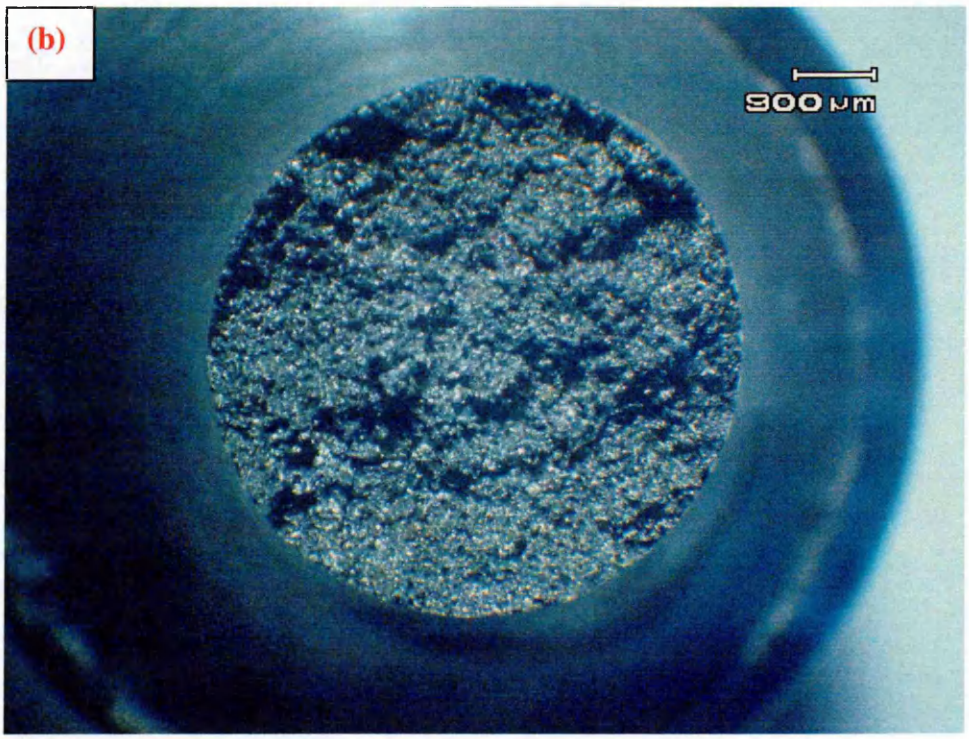

Fig. 5.14 Macro images showing the fracture surfaces of (a) ODS 50 nm and (b) 0.9 µm to show the densification problem

To have a better understanding of this densification issue SEM imaging was performed. The ODS 0.9 µm fracture surface is like an agglomeration of many particles as in Fig. 5.15 whereas the ODS 50 nm shows typical ductile fracture features with smooth surface as in Fig. 5.16. Fig. 5.17 is an image of ODS 0.9 µm with higher magnification. It can be seen that some regions remained undistorted during fracture. Some particles are seen on the surface which is going to be explained later in this chapter.

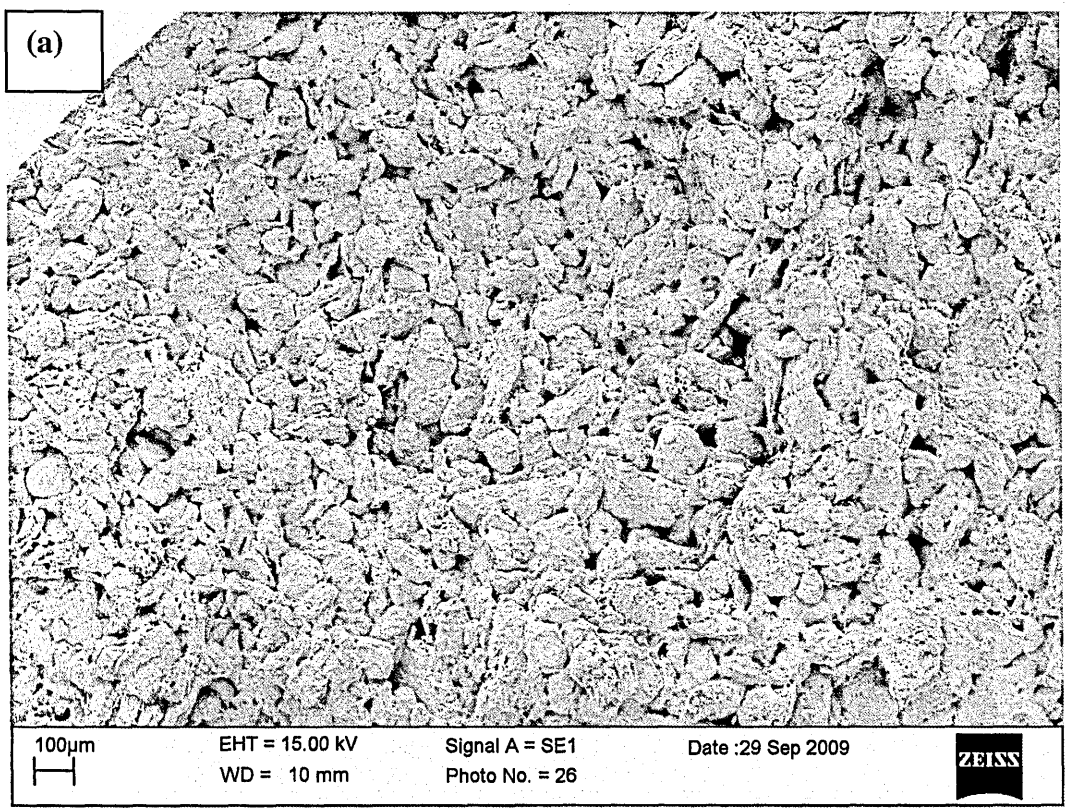

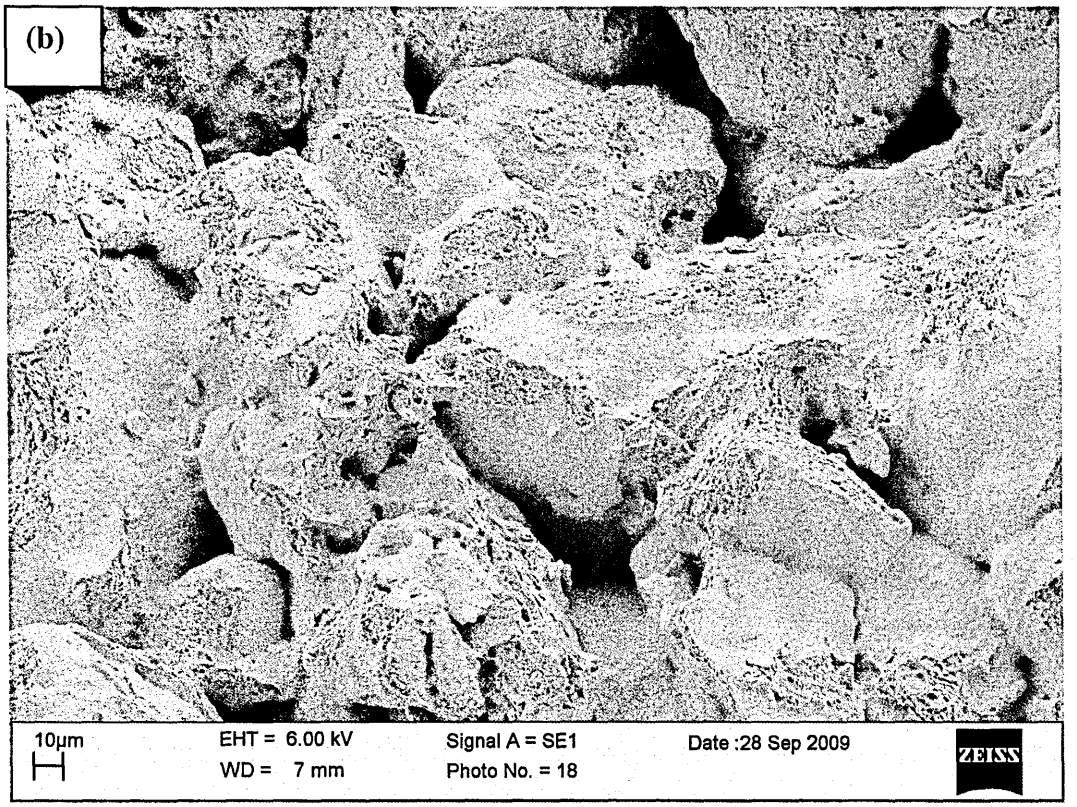

Fig. 5.15 SEM images of ODS 0.9 µm fracture surface showing densification problem

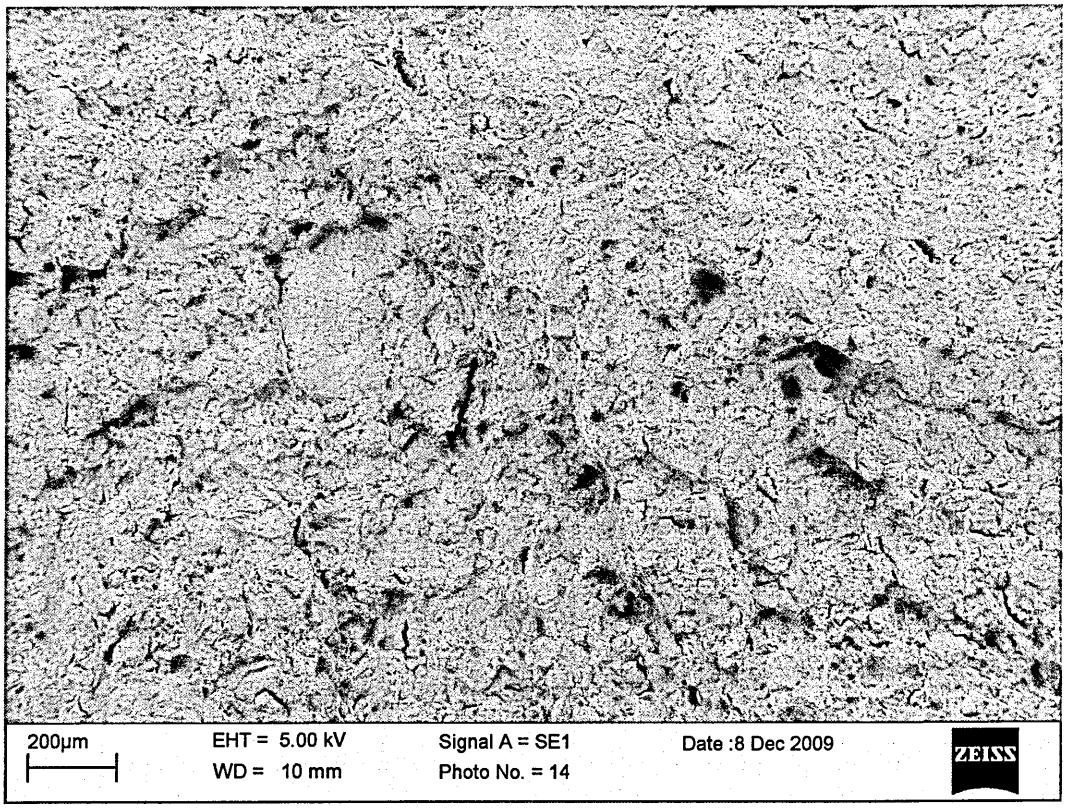

Fig. 5.16 SEM images of ODS 50 nm fracture surface showing typical fracture

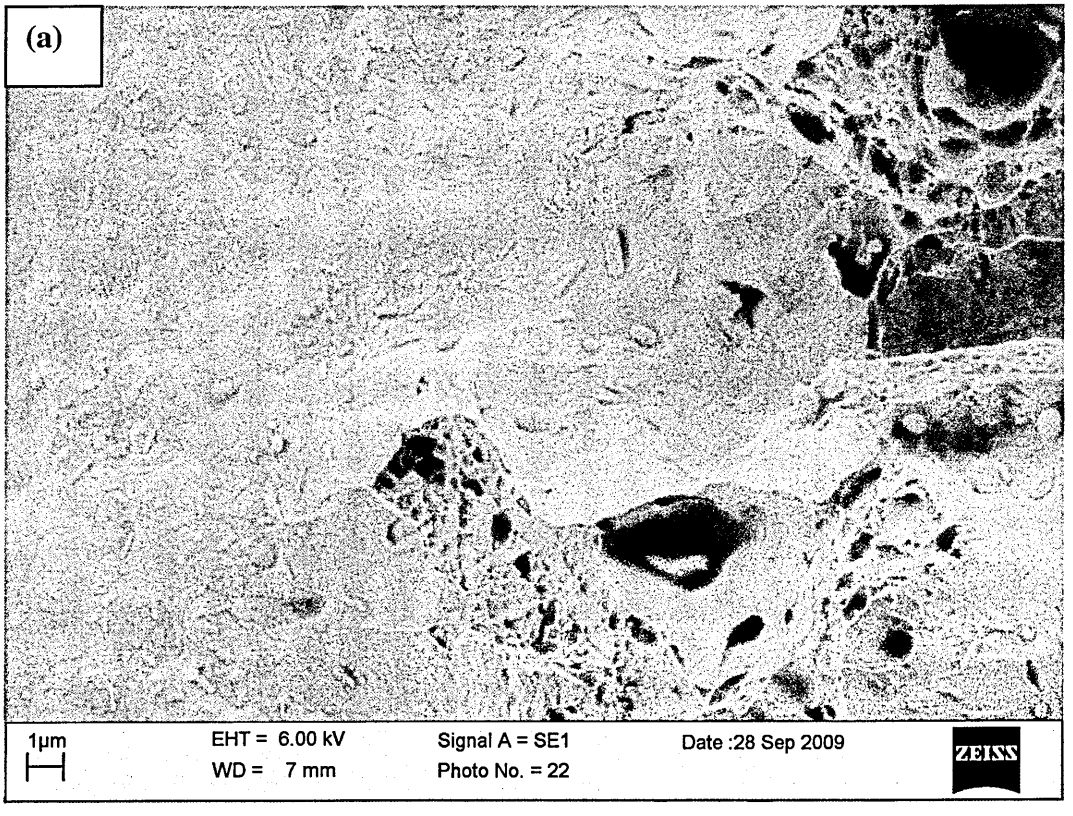

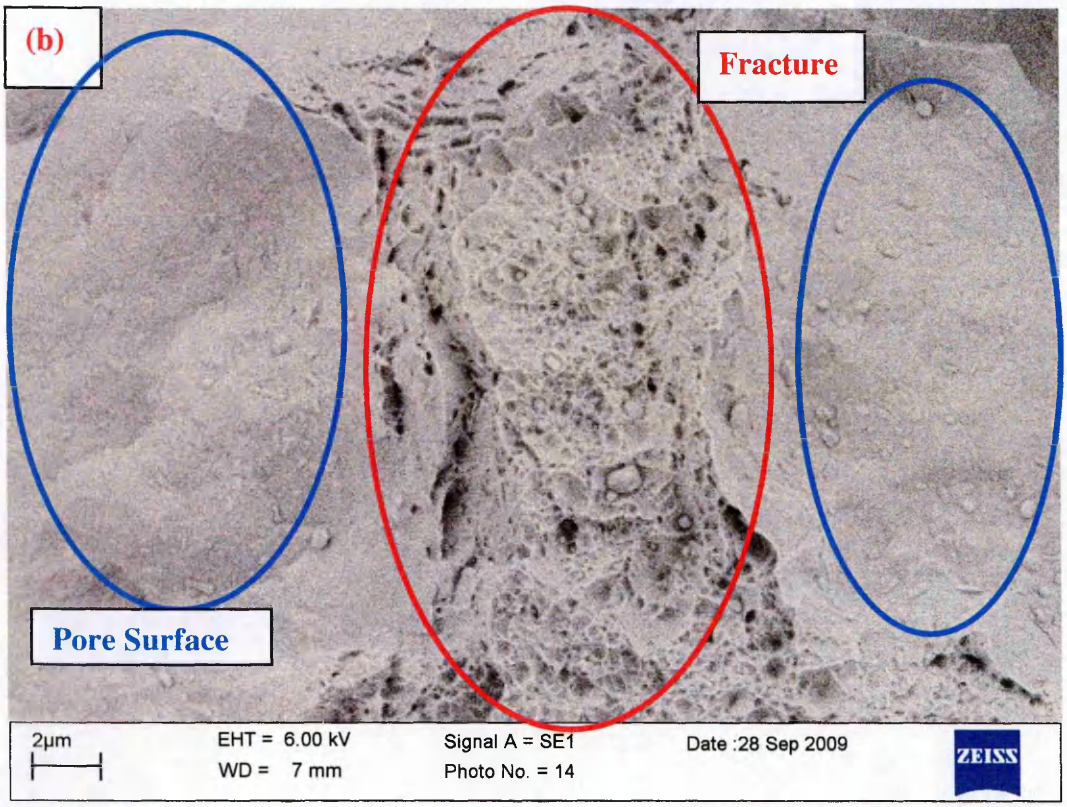

Fig. 5.17 Fracture surface image of ODS 0.9 µm with bigger magnification showing distinctive regions

5.4 SEM and EDX Analysis of Room Temperature Tensile Tests

After completing macro analysis of the tensile test specimens, SEM and EDX analysis were performed to explore the material in more detail. Fracture surfaces of the materials were examined under SEM. A common feature is there are inclusions sitting on the fracture surfaces of all samples. These inclusions are up to 2 µm in size. Usually they are round ended and mostly spherical however there are some particles in rod-like shapes. These particles are sitting in cup like structures and the surfaces of these regions are quite smooth even though these images are from fractured samples. It is very similar to effects of voids during fracture. Further explanation about these particles takes place in discussion

chapter (chapter 6). These inclusions and cup structures can be seen in Fig. 5.18 for all samples.

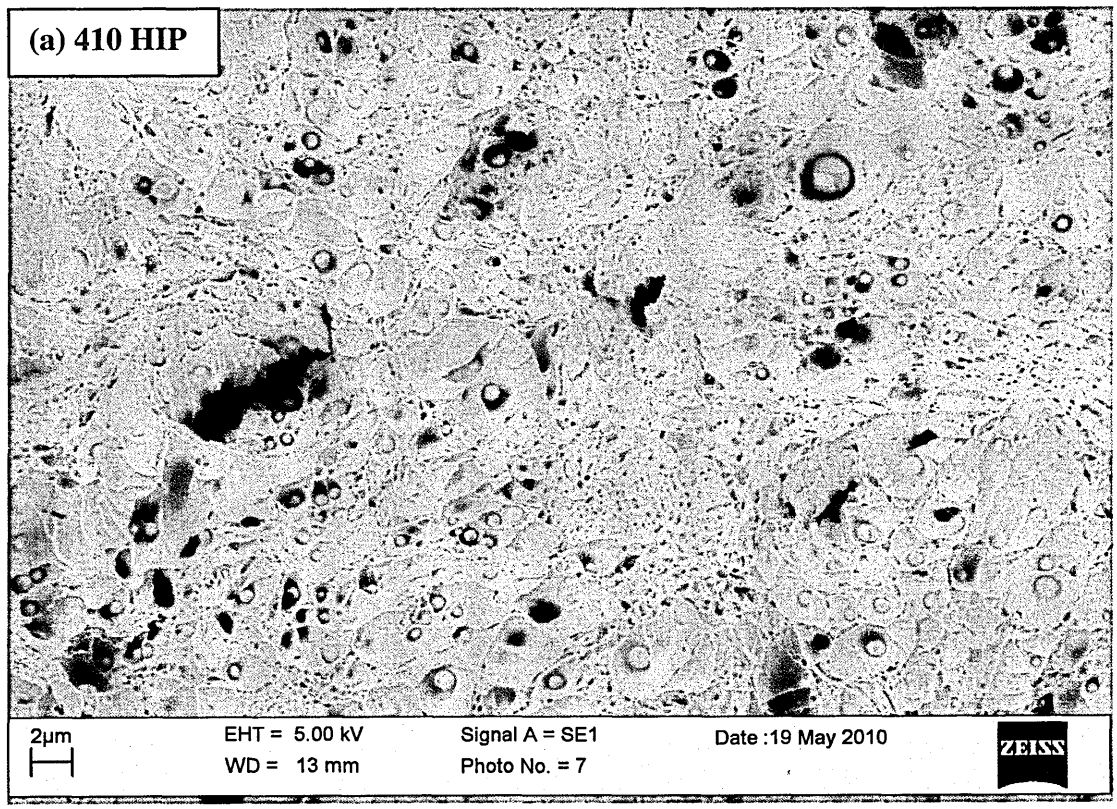

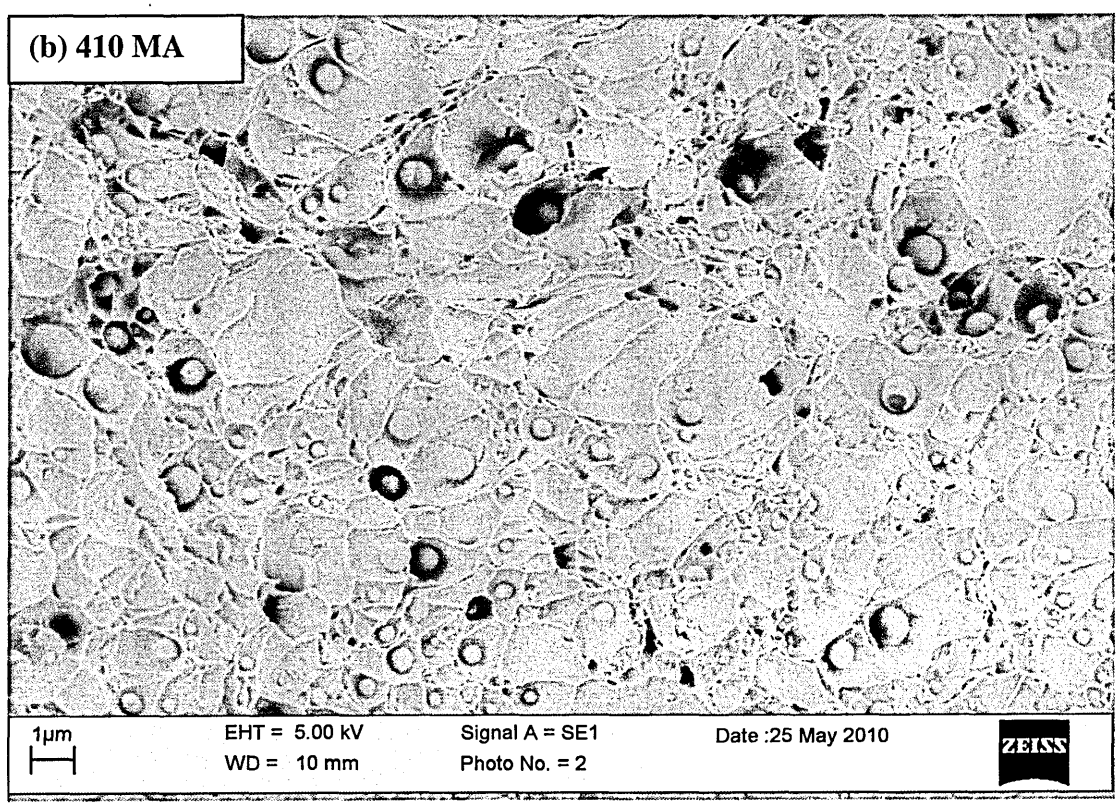

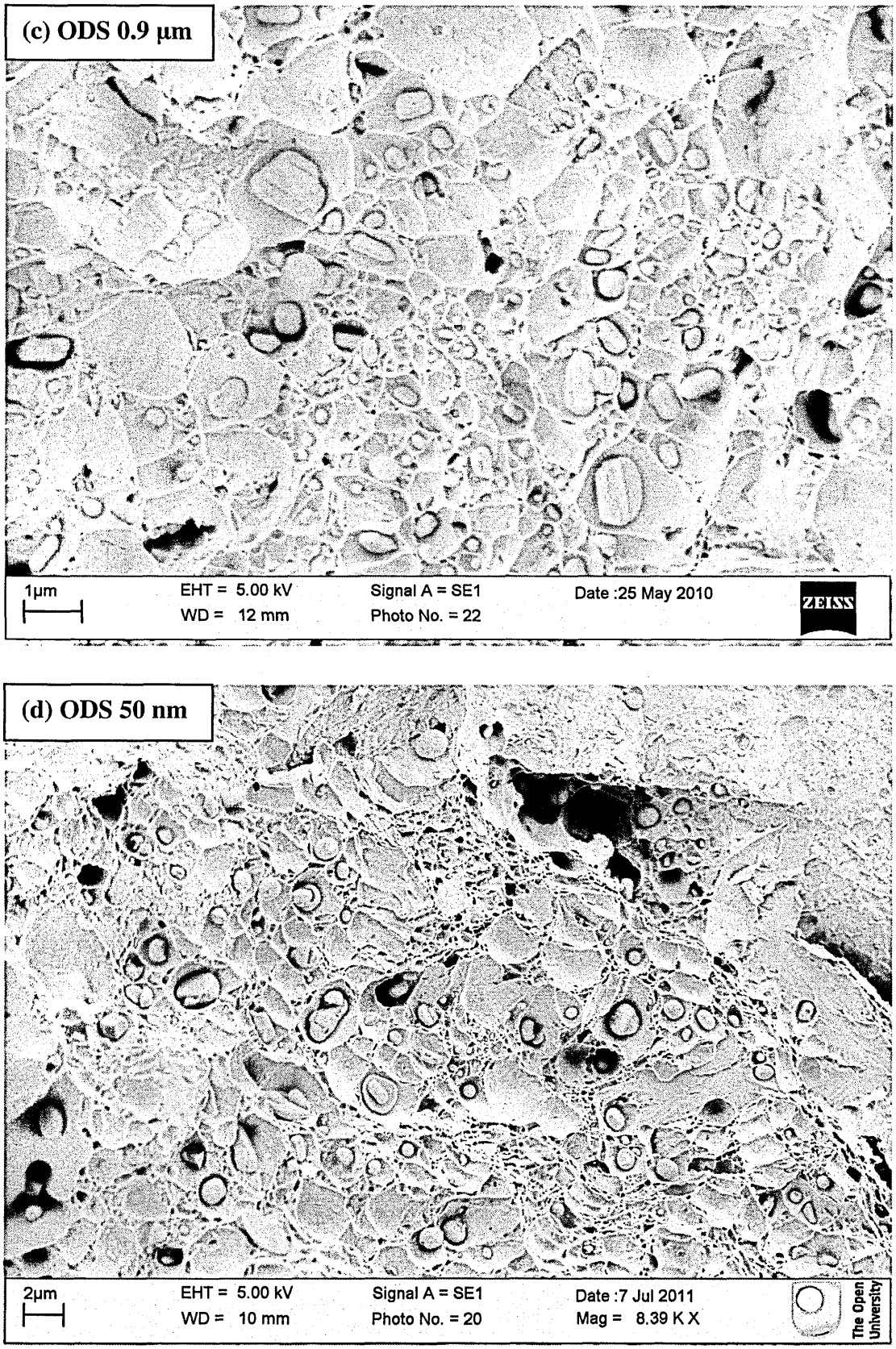

Fig. 5.18 SEM images of the fracture surfaces of the samples after room temperature tensile tests showing inclusion particles on the surface (a) 410L HIP, (b) 410L MA, (c) ODS 0.9 μm, (d) ODS 50 nm

There is one another important fact about these inclusions which is some of these inclusions appear to be a combination of 2 or more inclusions. It looks like they are stuck together. It can be observed in all samples. A clear example of this situation is showed in Fig. 5.19 in ODS 0.9 μm sample.

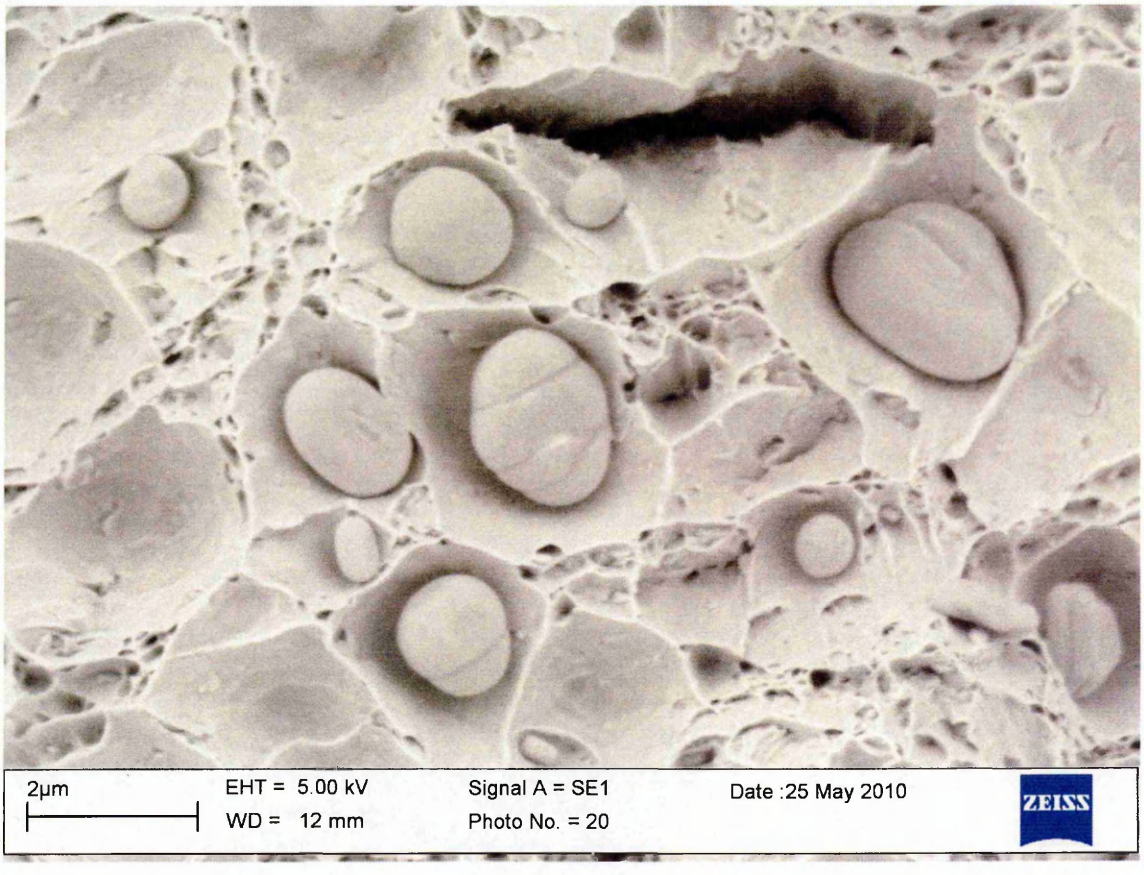

Fig. 5.19 SEM image of fracture surface of ODS 0.9 μm showing inclusions where some of them are a combination of two or more inclusions.

For better understanding these inclusions, EDX analyses were carried out to reveal their compositions. The results were quite interesting showing that these inclusions are silicon-oxygen, silicon-oxygen-yttrium and manganese-sulphur particles. Obviously particles with yttrium are only observed in ODS samples however the other particles are common for all samples. EDX analysis on particles

of combination of two or more inclusions showed that each constituent part may have different composition. For example one part may be a silicon-oxygen rich particle while the other part was manganese-sulphur. EDX analysis of some of these particles can be seen in Fig. 5.20. Even in some particles in ODS samples, two particles with compositions of silicon-oxygen and silicon-oxygen-yttrium sitting together in the same particle was observed which can be seen from the TEM analysis of one of those particles in Fig. 5.21.

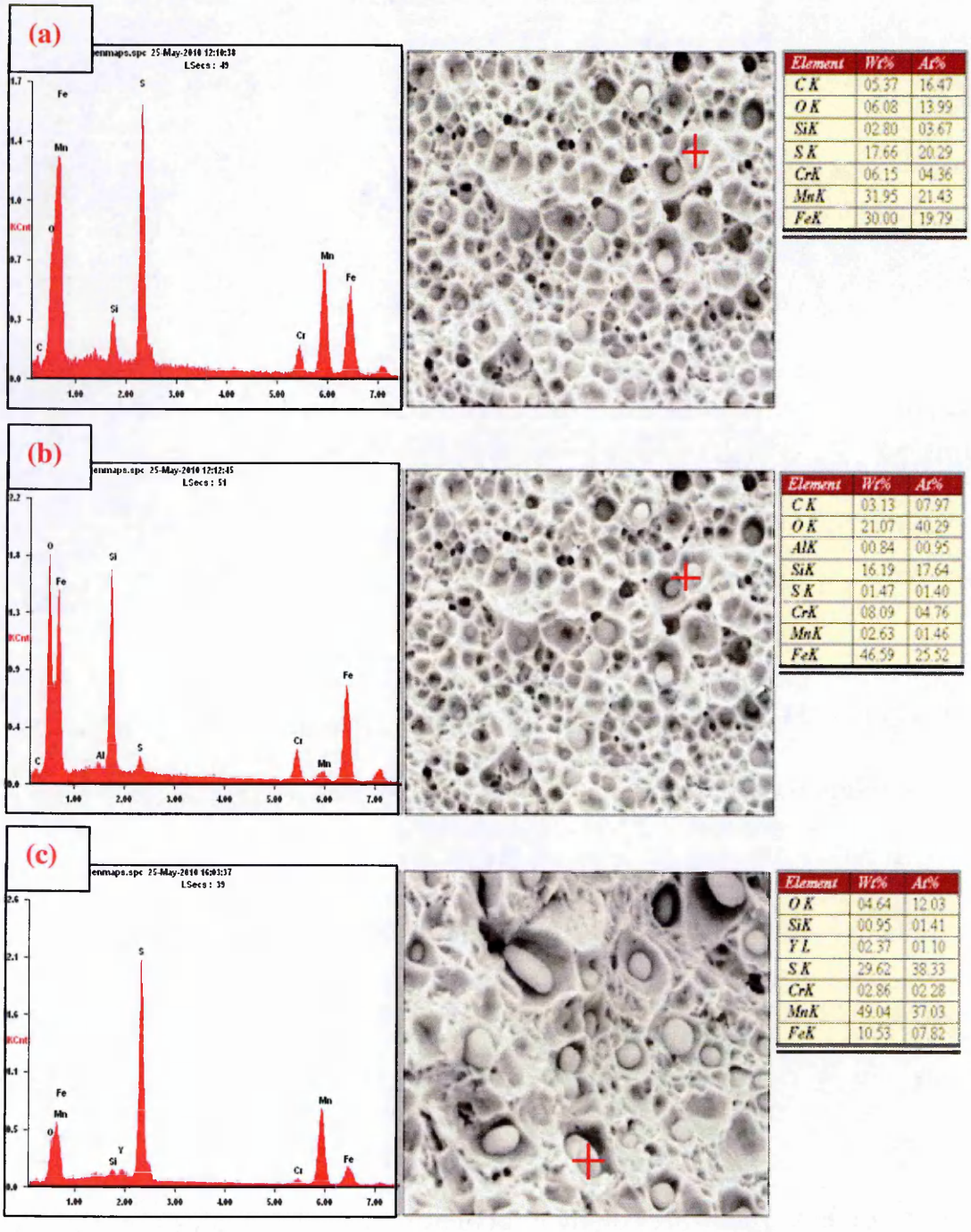

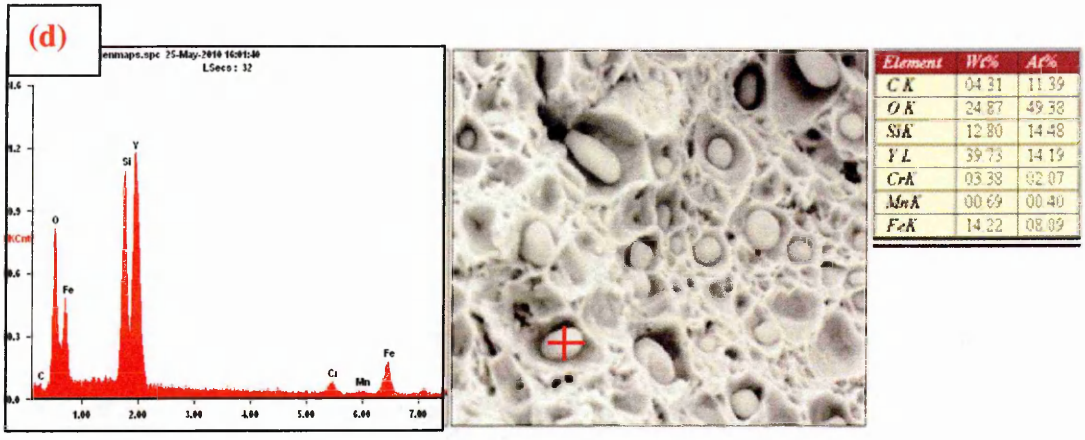

Fig. 5.20 EDX results of some inclusions showing composition (a), (b) 410 MA sample (c), (d) ODS 0.9 μm sample

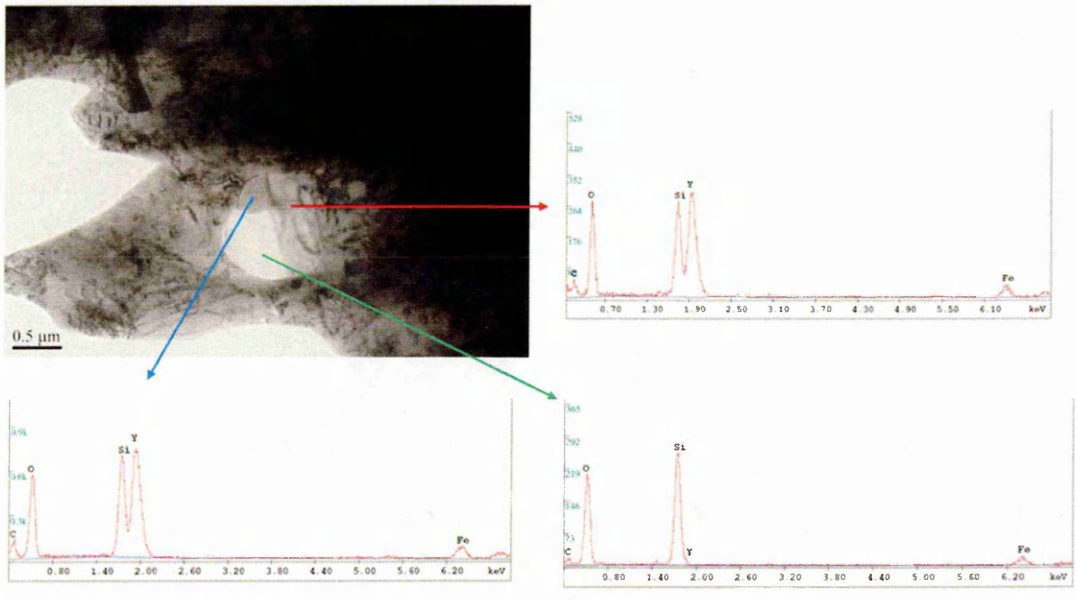

Fig. 5.21 EDX results of one of the inclusions in ODS 50 nm sample showing that silicon-oxygen-yttria region and silicon-oxygen region sitting together in the same particle.

These inclusions are also visible in the metallography specimens. Unetched metallography specimens were examined under SEM. The amount of inclusions in the metallography specimens is much less than on the fracture surface. SEM images of two metallography samples, one from 410L HIP and one from the ODS 50 nm, are shown in Fig. 5.22. Combined inclusions can be seen clearly in these

images. The sizes of the inclusions range from few nanometers up to 2 μm. This was observed in the fracture surface analysis as well.

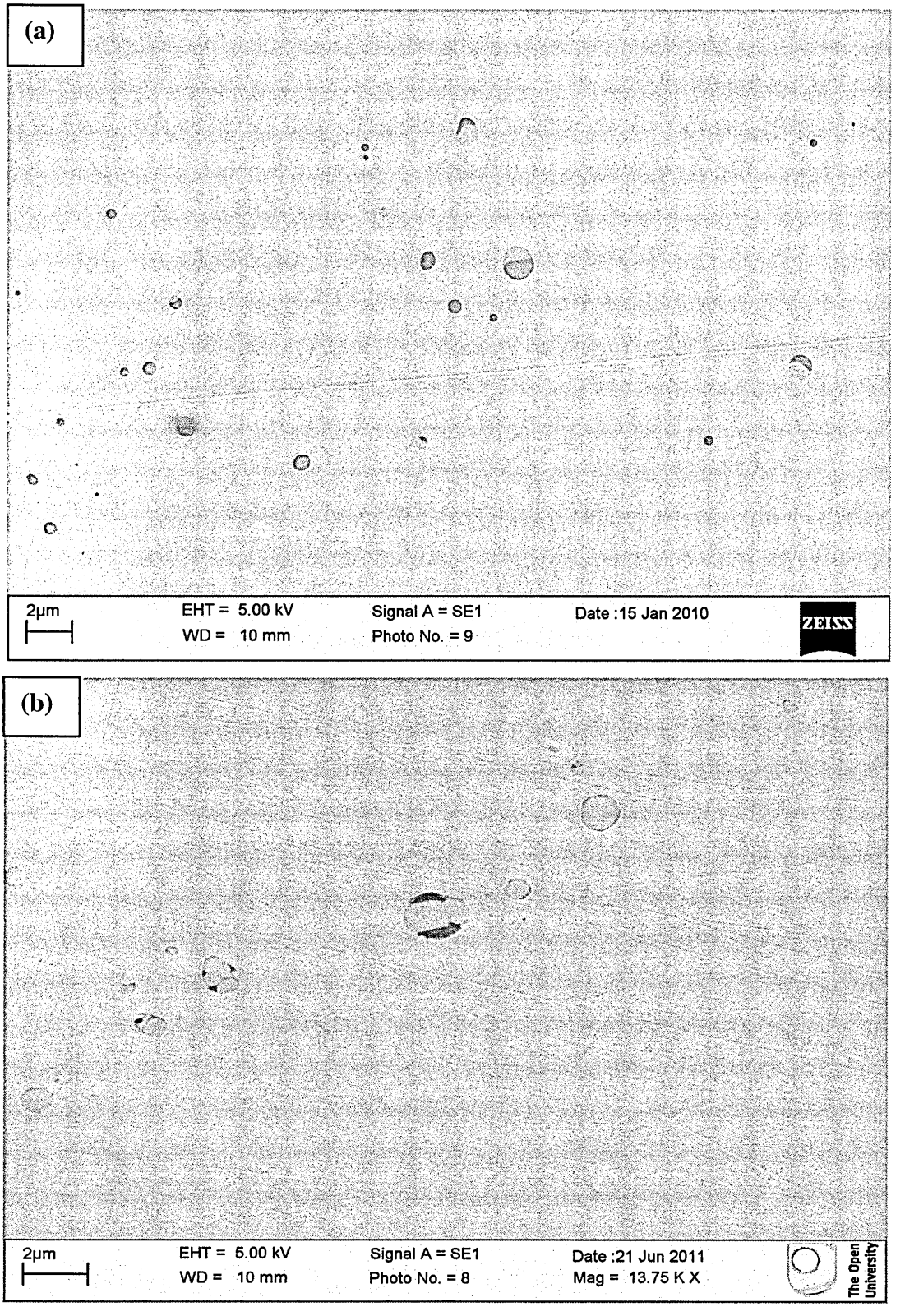

Fig. 5.22 SEM images of unetched metallography samples (a) 410L HIP and (b) ODS 50 nm sample showing inclusions

During the analysis of ODS 50 nm from the second batch, important information was obtained related to the microstructure of the ODS 50 nm. Some regions on the surface of the sample shows porosity as can be seen from Fig. 5.23.

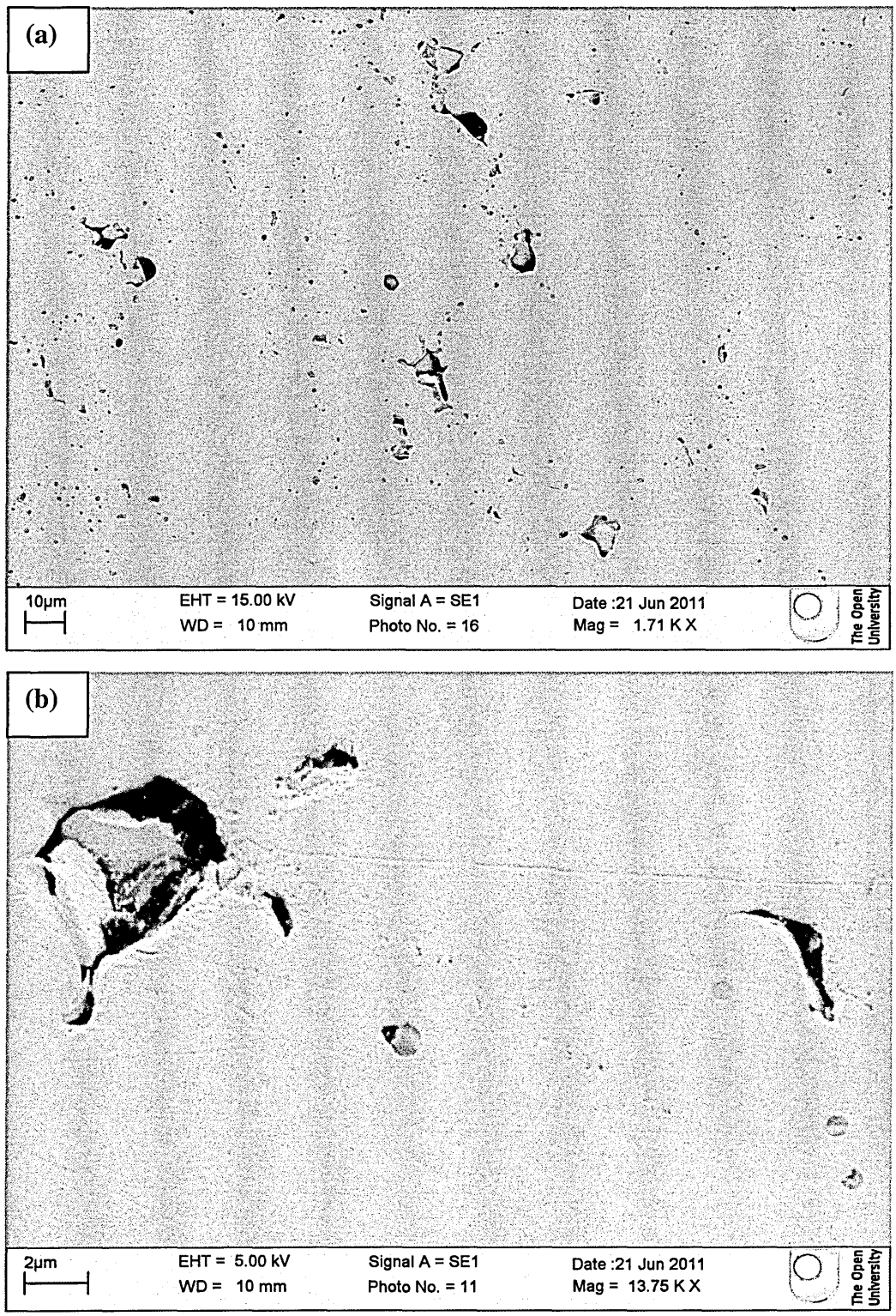

Fig. 5.23 SEM images of metallography sample of ODS 50 nm showing porosity

To clarify this porosity issue some more SEM analyses were carried out on the fracture surface of the ODS 50 nm sample. These examinations showed similar results to the ODS 0.9 μm from the first batch which also has a porosity problem (Fig. 5.17). The fracture surface appears to have two distinctive features: first one encircled has dimples whereas the rest of it appears to be smooth with some pores shown in Fig. 5.24.

Inclusion particles and oxide particles can be seen on the porous region as well but obviously they are not sitting inside of dimples. Dimples are main characteristics of ductile fracture. Reasons of porosity and its effect on mechanical properties are explained in discussion chapter.

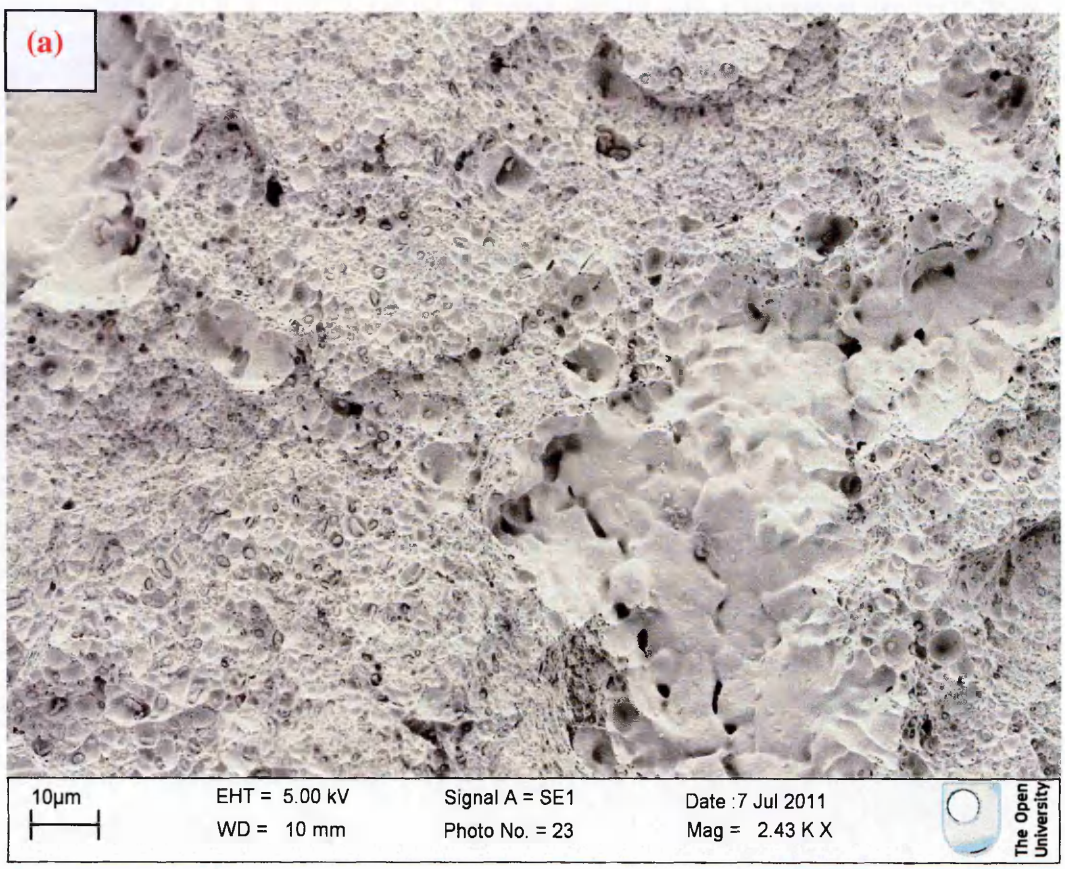

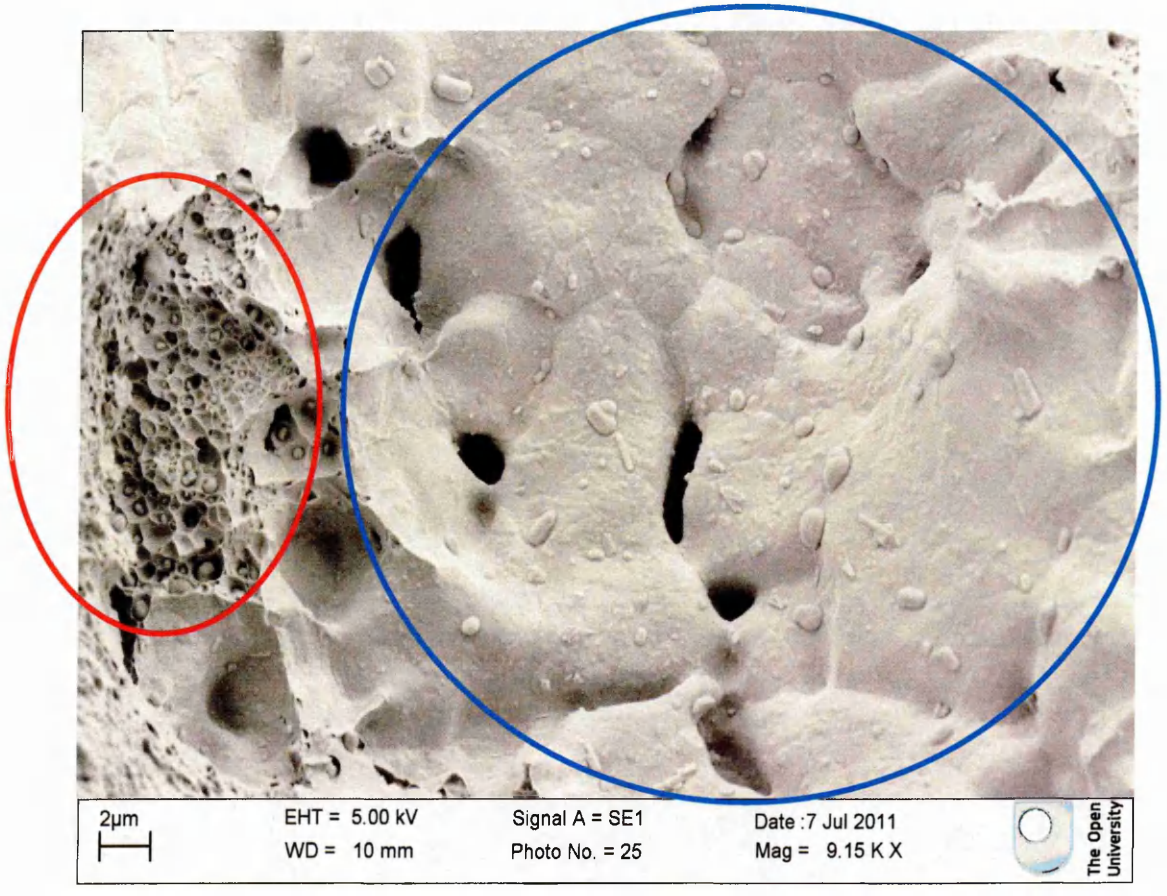

Fig. 5.24 SEM images from fracture surface of ODS 50 nm showing porosity problem via undistorted regions.

5.5 Analysis of High Temperature Tensile Tests

After high temperature tensile tests at 625 °C, all samples were analysed using SEM and EDX for better understanding of fracture and materials properties. Fracture surfaces of the samples were highly oxidized due to high temperature exposure after sample rupture. The same inclusions particles are observed on each sample in dimples, mainly Mn-S, Si-O in non-ODS materials and in addition to those particles Y-Si-O particles are observed in the ODS samples. Some of those particles and oxidized surfaces are shown in Fig. 5.25 after high temperature tensile tests. The basic characteristics of the high temperature tensile test samples

are quite similar to room temperature tensile tests: even the fracture surfaces of the materials are nearly the same as the room temperature tests if we do not consider oxidation on the surface. Fig. 5.26 is a low magnification image of the fracture surface of the ODS 50 nm sample which is very similar to the room temperature one.

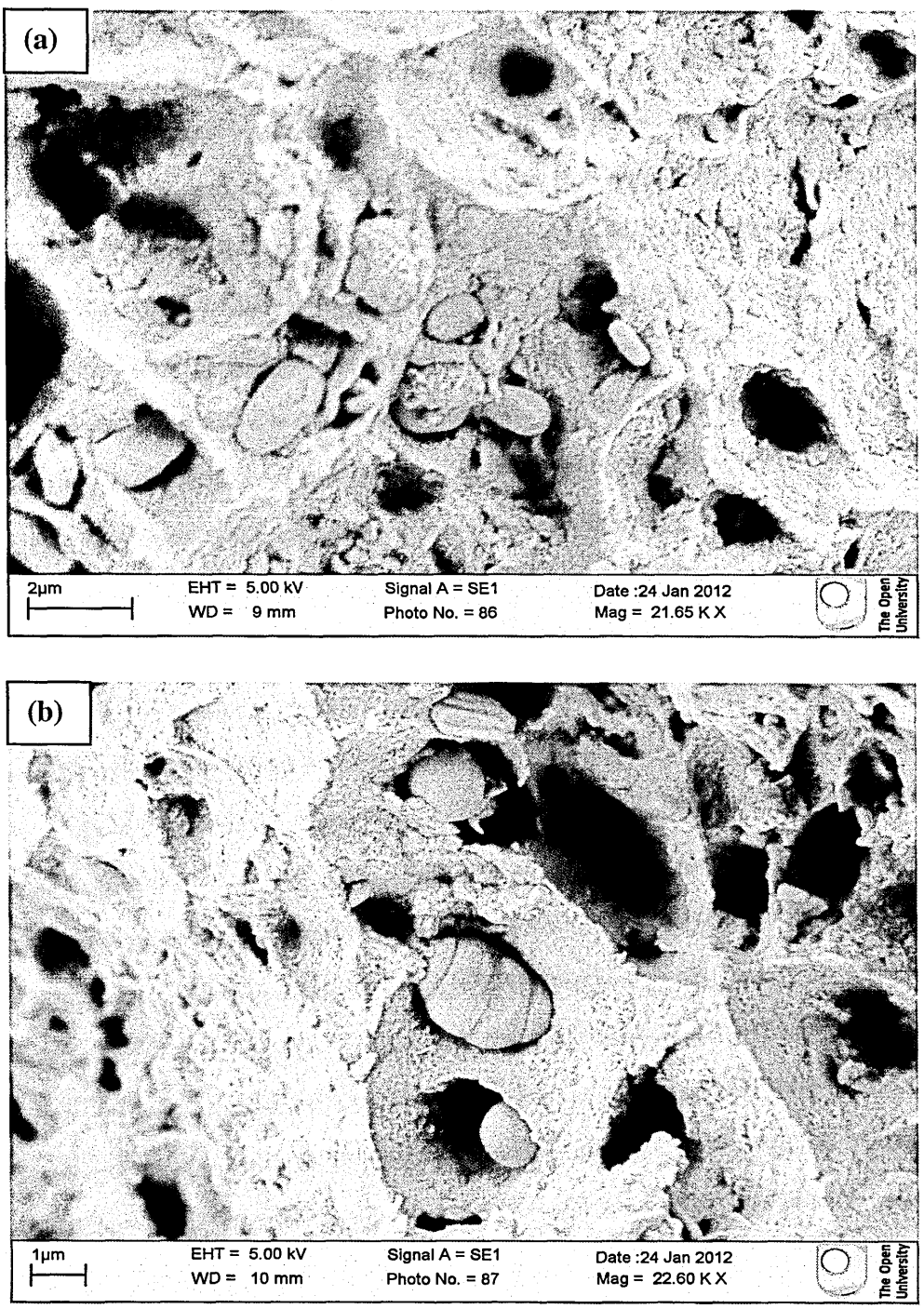

Fig. 5.25 Intermetallic particle on Fracture surface of (a) 410L MA and (b) ODS 0.9 μm after high temperature tensile tests

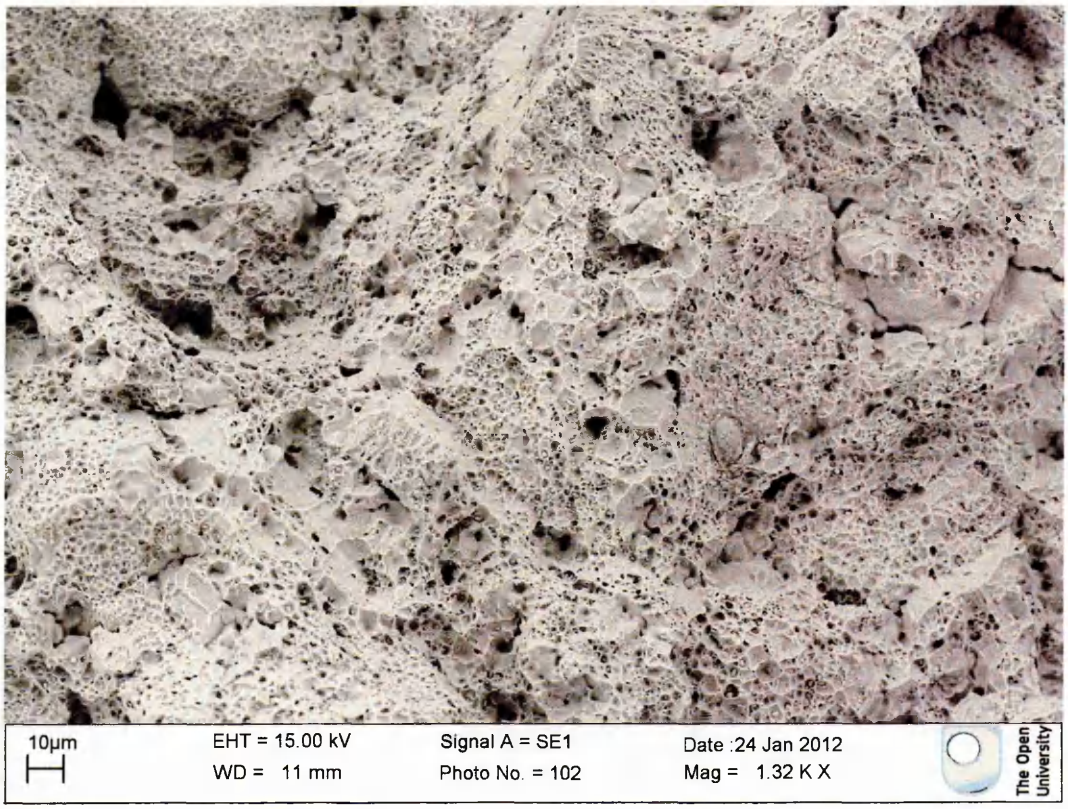

Fig. 5.26 Fracture surface image of ODs 50 nm with low magnification

5.6 Analysis of Creep Tests

All creep samples were analysed with both SEM and optical microscopy. SEM and EDX are used for examining the fracture surface and creep rupture. Optical microscopy is used for viewing creep cracks and voids that occurred during creep test. For optical microscopy analysis the ruptured creep samples were sliced into two longitudinally and these slices were ground and polished but not etched because the un-etched condition is the best condition for pore and crack viewing. Cutting directions and the Bakelite with the mounted piece is shown in Fig. 5.27.

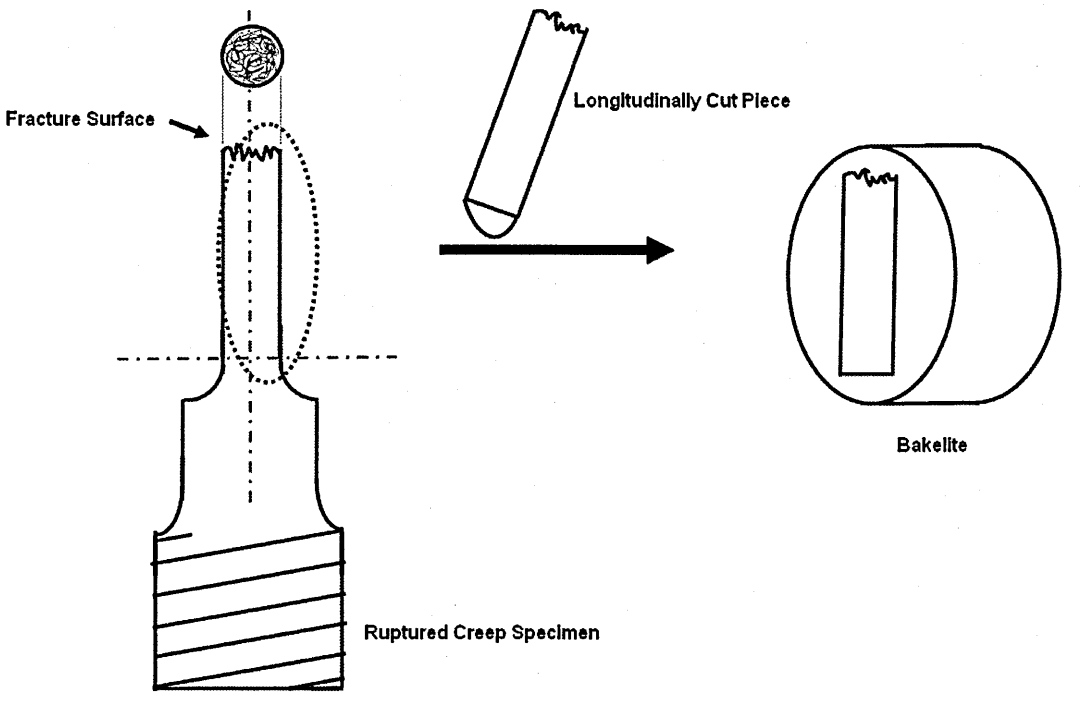

Fig. 5.27 Specimen preparation from creep samples for optical microscopy examinations

Optical microscopy analysis of all samples in each condition (75, 100, 150 MPa at 625 °C) were performed with a Leica DMI4000B automated microscope. Optical images of the samples close to the fracture surface are shown in Fig. 5.28 for 410L HIP, Fig. 5.29 for 410L MA, Fig. 5.30 for ODS 0.9 μm and Fig. 5.31 for ODS 50 nm.

The first thing that can be seen from the figures is that number of cracks and voids is increasing for the samples with longer creep lives. Cracks are mainly parallel to the fracture surface so perpendicular to applied load which is expected and cracks and voids grew along the grain boundaries where the inclusions and oxide particles mainly situated as can be remembered from previous sections.

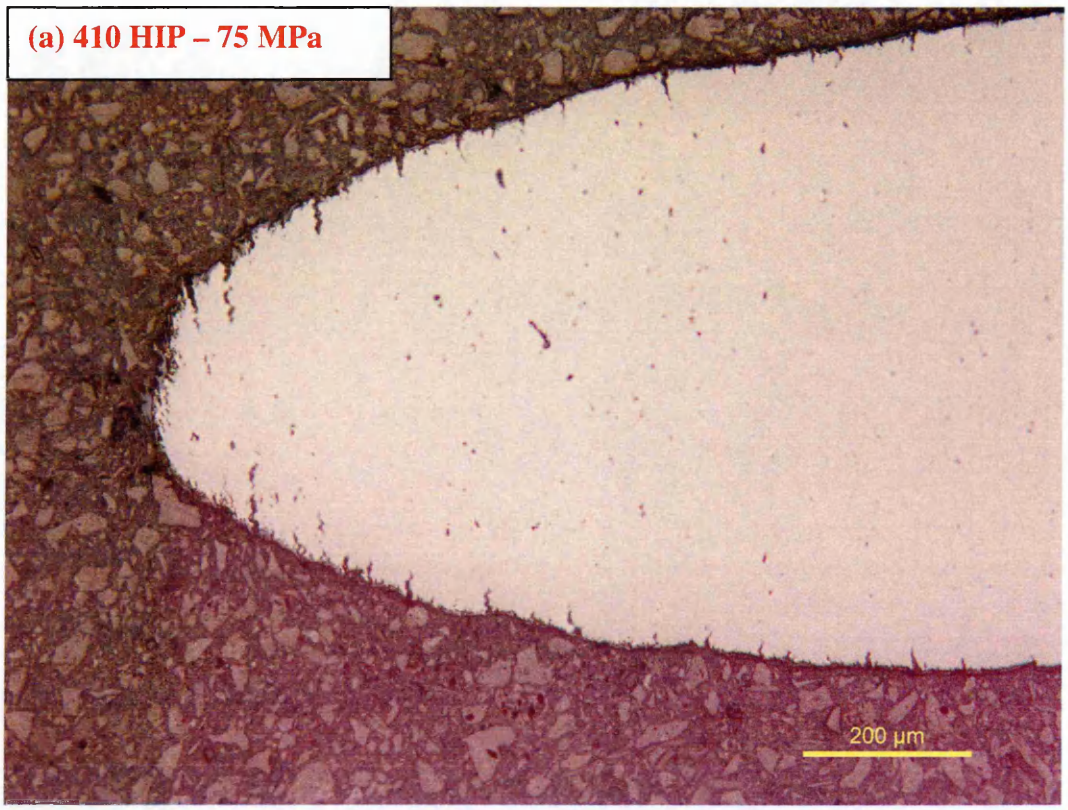
(a) 410 HIP – 75 MPa
200 µm

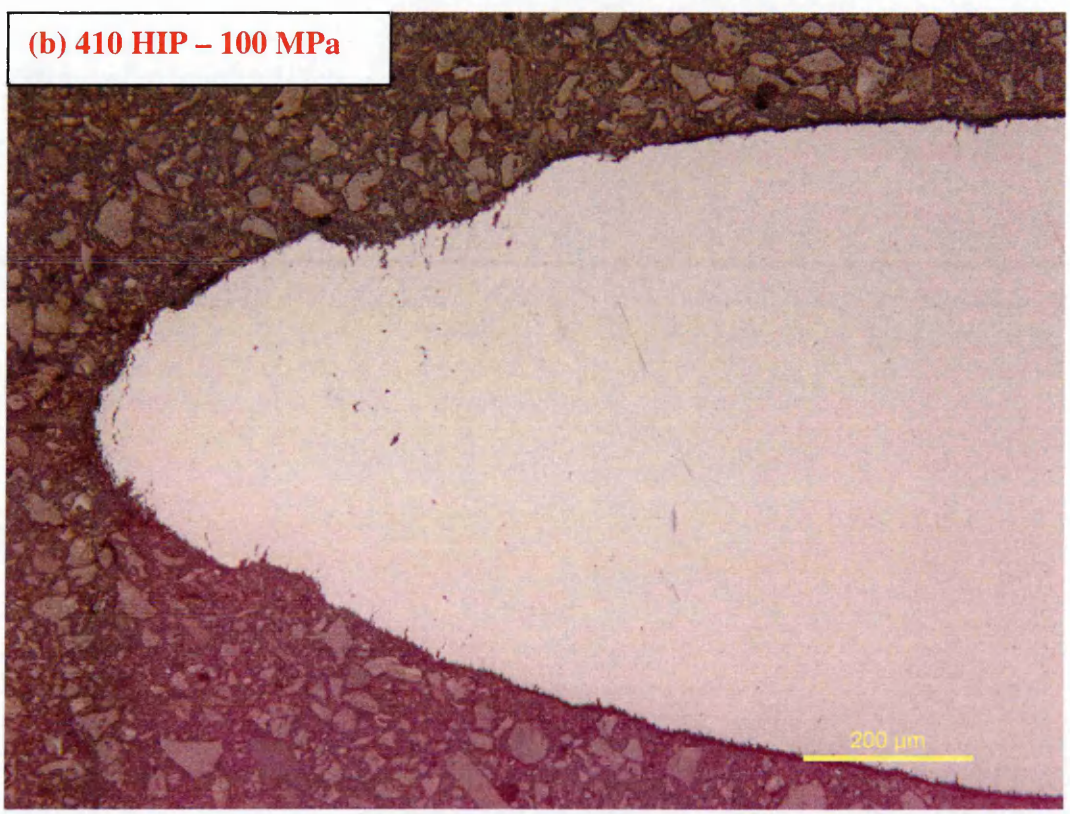
(b) 410 HIP – 100 MPa
200 µm

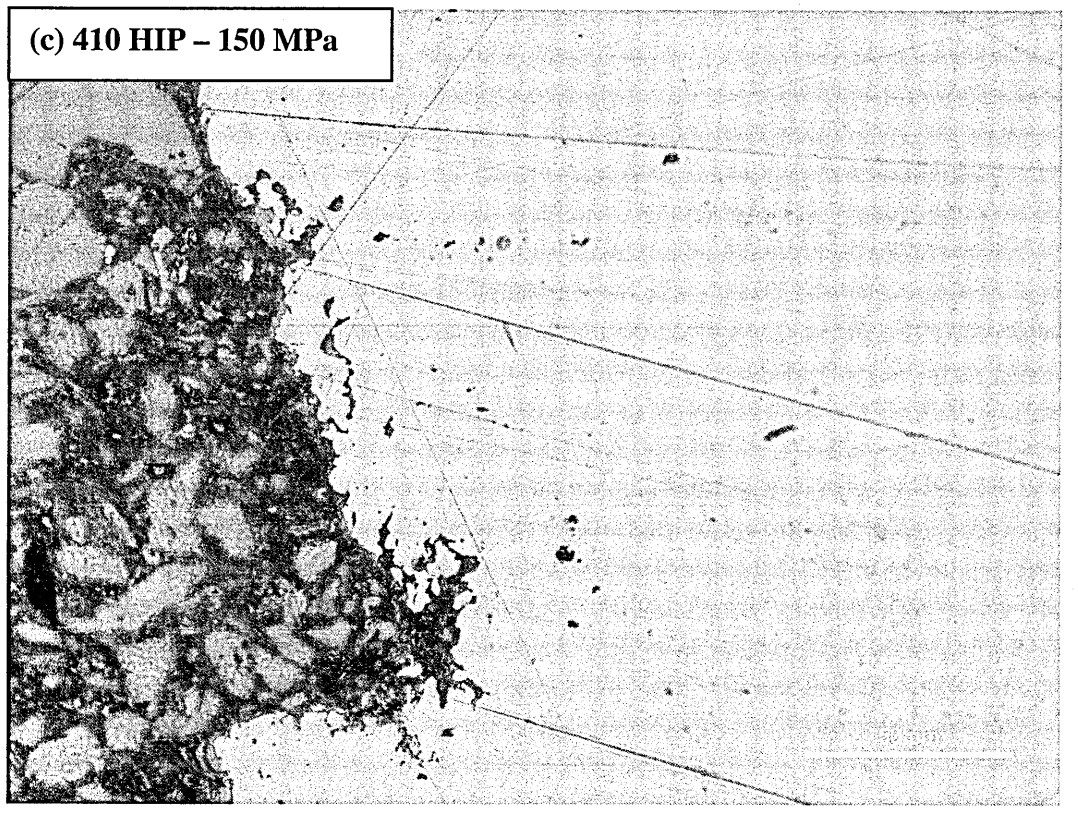

Fig. 5.28 Optical microstructure analysis of 410L HIP mini-creep sample tested at 625 °C with stress of (a) 75 MPa (b) 100 MPa and (c) 150 MPa

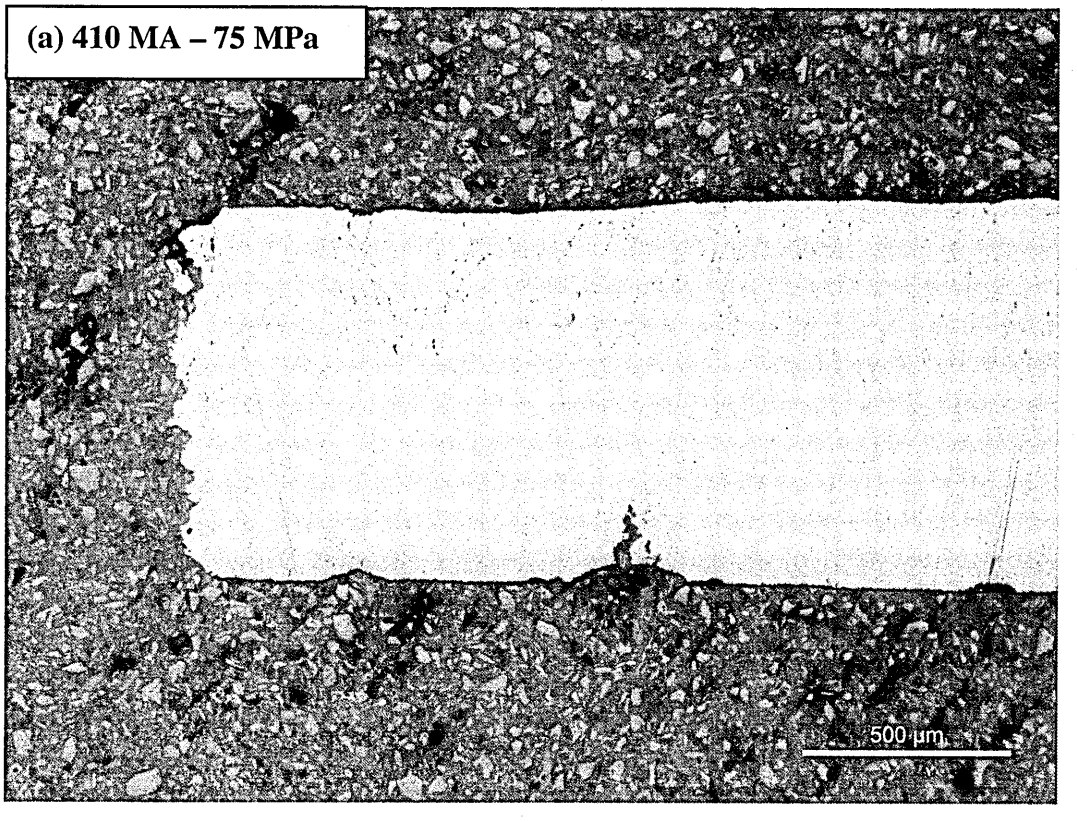

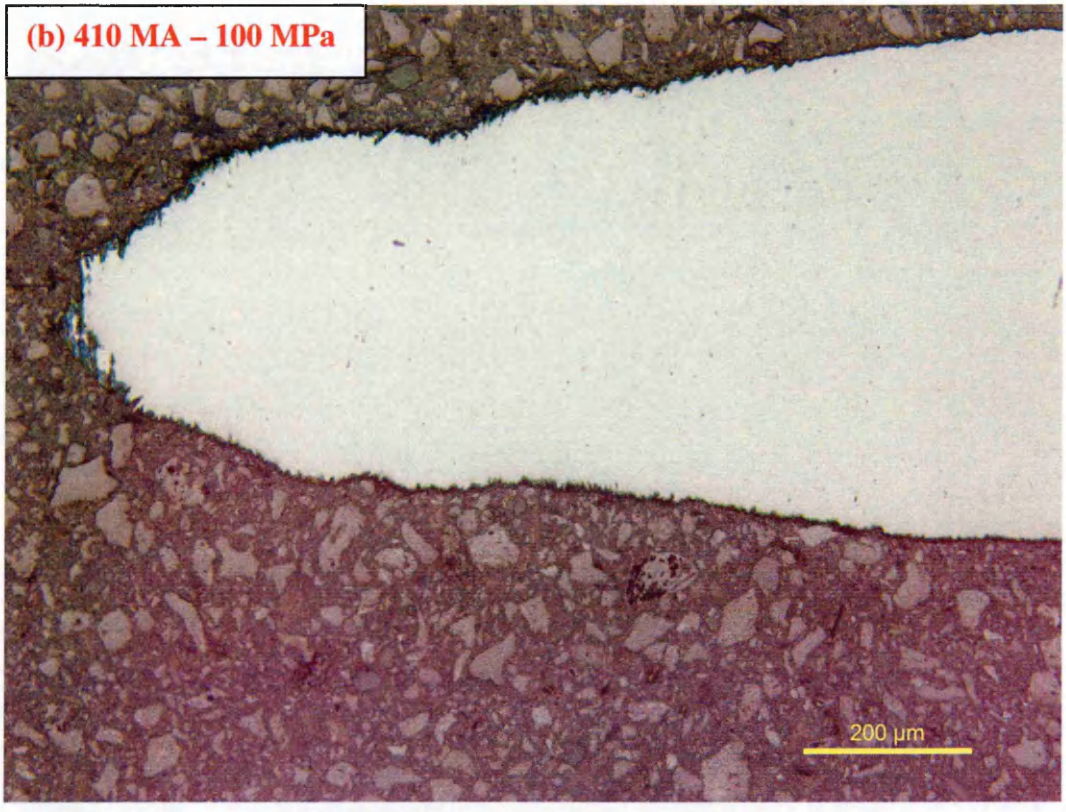

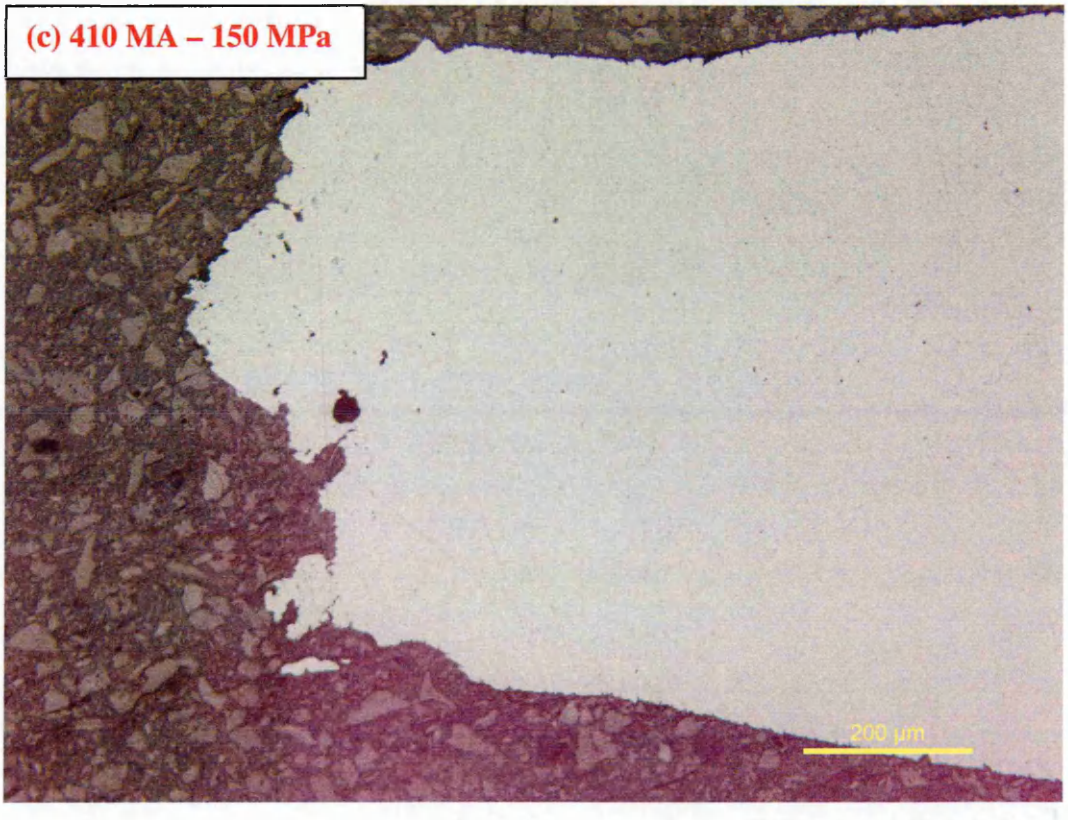

Fig. 5.29 Optical microstructure analysis of 410L MA mini-creep sample tested at 625 ˚C with stress of (a) 75 MPa (b) 100 MPa and (c) 150 MPa

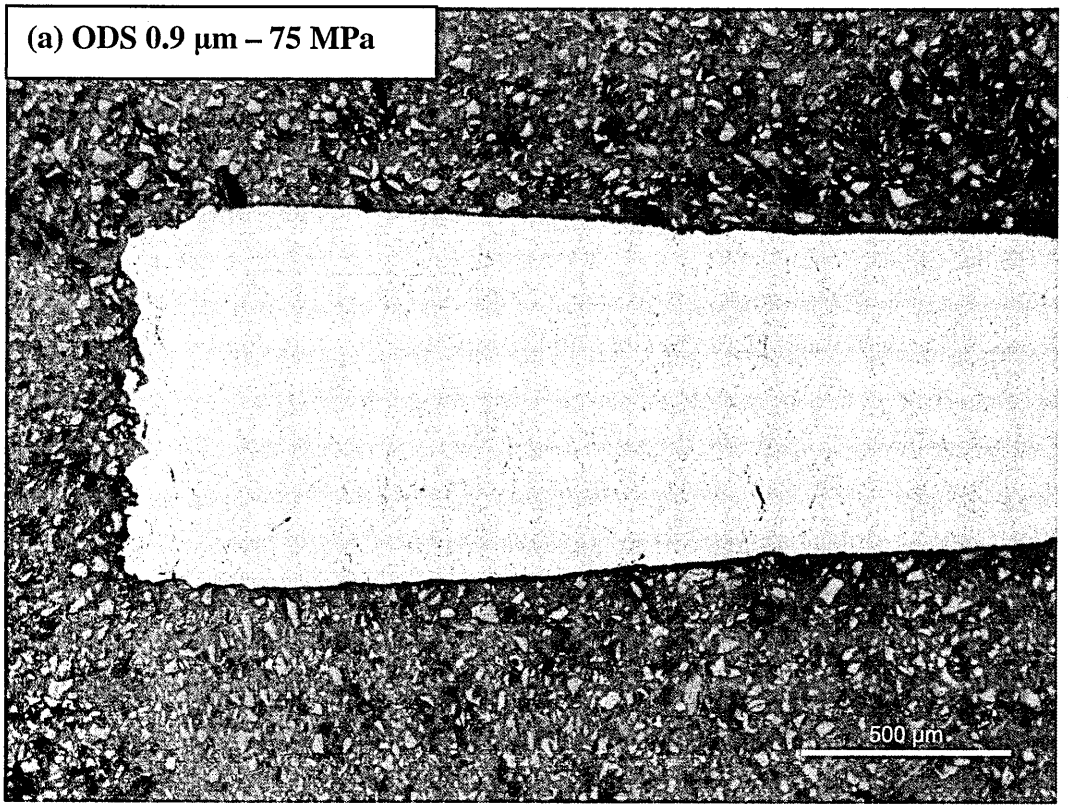
(a) ODS 0.9 µm – 75 MPa
500 µm

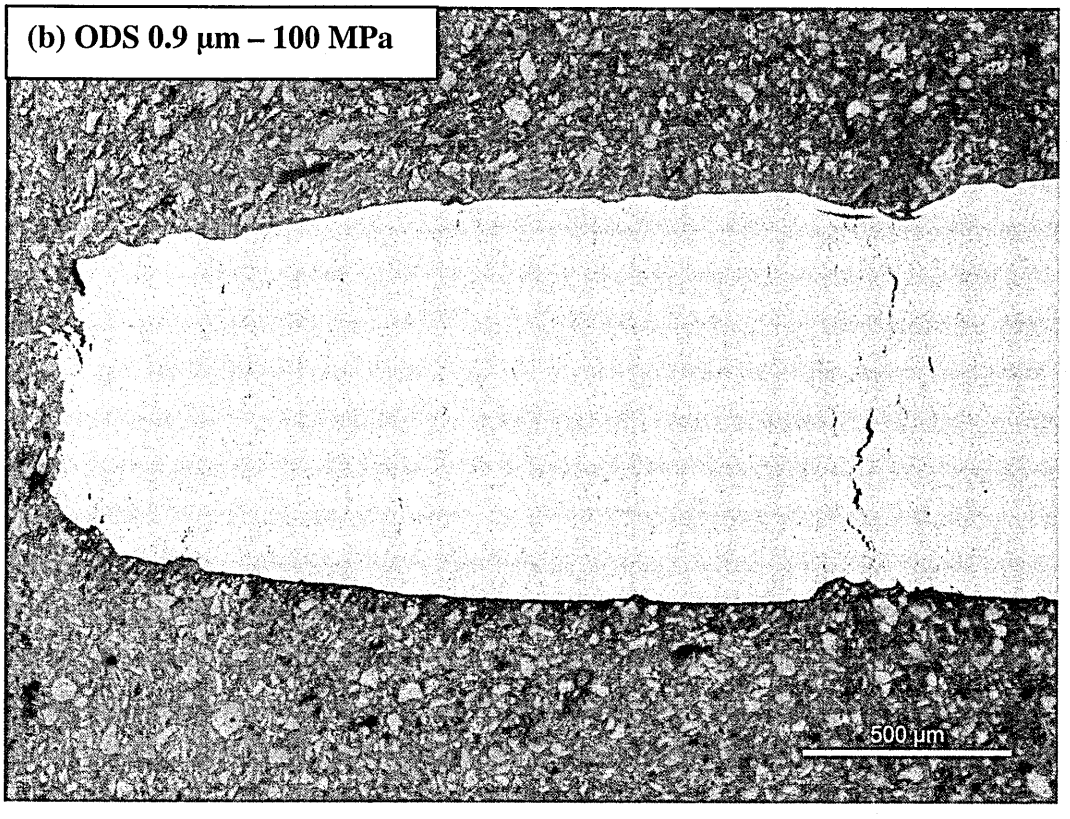
(b) ODS 0.9 µm – 100 MPa
500 µm

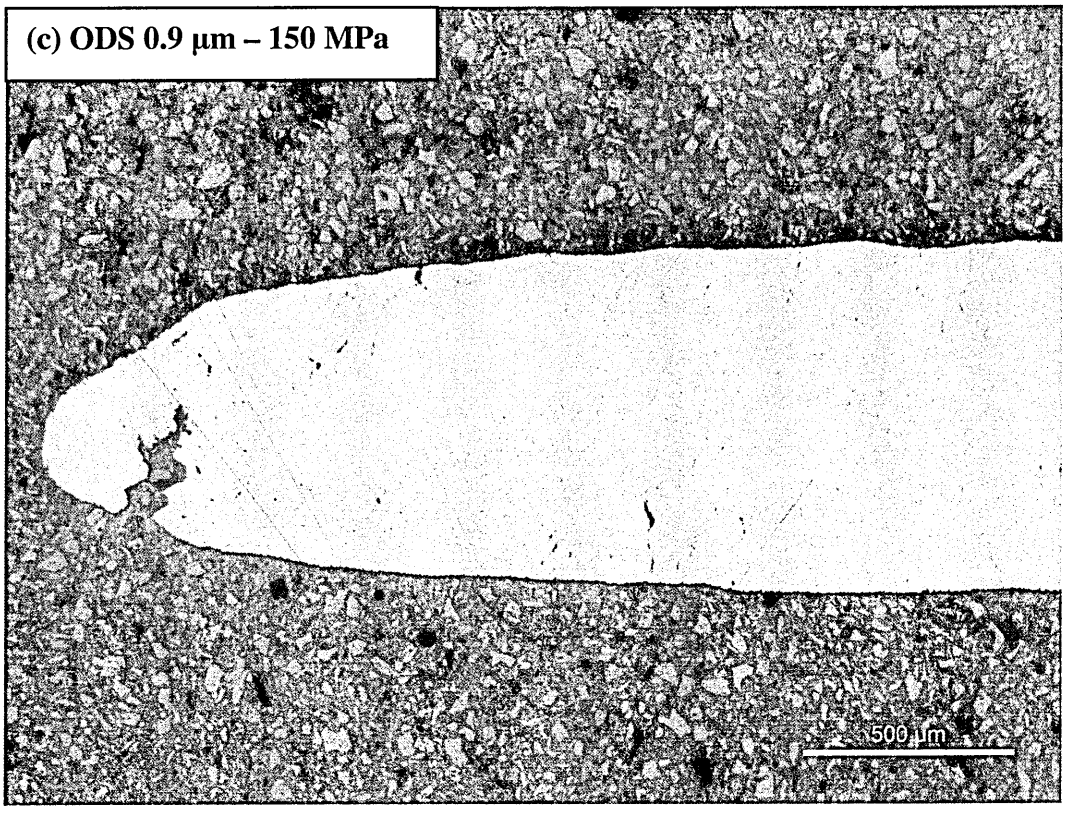

Fig. 5.30 Optical microstructure analysis of ODS 0.9 μm mini-creep sample tested at 625 °C with stress of (a) 75 MPa (b) 100 MPa and (c) 150 MPa

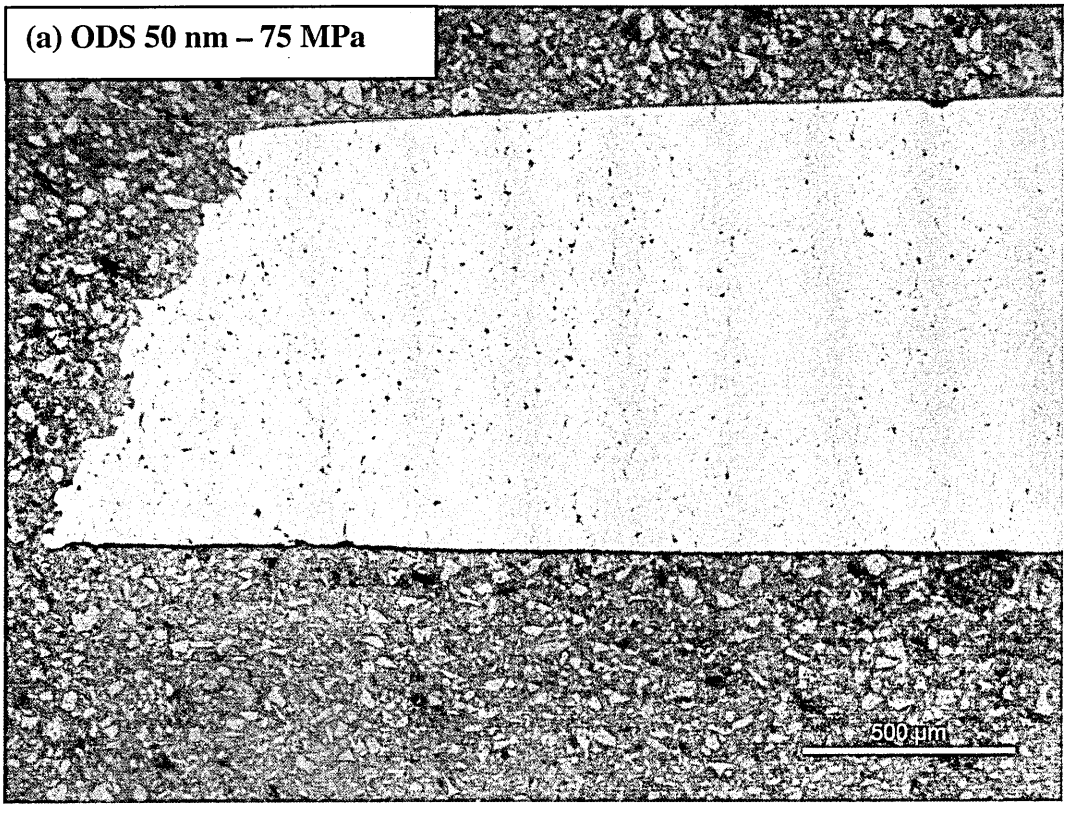

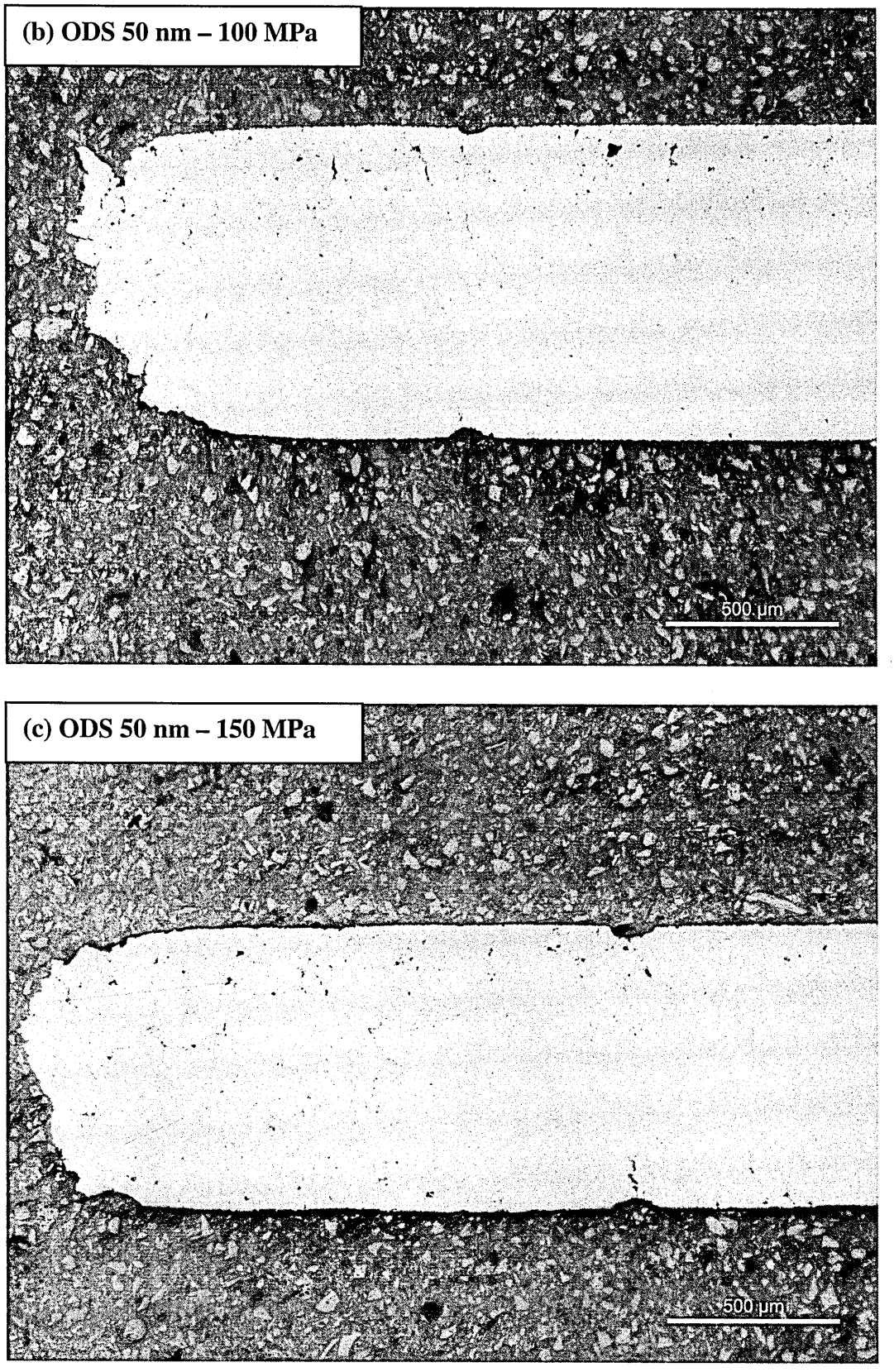

Fig. 5.31 Optical microstructure analysis of ODS 50 nm mini-creep sample tested at 625 °C with stress of (a) 75 MPa (b) 100 MPa and (c) 150 MPa

Propagation of cracks and voids can be seen well in Fig. 5.32. As can be seen from Fig. 5.32 some voids were generated at the sites where inclusion particles and oxide particles were present and those voids grew through neighbour particles so that they followed the route of grain boundaries.

Another important point with this analysis is the images showed that surface roughness has a great effect on crack and void initiation and growth and so on creep life. Surface finish is not ideal in most of the samples due to machining. Fig. 5.33 shows the surface finish and how cracks and voids accumulate around machining marks. Those regions are potential failure regions. In some of them cracks nearly reached through-thickness which would cause rupture.

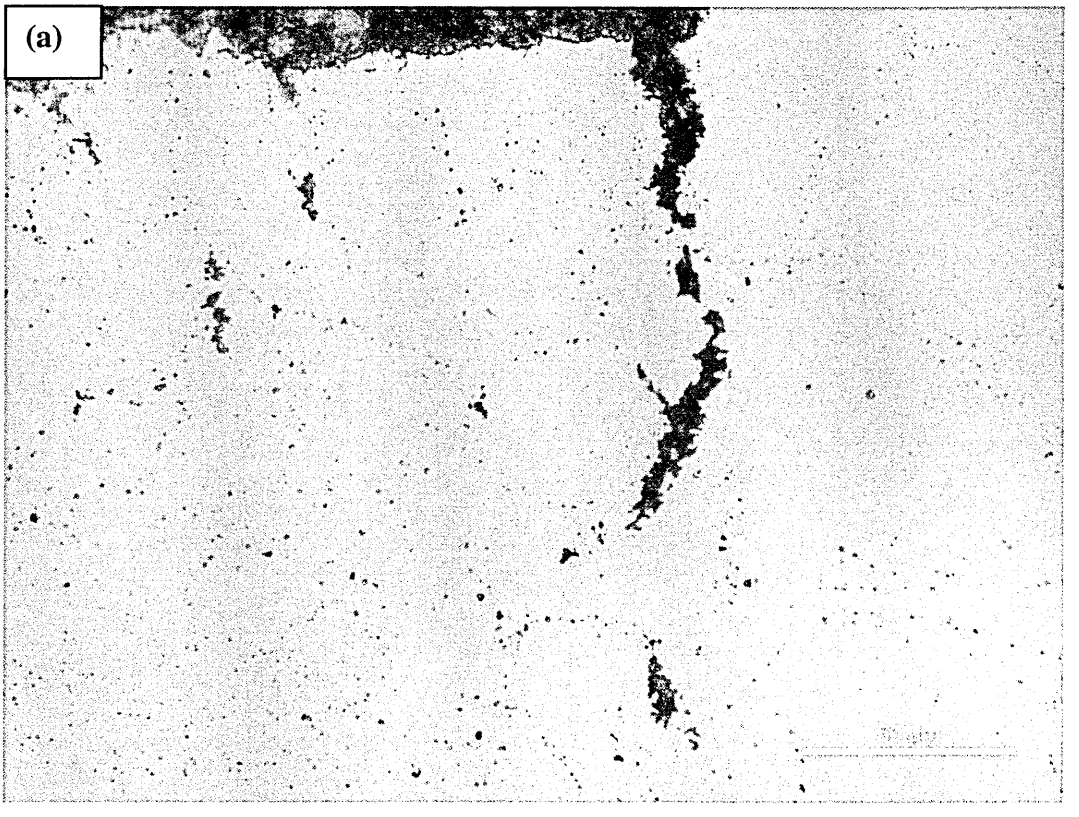

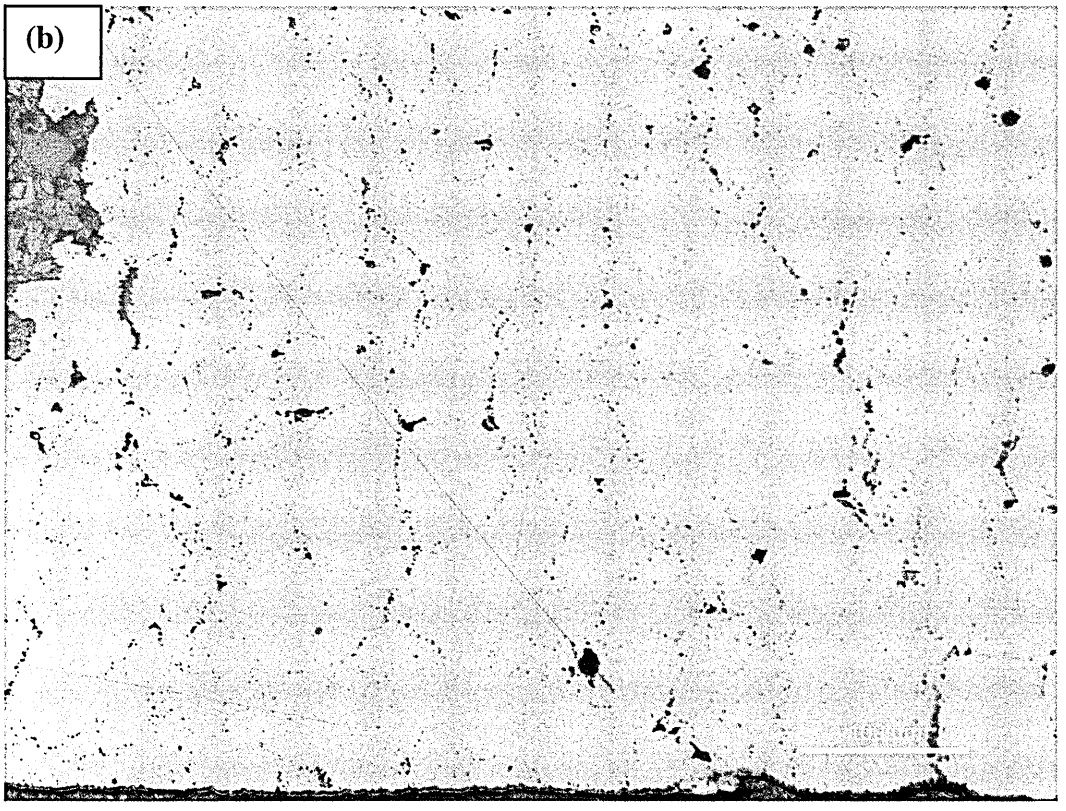

Fig. 5.32 Optical microstructure images of mini-creep samples from (a) 410L MA under 100 MPa and (b) ODS 50 nm under 75 MPa showing propagation of cracks and voids

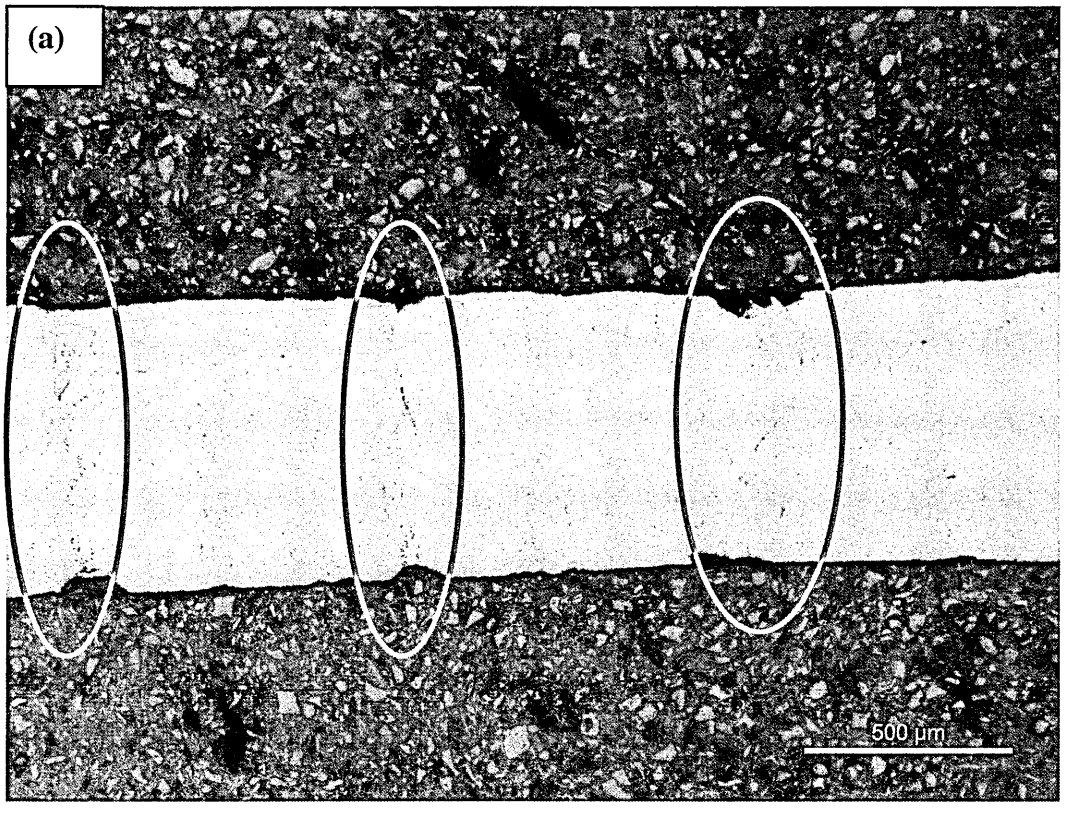

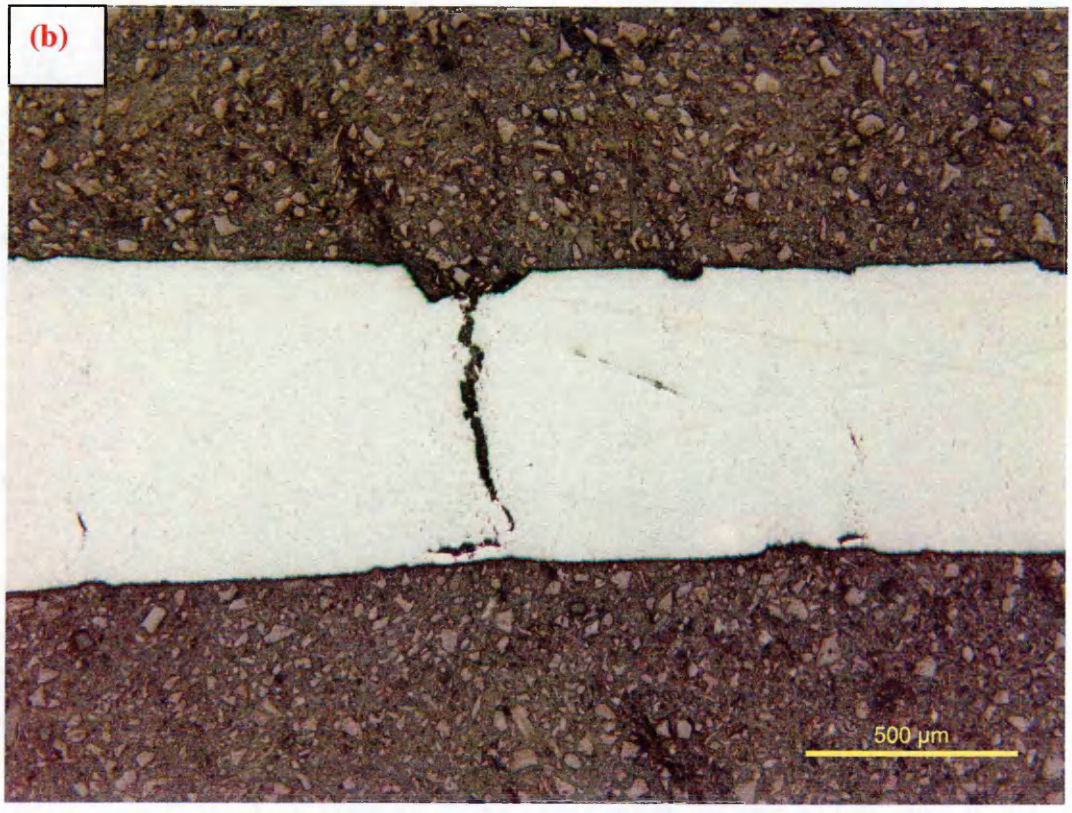
(b)
500 µm

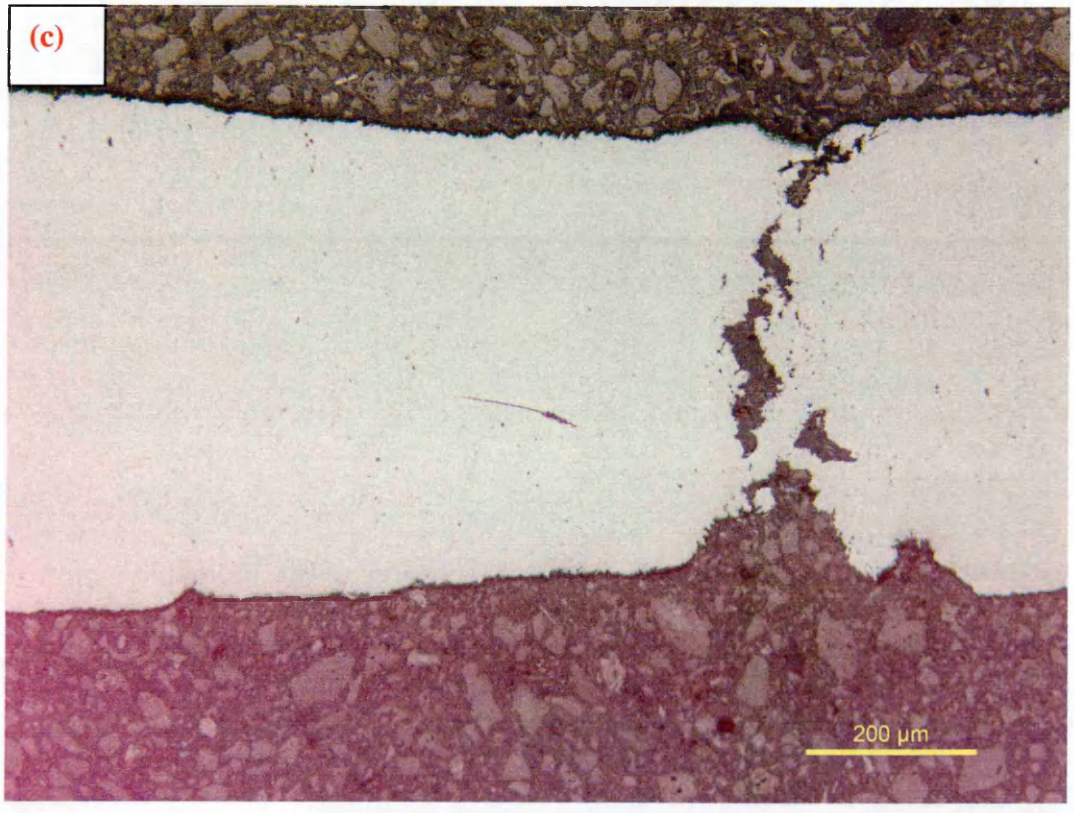
(c)
200 µm

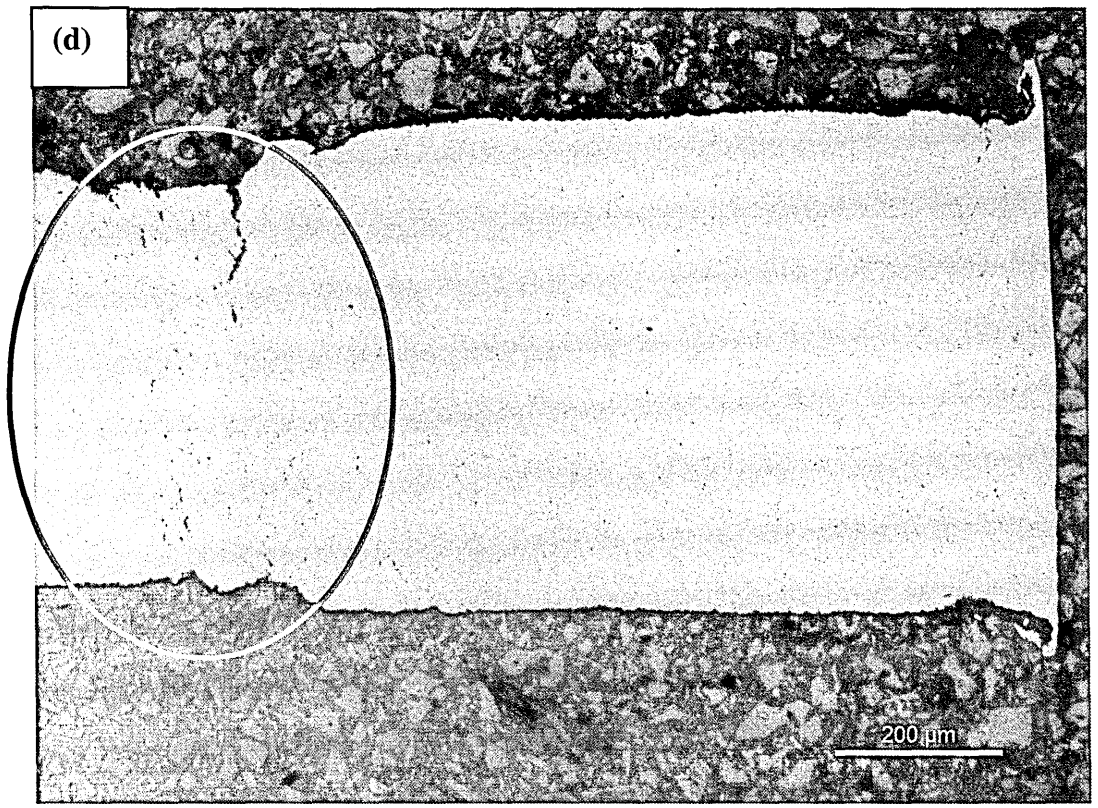

Fig. 5.33 Optical images of mini-creep images showing surface roughness effect and related cracks in (a), (b) ODS 0.9 µm under 75 MPa and (c),(d) 410L MA under 100 MPa

Fracture surfaces of all the mini creep samples were examined under SEM. However the fracture surfaces are highly oxidized so just basic characteristics could be revealed. Features on the fracture surfaces after tests under 150 MPa load are quite similar to the fracture surfaces after high temperature tensile tests. Many dimple structures with inclusions and oxide particles are observed. Fig. 5.34 is showing how the fracture surface looks after 150 MPa test.

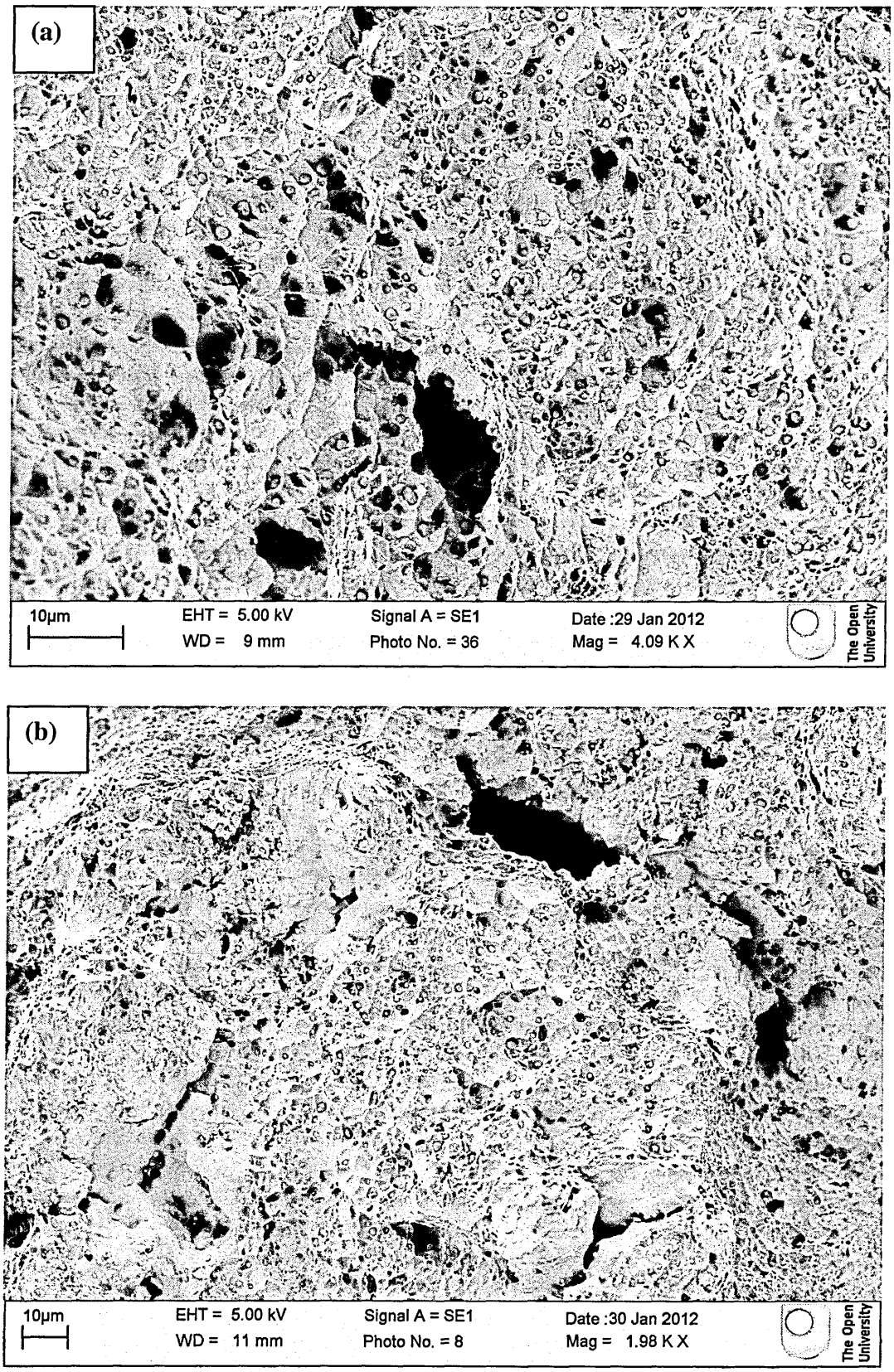

Fig. 5.34 Fracture Surface images of (a) 410L MA and (b) ODS 50 nm after 150 MPa mini creep test

The porosity in ODS 50 nm can be seen after creep tests on the fracture surface in Fig. 5.34 (b). Oxidation on the surface prevents further examination of the samples. Fig. 5.35 shows the amount of oxidation on the fracture surface after 75 MPa test. It can be seen from that some inclusions and oxide particles are not oxidized so that they can be still viewed. A similar fracture surface is observed after 100 MPa test as well with a high amount of oxidation as seen in Fig. 5.36. It is obvious that, as time at high temperature increases, the amount of oxidation also increases.

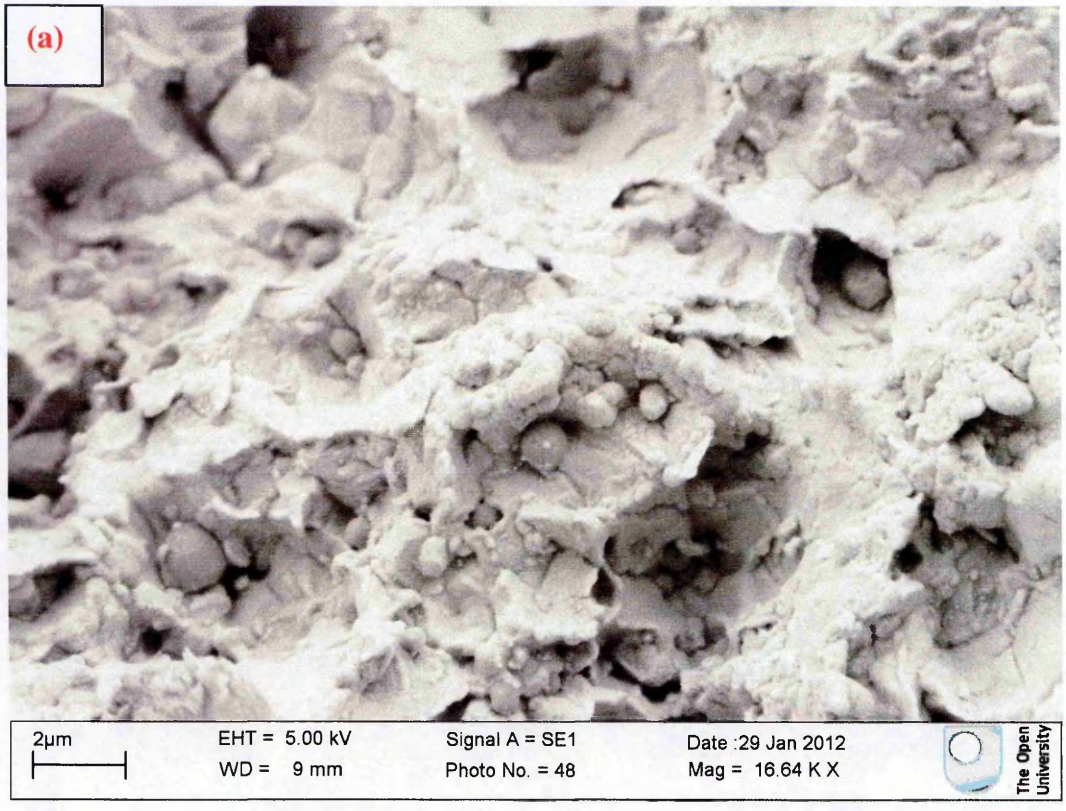

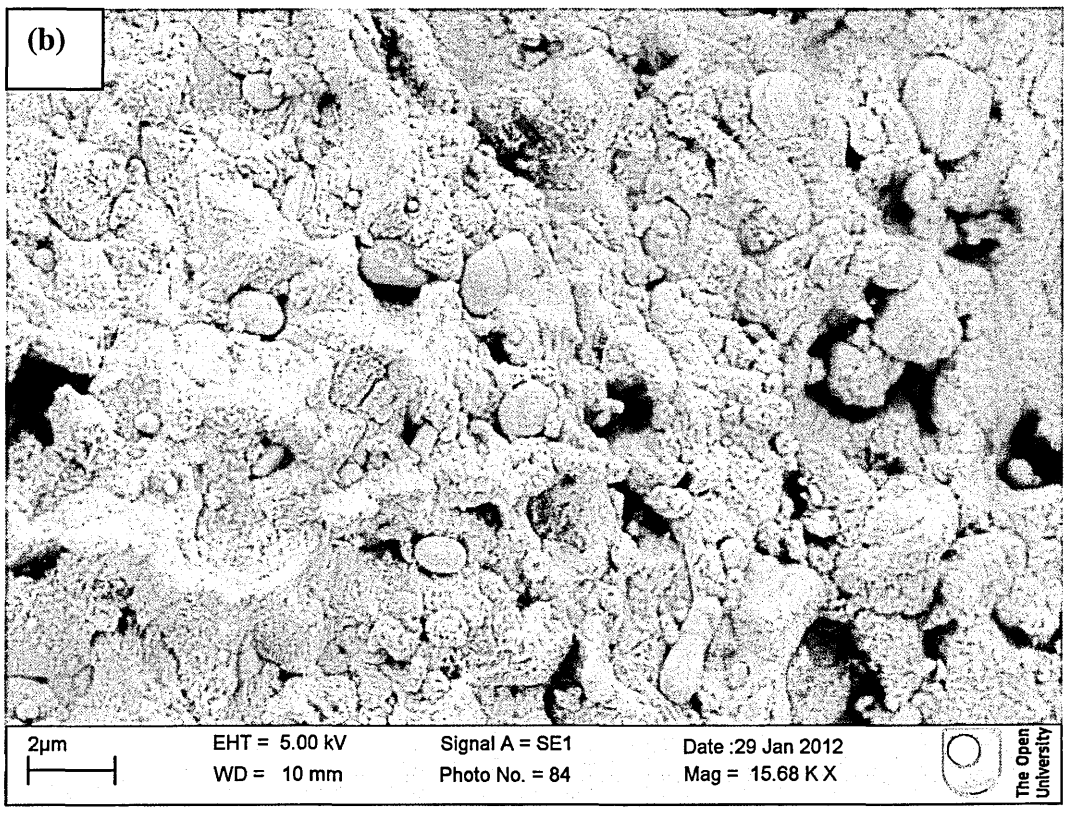

Fig. 5.35 Fracture surface of (a) 410L MA and (b) ODS 0.9 μm after 75 MPa mini-creep test showing oxidized structure

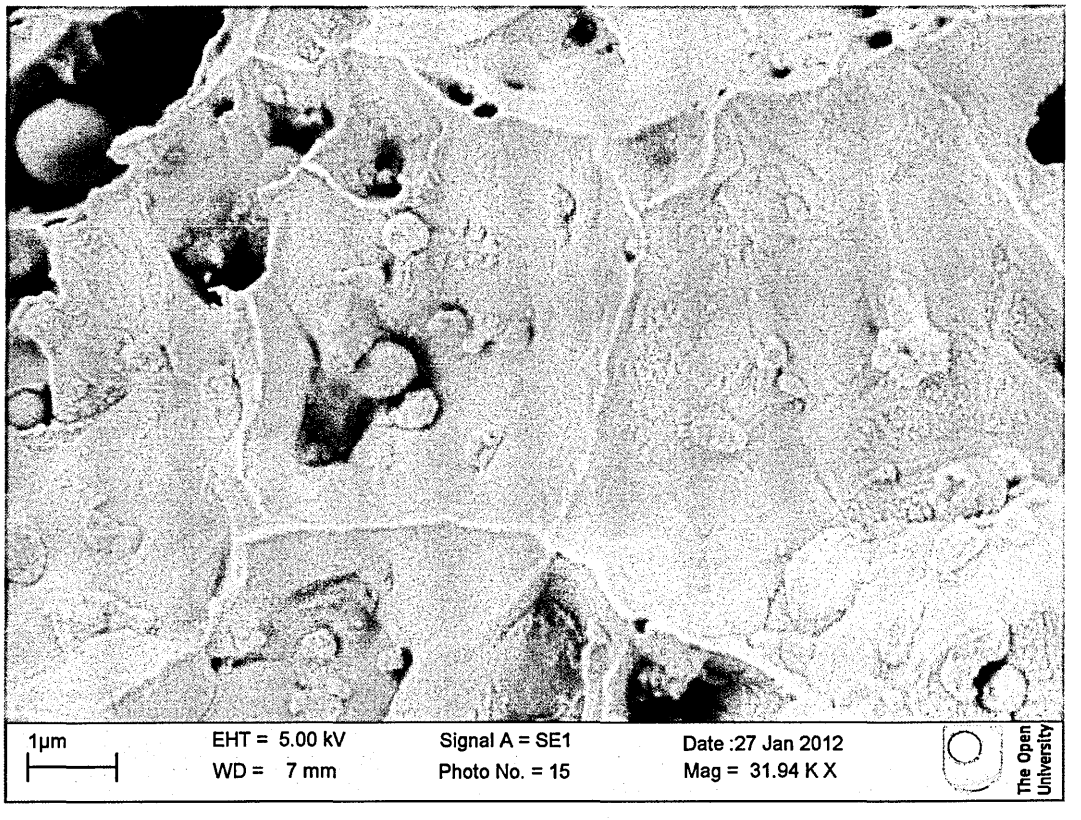

Fig. 5.36 Fracture surface of 410L HIP after 100 MPa mini-creep test

5.7 Summary

Analysis of the yttria powders revealed large powder particles up to 30 μm in size with a composition fairly close to pure yttrium.

Residual ferrites were observed the in as-received conditions of the materials but they are removed with heat treatment.

A TiN inclusion was observed in two of the materials, ODS 50 nm from the first batch and 410L MA from the second batch.

In ODS 0.9 μm from the first batch and ODS 50 nm from the second batch porosity was detected.

SiO_2, MnS and $Y_2Si_2O_7$ inclusion particles are observed with SEM and EDX analysis after mechanical tests. Some particles that are a combination of two or more inclusions are observed.

In high temperature tensile tests and creep tests oxidation is observed. Non-metallic inclusion particles were observed on fracture surfaces.

Surface roughness and its relation with the development of cracks are revealed. The effect of non-metallic inclusions on void nucleation and coalescence is cleared after optical microscopy analysis after mini-creep tests.

CHAPTER 6: DISCUSSION

In this chapter the results of mechanical property and material characterization are discussed in detail. Some problems were identified in the material fabrication and the root cause was identified. Their potential implications on the mechanical and microstructural behaviour are discussed. In addition, possible solutions to the problems are mentioned. In this section the relationship between microstructural constituents and mechanical properties will be developed and understood.

The SEM observations on the atomised, pre-milled 410L powder have shown that the size of the metal powder is quite variable in a range of a few μm up to 120-130 μm. The maximum size of the metal powder was expected to be 106 μm as written by the manufacturer on the delivery sheet (Fig. 5.1). The morphology of the alloyed powder allows clear observation of the spherical shape of the particles. Spherical powder particles are usually achieved after gas atomisation so it can be assumed that the atomisation type was gas atomisation [1]. It is also possible to identify large metal powder particles. These particles have many small 'satellites' stuck around them. They are like small bumps not separate particles. Those features are expected to be eliminated for good packing and flow attributes [2]. EDX analysis showed that the composition of the metal powder is as expected and matches the theoretical values.

Powder yttria observations under SEM revealed that there are some particles around 30 μm in size which is not desired because the sizes of the yttria

powders are expected to be 0.9 μm and 50 nm (Fig. 5.2 and 5.3). Compositional EDX results from those big particles were not matching with yttria composition. They showed a very high amount of yttrium, more than 90 wt. % in the composition which suggests some pure yttrium may be mixed into the powders. During the ball milling stage when the metal powders and yttria powders are mixed those big particles have very high chance to interact with other particles in the system due to their large contact area, and may cause some inclusion particles and oxide particles to form, like Si-O-Y particles. Those inclusions can form from small yttria particles as well, however large particles ease the process, because the larger the specific surface area of the powder, the easier it will react with environment [3].These inclusions and oxide particles are discussed in more detail later in this chapter.

Metallographic examinations before mechanical testing revealed the need for heat treatment. Residual ferrites at the grain boundaries were revealed by NaOH + water electrolytic etchant. Those residual ferrites occur due to the cooling rate after hot isostatic processing (HIP). HIP took place at around 1120 °C where 410L was fully austenitized as can be seen from Fig. 6.1 [4].

410L is a martensitic stainless steel [5]. The cooling after the HIP process was not fast enough to make the microstructure fully martensitic. Inside the grains the microstructure is martensitic but along the grain boundaries residual ferrites were formed. Ferrite is softer than martensite which is the hardest phase for steels [6]. Since grain boundaries have major detrimental role in fracture, a weaker phase

in these regions is not desirable as this will promote the nucleation of defects. Thus, heat treatment was necessary to remove the residual ferrites.

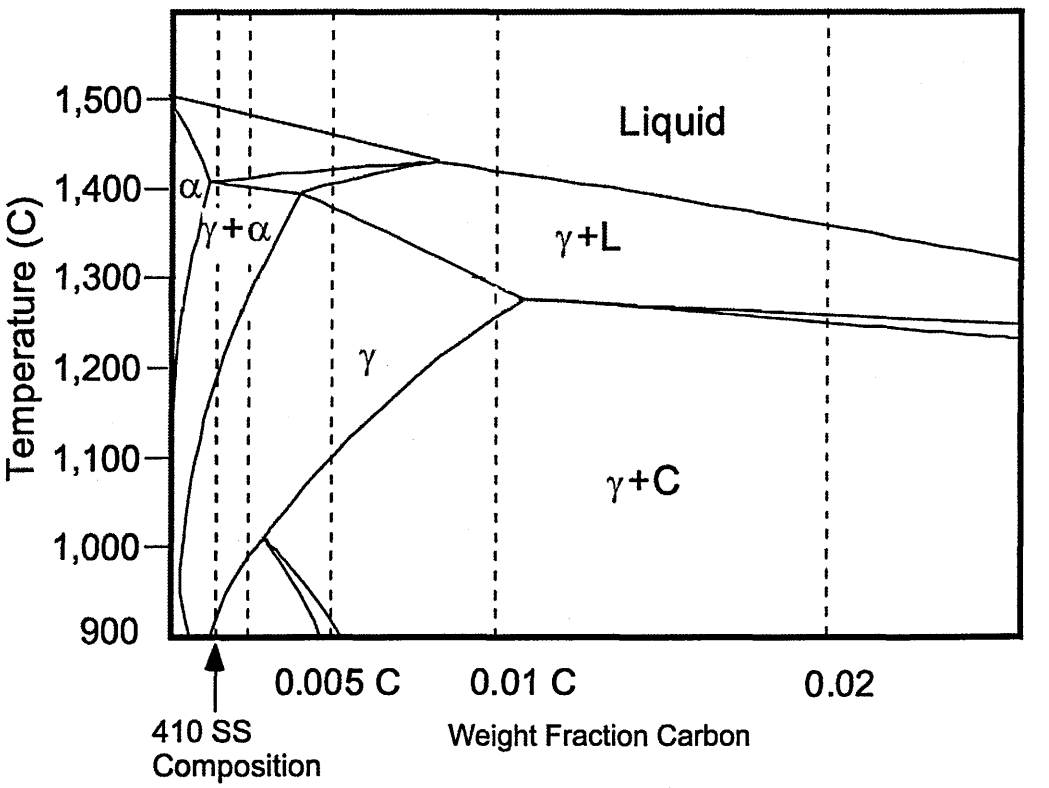

Fig. 6.1 Phase diagram of 410 stainless steel showing the austenite is the phase at the HIP temperature [4]

In addition to residual ferrite, having a standard microstructure for all of the samples is very important to make a good comparison and/or to see the effect of a constituent like the oxide particles, so all of the materials were subjected to the same heat treatment process. The heat treatment was austenitizing at 1000 °C for 30 mins followed by oil quenching to achieve a fully martensitic microstructure, then tempering at 650 °C for 2 hrs followed by furnace cooling. Heat treatment parameters are matching with data sheets of 410L steel [7].The heat treatment was performed under ambient atmosphere. At the end of the heat treatment a

tempered martensitic microstructure is achieved without any residual ferrite regions along the grain boundaries as can be seen from Fig. 5.10.

With this heat treatment process some ductility is also introduced to the samples as the microstructure is changed to tempered martensite. Martensite partially transforms into ferrite and cementite during tempering and entrapped carbon diffuses out. In addition some internal stress relaxation occurs as well. From Table 4.1, it can be seen how the ductility of samples are changed after heat treatment process by room temperature tensile tests.

Results of room temperature tensile tests are tabulated in Fig. 4.1. Yield strength values are around 670 - 690 MPa and ultimate tensile strength (UTS) values are around 815 – 860 MPa. The conventionally produced, cast and machined, steel presents yield and ultimate strengths of about 589 and 767 MPa respectively which is lower than the powder metallurgy produced materials in this project [7]. Mechanical values of the samples are very close to each other: ODS samples and non-ODS samples have similar yield strength and UTS values. The addition of Y_2O_3 did not impact on the strength of the material at room temperature. There is a slight improvement but not significant. This may be because the non-ODS materials have particles similar to the oxide particles in the ODS ones which act as obstacles to hinder dislocation motion to improve mechanical properties which is the main criteria of strengthening by dispersion of particles [8]. The amount of yttria in the ODS samples of this project is very low at 0.25 wt. %. Although the amount is very limited, however the effect of those oxide particles to the mechanical properties (yield and ultimate tensile strength) of the

ODS samples is significant around in some other ODS alternatives from literature like in Eurofer ODS which has an increase from 634 MPa to 884 MPa for yield strength and increase from 785 MPa to 1015 MPa for UTS [9]. Ductility values agrees with theory as mechanical alloying reduces the ductility [9]._Ball milling reduces the ductility because during ball milling the material is deformed plastically and dislocations are introduced into the system in other words it gets work hardened. But elongation or ductility of a material which is work hardened is decreased because ductility is related to plastic deformability [10]. It is actually the limit of plastic deformation before fracture occurs. If the material is deformed up to some level previously such as during ball milling, later deformations will cause fracture in shorter time. However this deformation effect of milling can be eliminated by HIPing process as it can be annealed out due to very high temperatures above 1000 °C. Main point of reduced ductility during milling can be attributed to contamination. Gas entrapments and contamination from milling eqipments have detrimental effects as they can cause porsity and inclusions in the material [11, 12].

When results of the room temperature tensile tests are compared with other ODS steels, the performance of 410L ODS steels from this project is far below the properties of some other ODS alternatives. For example 14YWT, composition of 14 Cr, 3 W and 0.4 Ti + 0.3 Y_2O_3 (wt. %), has mechanical properties of 1600 MPa and 1749 MPa for yield strength (YS) and ultimate tensile strength (UTS) respectively [13]. 12YWT with 12 Cr, 2.5 W, 0.4 Ti + 0.25 Y_2O_3 (wt. %) has 1300 MPa and 1400 MPa for YS and UTS respectively [14]. ODS Eurofer 97 without secondary processing after heat treating at 750 °C for 2 hrs with composition of 8.9

Cr, 1.1 W, 0.2 V, 0.14 Ta, 0.42 Mn, 0.10 C + 0.3 Y_2O_3 (wt. %) has 966 MPa and 1085 MPa for YS and UTS respectively [15, 16]. The reason of this difference in mechanical properties can be firstly secondary processings after manufacturing the materials like extrusion, rolling etc, because these secondary processings work harden the materials [8]. 14YWT and 12YWT were not subjected to heat treatment processes after secondary processing and that may be another reason that they have very high mechanical properties like the materials we have in as-received condition shown in Table 4.1. The second reason can be compositional differences as each material has a different composition. Alloying elements can change mechanical properties as each element may have a different effect on mechanical properties: Cr is good for corrosion and C is good for hardening [17]. Finally the negative effect of inclusion particles in our materials on crack initiation and propagation under applied load can cause this difference in performance compared to various ODS alternatives. It is not reported the other ODS materials have inclusions in their microstructures, the particles mentioned are pure precipitated oxide particles either Y_2O_3 and/or Y-Ti-O complex oxides.

From Table 4.1 it is clearly seen that there is a problem with the ODS 0.9 μm sample which has yield strength and UTS values of 360 MPa and 530 MPa respectively in the as-received condition whereas other materials have more than double the mechanical properties. From Fig. 5.14 it can be seen that the fracture surface of the ODS 0.9 μm sample is very rough whilts the ODS 50 nm has a very flat fracture surface as expected for a material with low ductility [18]. Extensive investigation was carried out on the ODS 0.9 μm material to understand the fracture surface roughness problem in more detail. SEM images showed in Fig.

5.15 that there is an obvious densification problem. This porosity explains the weaker mechanical properties in the material [19]. The fracture surface of the ODS 0.9 μm sample looks like an accumulation of small particles with voids between them. Separation of the matrix can also be seen from the images in Fig. 5.17. This porosity issue is a result of argon gas entrapment during the manufacturing processes most probably during the hot isostatic pressing stage as indicated by the manufacturer [12]. It can be the result of argon ingress to the system from the isostatic press. Argon is used in the facility to move the press in HIP. It is clear that separation was along the intermetallic particles and porous regions are left undistorted with some intermetallic particles sitting on the surface. How fracture propagates along the particles will be explained later in this chapter.

After room temperature tensile tests all of the samples' fracture surfaces are examined first at the macro scale, and gold coloured inclusions were detected on some of the materials' fracture surfaces. After SEM and EDX analysis the inclusions were determined to be titanium nitride (TiN). TiN is detected in only 410L MA sample from the second batch sample and ODS 50 nm sample from the first batch. This TiN inclusion can be contamination from the original metal powder or other processes up to billet condition because it is mentioned by the manufacturer that equipment used for producing ODS materials had never handled TiN. However mechanical properties of the materials that include TiN are still quite comparable with other materials. Yield strengths are 690 MPa and 677 MPa and UTS are 845 MPa and 842 MPa for ODS 50 nm from the first batch and 410L MA from the second batch respectively. These strength values are very comparable with other materials without TiN as can be seen from Table 4.1. So it

can be concluded that TiN did not have a significant effect on mechanical properties.

All samples' fracture surfaces were examined under SEM for better understanding about the failure mechanism after room temperature tensile tests. Main conclusion after these analyses was the observation of inclusion particles and oxide particles on the fracture surface. These particles can be seen also from optical microscopy, in Fig. 5.19. High magnification images of metallography samples show those particles clearly under SEM in Fig. 5.22. The sizes of the particles are quite variable and can go up to 2 μm. EDX analysis showed that these inclusions are rich in silicon-oxygen and manganese-sulphur in non-ODS materials and in ODS materials in addition to those particles some silicon-oxygen-yttrium particles were detected. Some of the particles were a combination of two or more different particles as can be seen in Fig. 5.19.

The reason of seeing association of Si and O is due to the fact that silicon is the most common de-oxidizing agent [20]. Oxygen is considered as an undesirable element due to reducing mechanical properties by formingoxides and inclusions [21]. So SiO_2 particles are formed due to interaction of Si and O. Mn-S particles are formed on a similar theory, manganese is a good de-sulphurizer, it is employed in alloying to form the stable MnS phase so that it eliminates formation of hot-shortness or sulphur embrittlement which reduces mechanical properties. In ODS samples due to the interaction of silicon to oxygen of the yttria (Y_2O_3) particles, we observed Y, Si and O atoms clusters as a particle formation involving on one side a Si-O part and Y-Si-O on the other side of a particle cluster which can be seen in

Fig. 5.21. These particles with Y-Si-O elements are formed to be $Y_2Si_2O_7$ by EDX which is encountered in some other ODS projects also [22]. Fig. 5.20 (d) shows some EDX data taken from the fracture surface of a ODS 0.9 μm sample after room temperature tensile tests. These EDX results show that the atom percentages of Y, Si and O are satisfying the condition of $Y_2Si_2O_7$ as 1 atom for each Y and Si and 3.5 atoms for O, it proves the composition of these particles. Similar atomic calculations show that the other particles are SiO_2 and MnS particles.

These SiO_2 and MnS particles are inclusions in liquid state of matrix material. 410L was already in alloyed form before starting powder metallurgy process because pre-alloyed powder (steel + atomisation) is used instead of elemental powder (putting each element in the composition separately in the milling stage). Formations of these particles started during liquid stage of the steel fabrication as a result of super saturation of the solution with the solutes due to dissolution of additives (de-oxidation and de-sulphurization reagents) [23]. So this would suggest that these particles were in the system before the ball milling stage. These inclusions were observed in 410L just HIPed material (no mechanical alloying) as well which is another point that shows the inclusions occurred before milling. However the interaction of Si-O-Y was started during the milling stage, because mechanical alloying is the first step where yttria is added to the system. These facts can be used to infer that a nucleation and growth process occurred. These particles of SiO_2 and MnS nucleated very close to each other to minimize energy as in heterogeneous nucleation (Fig. 5.20 (a) & (b)). After that probable phenomena were as follows: during milling some SiO_2 particles interacted with yttria particles due to the high energy of the milling process and formed a new

composition which is $Y_2Si_2O_7$ (Fig. 5.21). And during high temperature HIP process those particles or clusters joined and grew together forming a minimum energy shape, most of the time spherical. These clusters' size could also have been enhanced by the heat treatment.

There is an important point about the Y-Si-O interaction and formation of $Y_2Si_2O_7$ particles. It is quite common that yttria particles dissolve in the matrix during ball milling and precipitate again as pure yttria in the system due to high temperature later in the manufacturing process which is the main mechanism to disperse the matrix with oxide particles to make oxide dispersion strengthened alloys [24, 25]. This dissolution and precipitation is needed for a homogeneous microstructure and size control of oxide dispersions in the nanometre range [26]. If yttria dissolved in the matrix and then precipitated, then there should be separate particles with composition Y_2O_3 or complex oxides such as $Y_2Ti_2O_7$ if Ti was added to the system [27, 28]. In our case the yttria detected under SEM and EDX analysis are all in $Y_2Si_2O_7$ condition. However, small angle neutron scattering (SANS) experiment results showed that there are pure Y_2O_3 oxide particles as well in the system in nanometer level which is hard to detect under SEM due to poor resolution in very high magnification. SANS results of ODS 50 nm material from the second batch are shown in Fig. 6.2. The size of the Y_2O_3 particles in the as-received condition was measured as 33 nm. So, in the system there is pure Y_2O_3 and $Y_2Si_2O_7$ particles together. Based on the available information and observations, three possible scenarios are proposed for our ODS alloys. First, the yttria did not fully dissolve in the system during milling and some of the powders interacted with SiO_2 particles during high energy ball milling and formed $Y_2Si_2O_7$

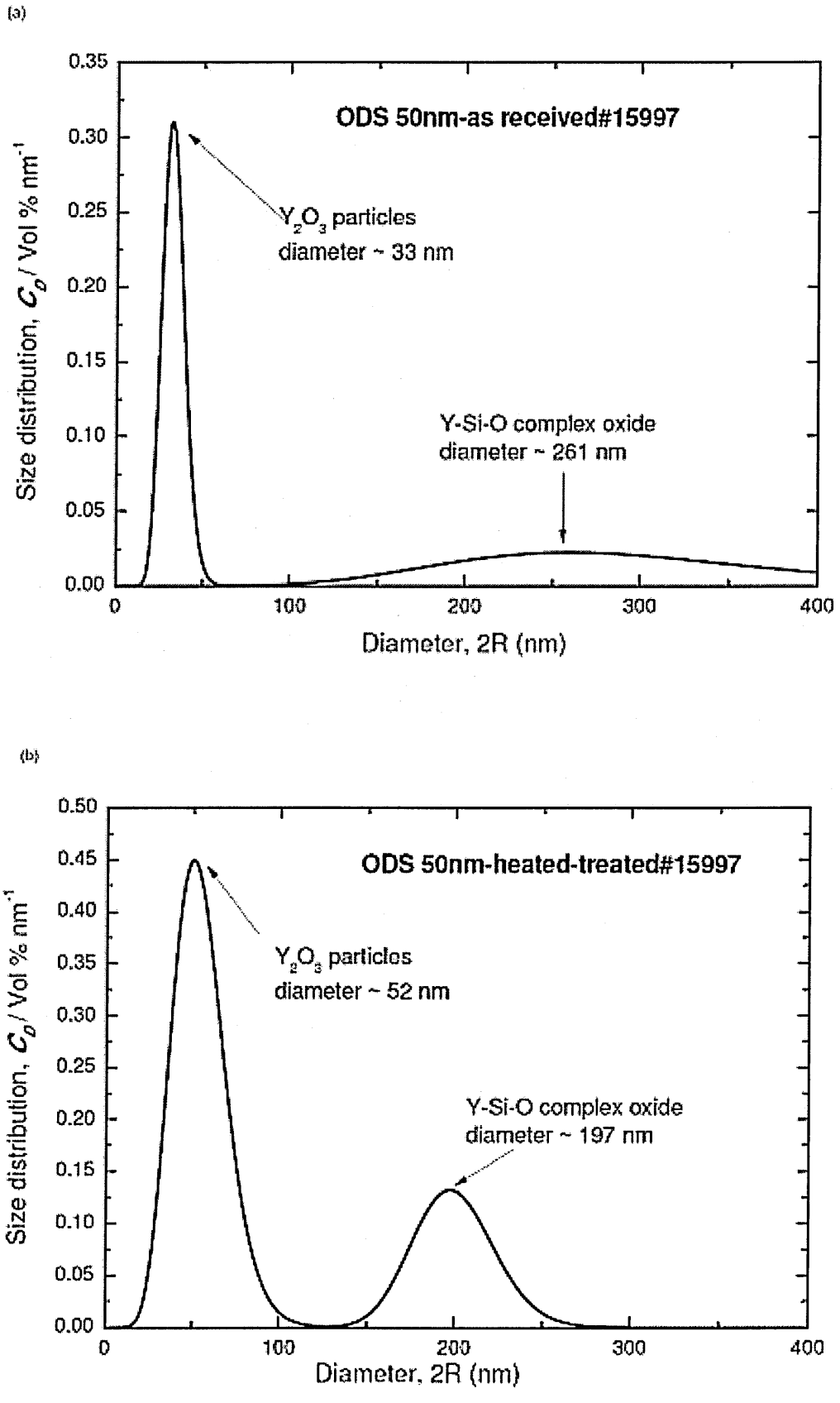

Fig. 6.2 SANS results of ODS 50 nm material (a) as-received (b) heat treated

and either remaining ytrria dissolved and precipitated as Y_2O_3 or remaining yttria stayed intact but just reduced in size so stayed in pure Y_2O_3 condition. Secondly, all the yttria powder were dissolved and some of them precipitated at SiO_2 particles and formed a new compound, $Y_2Si_2O_7$ and the rest precipitated homogeneously as Y_2O_3. Thirdly, it is the combination of the two possibilities as yttria interacted with SiO_2 during milling and the remaining yttria dissolved and precipitated both homogeneously (Y_2O_3) and at SiO_2 particles. In Fig. 6.3, an EDX result on a particle from ODS 50 nm material is shown. It can be seen that the amount of silicon (atomic %) is much higher than yttrium. However, as mentioned earlier, the formation of the complex oxide $Y_2Si_2O_7$, requires same amount of yttrium and silicon (2 Si + 2 Y atoms). Thus, the above observation may be attributed to the data collection from both SiO_2 and $Y_2Si_2O_7$ which favours the idea of interaction between particles.

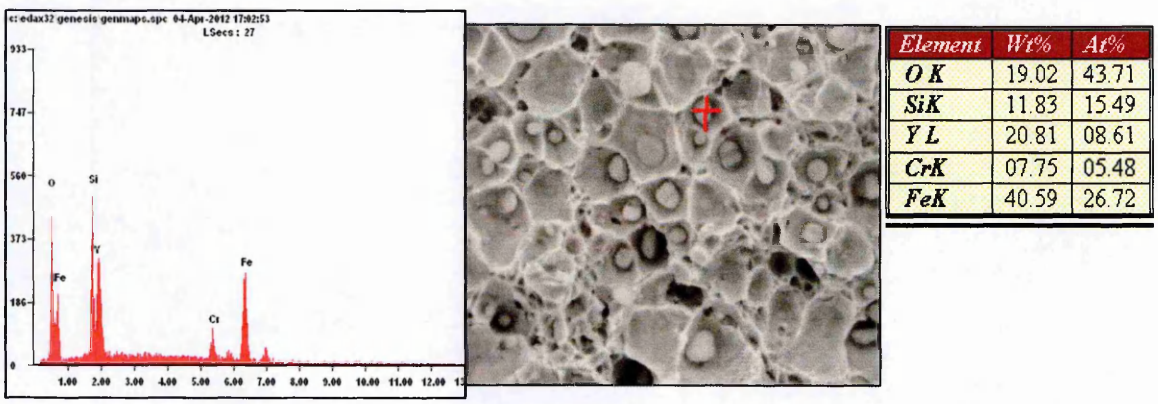

Element	Wt%	At%
O K	19.02	43.71
SiK	11.83	15.49
Y L	20.81	08.61
CrK	07.75	05.48
FeK	40.59	26.72

Fig. 6.3 EDX result from ODS 50 nm showing Si – Y atomic amounts

In the literature, it is reported that up to 15 wt. % yttria has been dissolved in ball milling in Fe-24 wt. % Cr steel [29]. Since the material being investigated contains 0.25 wt. % yttria, it can be assumed that it is highly likely that yttria

would have dissolved. On the other hand research on ODS manufacturing show that yttria doesn't dissolve during ball milling [27, 30]. It is just reduction in size to a few nanometers due to fracturing or amorphisation of yttria which take place at the interfaces of the matrix [27, 30]. In many ODS alternatives' research, the size of oxide clusters were found around 1-4 nm after dissolution and precipitation [31-35]. Even after heat treatment processes, after coarsening of particles, oxide clusters of size around 10 nm are observed [35]. So it is not likely to have oxide particles of 33 nm due to dissolution and precipitation mechanisms, because even initially, the yttria particles were reported as 50 nm. It looks like formations of oxide clusters in this project are mainly due to the interaction with SiO_2 particles during ball milling. Formation of pure Y_2O_3 particles (33 nm) detected in SANS can be attributed to size reduction due to fracturing in mechanical alloying process. Thus, it can be concluded that dissolution of yttria in ODS steels is not only amount dependant, but more particle size dependant because even 50 nm yttria could not be dissolved in the matrix which can be attributed to insufficient milling to reduce particle size. Size of the yttria particles should decrease to some extent for dissolution to occur as in theory; Y and O are thought to enter in the matrix lattice. So if the mechanical alloying process is not sufficient, fracturing of yttria particles may not be enough to dissolve in the matrix. However it is not possible to draw solid conclusions without carrying out some experiments during milling, for example interrupted milling X-ray diffraction to reveal content of the material after various times which was unfortunately not possible in this project. Another way of understanding the situation can be measuring the matrix lattice size before and after mechanical alloying. If there is dissolution mechanism, the lattice of the matrix must be distorted and this can be observable by diffraction

experiments. For example it was found that there is no lattice distortion in 9 Cr ODS steel and it was concluded that yttria did not dissolve [27]. Although it is not possible to be certain about amount of dissolution of yttria before carrying out actual experiments related to manufacturing of ODS steels, it can be noted that SiO_2 particles have a big effect on microstructure of ODS steels by possible preventing dissolution of some of the yttria and/or helping them to nucleate (if there is dissolution and precipitation) and form complex $Y_2Si_2O_7$ oxides. This complex oxide should not be mistaken with $Y_2Ti_2O_7$ or Y_2TiO_5 which are known to be better in strengthening ODS systems as Ti is added to ODS systems purposely to improve mechanical performance [28, 36, 37]. The sizes of the complex $Y_2Si_2O_7$ particles are relatively large due to interaction with large SiO_2 inclusions, with the size of the particles reaching 2 μm level in some cases which is not desirable.

As shown in Fig. 6.2, the size of the particles changed with heat treatment. The mean size of the Y_2O_3 increased from 33 nm to 52 nm after heat treatment whereas the mean size of the complex oxide $Y_2Si_2O_7$ decreased from 261 nm to 197 nm. It is expected to have larger clusters after heat treatment as particles coarsen at high temperatures. However the size of the complex oxide decreased. This can be as a possible result of some part of the complex oxide debonding and Y and O leaving the complex oxide and entering Y_2O_3 particles and the remaining Si entering into the matrix. Prolonged heat treatments and SANS experiments may help clarify this situation when compared with as-received condition and short term heat treated condition. It can also be seen that the peak of pure yttria (Y_2O_3) broadened and the peak of the complex oxide (Y-Si-O) became narrower after heat treatment. The broader peak can be due to an increase in size of the particles. The

narrower peak in the complex oxide is due to debonding of complex particles. The results also suggest that bigger complex oxide particles debonded prior to small ones because it is shown that minimum size of the complex particles increased in heat treated condition from around 100 nm to 150 nm but the average size together with the maximum size decreased So this can be attributed to preferential debonding of bigger particles.

When looking at the size distribution (volume fraction) of the particles, it can be seen that with heat treatment, volume % of the average sized particles of both yttria and the complex oxide increased. This percentage is the volume fraction of the particle to the overall volume of the same particle in the system not the whole system. Volume % of average size of yttria increased from 0.31 % to 0.45 % and for complex oxide, increased from 0.025 % to 0.15 %. For yttria it is due to size increase of the particles with heat treatment. So, average sized particles occupy more volume in the heat treated condition. On the other hand, the average size of the complex oxide particles decreases with heat treatment but the size distribution got narrower. So, although the average size decreased, this time there are fewer particles with very large particle size, thus relative volume occupied by average sized particles increased automatically.

SANS results from the ODS 0.9 μm are shown in Fig. 6.4. As the maximum size of the particles that can be measured by the available SANS instrument was limited to 400 nm, SANS results of ODS 0.9 μm do not give much information related to the particle sizes. Only the start of the size distribution graph of Y_2O_3 particles is obtained. However when compared to heat treated and as received

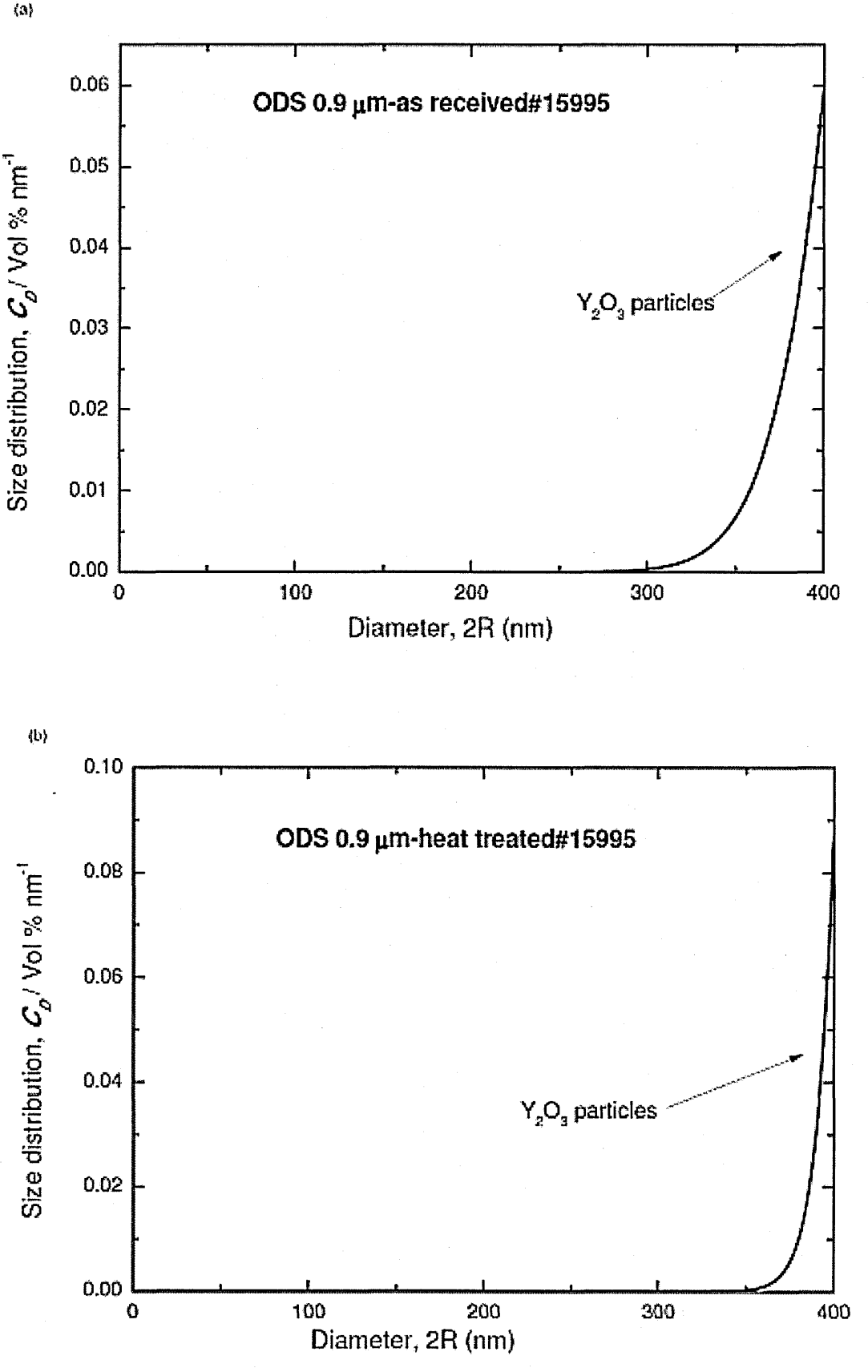

Fig. 6.4 SANS results of ODS 0.9 μm material (a) as-received (b) heat treated

results, it can be noted that the minimum size of the Y_2O_3 particles increases with heat treatment. Complex particles are much larger than 400 nm so these are not shown in the results. An important outcome of the SANS experiment on ODS 0.9 μm is the effect of the initial yttria size on the size of the oxide particles after manufacturing. SANS results showed that the average size of the pure Y_2O_3 particles in ODS 0.9 μm is greater than 400 nm in both as-received and heat treated conditions. This can contribute to the conclusion of dissolution of the yttria in ball milling did not occur due to very large yttria particle size which is 0.9 μm like in ODS 50 nm. Because if the yttria was dissolved in the matrix, then after precipitation during compaction few nanometer sized yttria particles would be observed in SANS which can have sizes even less than 1 nm [38]. It looks like yttria particles fractured into smaller pieces in the ball milling and some of those particles interacted with SiO_2 and formed complex oxides and the remaining ones stayed as pure Y_2O_3 particles.

SiO_2, MnS and $Y_2Si_2O_7$ inclusion particles are observable from both SEM and optical microscopy. SEM revealed another porosity issue in ODS 50 nm sample from the scond batch. Fig. 5.23 shows how the material is deformed in some areas as a consequence of porous regions just underneath the surface. Detailed investigations revealed porous regions very similar to the ones in ODS 0.9 μm from the first batch. From Fig. 5.24 it is very clear that those porous regions (as a result of argon entrapment) appear very smooth whereas the matrix separated regions (fractured) are rough and dimpled. Tiny voids are also visible in the porous region. This is why the fracture elongation of ODS 50 nm sample from

the second batch is limited to 6 % whereas ODS 0.9 μm from the same batch has 12 %. This is the effect of the porosity on the ductility of the materials.

Inclusions are known to have a negative effect on mechanical properties of steels since they are potential nucleation sites for microvoids and cracks [39-41]. The basic principle of fracture is microvoid nucleation and coalescence [42]. Propagation of a fracture is the combination of the nucleation of voids and the growth and/or coalescence of these voids due to plastic strain. One of the most important factors in the nucleation of voids is the interface bonds [43]. As the inclusions in the materials tend to have very low strength interface bonds, they are potential void nucleation points [44]. Even some inclusions like MnS, as found in our materials, can be considered as virtual voids. The reason is because such particles have lower interfacial energy, i.e. very little or no bond to the matrix surrounding them [45]. When the bond between particles and matrix is very low, the applied load on the sample can easily start separation of the matrix from the particles.

After voids are nucleated at the inclusions, they tend to elongate along the tensile direction by plastic extension up to a certain limit. This limit is defined as the distance between neighbour inclusions. When they reach that limit a slip plane occurs between voids and they coalesce [46]. This continues through all neighbouring inclusions and then fracture propagates leading material to complete rupture. The fractography analyses show inclusions inside the dimples which is the sign of microvoid nucleation and propagation. Fig. 6.5 shows the idea

of void elongation and coalescence under plastic extension, and crack propagation and matrix separation during fracture [46].

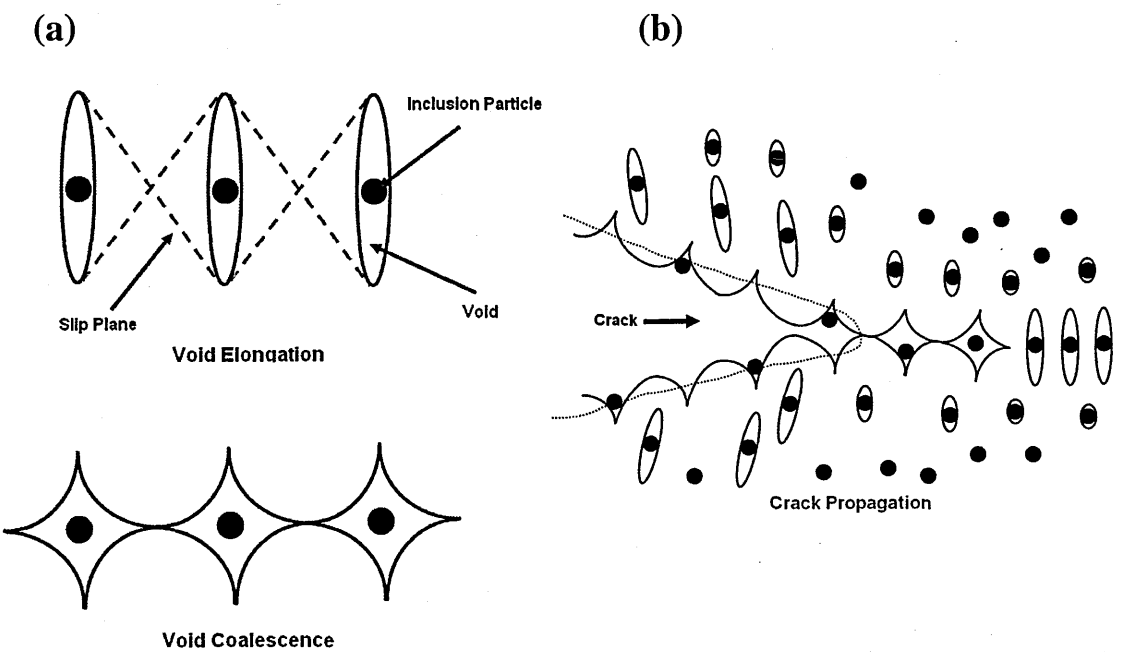

Fig. 6.5 Schematic illustration of a) void elongation and coalescence b) crack propagation

Thus, if the distance between these inclusions is small the plastic strain needed to coalesce the nucleated voids will be less, which means total fracture strain will be smaller and in consequence the material will present low ductility. So the amount and distribution of these particles are very important for mechanical properties of the materials.

There is another point affecting the microvoid nucleation and coalescence mechanism. It was shown that some of these inclusion particles are a formation of two or more particles which consequently increases particle sizes. This has a negative effect when compared to particles of smaller sizes, as larger particles tend to form voids at lower strains than smaller particles [46].

Another point with these non-metallic inclusions is that these particles can hinder dislocation motions as well however this needs a homogenous distribution of particles in the matrix. As these particles are mainly at grain boundaries and grain boundaries also hinder dislocation motion itself, there is no benefial effect. On the contrary, these particles help voids to nucleate and worsen the properties.

The non-metallic inclusion particles were better observed and quantified by the SEM fractography images than the optical metallography, as seen in Fig. 6.6. These particles are distributed in the matrix especially along grain boundaries but we can only detect the ones revealed during grinding and polishing in metallography samples. But when the fracture surface is examined, it is seen that these particles are everywhere in the matrix because of the path of voids and cracks. This also shows that fracture was along these particles. A basic illustration of why the particles in fracture surface of the tests are higher than the optical images in numbers is shown in Fig. 6.7.

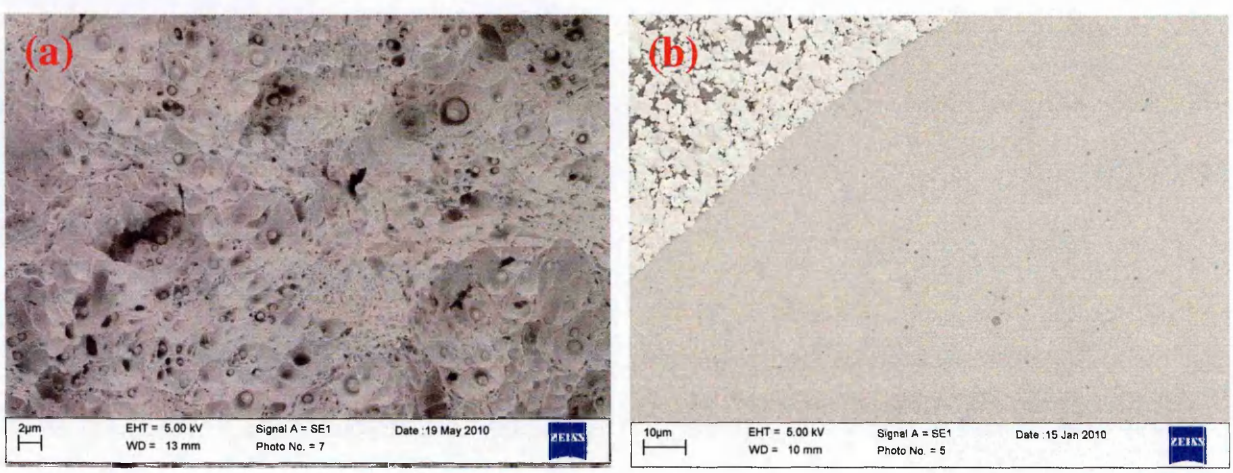

Fig. 6.6 SEM images of un-milled 410L (a) fracture surface and (b) unetched metallography

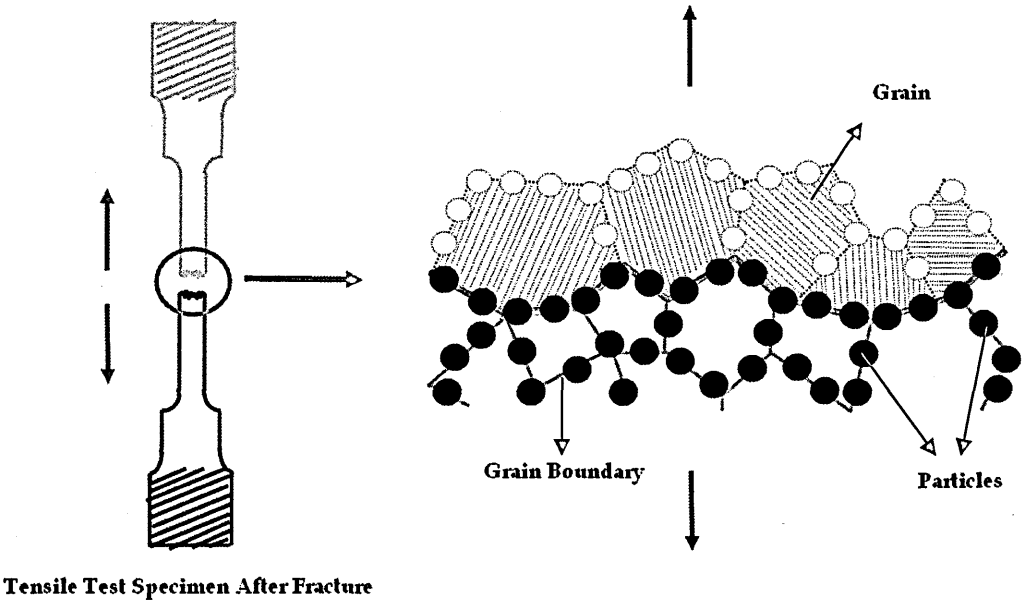

Fig. 6.7 Illustration showing why particle numbers in fracture surface and optical images is different after mechanical tests

In porous materials like ODS 0.9 μm from the first batch and ODS 50 nm from the second batch crack propagation is faster due to argon entrapped regions. No load is necessary to nucleate and caolesce micro voids. The schematic illustration in Fig. 6.8 shows how the crack propagation mechanism is in porous samples and explains the appearance of the SEM images after room temperature tensile tests of porous samples in Fig. 5.17 and Fig. 5.24 for ODS 0.9 μm from first batch and ODS 50 nm from second batch respectively. This is why some smooth regions are observed in fracture surfaces with some inclusion particles sitting on those regions.

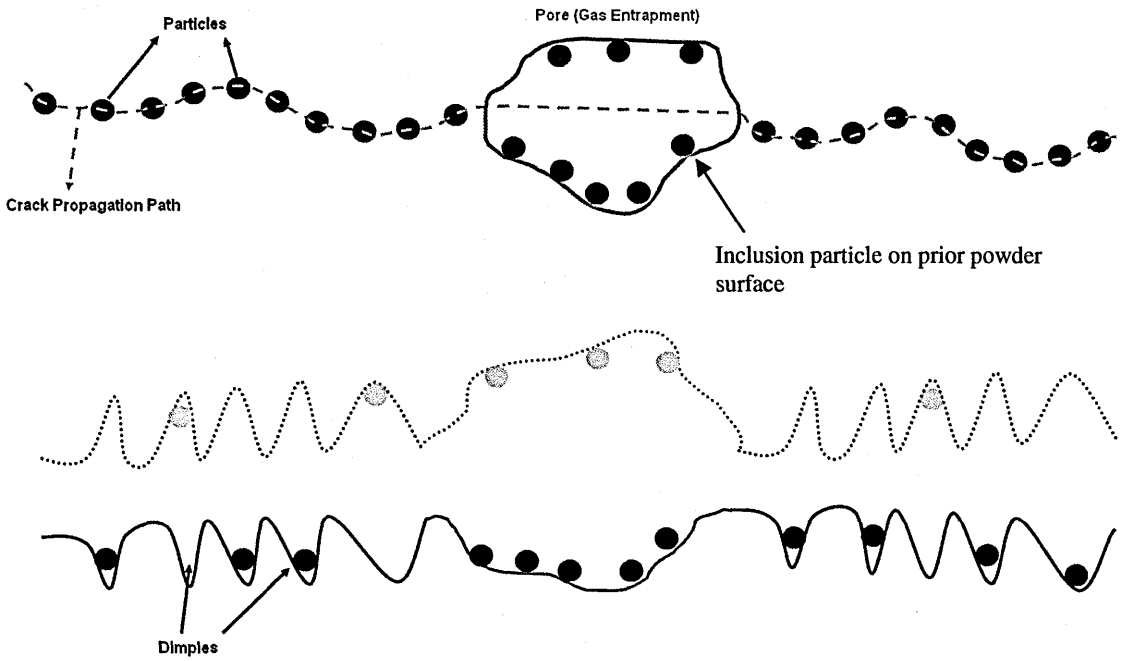

Fig. 6.8 Schematic illustration of crack propagation in porous material

High temperature tensile test values are around 270 MPa for yield strength and 290 MPa for ultimate tensile strength for all samples. As expected due to high temperature around 625 °C mechanical values decreased. If a dislocation meets an obstacle at room temperature, obviously where the diffusion process is very limited, dislocations pile up in front of the obstacle. So there are two options to go further in the materials: either Orowan loop or dislocation cutting. Because diffusion is limited so dislocation climb is not possible and this makes the material harder. But at high temperature vacancies can diffuse and let the dislocations to move more easily and so let them climb over obstacles. This is why hardened materials become weaker at high temperatures. In addition to that

due to temperature mobility of the atoms increase as well which also helps deformation.

Ductility values are nearly the same as room temperature values. Usually alloys with inclusions lose ductility at high temperatures due to diffusion of impurities to grain boundaries [47]. However in this case most of the particles are already at grain boundaries so there is no significant drop in ductility values.

The mechanism of fracture is the same which is void nucleation and propagation along particles through grain boundaries where the particles mainly situated. This can be easily observed from the SEM fracture surface images in Fig. 5.25 although there is huge amount of oxidation due to high temperature. Microvoid nucleation and coalescence is acting as the main mechanism for rupture.

Creep properties of both ODS and non-ODS samples are tabulated in Table 4.3. Best creep life belongs to 410 HIP with only 679 hours under 75 MPa load at 625 °C. Worst creep life is experienced with ODS 50 nm sample with 2.7 hours creep life under 150 MPa load. Creep performance of 410 ODS is way below the desired properties. Conventional produced 410 and 316 steels (316 - 16-18.5 % Cr, 10-14 % Ni, 2-3 % Mo) performed better in similar conditions. 410 reached creep life of 945 hours at 625 °C under 124 MPa stress and 316 has 8725 hours creep life at 650 °C under 108 MPa stress [48, 49].

Creep strain rates are increasing with increasing load as shown in Fig. 4.3. It is known that creep strain rates increase with increasing stress and temperature [47]. Larsson Miller parameters (LMP) have been proposed that predict the performance of the materials in the long term from short term tests and these are graphed in Fig. 4.5. All of the samples behaved similarly as in the stress vs time graph in Fig. 4.4. There is just one data point for 410L MA which is not in line with the others. Because of the scatter in the data as it is not possible to expect the material to behave the same every time in creep tests due to complex creep micro void mechanisms. If there were some more data in various conditions, trend line would be applied to data points to graph LMP. LMP results showed that these materials are not suitable for long term usage before some modifications and improvements related to either composition of manufacturing such as removing or replacing inclusion-making elements like Si, Mn and S.

Creep performance of the materials are compared with some other ODS steels from literature by LMP. Similar ODS alternatives' creep results are calculated from their LMP graphs for 625 °C under various stresses. For example ODS Eurofer with 0.3 wt. % Y_2O_3 after tempering at 750 °C for 2 hours has around 9200 hours creep life under 150 MPa load [50]. At 700 °C under 250 MPa load 12YWT with 0.25 wt. % Y_2O_3 after extrusion has a creep life of around 5000 hours [36]. Another ODS sample with 8 Cr and 1 W + 0.3 Y_2O_3 (wt. %) after rolling and heat treating at 750 °C for 1 hour performed around 700 hours under 200 MPa load at 700 °C [51]. This poor creep performance is again related to the particles at grain boundaries in the materials that has a big effect on the creep void nucleation and propagation and so failure of the sample. Porosity might be another reason for

poor creep life in ODS 50 nm sample which has 2.7 hours creep life under 150 MPa load at 625 °C but as comparison was not possible between porous and non-porous samples, this can not be proved. However it is very well known that pores at the boundaries help propagation of cracks and so shorten life [52].

Creep samples were sliced into two in the longitudinal direction and mounted and prepared for optical microscopy for crack and void investigations. These investigations showed clearly that particles are mainly at grain boundaries and cracks propagated along these particles. Very tiny voids are also visible around some particles showing the initial stages of void nucleation. These voids then combined together and formed big cracks which lead to rupture. The amount of cracks and voids are increasing with decreasing load because time of deformation is increasing as creep life increases. So more voids and cracks are generating and propagating as shown in Fig. 5.32.

It is very well known since the early 1900s that fracture mechanisms change from transgranular type to intergranular type with increasing temperature [53]. So grain boundaries have a very important role in creep life. These inclusions at grain boundaries are weakening the boundaries by leading to void nucleation and propagation. Homogenous distributions of particles are desired for better mechanical performance.

The other outcome of optical microscopy examinations is the effect of surface roughness. As can be seen from Fig. 5.33 the samples have a poor surface finish after machining. A macro image of a creep sample is shown in Fig. 6.9 to

reveal the surface profile. A laser scan was used on the surface of the sample to quantify the depth of the machining marks and to obtain the surface profile and the resulting graph is shown in Fig. 6.10. The macro image in Fig. 6.9 has been superimposed on the graph to show clearly how the surface varies along the length of the specimen. It can be seen from Fig. 6.10 that there are some scratches reaching 40 μm in depth. During machining material was tearing and the insert of the turning machine was broken many times. This is due to there being soft and hard regions in the material which makes the selection of tooling equipment very difficult to cover the whole range. Machining of Al-SiC is a comparable example. SiC is very hard and can be tooled by diamond but aluminium is very soft. For machining a radius tool was used and this caused grooves on the surface. It is thought that single point tool may produce a much better surface finish.

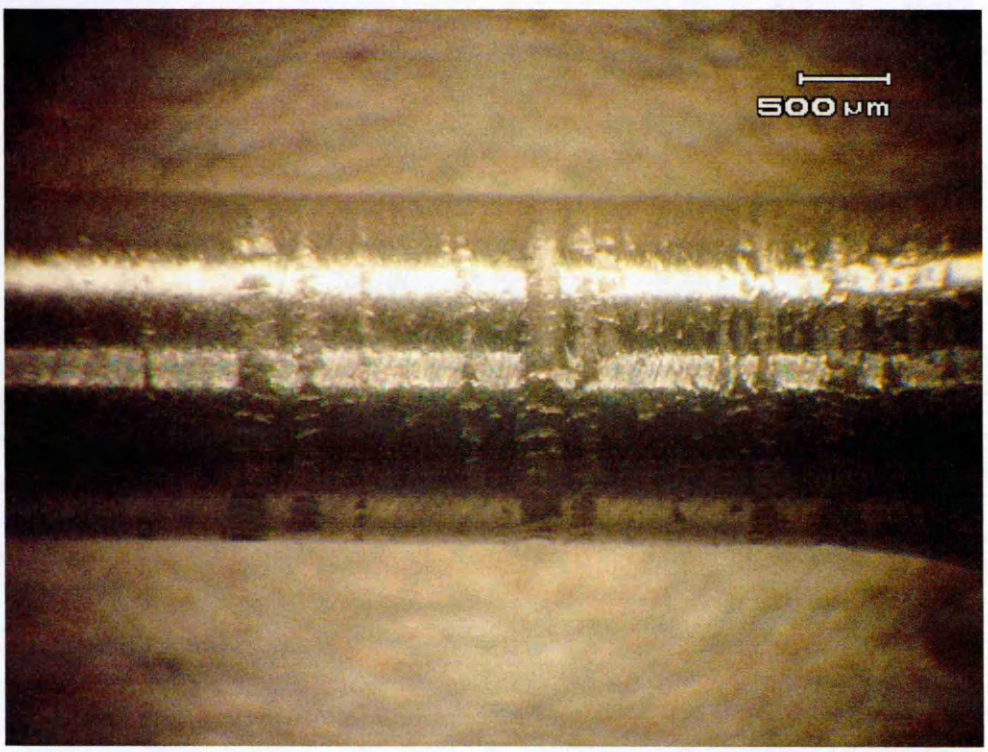

Fig. 6.9 Macro image of 410 MA mini creep sample revealing deep indents on the surface

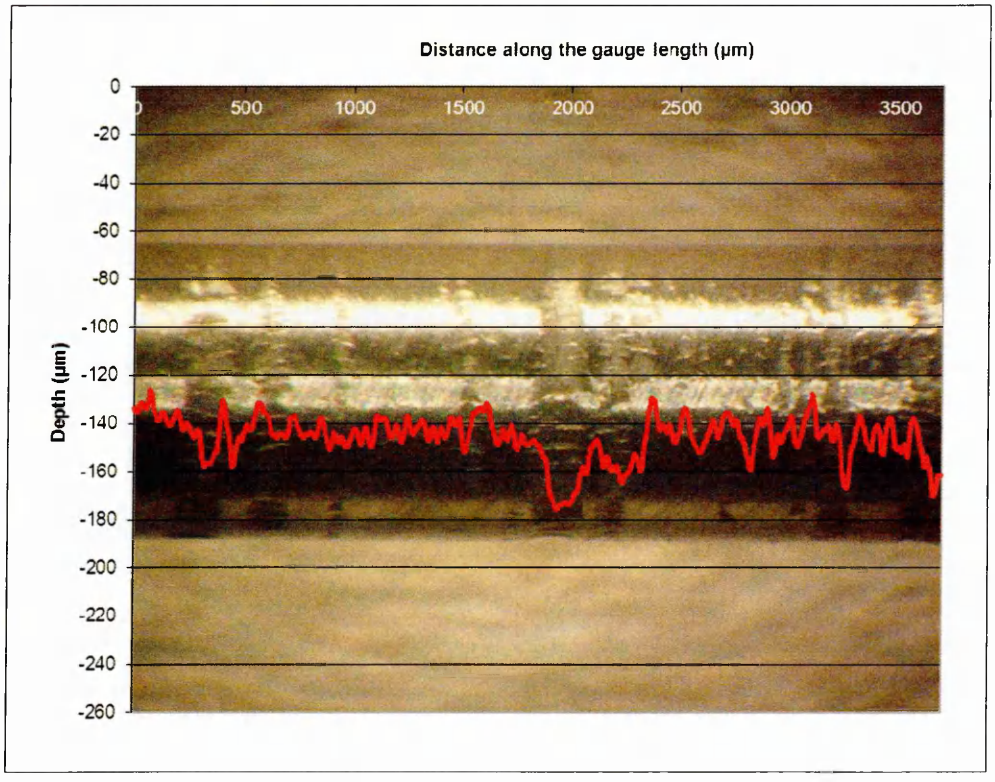

Fig. 6.10 Laser scan surface profile result on the surface of 410 MA mini creep sample showing dents up to 40 µm in depth

Surface roughness is a concern for the tests in two ways. Initially the cross sectional area of the sample is less than actually measured by calliper before the test. The calliper is not sensitive enough to consider scracthes on the surface which makes the actual area that load is applied to smaller than the appeared measured area. So load-stress calculations may not be correct if the surface is highly scratched and this will cause early failures. Secondly these scracthes are stress concentration points due to their sharp egdes which are initiating cracks and voids more easily than the ones inside the material. From Fig. 5.33, it can be seen that cracks were initiated and grown between scratches and they were about to cause the rupture in the material. It can be easily seen that regions with less rough surfaces are not showing any deep cracks in the same images. This is because

stress in those scratched regions are higher than calculated due to the reduction in cross sectional area, and easily initiated cracks by stress concentration.

The fracture surfaces of creep samples were also examined under SEM. Just like the high temperature tensile tests the surfaces of the samples are highly oxidized but still some features were observable as in Fig. 5.34 after 150 MPa tests. As the duration of these creep tests are very short they are like longer high temperature tensile tests. Fracture surface analyses are identical in both creep tests and high temperature tensile tests. The facture mechanism was through non-metallic inclusions and oxide particles. For this reason many particles are seen in dimples on the fracture surfaces.

Another point is that as creep life increases the amount of oxidation increases. However. only MnS particles are oxidized. SiO_2 and $Y_2Si_2O_7$ particles are seen as their initial condition. This is because these particles are already in a compound of oxygen. Oxidation of MnS can be seen in Fig. 6.11, (a) after creep test of 410L MA sample under 100 MPa load and (b) after high temperature tensile test of ODS 50 nm sample. It is clearly seen that how the morphology of the MnS side of particle is changing as it gets oxidized when compared with Fig. 6.12 which is MnS in an un-oxidized condition. EDX result is given in Fig. 6.13 to show the reaction.

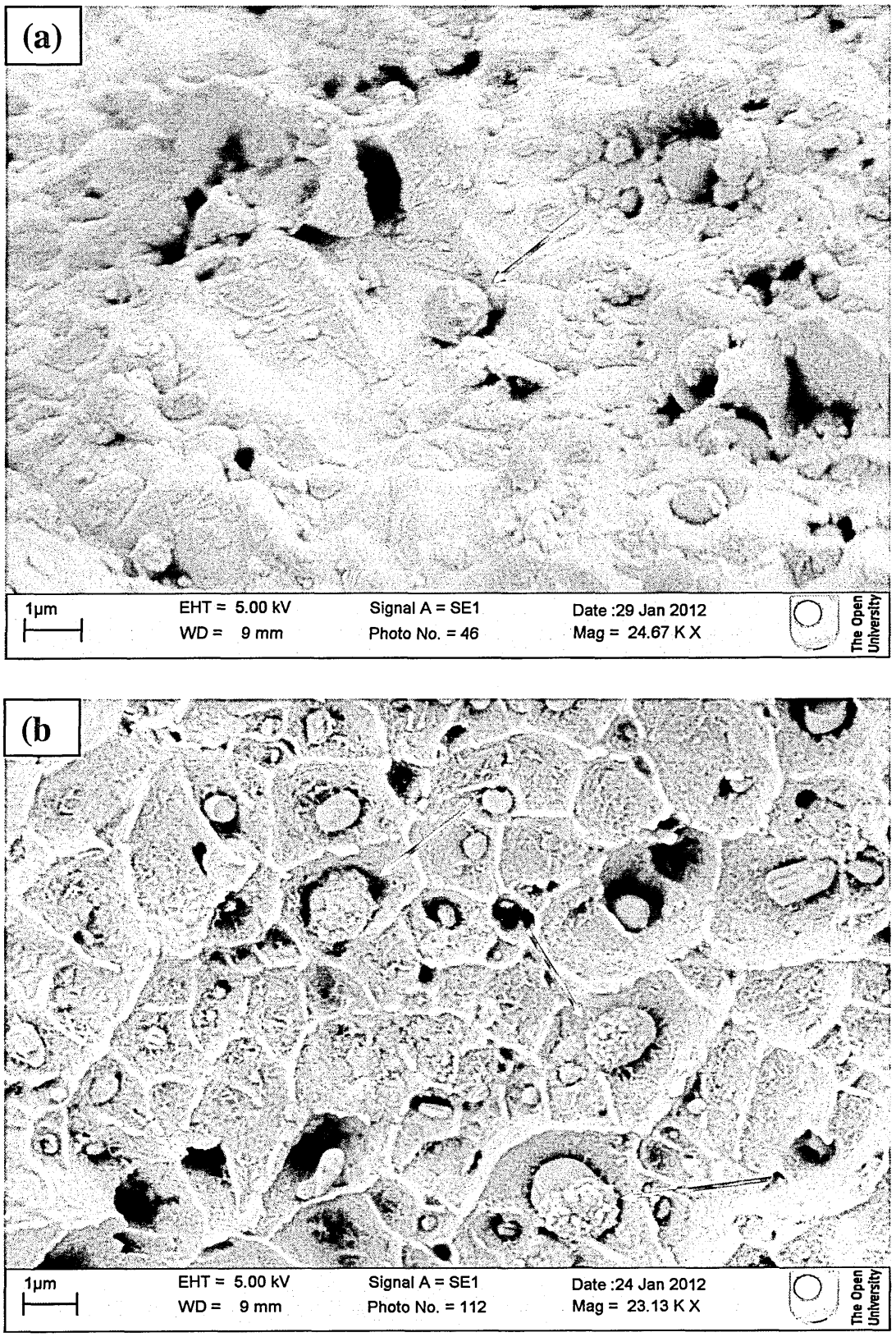

Fig. 6.11 SEM images of fracture surfaces of (a) 410L MA sample after 100 MPa creep test and (b) ODS 50 nm sample after high temperature tensile test

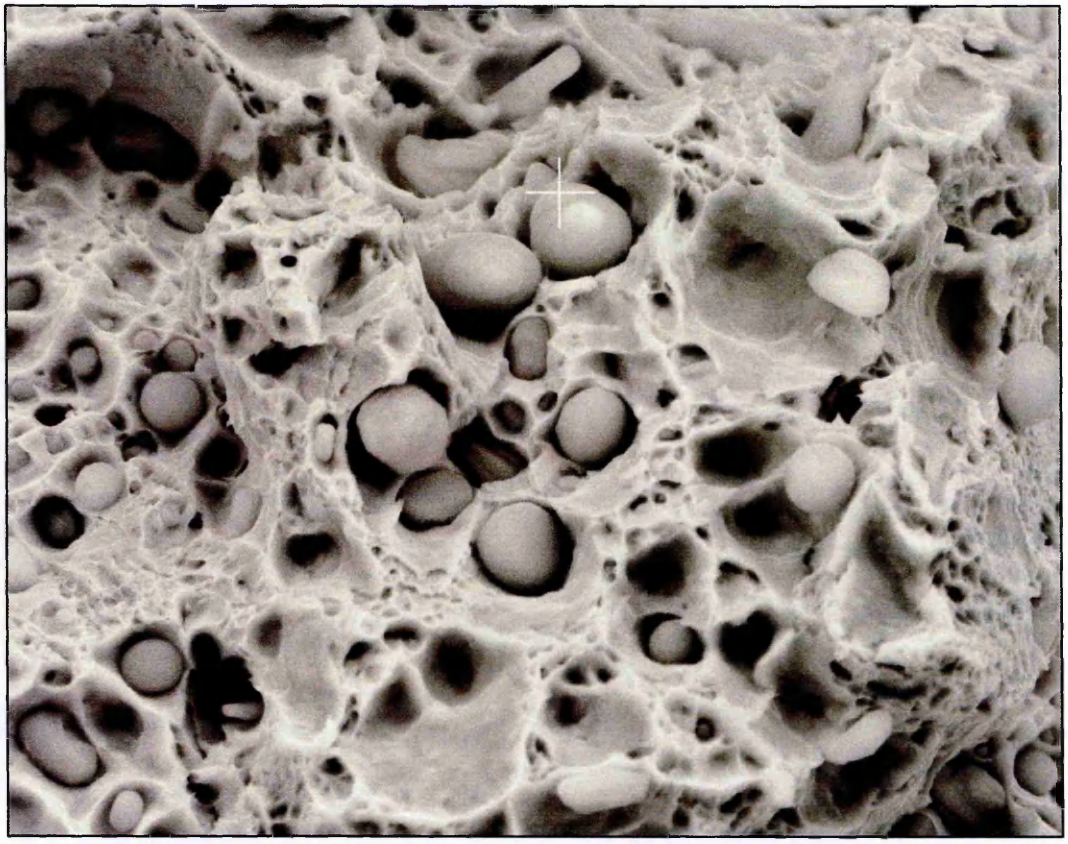

Fig. 6.12 Un-oxidized MnS particle in ODS 0.9 μm sample after tensile test

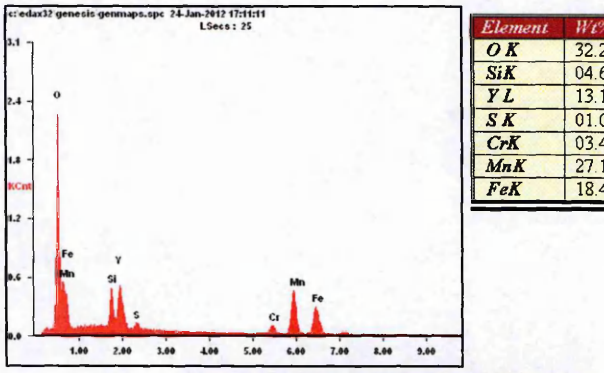

Element	Wt%	At%
O K	32.23	62.01
SiK	04.62	05.06
Y L	13.11	04.54
S K	01.02	00.98
CrK	03.40	02.01
MnK	27.14	15.21
FeK	18.47	10.18

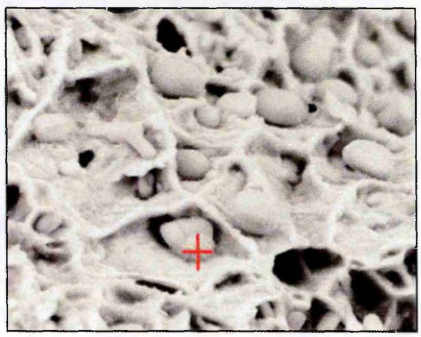

Fig. 6.13 EDX analysis result showing oxidation of MnS in ODS 0.9 μm sample after high temperature tensile test

Pure or small size oxide particles as Y_2O_3 distributed evenly are the aim when designing ODS material to achieve the desirable mechanical properties for high temperature applications. The material composition, alloying elements and production steps should be carefully considered in order to get a desirable designed microstructure. For example if the composition of the matrix does not include some inclusion prone elements such like silicon, manganese and sulphur, after manufacturing complex particles will not be experienced. There are some alternatives like 14YWT, 12YWT which includes only Cr, W and Ti and Y_2O_3 and performs very well during various mechanical tests. They have yield strength and ultimate strength values around 1600 MPa and 1300 MPa for YS and 1749 MPa and 1400 MPa for UTS for 14YWT and 12YWT respectively [13, 14]. Otherwise steel cleanness in the liquid state of the steel is very important before starting to manufacture the ODS steels. The amount of inclusions should be in ppm levels for desired properties [54]. For oxide inclusions using vacuum furnaces to melt the steel can be a solution to minimize oxygen content in the steel making atmosphere. For other inclusions like MnS, it is not possible to eliminate all of the inclusions because sulphur and manganese are not coming from outside of the system as they are already in the composition of 410L steel. Oxide powder for dispersion strengthening, which is Y_2O_3 in our case, is very important as well, especially purity and the size of the powder particles.

Manufacturing parameters and environment are very crucial for ODS steels. Milling parameters, type and time are important in powder metallurgy end products. Optimized milling conditions must be used for better results. Controlling and optimising the processing parameters should be investigated and

considered to achieve the desirable ODS microstructure and properties. Milling media, compaction, as well as degassing, are the most important steps for gas entrapment into the material which can cause porosity after consolidation because inclusions and porosity are the main concerns for powder metallurgy [55]. Process controls and leak checks can minimise the possibility of this argon entrapment during manufacturing. The milling media is important not only for porosity due to inert gas atmosphere, it is essential to have a clean milling environment to prevent up take of other elements and compounds from previous applications in the same media and/or from milling equipments. Contamination from the milling stage is quite common in powder metallurgy and is a major concern [56]. Using pure argon gas, minimizing milling times and also using the same materials as milling equipment can help to reduce the contamination from milling stage [57]. Studies on Eurofer showed that extension of milling time above 24 hours did not produce any apparent changes in the morphology and size of the particles so over milling just introduces more contamination rather than improvement [58].

After all milling and degassing stages, compaction is important as well. Pressure and temperature are the two main parameters for compaction because they can lead to incomplete densification in case of an insufficient compaction. However they can not resolve the gas entrapment issue because pressing the sample in a closed system can only change the shape and the place of the pores as there is gas in it. It would be the case if there is a stacking issue that in that case high pressures can increase the compaction percent.

After compaction, secondary processes may be very useful to improve mechanical properties. As these ODS materials are mainly used for nuclear structural components, industrial production will include some secondary treatments such as hot extrusion, rolling etc. As such, it is easier to interpret test results on such materials, because in reality all the samples will undergo some form of secondary processes. Heat treatment is a crucial step for all materials' productions. They can enhance the mechanical properties to a large extent.

References:

1. Morakotjinda, M., K. Fakpan, T. Yotkaew, N. Tosangthum, R. Krataithong, A. Daraphan, P. Siriphol, P. Wila, B. Vetayanugul, and R. Tongsri, *Gas Atomization of Low Melting-Point Metal Powders.* Chiang Mai Journal of Science, 2010. **37**(1): p. 55-63.
2. German, R.M., *Powder Metallurgy & Particulate Materials Processing.* 2005, New Jersey: Metal Powder Industries Federation.
3. Arias, A., *Metal Powder Reactions in Ball Milling.* Industrial & Engineering Chemistry Product Research and Development, 1976. **15**(2).
4. Crane, N.B., J. Wilkes, E. Sachs, and S.M. Allen, *Improving accuracy of powder-based SFF processes by metal deposition from a nanoparticle dispersion.* Rapid Prototyping Journal, 2006. **12**(5): p. 266-274.
5. Davis, J.R., *Stainless steels.* 1994: ASM International.
6. John D. Verhoeven, *Steel Metallurgy for the Non-Metallurgist.* 2007: ASM International. 203.
7. *410 Specification Sheet*, Sandmeyer Steel Company.
8. William D. Callister, J., *Materials Science and Engineering: An Introduction.* 2007: John Wiley & Sons.
9. de Castro, V., T. Leguey, A. Muñoz, M.A. Monge, P. Fernández, A.M. Lancha, and R. Pareja, *Mechanical and microstructural behaviour of Y2O3 ODS EUROFER 97.* Journal of Nuclear Materials, 2007. **367-370**(Part 1): p. 196-201.
10. Li, J.C.M., *Microstructure and Properties of Materials.* Vol. 2. 2000: World Scientific Publishing Co. Pte. Ltd.
11. Avettand-Fènoël, M.N., R. Taillard, J. Dhers, and J. Foct, *Effect of ball milling parameters on the microstructure of W-Y powders and sintered samples.* International Journal of Refractory Metals and Hard Materials. **21**(3-4): p. 205-213.
12. Iwata, N.Y., T. Liu, P. Dou, R. Kasada, A. Kimura, T. Okuda, M. Inoue, F. Abe, S. Ukai, S. Ohnuki, and T. Fujisawa, *Effects of MA environment on the mechanical and microstructural properties of ODS ferritic steels.* Journal of Nuclear Materials, 2011. **417**(1): p. 162-165.
13. Kim, J.H., T.S. Byun, and D.T. Hoelzer, *Tensile fracture characteristics of nanostructured ferritic alloy 14YWT.* Journal of Nuclear Materials, 2010. **407**(3): p. 143-150.
14. Sokolov, M.A., D.T. Hoelzer, R.E. Stoller, and D.A. McClintock, *Fracture toughness and tensile properties of nano-structured ferritic steel 12YWT.* Journal of Nuclear Materials, 2007. **367-370**(Part 1): p. 213-216.
15. McClintock, D.A., M.A. Sokolov, D.T. Hoelzer, and R.K. Nanstad, *Mechanical properties of irradiated ODS-EUROFER and nanocluster strengthened 14YWT.* Journal of Nuclear Materials, 2009. **392**(2): p. 353-359.
16. Paúl, A., E. Alves, L.C. Alves, C. Marques, R. Lindau, and J.A. Odriozola, *Microstructural characterization of Eurofer-ODS RAFM steel in the normalized and tempered condition and after thermal aging in simulated fusion conditions.* Fusion Engineering and Design, 2005. **75-79**: p. 1061-1065.
17. Bain, E.C., *The Alloying Elements in Steel.* 1939, Cleveland: ASM International.
18. Ballard, J., *Brittle Fracture.* 1997, Virginia Tech Materials Science and Engineering.
19. Schaeublin, R., T. Leguey, P. Spätig, N. Baluc, and M. Victoria, *Microstructure and mechanical properties of two ODS ferritic/martensitic steels.* Journal of Nuclear Materials, 2002. **307-311**(Part 1): p. 778-782.
20. Wu, C.P.P., *Inclusion Characterization in High Strenght Low Alloy Steel*, in *Materials Science and Engineering.* 2009, University of Toronto: Toronto.

21. Kutz, M., *Handbook of Materials Selection*, John Wiley & Sons. p. 44-46.
22. Kim, T.K., C.S. Bae, D.H. Kim, J. Jang, S.H. Kim, C.B. Lee, and D. Hahn, *Microstructural Observation and Tensile Isotropy of an Austenitic ODS Steel.* Nuclear Engineering and Technology, 2008. **40**(4).
23. Kopeliovich, D. *Non-metallic Inclusions in Steel.* [Online] Available from: http://www.substech.com/dokuwiki/doku.php?id=non-metallic_inclusions_in_steel [Accessed February 2012]
24. Sagaradze, V., A. Litvinov, K. Kozlov, V. Shabashov, N. Vil'danova, and N. Kataeva, *Manufacturing of oxide-dispersion-strengthened steels with the use of preliminary surface oxidation.* The Physics of Metals and Metallography. **112**(1): p. 53-60.
25. Olier, P., A. Bougault, A. Alamo, and Y. de Carlan, *Effects of the forming processes and Y2O3 content on ODS-Eurofer mechanical properties.* Journal of Nuclear Materials, 2009. **386-388**: p. 561-563.
26. Liu, D.-h., Y. Liu, D.-p. Zhao, Y. Wang, J.-h. Fang, Y.-r. Wen, and Z.-m. Liu, *Effect of ball milling time on microstructures and mechanical properties of mechanically-alloyed iron-based materials.* Transactions of Nonferrous Metals Society of China. **20**(5): p. 831-838.
27. Toualbi, L., M. Ratti, G. Andre, F. Onimus, and Y. de Carlan, *Use of neutron and X-ray diffraction to study the precipitation mechanisms of oxides in ODS materials.* Journal of Nuclear Materials. **417**(1-3): p. 225-228.
28. Ratti, M., D. Leuvrey, M.H. Mathon, and Y. de Carlan, *Influence of titanium on nano-cluster (Y, Ti, O) stability in ODS ferritic materials.* Journal of Nuclear Materials, 2009. **386-388**: p. 540-543.
29. Kimura, Y., S. Takaki, S. Suejima, R. Uemori, and H. Tamehiro, *Ultra Grain Refining and Decomposition of Oxide during Super-heavy Deformation in Oxide Dispersion Ferritic Stainless Steel Powder.* Iron Steel Inst Jpn, 1999. **39**(2): p. 176-182.
30. Dai, L., Y. Liu, and Z. Dong, *Size and structure evolution of yttria in ODS ferritic alloy powder during mechanical milling and subsequent annealing.* Powder Technology. **217**(0): p. 281-287.
31. Aleev, A.A., N.A. Iskandarov, M. Klimenkov, R. Lindau, A. Möslang, A.A. Nikitin, S.V. Rogozhkin, P. Vladimirov, and A.G. Zaluzhnyi, *Investigation of oxide particles in unirradiated ODS Eurofer by tomographic atom probe.* Journal of Nuclear Materials. **409**(2): p. 65-71.
32. Brocq, M., B. Radiguet, S. Poissonnet, F. Cuvilly, P. Pareige, and F. Legendre, *Nanoscale characterization and formation mechanism of nanoclusters in an ODS steel elaborated by reactive-inspired ball-milling and annealing.* Journal of Nuclear Materials. **409**(2): p. 80-85.
33. Heintze, C., F. Bergner, A. Ulbricht, M. Hernández-Mayoral, U. Keiderling, R. Lindau, and T. Weissgärber, *Microstructure of oxide dispersion strengthened Eurofer and iron-chromium alloys investigated by means of small-angle neutron scattering and transmission electron microscopy.* Journal of Nuclear Materials, 2011. **416**(1-2): p. 35-39.
34. Miller, M.K., K.F. Russell, and D.T. Hoelzer, *Characterization of precipitates in MA/ODS ferritic alloys.* Journal of Nuclear Materials, 2006. **351**(1-3): p. 261-268.
35. Miller, M.K., D.T. Hoelzer, E.A. Kenik, and K.F. Russell, *Nanometer scale precipitation in ferritic MA/ODS alloy MA957.* Journal of Nuclear Materials, 2004. **329-333**(Part 1): p. 338-341.
36. Kim, I.-S. and B.-Y. Choi, *Development of Fe–12%Cr mechanical-alloyed nano-sized ODS heat-resistant ferritic alloys.* Metals and Materials International, 2002. **8**(3): p. 265-270.

37. Oksiuta, Z. and N.L. Baluc, *Role of Cr and Ti Contents on the Microstructure and Mechanical Properties of ODS Ferritic Steels.* Advanced Materials Research, 2008. **59**: p. 308-312.
38. Coppola, R., M. Klimiankou, R. Lindau, R.P. May, and M. Valli, *SANS and TEM study of Y2O3 particle distributions in oxide-dispersion strengthened EUROFER martensitic steel for fusion reactors.* Physica B: Condensed Matter, 2004. **350**(1-3, Supplement 1): p. E545-E548.
39. Nowosielski, R., P. Akiewicz, and J. Mazurkiewicz, *Ductility Minimum Temperature phenomenon in as cast CuNi25 alloy.* Journal of Achievements in Materials and Manufacturing Engineering, 2006. **17**: p. 193-196.
40. Ozgowicz, W. and Gliwice-Wis, *The relationship between hot ductility and intergranular fracture in an CuSn6P alloy at elevated temperatures*, in *Achievments in Mechanical and Materials Engineering*. 2005: Poland. p. 503-508.
41. J.Sojka, P. Betakova, L. Hyspecka, L. Cizek, and M. Soza, *Role of non-metallic inclusion shape in hydrogen embitterment tested Rusing slow strain rate test*, in *Achievements in Materials and Manufacturing Engineering*. 2003: Gliwice-Zakopane, Poland. p. 821-824.
42. Sabirov, I. and O. Kolednik, *The effect of inclusion size on the local conditions for void nucleation near a crack tip in a mild steel.* Scripta Materialia, 2005. **53**(12): p. 1373-1378.
43. Liu, A.F., *Mechanics and Mechanisms of Fracture: An Introduction.* 2005: ASM International.
44. Jun, S., *Strength for decohesion of spheroidal carbide particle-matrix interface.* International Journal of Fracture, 1990. **44**(4): p. R51-R56.
45. Becker, W.T. and R.J. Shipley, *ASM Handbook, Volume 11 - Failure Analysis and Prevention*, ASM International. p. 591-593.
46. Brown, L.M. and J.D. Embury, *The Initiation and Growth of Voids at Second Phase Particles* in *3 rd International Conference on Strength of Metals and Alloys.* 1973, Institution of Metals: London. p. 164-169.
47. Campbell, F.C., *Elements of Metallurgy and Engineering Alloys.* 2008: ASM International.
48. MatNavi, *Creep Data Sheet*, National Institute for Materials Science (NIMS).
49. Polar, A., J.E. Indacochea, and M.L. Wang, *Sensing Creep Evolution in 410 Stainless Steel by Magnetic Measurements.* Journal of Engineering Materials and Technology. **132**(4): p. 041004-7.
50. Lindau, R., A. Möslang, M. Rieth, M. Klimiankou, E. Materna-Morris, A. Alamo, A.A.F. Tavassoli, C. Cayron, A.M. Lancha, P. Fernandez, N. Baluc, R. Schäublin, E. Diegele, G. Filacchioni, J.W. Rensman, B.v.d. Schaaf, E. Lucon, and W. Dietz, *Present development status of EUROFER and ODS-EUROFER for application in blanket concepts.* Fusion Engineering and Design, 2005. **75-79**: p. 989-996.
51. Shinozuka, K., M. Tamura, H. Esaka, K. Shiba, and K. Nakamura, *Creep behavior of oxide dispersion strengthened 8Cr-2WVTa and 8Cr-1W steels.* Journal of Nuclear Materials, 2009. **384**(1): p. 1-5.
52. Sakasegawa, H., S. Ohtsuka, S. Ukai, H. Tanigawa, M. Fujiwara, H. Ogiwara, and A. Kohyama, *Microstructural evolution during creep of 9Cr-ODS steels.* Fusion Engineering and Design, 2006. **81**(8-14): p. 1013-1018.
53. KURT, A.O., *Malzemelerin Yuksek Sicaklik Davranıslari*, in *Metallurgical and Materials Engineering Lecture Notes*. 2008-2009, Sakarya University: Sakarya.
54. Wünnenberg, K., *IISI study on clean steel.* La Revue de Métallurgie, 2005.
55. Miner, R. and R. Dreshfield, *Effects of fine porosity on the fatigue behavior of a powder metallurgy superalloy.* Metallurgical and Materials Transactions A, 1981. **12**(2): p. 261-267.

56. Suryanarayana, C., E. Ivanov, and V.V. Boldyrev, *The science and technology of mechanical alloying.* Materials Science and Engineering, 2001. **A304-306**: p. 151-158.
57. King, M., *Review of Ball Milling*. 2004, Durham University: Durham.
58. de Castro, V., T. Leguey, M.A. Monge, A. Muñoz, R. Pareja, D.R. Amador, J.M. Torralba, and M. Victoria, *Mechanical dispersion of Y2O3 nanoparticles in steel EUROFER 97: process and optimisation.* Journal of Nuclear Materials, 2003. **322**(2-3): p. 228-234.

CHAPTER 7: SUMMARY, CONCLUSION AND FUTURE WORK

In this chapter all the activities, experiments and findings in this project are briefly summarized, key points are emphasized, and ideas and advices to take forward and broaden the project and area of interest are presented.

This work presents the results of a study on characterization of a powder metallurgy processed oxide dispersion strengthened 410L alloy in order to assess the production route, an industrial/commercial one rather than lab conducted. For this reason the materials were manufactured by a professional company with high tech powder metallurgy facilities. The microstructural evolution, characterization and mechanical properties were examined and measured before and after final production. Discovered problems and results from the tests are examined and possible reasons and outcomes are discussed and possible solutions are presented.

The base material used as the matrix is AISI 410 (12Cr) an extensively tested martensitic grade stainless steel. The ODS variations were produced with Y_2O_3 (yttria) precipitates of 0.9 μm and 50 nm. Four different materials were prepared from 12 Cr martensitic steel alloyed powders. One material was produced by mechanical alloying (MA) and compacted via hot isostatic pressing (HIP). The other was manufactured using un-milled metal powder. The other two materials were ODS steels with 0.25 wt. % Y_2O_3 produced by MA followed by HIP with different oxide particle sizes. One ODS material has Y_2O_3 particle size of 0.9 μm and the other has 50 nm. All of the materials are delivered after HIP process

without any further treatments, so they are all as-HIP condition, which is referred to as the as-received condition.

Characterization of the materials were carried out in both mechanical and microstructural characterization which includes room and high temperature tensile tests and creep tests for mechanical characterization and visual with compositional analysis for material characterization just before and after the tests. In addition SANS and SEM techniques were utilized.

The yttria powders contained some powder particles more than 30 μm in size and composition of nearly pure yttrium. The metal 410L powder particles have small satellites attached to the big particles which are detrimental for compaction [1].

Next step was heat treatment. Samples were heat treated to obtain a standard microstructure of tempered martensite and to remove residual ferrites from manufacturing processes. Heat treatment parameters were austenitizing at 1000 °C for 30 mins and quenching after that tempering at 650 °C for 2 hours and furnace cooling.

Mechanical tests started with room temperature tensile tests. Yield strength (YS) values are around 670-690 MPa and ultimate tensile strength (UTS) values are in between 815-860 MPa. The oxide particles give a slight improvement on mechanical properties of the ODS materials however it is not significant which is because all samples including non-ODS ones have some inclusion particles

hindering dislocation motions in the system and hardening the materials [2]. Results of room temperature tensile tests are way below other ODS alternatives such as 14YWT, 12YWT and ODS Eurofer 97 [3-5]. The reasons for this difference are explained in the discussion chapter (chapter 6) as the effect of inclusion particles, secondary processes and compositional variations. Inclusion particles in our ODS alloys help void nucleation and coalescence and so decrease mechanical performance. Secondary processes on alternative ODS alloys introduce work hardening on the materials so improve mechanical properties. Compositional variation is very crucial on ODS alloys as each element may effect mechanical strength of the materials.

Some porosity is detected in two of the samples, ODS 0.9 μm from first batch and ODS 50 nm from second batch, due to argon gas entrapment during the milling process. Detrimental effect of porosity on properties is clearly explained in discussion chapter as it accelerates the void and crack coalescence and growth during mechanical tests [6].

In two of the samples (410L MA from second batch and ODS 50 nm from first batch) TiN inclusions were detected which is most probably coming from the steel powder as it was not a clean steel. However the TiN did not have a significant effect on mechanical properties.

Extensive investigation was carried out on inclusion particles in the materials. These particles are found to be SiO_2, MnS and $Y_2Si_2O_7$ (only in ODS samples) and formation of these particles are explained as elemental interaction

due strong de-oxidation (SiO_2), de-sulfurization (MnS) reactions and interactions during the milling stage between SiO_2 and Y_2O_3 and/or dissolution and precipitation of Y_2O_3 at SiO_2 particles [7]. Some particles are a combination of two or more particles. These particles are potential nucleation sites for microvoids and cracks because of their weak bonds to the matrix [8-10].

High temperature tensile tests were done at 625 °C. Results are around 270 MPa for YS and 290 MPa for UTS. The failure mechanism was the same as at room temperature, as microvoid nucleation and propagation along inclusion particles and oxide particles in the system.

Creep tests are again conducted at the same temperature, 625 °C, under 75 MPa, 100 MPa and 150 MPa stresses. Results are not promising as the worst creep life is 2.7 hours under 150 MPa load belonging to ODS 50 nm sample. Creep performance of the steels are worse than other ODS alternatives like ODS Eurofer 97, 12YWT and 8Cr-1W [11-13]. Particles at grain boundaries were again the main reason for poor creep life.

With optical analyses after creep tests, the effects of particles at grain boundaries are clearly indicated as it was observed that voids were mostly situated along grain boundaries at particles. Poor surface quality was revealed during optical analyses and negative effects for mechanical properties are discussed which are potential stress concentration points at scratches on the surface and smaller actual cross-section area of the sample than apparent

measured area of the sample. The reason for poor surface quality is linked to improper selection of tooling equipment.

Possible roots of problems like steel cleanness for inclusion problem and manufacturing defects like porosity are discussed and potential solutions like optimizing manufacturing conditions especially milling, degassing and compaction and using vacuum furnaces for decreasing oxygen content are discussed in the discussion chapter (chapter 6). As manufacturing parameters were not provided due to commercial sensitivity of the information, accurate solutions and certain roots of problems could not be defined.

A SANS experiment revealed pure Y_2O_3 particles in ODS 50 nm. Size of the oxides are around 33 nm in as-received condition which is quite big compared to other ODS systems with up to 4 nm oxide cluster size. It is concluded that yttria did not dissolve during ball milling. Formations of complex oxide, $Y_2Si_2O_7$, particles were explained as interaction of yttria and SiO_2 particles during high energy ball milling. As a result, it is discovered that SiO_2 inclusions also affect ODS manufacturing by causing complex oxide formations in addition to their effect on void nucleation and propagation. It is also realized that size of the initial yttria powder is very important for ODS manufacturing as it is a key factor in ytrria dissolution during mechanical alloying which is desired for ODS alloys in theory. Because even 50 nm size yttria powders in ODS 50 nm material could not be dissolved during the ball milling either because of SiO_2 interactions or having big size to dissolve. It may be due to insufficient ball milling as it can limit the size

reduction due to fracturing. SANS results of ODS 0.9 μm could not be observed because of the upper size limit (400 nm) of particles that can not be resolved.

After all these mechanical and material characterization work, main outcomes of this work are:

1) What are the possible problems and facts due to steel preparation and existing industrial/commercial powder metallurgy manufacturing route because in real time application, materials cannot be processed in laboratories.
2) How these problems and facts affect the material production and mechanical performance of an off the shelf extensively tested basic 12 Cr 410L martensitic novel ODS steel rather than specifically modified composition.
3) Effect of the size of initial yttria powder on dissolution mechanism during mechanical alloying.

First one is about the non-metallic and complex inclusion particles (SiO_2, MnS and $Y_2Si_2O_7$), TiN inclusion and porosity problem. The findings about the SiO_2 and MnS inclusion particles and their detrimental role (aiding void nucleation and coalescence) in mechanical performance of the steel enhance our understanding of the importance of having a clean steel first of all before starting manufacturing of an ODS alloy. In addition, having inclusion particles of SiO_2 can cause chemical interactions with Y_2O_3 powder particles and form complex oxides, $Y_2Si_2O_7$. TiN inclusion was observed in two materials but it is realized that it did

not have significant effect on mechanical properties. Porosity is a major concern for powder metallurgy applications and if can not be eliminated it can cause poor mechanical performance. All these findings above are some of possible problems that can be faced during industrial production of ODS alloys and it is important to understand what kind of effects they can have on the mechanical and material performance of the ODS alloys.

Second one is about the mechanical and material characterization of the commercial 410L steel. As this project was a trial experiment of using commercially available steel rather than using specifically modified steel, mechanical tests helped to observe how an industrial ODS alloy behaved at different conditions and tests. As a result of all the mechanical analysis and investigations, performance of 410L ODS and non-ODS materials are not comparable with other ODS alternatives. The reason is defined as compositional variations, inclusion particles and missing secondary processes.

Last one is related to the mechanisms during high energy ball milling. ODS alloys are proposed to dissolve yttria powders during ball milling and then they precipitate yttria in few nanometer size during HIPing. The empirical findings in this study provide a new understanding of interactions of yttria powders during ball milling. SANS results show that 50 nm yttria did not dissolve during ball milling, just fracturing and size reduction to mean size of 33 nm took place in as-received condition. SANS results of ODS 0.9 μm also agrees with the conclusion. This phenomenon can be either due to insufficient milling or interference of yttria and SiO_2 to form complex $Y_2Si_2O_7$ particles. It is also obtained with SANS that

during heat treatment size of complex oxide particles decreased whilst size of pure yttria particle increased. This can be concluded as Y and O leaves complex oxide particles and enter pure yttria particles due to de-bonding and remaing Si enters the matrix.

This work helped to understand some key points but further research is necessary to broaden the ODS steels area and improve the performance of the materials.

First of all it is obvious that there should be some modifications and improvements to be done for the material. Choosing a different composition without potential inclusion-making elements like Si, Mn and S or achieving a microstructure with no inclusion particles by controlling the steel making process would help to understand powder metallurgy effects better, because eliminating liquid inclusions effects will clarify other effects. It would verify the effect of particles on mechanical properties if pure 410L steel powder without non-metallic inclusions can be produced. Actual performance of 410L ODS steel in mechanical tests can be seen as well. Otherwise 14YWT and 12YWT are good alternatives with only Cr and W elements in the composition to be produced in industrial/commercial production route and thereafter tested.

In order to make a good comparison with other ODS alternatives and simulate real conditions manufactured materials should go for a secondary processing like extrusion or rolling etc, because in real applications these materials

will be in a specific shape like tubes. And these secondary deformations will introduce strength to the material [2].

Future work shall include controlling and optimizing process parameters especially the mechanical alloying step. Controlling and analysing the mechanisms in the alloying is very important especially dissolution of yttria particles and their precipitation in compaction. X-ray diffraction can be utilized for examining the material in interrupted milling. Diffraction techniques are usable as well by determining the lattice parameters of the matrix to see if there is any dissolution of oxide dispersions in the steel matrix as it is expected that lattice parameters will increase if dissolution occurs.

Very detailed TEM investigations can be done for deeper understanding of the dislocation mechanisms and void evolutions and their relations with the particles inside the system. TEM experiments can also give some detailed information about the particle formation and structure via diffraction patterns.

Neutron irradiation experiments can be done in order to see the performance of the steel in similar operating environment. Effects of oxides and other non-metallic inclusions can be discussed as they are potential radiation defects nucleation sites [14].

Atom probe tomography experiments can help to understand the distribution of the elements inside the microstructure and in addition to that XRD measurements can indentify the compounds, particles and oxides in the system so

considering both of the results detailed information about particle distribution and interaction can be achieved.

SANS experiments after long term heat treatment may help to understand better the effect of heat treatment on size of pure Y_2O_3 and $Y_2Si_2O_7$ particles. It can clarify the issue of transfer of Y and O from complex oxide to pure yttria particles.

Although there is some more future work can be done on these materials it is highly recommended to continue research in this area (mechanical and material characterization of ODS steels) with a different composition material without non-metallic inclusions in the system. Same tests can be done on the new material. That time there will be just oxide particles in the system as Y_2O_3 without any chemical reaction with other inclusion elements.

References

1. German, R.M., *Powder Metallurgy & Particulate Materials Processing*. 2005, New Jersey: Metal Powder Industries Federation.
2. William D. Callister, J., *Materials Science and Engineering: An Introduction*. 2007: John Wiley & Sons.
3. Kim, J.H., T.S. Byun, and D.T. Hoelzer, *Tensile fracture characteristics of nanostructured ferritic alloy 14YWT*. Journal of Nuclear Materials. **407**(3): p. 143-150.
4. Sokolov, M.A., D.T. Hoelzer, R.E. Stoller, and D.A. McClintock, *Fracture toughness and tensile properties of nano-structured ferritic steel 12YWT*. Journal of Nuclear Materials, 2007. **367-370**(Part 1): p. 213-216.
5. McClintock, D.A., M.A. Sokolov, D.T. Hoelzer, and R.K. Nanstad, *Mechanical properties of irradiated ODS-EUROFER and nanocluster strengthened 14YWT*. Journal of Nuclear Materials, 2009. **392**(2): p. 353-359.
6. Schaeublin, R., T. Leguey, P. Spätig, N. Baluc, and M. Victoria, *Microstructure and mechanical properties of two ODS ferritic/martensitic steels*. Journal of Nuclear Materials, 2002. **307-311**(Part 1): p. 778-782.
7. Kim, T.K., C.S. Bae, D.H. Kim, J. Jang, S.H. Kim, C.B. Lee, and D. Hahn, *Microstructural Observation and Tensile Isotropy of an Austenitic ODS Steel*. Nuclear Engineering and Technology, 2008. **40**(4).
8. Nowosielski, R., P. Akiewicz, and J. Mazurkiewicz, *Ductility Minimum Temperature phenomenon in as cast CuNi25 alloy*. Journal of Achievements in Materials and Manufacturing Engineering, 2006. **17**: p. 193-196.
9. Ozgowicz, W. and Gliwice-Wis, *The relationship between hot ductility and intergranular fracture in an CuSn6P alloy at elevated temperatures*, in *Achievments in Mechanical and Materials Engineering*. 2005: Poland. p. 503-508.
10. J.Sojka, P. Betakova, L. Hyspecka, L. Cizek, and M. Soza, *Role of non-metallic inclusion shape in hydrogen embitterment tested Rusing slow strain rate test*, in *Achievements in Materials and Manufacturing Engineering*. 2003: Gliwice-Zakopane, Poland. p. 821-824.
11. Lindau, R., A. Möslang, M. Rieth, M. Klimiankou, E. Materna-Morris, A. Alamo, A.A.F. Tavassoli, C. Cayron, A.M. Lancha, P. Fernandez, N. Baluc, R. Schäublin, E. Diegele, G. Filacchioni, J.W. Rensman, B.v.d. Schaaf, E. Lucon, and W. Dietz, *Present development status of EUROFER and ODS-EUROFER for application in blanket concepts*. Fusion Engineering and Design, 2005. **75-79**: p. 989-996.
12. Kim, I.-S. and B.-Y. Choi, *Development of Fe–12%Cr mechanical-alloyed nano-sized ODS heat-resistant ferritic alloys*. Metals and Materials International, 2002. **8**(3): p. 265-270.
13. Shinozuka, K., M. Tamura, H. Esaka, K. Shiba, and K. Nakamura, *Creep behavior of oxide dispersion strengthened 8Cr-2WVTa and 8Cr-1W steels*. Journal of Nuclear Materials, 2009. **384**(1): p. 1-5.
14. Hsiung, L., M. Fluss, S. Tumey, J. Kuntz, B. El-Dasher, M. Wall, B. Choi, A. Kimura, F. Willaime, and Y. Serruys, *HRTEM study of oxide nanoparticles in K3-ODS ferritic steel developed for radiation tolerance*. Journal of Nuclear Materials. **409**(2): p. 72-79.